Organic-inorganic composite materials for specific recognition and optical detection of environmental, food and biomedical analytes

Maria Panagiotopoulou

Par **Maria PANAGIOTOPOULOU**

Organic-inorganic composite materials for specific recognition and optical detection for environmental, food and biomedical analytes

Thèse présentée
pour l'obtention du grade
de Docteur de l'UTC

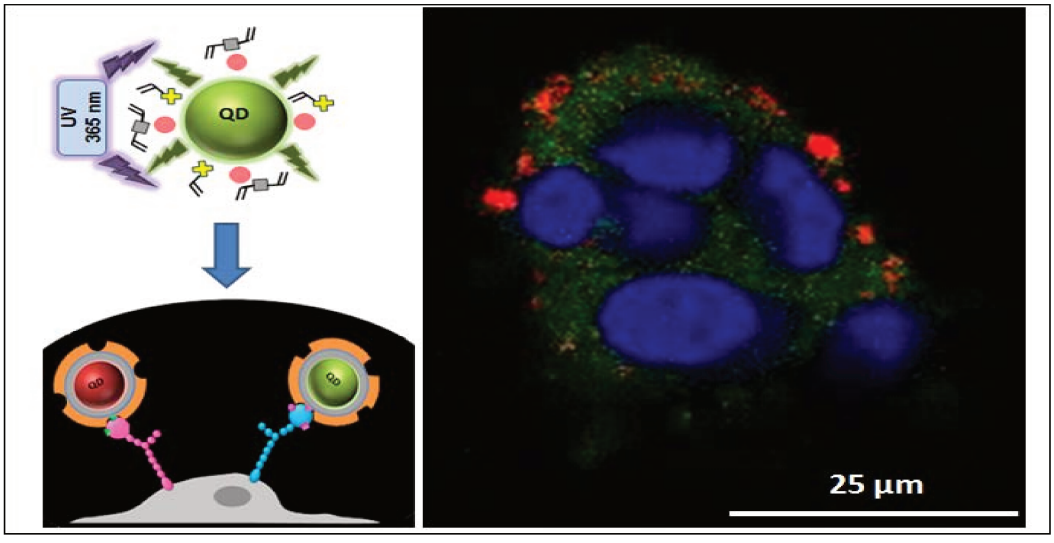

Soutenue le 9 décembre 2016
Spécialité : Biotechnologie

D2315

Université de Technologie de Compiègne

Dissertation submitted for the obtention of the degree of

Docteur de l'UTC
Spécialité: Biotechnologie

Research unit: CNRS FRE 3580 GEC

By
Maria Panagiotopoulou

Organic-inorganic composite materials for specific recognition and optical detection of environmental, food and biomedical analytes

Thesis supervised by Prof. Karsten Haupt & Dr. Bernadette Tse Sum Bui

Disputation on 9th December 2016, in front of the jury composed of:

- TAKEUCHI Toshifumi — Reviewer, KOBE University, Japan
- WEGENER Joachim — Reviewer, Universität Regensburg, Germany
- HILDEBRANDT Niko — Examiner, Université Paris-Sud, UMR 8622, Orsay
- FRIBOULET Alain — President, CNRS/FRE 3580, GEC, UTC
- TSE SUM BUI Bernadette — Supervisor, CNRS/FRE 3580, GEC, UTC
- HAUPT Karsten — Supervisor, CNRS/FRE 3580, GEC, UTC

Université de Technologie de Compiègne

Thèse présentée pour l'obtention du grade de Docteur de l'UTC

Spécialité: Biotechnologie
Unité de recherche: CNRS FRE 3580 GEC

Par
Maria Panagiotopoulou

Matériaux composites organiques-inorganiques pour la reconnaissance spécifique et la détection optique des analytes environnementaux, alimentaires et biomédicaux

Thèse dirigée par le Pr. Karsten Haupt & et la Dr. Bernadette Tse Sum Bui

Soutenance prévue le 9 Décembre 2016, devant le jury composé de:

- M. TAKEUCHI Toshifumi — Professeur, KOBE University, Japon
- M. WEGENER Joachim — Professeur, Universität Regensburg, Allemagne
- M. HILDEBRANDT Niko — Professeur, Université Paris-Sud, UMR 8622, Orsay
- M. FRIBOULET Alain — Directeur de Recherche, CNRS/FRE 3580, GEC, UTC
- M^{me} TSE SUM BUI Bernadette — Ingénieur de Recherche, CNRS/FRE 3580, GEC, UTC
- M. HAUPT Karsten — Professeur des universités, CNRS/FRE 3580, GEC, UTC

There is nothing noble in being superior to your fellow men. True nobility lies in being superior to your former self.

Ernest Hemingway

Acknowledgments

First and foremost I would like to thank my advisors, Karsten Haupt and Jeanne-Bernadette Tse-Sum-Bui. Thank you for believing in me in a period when I did not believe in myself and for being there for me in both everyday and research struggles. I appreciate all of your contributions in time, ideas, and experience. Karsten, thank you very much for all of your advice and encouragement. Seeing the way you handle things, always with smile, patience and understanding provided my necessary motivation to try and do likewise. Bern, thank you for everything. Your patience, passion, dedication, reliability, honesty, trust, understanding, kindness. Your hard work always made me want to try my best. This thesis would have been an impossible mission without you two.

Next, I would like to thank all the members of GEC, especially the members of the MIP group, old and new ones. Selim and Stephanie, thank you for your hard work and for sharing your knowledge with me. You provided me with all the necessary tools in order to succeed. My girl-team: Paulina, Nadja, Sofia and Jingjing thank you for everything you have done for me. Thank you for your help in experiments, for the nice lunch and dinners we shared, for the stimulating conversations we had. Each and every one of you has a special place in my heart. Frank, Jean, Paolo and Bilo thank you for being the most patient and optimistic officemates. Jacqueline and Sere thank you for the time you spent teaching me things. Thierry thanks for always trying to make the others smile. Yi, Marcelina, Mira, Ces and Zeynep thank you for the wise advice regarding life decisions. I have always valued your opinion. Nicolas thanks for introducing me to the “Breton” lifestyle. Carlo and Mariano thank you for our stimulating discussions. You were always there when I needed to pick your brains about any subject. Elise and Lumi thanks for the excellent emotional and experimental support. I am sure that after almost 4 years in the MIP team I am forgetting to thank many lovely people…To these people: Big thanks! Working with you had been a great honor.

Looking back to how my Ph.D journey started I would like to thank my friends from Greece: Maria, Kostas, Sofia(again) and Mr. Theo. Thank you for literally dragging me out of my comfort zone and convincing me to go for an Erasmus exchange in France. Thanks for all of your support, trust and love since then. I wouldn’t be the person I am today without you.

The SAMOSS team…All the supervisors and fellows are amazing! Thanks for everything you taught me…your advice and support. I really enjoyed our time together during the summer schools and workshops. We share many unforgettable moments.

My family…I can fill another 200 pages thanking you for everything you have done for me throughout my life. You know that doing a Ph.D is a big challenge…what you do not know is that living far from you all this time was an equally big challenge. Thanks for your unconditional love and support throughout my life.

Last but for sure not least I have to thank Cristina, Marina, Ricardo, Miguel, Felipe, Lauri, Emna, Diego, Aliki, Mara, Vaso, Argi, Mathilde, Manon, Jean, Frederico and Yolanda…mostly because they were patiently listening to me complaining… but also for many many other reasons! Thank you guys!

Acknowledgments

Finding the right words to express my gratitude to each and every one is a hard task. I have got so much out of this thesis. For sure how to be a better scientist…but most importantly how to be a better person. And it is thanks to you all.

This thesis is dedicated to my beloved grandma.

Table of Contents

List of Abbreviations

AA	Acrylic acid
Ab	Antibody
AB	(4acrylamidophenyl)(amino)methaniminium acetate
ABDV	2,2'-azobis(2,4dimethylvaleronitrile)
ACN	Acetonitrile
AIBN	2,2' -azobis(2-methylpropionitrile)
APTES	3-aminopropyltriethoxysilane
BPO	Benzoyl peroxide
CCK2	Cholecystokinin-2
CDs	Carbon dots
CL	Cross-linking degree
CNTs	Carbon nanotubes
COSY	Correlation Spectroscopy
CT	Computed Tomography
DLS	Dynamic Light Scattering
DMF	Dimethylformamide
DMPA	2,2-dimethoxy-2- phenylacetophenone
DMSO	Dimethyl sulfoxide
DOX	Doxorubicin
DVB	Divinylbenzene
EbAM	N,N'-ethylenebis(acrylamide)
EGDMA	Ethylene glycol dimethacrylate
EGF	Epidermal Growth Factor
EGFR	Epidermal Growth Factor Receptor
EpCAM	Epithelial cell adhesion molecule
EPR	Enhanced Permeability and Retention
FA	Folic acid
FITC	Fluorescein isothiocyanate

FR	Folate Receptor
FRET	Fluorescence Resonance Energy Transfer
FWHM	Full width at half-maximum
GlcA	Glucuronic acid
GO	Graphene oxide
GQDs	Graphene quantum dots
GRP	Gastrin-Releasing Peptide
HA	Hyaluronic acid
HABP	Hyaluronic acid binding protein
HEMA	Hydroxyethyl methacrylate
HEPES	4-(2-hydroxyethyl)-1-piperazineethanesulfonic acid
HUVEC	Human umbilical vein endothelial cell
IF	Imprinting Factor
LED	Light Emitting Diode
MAA	Methacrylic acid
mAb	Monoclonal antibody
MAM	Methacrylamide
MEH-PPV	Poly[2-methoxy-5-(2-ethylhexyloxy)-1,4-phenylenevinylene]
MIPs	Molecularly Imprinted Polymers
MRI	Magnetic Resonance Imaging
MTS	3-(4,5-dimethylthiazol-2-yl)-5-(3-carboxymethoxyphenyl)-2-(4-sulfophenyl)-2H-tetrazolium
MUG	4-methylumbelliferyl-β-Dglucuronide
MWCNTs	Multi-walled carbon nanotubes
NANA	N-acetylneuraminic acid
NC	Nanocluster
NDs	Nanodiamonds

NIR	Near Infrared
NMR	Nuclear Magnetic Resonance
NPs	Nanoparticles
OI	Optical Imaging
PA	Propargyl acrylamide
PAMAM	Poly(amidoamine)
PCA	Principle component analysis
PDHF	Poly(9,9-dihexylfluorene)
PDs	Polymer dots
PDT	Photodynamic therapy
PEG	Polyethylene glycol
PEI-PEG-PEI	Poly(ethylenimide)-β-poly(ethylene glycol)-β-poly(ethylenimide)
PET	Positron Emission Tomography
PETA	Pentaerythritol
PFBT	Poly(9,9-dioctylfluorene-2,7-diyl-co-benzothiadiazole)
PFO	Poly(9,9-dioctylfluorene)
PFPV	Poly[2-methoxy-5-(2-ethylhexyloxy)-2,7-(9,9-dioctylfluorene)]
PLA	Poly(lactic acid)
PLGA	Poly(lactic-co-glycolic acid)
PPE	Poly(p-phenylene ethynylene)
PPEI-EI	Poly-(propionylethylenimine-co-ethylenimine)
PS	Polystyrene
PTT	Photothermal therapy
TAME	N_a-p-tosyl-*L*-arginine methyl ester hydrochloride
QD	Quantum Dot
QY	Quantum yield
RGD	Arginine-glycine-aspartic acid peptide

RCP	Riboflavin Carrier Protein
SA	Sialic acid
SELEX	Systematic Evolution of Ligands by EXponential enrichment
SEM	Scanning Electron Microscopy
SiNPs	Silica Nanoparticles
SLN	Sentinel Lymph Node
SNR	Signal to noise ratio
SPECT	Single Photon Emission Computed Tomography
SPIONS	Small Particles of Iron Oxide
SPR	Surface Plasmon Resonance
SSTRs	Somatostatin receptors
SWCNTs	Single-walled carbon nanotubes
TEA	Triethylamine
TEM	Transmission Electron Microscopy
TEOS	Tetraethylorthosilicate
TFR	Transferrin-receptor
THF	Tetrahydrofuran
TSPO	Translocator Protein
UCL	Upconversion luminescence
UCNPs	Upconverting nanoparticles
UREA	1-(4-vinylphenyl)-3-(3,5bis(trifluoromethyl)phenyl) urea
USI	Ultrasound Imaging
VEGF	Vascular Endothelial Growth Factor
2,4-D	2,4-dichlorophenoxyacetic acid
4VP	4-Vinylpyridine

Abstract in English

***Keywords*:** bioimaging, multiplexing, glycosylation, hyaluronan, sialic acid, molecularly imprinted polymer, plastic antibody, quantum dot, initiator-free polymerization, self-initiated monomer.

This thesis describes the state of the art in nanomaterials-based targeted bioimaging and introduces molecularly imprinted polymers, also termed 'plastic antibodies' as novel biorecognition agents for labeling and imaging of cells and tissues.

In fundamental biology and medical diagnostics, there is a constant need to localize and quantify specific molecular targets. Abnormal glycosylation levels or distributions of hyaluronan or sialic acids on cells are indicators of infection or malignancy. In general, bioimaging with fluorescent probes enables the localization and qualitative or quantitative determination of these pathological biomarkers. However, no reliable tools for the recognition of glycosylation sites on proteins exist, because the commercially available antibodies or lectins have poor affinity and selectivity for these targets. In this context, tailor-made molecularly imprinted polymers (MIPs) are promising synthetic receptor materials since they present a series of advantages over their natural counterparts such as the ease and low cost of preparation and their physical and chemical stability. Thus, MIPs could provide a robust and specific imaging tool for revealing the location/distribution, time of appearance and structure of glycosylation sites on/in cells, which would lead to a better insight of the tremendously diverse biological processes in which these molecules are involved.

Herein, we describe the synthesis of water-compatible MIPs for the molecular imaging of hyaluronan and sialylation sites on cells and tissues. Since molecular imprinting of entire biomacromolecules like oligosaccharides is challenging, we opted for what is commonly called the 'epitope approach', which was inspired by nature. The monosaccharides, glucuronic acid and N-acetylneuraminic acid were imprinted, and the resulting MIPs were able to bind these molecules when present and accessible on the terminal unit of hyaluronan and sialylation sites. Fluorescent MIPs were synthesized as rhodamine-labeled nanoparticles and as MIP-coated InP/ZnS core-shell quantum dot (QD) particles. For the coating of the QDs, a novel versatile solubilization and functionalization strategy was proposed, which consists of creating polymer shells directly on QDs by photopolymerization using the particles as individual internal light sources. A standard immunostaining protocol was then successfully adapted for the application of the fluorescently labeled MIPs to image fixed and living human keratinocytes and skin tissues, by epifluorescence and confocal fluorescence microscopy. The results were comparable to those obtained with a reference method where staining was done with a biotinylated hyaluronic acid binding protein. Multiplexed and cancer cell imaging were also performed, demonstrating the potential of molecularly imprinted polymers as a versatile biolabeling and bioimaging tool.

Although the MIPs were not cytotoxic at the concentrations used for bioimaging, in order to render them generally applicable in biomedicine, where toxicity of the polymerization precursors is a matter of concern, we suppressed the initiator, a toxic chemical. Initiator-free MIPs were thus synthesized by using monomers that can self-initiate under UV irradiation or heat. The specificity and selectivity of the obtained MIPs were as good as the ones prepared with initiators.

In conclusion, we have demonstrated for the first time the great potential of MIPs as synthetic antibody mimics for bioimaging. The possibility to associate other functionalities such as QDs and additionally attach drugs to the same material appears rather straightforward due to the synthetic polymeric nature of MIPs, which paves the way to new potential applications in theranostics.

Résumé en français

***Mots-clés*:** bioimagerie, glycosylation, acide hyaluronique, acide sialique, polymère à empreinte moléculaire, anticorps plastique, boîte quantique, monomère auto-initiant.

Cette thèse décrit l'état de l'art des sondes et nanoparticules fluorescents traditionnels utilisés en imagerie de fluorescence ainsi que le développement de nouveaux nanomatériaux à base de polymère à empreinte moléculaire, aussi dénommé 'anticorps plastique', pour le ciblage et la bioimagerie.

En biologie et en médecine, il y a un besoin constant de diagnostiquer diverses maladies pour leur éventuel traitement et prévention. Une distribution anormale et un taux élévé de glycosylation (e.g. acides hyaluronique et sialique) à la surface ou dans les cellules sont indicateurs d'une infection ou d'un cancer. Généralement, l'imagerie par fluorescence permet de visualiser, localiser et quantifier les biomarqueurs de pathologie mais à l'heure actuelle, il n'existe pas d'outil analytique fiable pour cibler spécifiquement les molécules de glycosylation car les anticorps et les lectines vendus dans le commerce ont une faible affinité et sélectivité vis-à-vis de ces cibles. Dans ce contexte, les polymères à empreintes moléculaires (MIPs) pourraient apporter une solution. Les MIPs sont des récepteurs synthétiques possédant des affinités et sélectivités comparables à ceux des anticorps, mais exhibant une stabilité physique, thermique et chimique bien plus accrue. De plus, leur fabrication est peu coûteuse et ne nécessite pas de tuer des animaux comme pour l'obtention des anticorps biologiques.

Dans cette thèse, nous avons optimisé et synthétisé des MIPs biocompatibles pour leur utilisation en bioimagerie afin de détecter et quantifier l'acide hyaluronique et l'acide sialique sur les cellules et les tissus de peau humaine. L'acide glucuronique, une composante de l'acide hyaluronique et l'acide N-acétylneuraminique, l'acide sialique le plus commun, ont été utilisés comme molécules 'patron', générant des MIPs très sélectifs envers leur cible en milieu aqueux. Deux types de nanoparticules de MIPs fluorescents ont été synthétisés: (1) en incorporant un colorant rhodamine polymérisable dans la solution de pré-polymérisation et (2) en encapsulant des boîtes quantiques InP/ZnS générant ainsi des MIPs de type coeur-coquille. Pour cela, nous avons adopté une stratégie innovante qui consiste à synthétiser les coquilles de MIPs directement autour des boîtes quantiques en utilisant l'énergie de l'onde fluorescente émise par l'excitation des points quantiques, pour initier la polymérisation. Un protocole d'immunocoloration standard a ensuite été optimisé afin d'imager des kératinocytes humains fixés et vivants ainsi que des tissus de peau, par microscopie à épifluorescence et confocale. Les résultats étaient similaires à ceux obtenus par la méthode de référence utilisant une protéine biotinylée reconnaissant l'acide hyaluronique. L'imagerie multiplex en combinant deux MIPs couplés à deux couleurs de boîtes quantiques et l'imagerie des cellules cancéreuses ont également été démontrées.

Bien que les MIPs n'étaient pas cytotoxiques aux concentrations utilisées pour la bioimagerie, la toxicité des différentes composantes du MIP pourrait être un frein à leur utilisation dans le domaine biomédical. Afin de rendre ces MIPs plus 'inoffensifs', nous avons supprimé l'amorceur de polymérisation, une molécule considérée comme toxique. Les MIPs ont été synthétisés en employant des monomères qui s'auto-initient sous l'effet de l'UV ou de la chaleur. La spécificité et la sélectivité des MIPs obtenus étaient similaires à ceux préparés avec des amorceurs.

En conclusion, cette thèse décrit la première utilisation des MIPs comme anticorps synthétique pour la bioimagerie de fluorescence. Ce travail ouvre la voie à de nouvelles applications en détection, diagnostique et thérapie par des MIPs.

General Introduction

The work presented in this Ph.D thesis was carried out within the EU Marie Curie Research Training Network SAMOSS (Sample In – Answer Out Optochemical Sensing Systems), which focuses on the fabrication of novel biosensors for the detection of analytes of interest in the food industry, biomedicine and environmental analysis. The described work was performed from December 2013 to November 2016 in the Laboratory of Enzyme and Cell Engineering at the Université de Technologie de Compiègne.

The aim of this thesis is to provide a comprehensive overview of the nanoparticles and targeting ligands currently used for fluorescent bioimaging and to introduce molecularly imprinted polymers (MIPs) as an advantageous alternative targeting ligand. Undoubtedly, nanoparticles have made an impressive "debut" in the biomedical field with applications ranging from intraoperative fluorescence imaging to drug delivery, photothermal and photodynamic therapy. Despite the fact, the routinely used targeting ligands such as antibodies, aptamers and peptides present certain disadvantages for bioimaging applications like high synthetic cost and fast degradation by proteases or nucleases. A proposed solution is the application of MIPs as a new targeting ligand for bioimaging. MIPs exhibit binding affinities and specificities comparable to those of antibodies. In contrast to their natural counterparts, their production is reproducible, economic and no animals are necessary. Moreover, they are physically and chemically stable and are not degraded by proteases, nucleases or denatured by organic solvents like in the case of antibodies, peptides and aptamers. Their size, biocompatibility and hydrophilicity can be tuned according to a given application. Thus, MIPs have a great potential in providing a robust, selective and biocompatible imaging tool that could reveal the localization and distribution of cellular targets, like the overexpressed glycosylations that serve as biomarkers for tumor and diseased cells. To date, no reliable tools for the recognition of glycosylation sites on cells exist, because the commercially available antibodies or lectins have poor affinity and selectivity for these targets. In this context, the application of MIPs would lead to a better understanding of the tremendously diverse biological role of these molecules and their implication in cancer and disease.

This Ph.D. thesis is divided into four chapters: one bibliographic chapter and three results chapters.

Chapter 1 provides a literature review which focuses on the application of nanoparticles in the biomedical field with an emphasis given on fluorescent bioimaging. The most important properties, such as quantum yield, size, cytotoxicity and water-compatibility are assessed. The routinely used targeting ligands, including antibodies and antibody fragments, aptamers, peptides and small molecules are also presented and their pros and cons are extensively discussed. In order to overcome some of their intrinsic disadvantages for bioimaging, molecularly imprinted polymers are proposed as a smart alternative targeting strategy.

Chapter 2 relates the synthetic methodologies employed to obtain water compatible MIPs for the sugar acids, D-glucuronic and N-acetylneuraminic acids, with the ultimate goal of targeted bioimaging of glycosylation sites such as hyaluronan and sialic acids. Different stoichiometric monomers are tested in order to find the optimum MIP composition and two fluorescent labeling methods are proposed, the direct incorporation of a polymerizable organic dye in the polymeric matrix and the coating of quantum dots with a MIP shell. For the coating of the QDs, a novel versatile solubilization and functionalization strategy is proposed, which consists of creating polymer shells directly on QDs by photopolymerization using the particles as individual internal light sources.

Chapter 3 describes the most commonly used approaches for the targeted imaging of the cell glycosylations with an emphasis given on the recent application of MIPs as imaging agents. The MIPs synthesized in **Chapter 2** are applied on fixed and living keratinocytes in order to target the overexpressed glycosylations found on the cell surface and in the cytosol. Exemplary tissue and cancer cell imaging are also provided and the particle cytotoxicity is assessed.

Chapter 4 reports the initiator-free synthesis of molecularly imprinted polymers in order to render them generally applicable in biomedicine, where toxicity of the polymerization precursors, like initiators, is a matter of concern. “Greener” MIPs were obtained by using acrylic and styrenic monomers, which can self-initiate under UV irradiation or heat respectively. For our

demonstrations, we employed the most commonly used functional monomers, cross-linkers and solvents applied in MIP synthetic protocols and the specificity and selectivity of the initiator-free MIPs were assessed.

CHAPTER 1

Nanoparticles for Bioimaging

1.1 Introduction to Nanoparticles and Nanotechnology

Nanotechnology is the science, engineering and technology conducted at the nanoscale, where novel properties occur as compared to bulk materials. For example, metallic nanoparticles exhibit different chemical and physical properties from bulk metals (different mechanical strength, lower melting point, higher specific surface area, specific optical properties and specific magnetization), properties that might be attractive for many industrial applications. A nanoparticle (1-100 nm) is the most fundamental component in the fabrication of a nanostructure, and is far smaller than the world of everyday objects as described by Newton's laws of motion, but still, bigger than a simple molecule or an atom that are governed by quantum mechanics.

The ideas and concepts behind modern nanoscience and nanotechnology started with a talk entitled *"There's Plenty of Room at the Bottom"* by the renowned physicist Richard Feynman at an American Physical Society meeting in 1959, long before the term nanotechnology was used. In his talk, Feynman described the possibility of direct manipulation of individual atoms and molecules as a powerful form of synthetic chemistry. Few years later, Professor Norio Taniguchi introduced the term nanotechnology. The modern nanotechnology actually began with the development of the scanning tunneling microscope in 1982 that could distinguish individual atoms. For the development of this microscope, Binnig and Rohrer received the Nobel Prize in Physics in 1986. Inspired by Feynman's ideas, Drexler used the term "nanotechnology" in his 1986 book "*Engines of Creation: The Coming Era of Nanotechnology*", which proposed the idea of a nanoscale "assembler" which would be able to build a copy of itself and of other items of arbitrary complexity with atomic control.

In 2000, the United States of America instituted the National Nanotechnology Initiative, which was soon followed by a plethora of projects in nanotechnology in nearly most of the U.S. Departments and Agencies. Nowadays, commercialization of products based on advancements in nanoscale technologies are emerging and nanoparticles find applications in manufacturing and materials science, energy and electronics, environment and biomedicine to name but a few, with the annual global nanotechnology research funding running at 10 billion dollars per year. The

vast variety of nanoparticles applications is summarized in Figure 1. Regarding bioimaging, nanoparticles are becoming a mainstay in modern biomedical research with many reports now discussing the future scope and commercialization prospects [1]. The fabrication, especially of multimodal nanoparticles, that serve as imaging agents utilizing more than one imaging modalities (see 1.2), imaging combined with drug and gene delivery, or imaging combined with therapy or diagnosis, is expected to be integral to the development of next generation therapeutics, diagnosis and medical imaging technologies (Table 2 ANNEX 1).

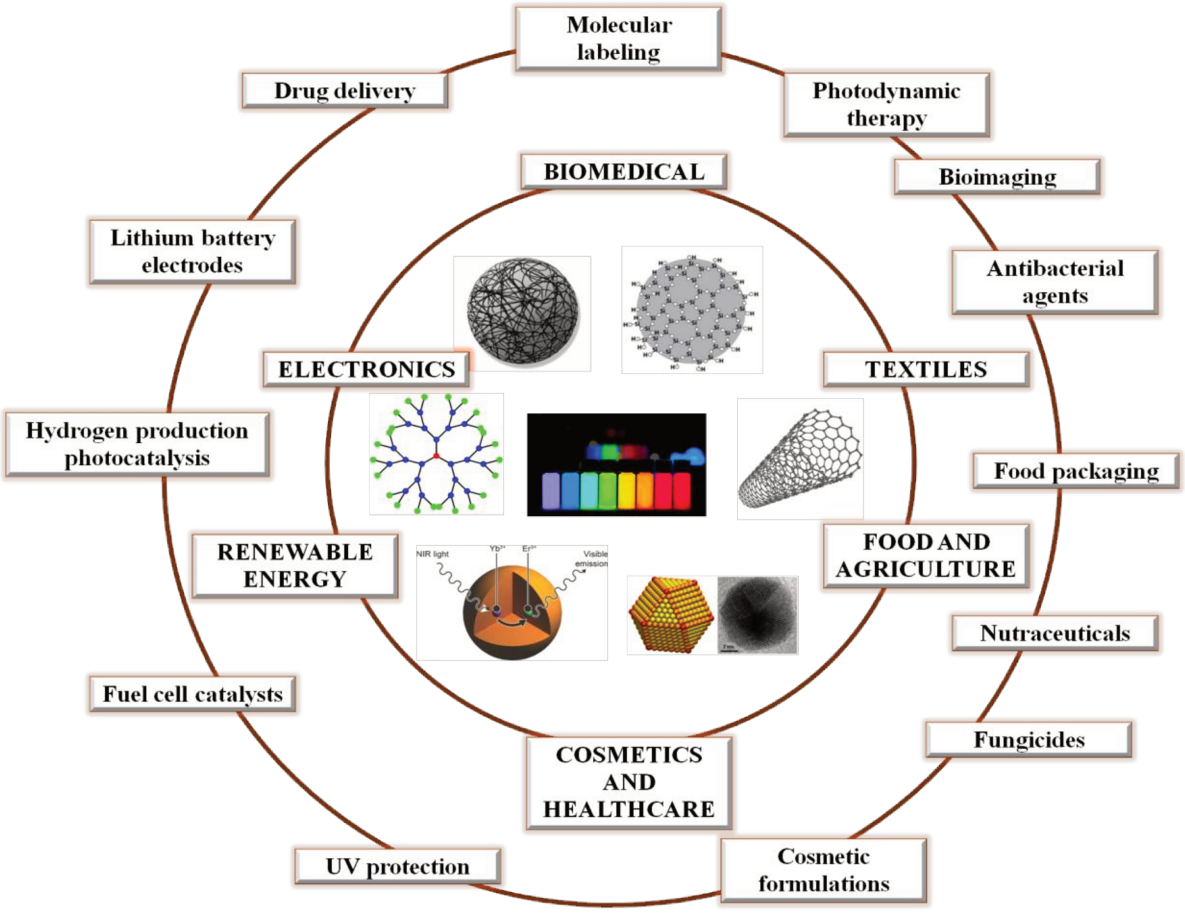

Figure 1 Applications of nanoparticles. Adapted from [2].

1.2 Bioimaging Modalities

In biomedical research, a number of non-invasive imaging approaches (modalities) towards disease such as computed tomography (CT), magnetic resonance imaging (MRI), positron emission tomography (PET), ultrasound imaging (USI) and optical imaging (OI), including their variations and subcategories have been developed (Figure 2). These bioimaging techniques differ in terms of sensitivity and resolution, complexity, time of data acquisition and financial cost and are, in general, complementary rather than competitive. The choice of the imaging modality depends primarily on the specific issue that needs to be addressed. A short analysis and comparison of the most employed techniques in diagnostic imaging is reported in this chapter.

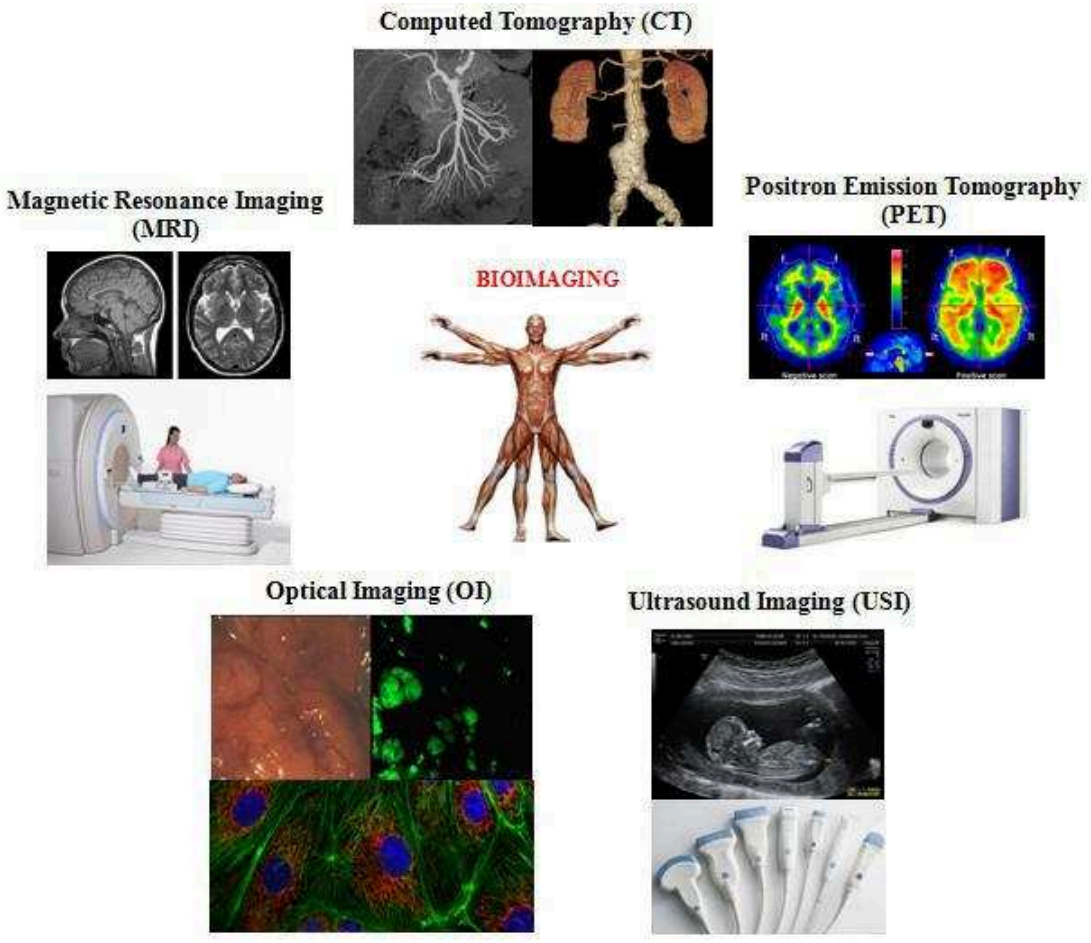

Figure 2 Bioimaging modalities: Magnetic Resonance Imaging (MRI), Computed Tomography (CT), Ultrasound Imaging (USI), Positron Emission Tomography (PET) and Single Photon Emission CT (SPECT), Optical Imaging (OI).

1.2.1 Magnetic Resonance Imaging

The Magnetic Resonance Imaging (MRI) technique was developed in the early 1970s and led to the attribution of the Nobel Prize for Physiology and Medicine to Paul Lauterbur and Peter Mansfield in 2003. This imaging technique is based on the fundamental principles of nuclear magnetic resonance and takes advantage of the tissue contrast that is created from the NMR signals coming from the hydrogen nuclei that are located in different physiological environments throughout an organism. More precisely, when a specimen is placed within a homogeneous static magnetic field, nuclear spins will resonate at a given frequency that depends on the magnitude of the applied magnetic field. Once the specimen has reached the equilibrium magnetization, it is then excited by a radiofrequency pulse at the appropriate resonant frequency resulting in a change in the net magnetization. When the radiofrequency pulse stops and the spins relax back to the equilibrium state, electromagnetic signals are transmitted to the spectrometer. The changes in induced electromagnetic signals in the presence of linear field gradients are used to construct 3D images of the body. Unfortunately, the sensitivity of the method is in the low micro- to millimolar concentration range and at present there are not many paramagnetic labels available (gadolinium chelates, iron and manganese oxides). In addition, image resolution is limited by the relatively low magnetic field strengths used in the clinic (1.5–3 T). Usually, a resolution in the range of 2–3 mm is obtained in clinical use, although, at the higher field strengths commonly used in laboratory research (7–9.4 T), higher sensitivity is possible to be obtained with resolution 50–100 μm [3]. The required time to acquire an image depends, in part, on the resolution needed for a given application and it is up to several minutes. ^{1}H MRI of tissue water protons can be used to indirectly visualize cell membrane receptors, such as HER-2 on breast cancer cells [4], the integrin $\alpha_v\beta_3$ on angiogenic endothelial cells [5] and the phospholipidphosphatidylserine on the surface of apoptotic cells [6]. However, as these receptors are usually present at low concentrations, it is necessary to use high concentrations of the paramagnetic labels like liposomes loaded with multiple gadolinium chelates. Although MR image resolution *in vivo* is not at the level where single cells can be observed, it is, nevertheless, possible to image the presence of single cells using iron oxide-based nanometre- or micrometre-sized particles, as the effect of the particles in the surrounding magnetic field extends beyond the cell boundaries. The technique has been also used, for example, to track implanted stem cells in the brain of mice, to

monitor T-cell trafficking in immunogenic tumors and to image the location of implanted dendritic cells in the clinic [7]. The current challenges faced by MRI molecular imaging have been reviewed [8]. MRI does not use ionizing radiation and no harmful side-effects are known to be linked with the temporary exposure to the strong magnetic field. Nevertheless, there are still important safety concerns to consider before performing or undergoing an MRI scan. The magnetic field, for example, may cause pacemakers or any other implanted medical devices that contain metal, to malfunction or heat up during the examination [9,10].

1.2.2 Tomography

Tomography refers to imaging by sections or sectioning, through the use of any kind of penetrating wave or mechanical method. The word itself is derived from ancient Greek *tomos*, "slice, section" and *graphō*, "to write". This imaging method is used in several fields like radiology, archaeology, biology, atmospheric science, geophysics, oceanography, plasma physics, materials science, astrophysics and other sciences. In this section, Positron Emission Tomography (PET), Single Photon Emission Computed Tomography (SPECT) and Computed Tomography (CT) are shortly reviewed.

Positron Emission Tomography and Single Photon Emission Computed Tomography

In nuclear medicine, images of different body parts are produced by using small amount of radioactive tracers administered orally or intravenously. Then, external detectors capture and form images from the radiation emitted by these radiopharmaceuticals. The two main nuclear imaging modalities, PET and SPECT, are characterized by a very high sensitivity range (femto- to picomolar concentration range) but a quite limited spatial resolution. The common SPECT radionuclides are γ photon emitters and are usually employed to label tracers of blood flow such as N-isopropyl-^{123}I-iodoamphetamine (^{123}I-IMP) and ^{99m}Tc-hexamethyl-propylene amine oxime (^{99m}TcHMPAO). Different SPECT radioisotopes can have one or more energy emission lines, therefore several processes can theoretically be imaged simultaneously by setting SPECT scanners at different energy windows. Some limitations of SPECT imaging include the low

temporal resolution, the limited number of available radiopharmaceuticals, and the difficulty to achieve absolute quantitative information due to lack of attenuation and scatter corrections necessary at the time of image reconstruction [11].

The main difference between PET and SPECT is that the first one relies on positron (β^+) emitters with shorter half-lives (Table 1). In addition, it offers several advantages over SPECT such as higher number of available radiolabeled compounds that allows imaging a large variety of functional cellular processes such as glucose and amino acid metabolism, neurotransmission, receptor affinity, gene expression, cell and molecular targeting. Moreover, the possibility of corrections at the time of image reconstruction allows quantitative measurements. However, one of the main disadvantages of PET is that all radionuclides decay at the same energy (photon energy of 511 KeV). Therefore, it is not possible to simultaneously discriminate between different radiotracers at different energy windows. PET has been especially utilized for cancer imaging as well as neurological functions and cardiovascular function [11]. The uses of PET in molecular imaging have been reviewed [12].

Table 1 Nuclides used in nuclear medicine to label radiopharmaceuticals. Adapted from [11].

SPECT		**PET**	
Nuclide	Half-life	Nuclide	Half-life
^{99m}Tc	6.02 h	^{18}F	109.8 min
^{111}In	2.83 d	^{11}C	20.4 min
^{123}I	13.2 h	^{13}N	9.98 min
^{125}I	60.14 d	^{15}O	2.03 min
		^{124}I	4.18 d
		^{64}Cu	12.7 h
		^{68}Ga	68 min
		^{82}Rb	1.2 min

Computed Tomography

Typically, a CT scan consists of an X-ray beam generated by an external source and passes through the body. There, part of the X-rays are either absorbed or scattered by the internal structures and organs, while the remaining X-ray pattern is transmitted to a rotating detector along multiple linear paths to create cross-sectional images of the body [13]. The contrast obtained is not as strong in comparison with the one obtained with MRI, but image resolutions of 100 μm are obtainable in small animal studies within ~15 min of data acquisition. Higher-resolution images (50 μm) are possible with longer scan times; however, radiation dose can limit repeated imaging of the same animal. At relatively high resolution (for example, 50 × 50 × 50 μm), radiation doses range from 100 to 300 mGy, which is much higher than the ones used in conventional radiography. However, the radiation dose for a particular study depends on the volume scanned, the number and type of scan sequences, the desired resolution and image quality. CT is often used to provide images of tissue anatomy and is increasingly being used in conjunction with PET, where it provides an anatomical context to the relatively low-resolution PET images. In the medicinal field, the fusion of X-ray CT and PET images has led to faster and more accurate tumor detection (Figure 3) [14]. CT scans are good at imaging bones, soft tissues and blood vessels, even if the use of dyes is sometimes necessary to improve the contrast. For this, iodine-based compounds are mainly used as water soluble CT contrast agents to be injected intravascularly or into any sinus or body cavity, and can also provide an indication of the renal function, such as for kidney filtration. In addition, regarding cancer diagnostics, detailed CT images can eliminate the need for exploratory surgery. The main health concerns related to CT scans derive from the exposure to ionizing radiation and possible allergic sensitization or toxic reaction due to the intravenous contrast agents. Two of the most prevalent clinical and diagnostic applications of CT in the cardiovascular field, are the CT angiogram and artery calcium scoring.

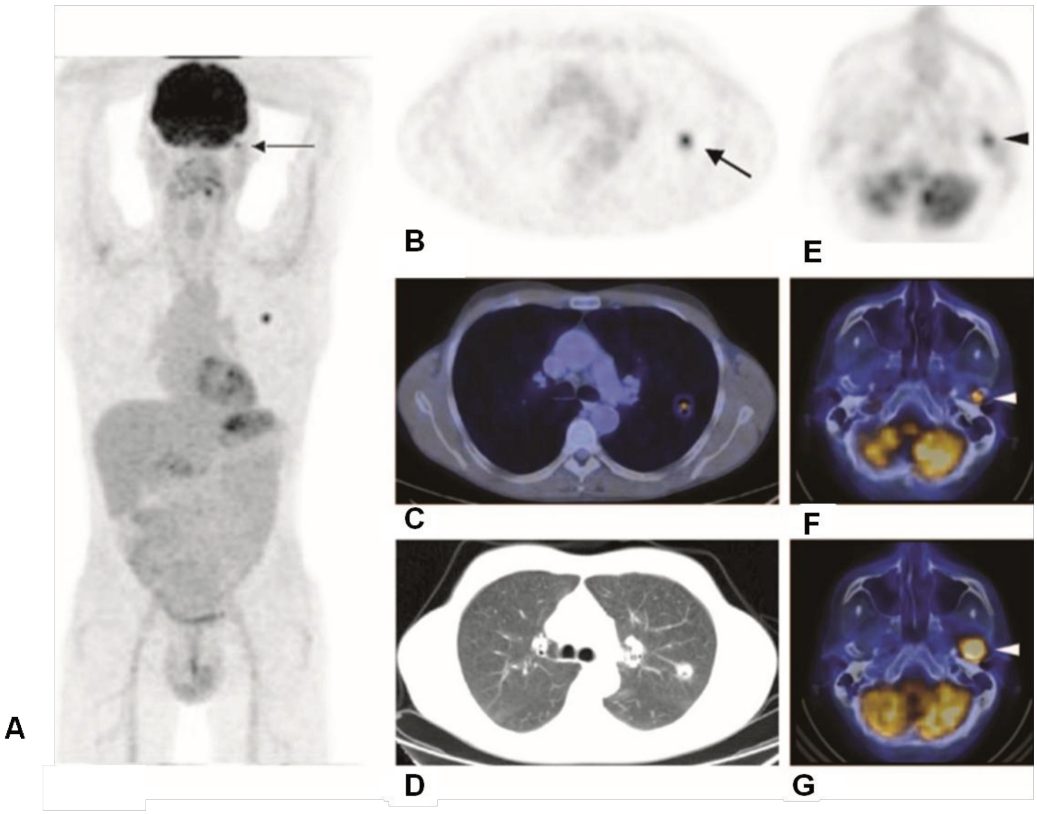

Figure 3 Non–small cell lung cancer (arrow in B) in the left upper lobe is shown in (A) coronal PET maximum intensity projection and (B) transverse PET image, (C) transverse PET/CT image, and (D) transverse CT lung window image. (E) Transverse PET image shows small focus at left skull base (arrowhead, arrow in A); (F) on transverse PET/CT scan, focus appears to be a bone metastasis (arrowhead) in the mandibular condyle. (G) This was confirmed with follow-up transverse PET/CT, where interval growth of the lesion (arrowhead) was seen. Reproduced from [14].

1.2.3 Ultrasound Imaging

Ultrasound (US) is an imaging method that uses high frequency sound waves (1 to 12 MHz) and their echoes to produce relatively precise images of structures within the body. The main part of an ultrasound machine is the transducer probe, which comes in different shapes, sizes and frequency of emitted sound waves. This latter parameter determines how deep the sound waves penetrate into the body, and so affects the resolution of the image. The probe generates and receives sound waves using a principle called the piezoelectric effect. The sound waves travel into the body and hit a boundary between tissues (for example between fluid and soft tissues or between soft tissues and bone). Some of the sound waves get reflected back to the probe, while some others travel on further until they reach another boundary and then get reflected. The machine calculates the distance from the probe to the tissue or organ (boundaries) by using the

speed of sound in tissue and the time of each echo's return, and then displays a 2D image based on the echoes' intensity. The relatively low cost, ease of use, sensitivity and speed of imaging make this an attractive imaging modality in laboratory research, particularly when looking for early signs of tumor formation [11]. Ultrasound imaging has also been demonstrated as a technique to monitor inflammation, angiogenesis and intravascular thrombi [15]. Tissue stiffness can be imaged by detecting the effects of small, local tissue deformations (elastography) and has been applied to enhance the sensitivity of detection of malignant lesions in the breast, which can show large changes in elasticity compared to the surrounding normal tissue. As there may be changes in tissue architecture following cancer therapy, elastography shows great potential in detecting treatment response. Contrast enhanced ultrasound extends ultrasound techniques to the exploitation of gas-filled microspheres (also known as "microbubbles") as an ultrasound contrast agent. Microbubbles are commercially available for clinical use in cardiovascular imaging, being confined by their size to the intravascular space. Their proven clinical tolerability, together with the advantages of real-time imaging, high spatial resolution, and the relatively low cost of the equipment renders molecular targeting of microbubbles an attractive option for future development from its current preclinical stage to the real-life clinical applications [11].

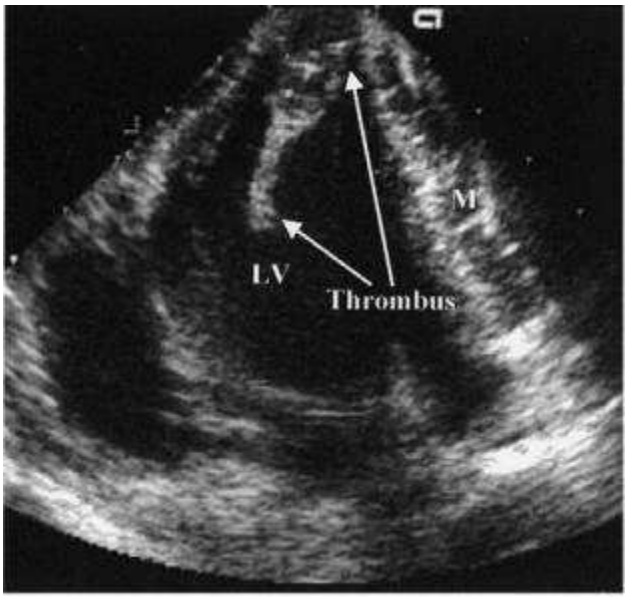

Figure 4 Echocardiography in a canine model demonstrating the presence of a left ventricular thrombus. Reproduced from [15].

1.2.4 Optical Imaging

Optical imaging is a non-invasive imaging technique for looking inside the body, like in the case of the X-ray-based imaging. Unlike X-rays though, which use ionizing radiation, optical imaging uses visible light and the special properties of photons to obtain detailed images of organs and tissues as well as smaller structures including cells and even molecules. Light is the most versatile imaging radiation, since it is able to create a contrast by intensity, wavelength, polarization, coherence, interference, lifetime and nonlinear effects. Optical imaging consists of several sub categories like epifluorescence or confocal fluorescence microscopy, single- or multi-photon, endoscopy, optical coherence tomography, photoacoustic imaging, fluorescence molecular tomography and bioluminescence imaging to name but a few (Table 2). These techniques use different physical parameters of light interaction with tissues and there are several excellent reviews regarding their biological application [16–19].

Table 2 ***In vivo*** **optical imaging techniques. A: Absorption, E: Emission, S: Scattering, Fl: Fluorescence. Reproduced from** [19].

Technique	Contrast	Depth	Commonly used wavelength	Clinical potential
Microscopic resolution				
Epi	A, FI	20 µm	Visible	Experimental
Confocal	FI	500 µm	Visible	Experimental
Two-photon	FI	800 µm	Visible	Yes
Mesoscopic resolution				
Optical projection tomography	A, FI	15 mm	Visible	No
Optical coherence tomography	S	2 mm	Visible, NIR	Yes
Laser speckle imaging	S	1 mm	Visible, NIR	Yes
Macroscopic resolution, intrinsic contrast				
Hyperspectral imaging	A, S, FI	< 5 mm	Visible	Yes

Endoscopy	A, S, FI	< 5 mm	Visible	Yes
Polarization imaging	A, S	< 1.5 cm	Visible, NIR	Yes
Fluorescence reflectance imaging	A, FI	< 7 mm	NIR	Yes
Diffuse optical tomography	A, FI	< 20 cm	NIR	Yes
Macroscopic resolution, molecular contrast				
Fluorescence resonance imaging	A, FI	< 7 mm	NIR	Yes
Fluorescence molecular tomography	FI	< 20 cm	NIR	Yes
Bioluminescence imaging	E	< 3 cm	500-600 nm	No

Of all the optical imaging techniques available, fluorescence microscopy has emerged as one of the most powerful imaging techniques. Fluorescence results from a process that occurs when certain molecules (organic dyes, semiconductor quantum dots, lanthanide compounds, etc.), called fluorophores or fluorescent probes, absorb light. When fluorophores absorb light of a certain wavelength they emit fluorescent light. Fluorescence emission can be of the conventional down or the upconversion type. Upconversion luminescence (UCL) is a non-linear, anti-Stokes process in which the absorption of two or more low-energy photons leads to the emission of a higher-energy photon. The general principle of conventional and UCL processes is depicted in Figure 5. In conventional luminescence, the absorption of a high-energy photon (hv_1) by a system in the ground state (1 in Figure 5) can lead to promotion of the system to the excited state (3 in Figure 5). The system can then undergo non-radiative decay to a lower-excited state (2 in Figure 5), followed by relaxation to the ground state accompanied by the emission of a lower-energy photon (hv_2). As the wavelength of the emitted light is longer than that of the excitation source, thus obeying the energy conservation rule, conventional luminescence is considered to be a Stokes process. In the UCL process, the system in the ground state is initially promoted into the first excited state by an excitation photon or an energy transfer process from a sensitizer. The system is then further excited into level 3 by receiving energy from another excitation photon or energy transfer process. Radiative transition of the excited state into the ground state or another low-energy state leads to UCL emission, in which the emitted photon has a higher energy than the individual excitation photons and achieves anti-Stokes luminescence. In contrast to typical

two-photon absorption, in which the excitation photons have to be absorbed almost simultaneously, the absorption of photons in UCL is sequential. Materials by which upconversion can take place often contain ions of the d-block and f-block elements. Examples of these ions are Ln^{3+}, Ti^{2+}, Ni^{2+}, Mo^{3+}, Re^{4+}, Os^{4+}, and so on [20].

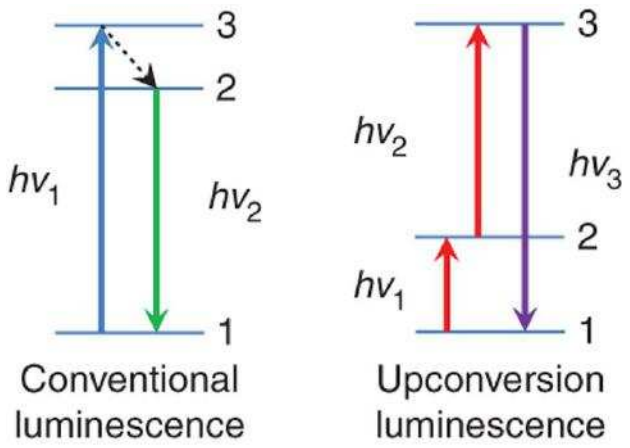

Figure 5 Schematic representation of the conventional luminescence and upconversion luminescence processes. Reproduced from [20].

Two important phenomena that need to be taken into account when optical fluorescence imaging is applied are cell and tissue autofluorecence or natural fluorescence and the so called "optical" or "therapeutic" window.

Autofluorescence or natural fluorescence

Autofluorescence is the natural emission of light by biological structures such as mitochondria and lysosomes when they absorb light. The most commonly observed autofluorescent molecules are NADPH and flavins. The extracellular matrix can also contribute to autofluorescence because of the intrinsic properties of collagen and elastin. Generally, proteins containing an increased amount of the amino acids tryptophan, tyrosine and phenylalanine show some degree of autofluorescence. Most of the cell and tissue autofluorescence occurs upon excitations in the UV-blue region with emissions in the green-yellow-orange region.

Optical or therapeutic window

When imaging a tissue in the mid-visible band (λ_{em}=450-600 nm), high light scattering, autofluorescence and high absorption by hemoglobin will interfere. UV–vis spectral range photons are strongly absorbed by deoxy- and oxyhemoglobin within the first few micrometers to a millimeter of tissue thickness, thus limiting the light penetration. Near-infrared light (650–1500 nm) achieves the highest tissue penetration, much more efficiently than visible light because tissues scatter and absorb less light at longer wavelengths. At wavelengths longer than 950 nm, however, this effect diminishes owing to increased absorption by water and lipids, which absorb significantly in the infrared region. Nonetheless, a clear window exists at wavelengths between 650 nm and 950 nm for optical imaging of live animals. The state of the art in fluorophore design for biological applications is towards NIR-emitters [21,22].

1.2.5 Conclusion-Why optical fluorescent imaging?

All of the imaging modalities described above come with certain pros and cons, summarized in Table 3, and the choice of imaging modality depends mostly on the application. The last 15 years with the development of biocompatible "smart" nanofluorophores and the vast variety of bioconjugation methods and targeting ligands available, the "revival" of optical imaging has led many researchers to suggest that optical technologies can replace some of the currently used techniques in clinical routine for some *in vivo* applications in order to complement for their weaknesses.

Indeed, in MRI, the equipment used is too expensive to purchase, maintain and operate. In addition, an MRI examination can cause claustrophobia, since the patient is within the large magnet up to one hour and the strong magnetic field used makes it unsafe for patients with electrically, magnetically or mechanically activated implants such as cardiac pacemakers, implantable defibrillators and artificial heart valves. MRI images become distorted by metal, which renders it less suitable for patients with surgical clips or stents. Bone, teeth, air and metallic objects all appear black, making differentiation difficult. Due to its low sensitivity, MRI cannot always distinguish between malignant tumors or benign diseases, which could lead to false positive results [23].

Regarding CT and PET/SPECT, the health risks induced by the use of ionizing radiation, hamper their wide and repeated application. Clearly, CT is a costly and relatively high-dose procedure, with levels of radiation often approaching and sometimes exceeding those known to increase the probability of cancer, which makes the carcinogenic potential of this test real [24]. PET scan risks are also due to the radioactive components used during this procedure. PET scans require cyclotrons, an expensive machine that creates the radioisotopes that are used in the radioactive tracers. In addition to that, PET imaging is extremely costy for patients, with the price of a whole-body scan in US ranging from 2.000-20.000 $.

There are also several disadvantages to using USI in medicine, one of which is the higher potential for operator error since most machines produce images with limited resolution. Another limitation is that it cannot be used to study any part of the body containing gas, so it is not a useful tool for diagnosing problems of the lung and digestive tract. This type of modality is also very limited when used to identify fractures and other problems with the bones. Ultrasound results often identify a potential area of concern that is not malignant. False-positive results can lead to unnecessary biopsies. Preliminary data from a clinical trial showed that there is a higher percentage of false-positive results with ultrasound examination than with mammography (2.4%-12.9% for ultrasound and 0.7%-6% for mammography) [25].

In order to overcome these obstacles in biomedical imaging, a number of arguments have been put forward to substantiate the development of optical imaging technologies for *in vivo* use:

- **Reduced health risk:** Since optical biocompatible and non-cytotoxic tracers have been developed that do not use radioactivity, the risk of side effects is limited.

- **Lower financial cost:** The cost of surgical fluorescence cameras is markedly lower than those of preclinical SPECT/CT, PET/CT or PET/MRI cameras.

- **Limited facility requirements:** The synthesis of optical tracers does not require dedicated radiochemistry laboratories or, in the case of PET tracers, cyclotron facilities.

- **Real-time imaging:** Light-sensitive fluorescence cameras provide video-rate feedback, enabling real-time visualization of superficially located areas of disease and allowing doctors to identify diseased areas during interventional procedures.

- **The big variety of bioconjugated nano-fluorophores available:** A great number of targeting ligands (antibodies, peptides, aptamers, small molecules, molecularly imprinted polymers, etc.) and fluorescent probes (organic dyes, polymer dots, quantum dots, carbon dots, upconverting nanoparticles, etc.) are available for the microscopic visualization of biomarkers *in vitro* and at histology. This enables a direct translation of the fluorescence technologies already available for molecular cell biology applications and *in vitro* applications to the *in vivo* situation.

- **Engineering towards higher tissue penetration:** The signal penetration of emissions between 400 and 650 nm is confined to the millimeter range, while using near-infrared emissions in the so called "therapeutic window" may result to tissue penetration of even 20 cm [19].

- **Multiplexing, multifunctional and multimodal abilities:** Multiplexing becomes easy by just selecting fluorophores of different emission wavelengths. In addition, synthesis of multifunctional optical nanoprobes for simultaneous diagnostic and therapeutic applications and multimodal-imaging tracers has been extensively reported.

Table 3 A comparison of the non-invasive imaging modalities used in biomedicine.

Imaging Modality					
Criteria	**MRI**	**CT**	**USI**	**SPECT and PET**	**OI**
	Magnetic field	X-rays	Ultrasonic waves	Ionizing radiation (γ and β)	Fluorescence
Imaging probes	Gadolinium Iron/Manganese oxides	Iodine Gold nanoparticles	Microbubbles	^{18}F, ^{64}Cu, ^{11}C, ^{15}O ^{99}mTc, ^{111}In	Fluorescent probes Bioluminescent probes
Sensitivity	+	+	++	++++	++++
Advantages	High resolution No tissue penetration limit	High resolution No tissue penetration limit	Low cost Real time	High sensitivity Quantitative result	High sensitivity Real time Quantitative result
Disadvantages	Expensive Long scanning times Low sensitivity	Ionizing radiation Low sensitivity	Limited depth Poor contrast Operator dependent	Ionizing radiation Low resolution	Limited depth
Cost	++++	+++	+	++++	+
Clinical use	Yes	Yes	Yes	Yes	Clinical trials

Nowadays, the transition of fluorescence imaging from an *in vitro* analytical tool to *in vivo* applications lies in the results of clinical trials currently carried out for the use of bioconjugated probes in surgical guidance. Intraoperative fluorescence imaging is a field rapidly expanding the last 5 years, with 36 publications on the topic in 1999 rising to over 300 in 2011 and over 1600 in 2015 (Figure 6). Many recent publications in high-impact journals, especially focusing on sentinel lymph node mapping using NIR fluorescence imaging, and the promising first results from the clinical trials (phases II and III) pave the way for fluorescence imaging in the medicinal reality [26–28].

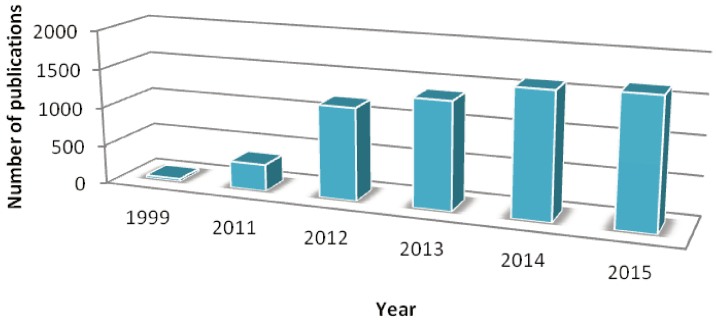

Figure 6 Number of publications regarding intraoperative fluorescence imaging from 1999 till 2015.

Sentinel lymph node (SLN) resection and evaluation are commonly performed in oncological surgery [27]. Identification of metastatic cancer in lymph nodes provides critical staging information for treatment planning. The intraoperative localization of lymph nodes is, however, complicated because lymph nodes are often embedded deep within adipose tissue and not accessible to visual inspection. Fluorescence guided surgery does not introduce significant additional costs and could accelerate the procedure by faster localization of the nodes of interest. Indocyanine green (ICG) is a dye that emits fluorescence light in the near-infrared, used for passive tumor targeting through the Enhanced Permeability and Retention Effect (see section 1.4.1). Some of the clinical results of the use of ICG for fluorescence guided surgery including SLN visualization and lymph node mapping, investigation of astomotic perfusion, and the visualization of the biliary tree anatomy in robot-assisted cholecystectomy are presented in Figure 7. The future of fluorescence guided surgery depends though, on the parallel development of reliable high-quality fluorescent compounds that perform specific targeting purposes. The types, properties and use of nanoparticles as suitable nanoprobe-candidates in bioimaging and the development of recognition-ligands for targeted cell imaging will be reviewed in the following sections.

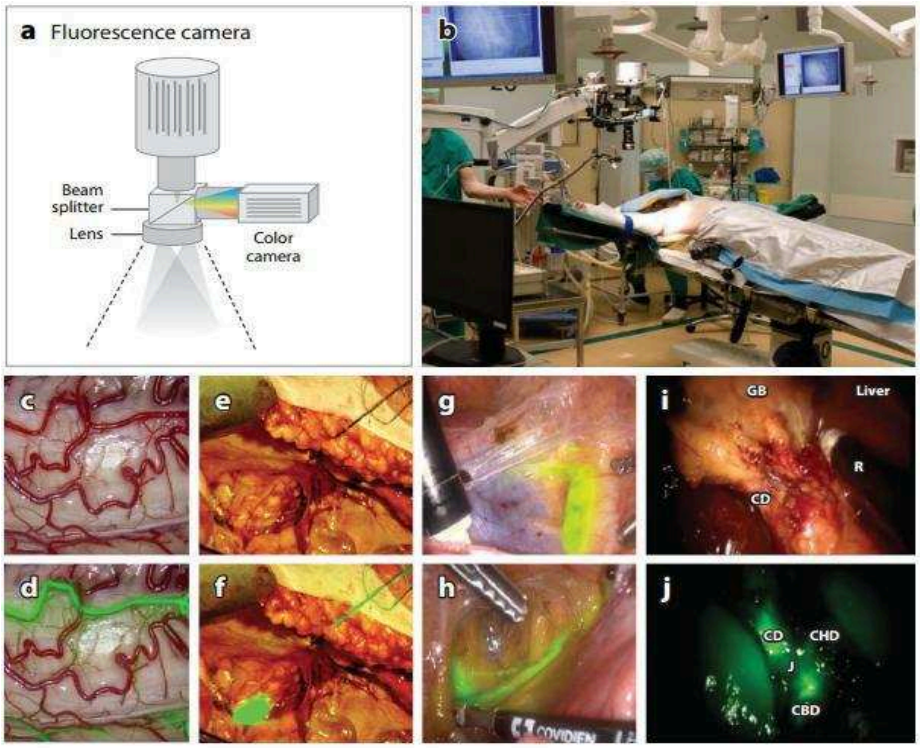

Figure 7 Indocyanine green (ICG)-enhanced interventional imaging. (a) Typical intraoperative fluorescence imaging system using simultaneous image collection from a fluorescence and white light (color) camera visualizing the same field of view through a common optical system (beam splitter and lens). Instead of a lens, an endoscope system could be connected. (b) Photograph of a camera in the operating room. The camera is placed above the patient; white light, fluorescence, and overlay images can be projected on monitors in the operating room. (c) Color reflection image of the spinal cord and (d) ICG-based video-angiography: The fluorescence signal was overlaid on the color reflection image. ICG-angiography visualized the microvascular flow and anatomical orientation, necessary to ensure safe and precise resection of spinal intramedullary tumors. The image shows an early stage shortly after ICG injection highlighting the posterior spinal arteries on both sides. (e) White light reflection (f) overlaid with a fluorescence image revealing a lymph node in early-stage cervical cancer surgery. The lymph node cannot be identified by human vision on the white light image as it is located under the tissue surface. (g) Endoscopic sentinel lymph node (SLN) mapping in the right external iliac region after cervical ICG injection in a woman with endometrial cancer and (h) endoscopic cervical lymph node mapping in the left obturator region likewise reveal a lymph node hidden under the tissue surface and not visible to the eye. (i) Color reflection image and (j) fluorescence pseudo-color image of intraoperative fluorescent cholangiography during robotic single-site cholecystectomy. The fluorescence image contributed to the identification of the extrahepatic biliary anatomy, necessary to minimize the risk of biliary injury. Abbreviations: CBD, common bile duct; CD, cystic duct; CHD, common hepatic duct; GB, gallbladder; J, junction between cystic duct and common hepatic duct; R, robotic instrument. Reproduced from [27].

1.3 Nanoparticles for optical fluorescence imaging

Over the last few decades, a huge variety of fluorescent nanoparticles (NPs) have been developed and found application in several fieds like optoelectronics, including light-emitting diodes, field-effect transistors and photovoltaic devices, as catalyst supports, for chemical and biological sensing, in the biomedicinal field as drug delivery vectors, for cellular, subcellular and

in vivo imaging, cell cytometry, gene delivery, blot-style assays, photodynamic therapy and as scaffolds for tissue engineering. Nanoparticles can be intrinsically fluorescent (quantum dots, up-converting nanoparticles, gold and silver nanoclusters, polymer dots, carbon dots etc.) or be doped with a fluorophore (organic dyes like Rhodamine B, cyanine, fluorescein, etc.)

Regarding their bioimaging application, there are a few factors that need to be taken into account in order to choose the right nanoparticle-candidate for a given application. These factors include the cytotoxicity of the nanoparticle (*in vitro* or *in vivo*), the bio- and water-compatibility, the quantum yield (QY), the size of the nanoparticle, the facile synthesis and surface-bioconjugation chemistries available for the attachment of targeting ligands (such as antibodies, aptamers, peptides, etc.), the photostability of the particles against photobleaching (for allowing a continuous cellular or molecular tracking), the desired emission wavelength and number of targets to be detected (multiplexing). The state of art regarding nanoparticle synthesis for bioimaging is the engineering of nontoxic multimodal nanoparticles, which can be used towards the reliable diagnosis of disease or as theranostic agents (for simultaneous drug delivery and imaging or imaging and photodynamic therapy). Wolfbeis in 2015 provided a review of the nanoparticles commonly used in fluorescent imaging [29].

In this section, a variety of fluorescent nanoparticles currently used in bioimaging will be reviewed with particular emphasis given in their properties interesting for bioimaging.

1.3.1 Quantum Dots

Quantum dots (QDs) are nanometer-scale semiconductor crystals (1 – 100 nm) composed of groups II–VI or III–V elements of the periodic tables. When a photon of visible light hits such a semiconductor, some of their electrons are excited into higher energy states. When they return to their ground state, a photon of a frequency characteristic of that material is emitted. Metal and semiconductor nanoparticles in the size range of 2–6 nm are of considerable interest, due to their dimensional similarities with biological macromolecules (for example nucleic acids and proteins) [30]. Compared with organic dyes and fluorescent proteins, QDs possess near-unity quantum yields and up to 10-100 times greater brightness than most dyes. Quantum dots also

show broad absorption characteristics, a narrow linewidth in emission spectra, continuous and tunable emission maxima due to quantum size effects, a relatively long fluorescence lifetime (5 to > 100 ns compared with 1 – 5 ns for organic dyes) and negligible photobleaching (100 – 1000 times less than fluorescent dyes) over minutes to hours [31]. They display Gaussian emission spectra (with full width at half-maximum (FWHM) of typically ~30 nm) and therefore have multiplexing capacity. One drawback is the blinking phenomenon, which means that the fluorescence intensity strongly varies over time. New generation of non-blinking quantum dots have been reported the last decade [32,33]. An excellent recent review covering from the preparation methods of QDs to single particle tracking, *in vitro*, *in vivo* and multimodal imaging was provided by Wegner and Hildebrandt [34].

There are two main chemical methods for synthesizing QDs: the one involves organometallic synthesis and the other synthesis in aqueous solution [35,36]. The first method involves depositing an inorganic capping shell composed of semiconductor materials of wider bandgap than the core materials CdSe and CdTe. CdS and ZnS were first considered as the ideal shell materials. The synthesis of QDs by the organometallic route is based on variation of the high-temperature pyrolytic reaction. Under stirring and the absence of moisture and oxygen, an appropriate metallic or organometallic precursor (zinc, cadmium, or mercury species) is injected into the corresponding chalcogen precursor (sulfur, selenium, or tellurium species) in a coordinating organic solvent at high temperatures. The advantages of the organometallic method are the ability to create nearly perfect crystal structures and the possibility of high fluorescence quantum yields (approximately 40–50%). The major disadvantage is that these QDs cannot be directly applied in biosystems due to their hydrophobic surfaces. Compared with the organometallic method, aqueous synthesis is more reproducible, cheaper, and more eco-friendly, while the prepared QDs have high stability and biological compatibility and are therefore more suitable for biomedical applications. Generally, the QDs synthesized with this method are CdTe QDs. The Cd precursor, such as $Cd(ClO_4)_2$, $CdCl_2$, or $CdAc_2$, is dissolved in water and stirred, an appropriate amount of thiol stabilizers is added, the pH of the solution is adjusted by addition of NaOH, and then degased. H_2Te or NaHTe is added under stirring to the solution, leading to the formation of CdTe precursors, which is accompanied by a color change of the solution.

Conveniently, several types of QDs emitting in a wide range of wavelengths are commercially available.

Regarding their biomedical potential, cytotoxicity of QDs, which humpers their wide applicability has been observed in many *in vitro* and *in vivo* studies, affecting the cell growth and viability. In other studies, no cytotoxicity is reported. Generally, the existing bibliographic reports regarding the cytotoxicity of QDs are rather controversial. In order to shed some light to this issue, Oh et al. analyzed the results obtained from 307 previous publications regarding QD cytotoxicity [37]. The extent of cytotoxicity has been found to be dependent upon a number of factors including size, capping materials, colour, concentration of QDs, surface chemistry, coating bioactivity, cell line tested, exposure time and cell viability assay used. Significant alterations in cell physiology have not been reported. A number of mechanisms have been postulated to be responsible for QD cytotoxicity. These include desorption of free Cd (QD core degradation), free radical formation, and interaction of QDs with intracellular components [37–40].

The first researchers to use QDs in cell imaging were the Alivisatos' [41] and Nie's groups [42] in 1998. Since then, QDs have experienced enormous success in fluorescence imaging because of their unique optical properties. In addition, QDs have been successfully used as fluorescent probes for a variety of bioanalytical applications, such as detection of DNA, proteins, and other biomolecules or cellular labeling [34,43–45] and binding assays that use fluorescence resonant energy transfer (FRET) to visualize target events [46].

Wu et al. [47] reported that QDs linked to IgG and streptavidin were successfully applied to specifically label different types of cellular biomarkers such as the breast cancer biomarker Her2, actin and microtubule fibers, and nuclear antigen. These targets can be found at different cell localizations such as the cell surface, intracellularly and inside the nucleus. To demonstrate the great potential of QDs as fluorescent probes in bioimaging, different types of specimens were visualized, including living cells, fixed cells and tissues (Figure 8). Green QDs and red QDs emitting at 535 nm and 560 nm respectively were used in this study and the obtained signals were specific for the aforementioned biomarkers, bright and considerably photostable. In addition, the multiplexed targeting of Her2 and nuclear antigen in the breast cancer SK-BR3

cells was assessed, demonstrating how QDs offer significant advantages over organic dyes in multiplexed targeted imaging.

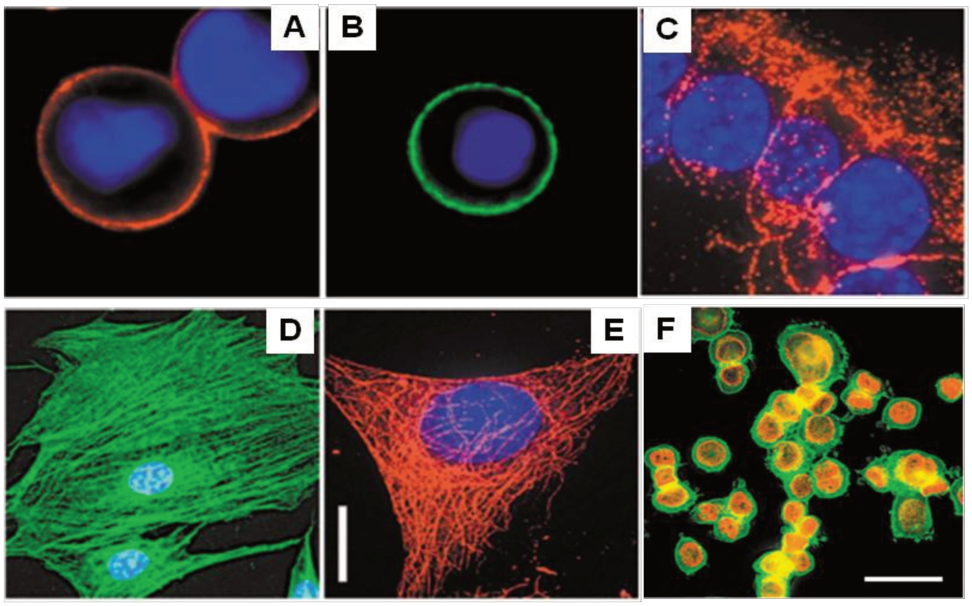

Figure 8 Detection of cancer marker Her2 with QD-IgG (A, B, C), actin (D), microtubule (E) and multiplexed detection for Her2 and nuclear antigens (F). (A, B) Fixed breast cancer SK-BR-3 cells were incubated with monoclonal anti-Her2 antibody and goat anti-mouse IgG conjugated to QDs. Her2 was clearly labeled with (A) QD 630–IgG and (B) QD 535–IgG (C) Detection of Her2 with QD 630–IgG on sections of mouse mammary tumor tissue in combination with a rabbit antiserum recognizing the cytoplasmic domain of the antigen. (D) Actin filaments were stained in n 3T3 mouse fibroblast cells with biotinylated phalloidin and QD 535–streptavidin (green). (E) Microtubules were labeled in 3T3 cells with monoclonal anti-α- tubulin antibody, biotinylated anti-mouse IgG and QD 630–streptavidin (red). Nuclei were counterstained blue with DAPI. (F) Multiplexed detection of Her2 and nuclear antigen (NA) in SK-BR-3 cells with QD 535-IgG and QD 630-streptavidin respectively. Her2 on the surface of SK-BR-3 cells was stained green with mouse anti-Her2 antibody and QD 535–IgG (green). Nuclear antigens were labeled with ANA, anti-human IgG–biotin and QD 630–streptavidin (red). Reproduced from [47].

Cai et al were the first to apply arginine-glycine-aspartic acid (RGD) labeled QDs for targeted imaging *in vitro*, *ex vivo* and in living mice. The results reported, opened up new perspectives for integrin-targeted NIR (λ_{em}= 705 nm) optical imaging with high potential in cancer diagnosis and imaging-guided surgery and therapy [48]. In this study it was demonstrated *via* fluorescence imaging that QDs labeled with RGD peptide can selectively target the $\alpha_v\beta_3$-positive tumor vasculature in a murine xenograft model with high contrast, although, 6 h after the injection, there was also particle accumulation in the liver, bone marrow and lymph nodes (Figure 9).

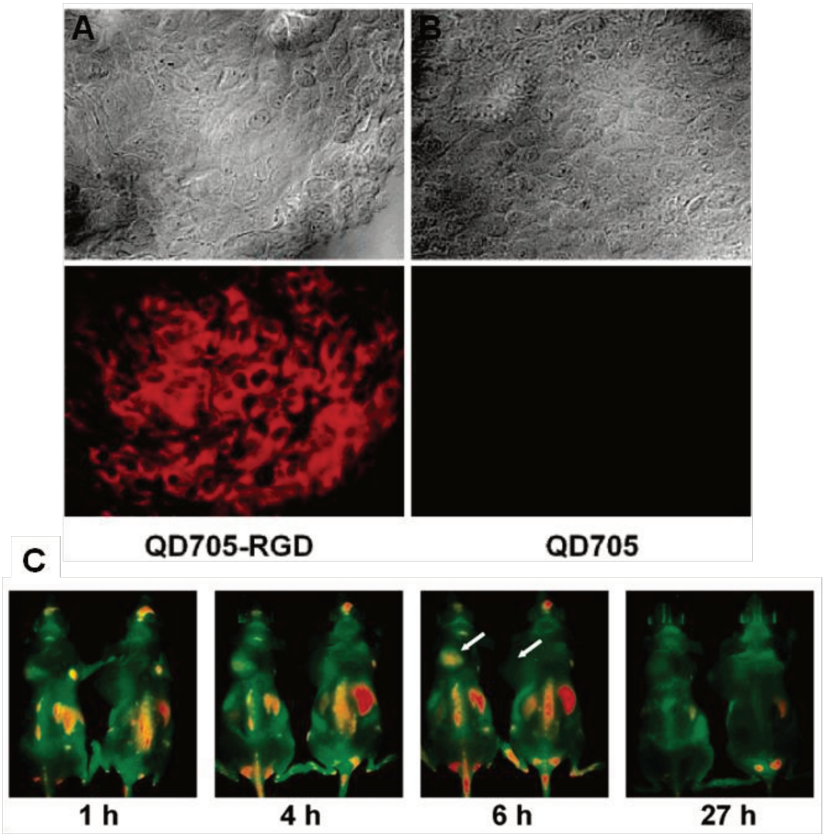

Figure 9 Frozen U87MG tumor tissue staining using (A) QD-RGD and (B) bare QDs. (C) *In vivo* NIR fluorescence imaging of U87MG tumor-bearing mice (left shoulder, pointed by white arrows) injected with 200 pmol of QD-RGD (left) and bare QDs (right), respectively. All images were acquired under the same instrumental conditions. The mice autofluorescence is color coded green while the unmixed QD signal is color coded red. Prominent uptake in the liver, bone marrow, and lymph nodes was also visible. Reproduced from [48].

Gao et al. [49] in order to demonstrate the feasibility of multiplexed labeling used QDs emitting at 525 nm, 565 nm, 605 nm, 655 nm and 705 nm directly conjugated to primary Abs against five tumor biomarkers in human breast cancer cells (MCF-7 and BT-474) and on single paraffin embedded clinical tissue sections. Simultaneous quantification of estrogen receptor, progesterone receptor, and Her2 receptor gave similar results to the traditionally applied methods like immunohistochemisty, western blotting, and fluorescence *in situ* hybridization, suggesting that the QD-based imaging is well suited for molecular profiling of tumor biomarkers *in vitro*, which paves the way to the translational application of QDs.

To image the lymphatic circulatory system, Kim et al. [50] injected intradermally near-infrared emitting QDs with a size of approximately 15–20 nm into large animals such as mouse and pig.

They found that when only 400 pmol of NIR QDs were injected intradermally into the thigh of a 35-kg pig, a surgeon was able to follow the lymphatic flow towards the sentinel lymph node (SLN). The real-time images obtained included lymph channels that diverge from the injection site and then coalesce into the SLN. For the localization of the SLN an approximate time of only 3–4 min was required, and the NIR QDs permitted image guidance through the whole operating procedure.

Five years later, the same group synthesized hyaluronic acid–QD (HA-QD) conjugates by a simple method using the electrostatic interactions between HA and the QDs and subsequently applied them for *in vitro* cancer cell imaging and real-time *in vivo* lymphatic vessel imaging [51]. This work marked the development of real-time QD-based imaging *in vivo* that may have a great potential in anticancer drug screening. First, the specific binding of HA-QDs to HeLa cells, used as a representative cancer cell line that overexpresses HA receptors was demonstrated. Subsequently, the researchers chose for the *in vivo* application HA-QDs with 58 nm average size since these afforded moderately efficient lymphatic flow transportations from the subcutaneous injection site. The slow lymphatic flow maximizes the retention time of the HA-QDs in the lymphatic vessels and allows them to bind to the lymphatic endothelial cells. Under UV irradiation the injection sites glowed as a result of the HA-QD fluorescence. The injected solutions entered into the lymphatic drainage within a few-minute time and began to reveal the lymphatic vessels around the injection site. The researchers also compared the lymphatic vessel visualizations made by HA-QDs and by unconjugated QDs. The aforementioned types of QDs were injected simultaneously, and images were taken 30 min after the injections (Figure 10). In the case of HA-QDs, clear visualization of lymphatic vessels and bright fluorescence signal was observed along the inner walls of the vessels that could even be retained up to a few days after the injection. In contrast, unconjugated QDs visualized the vessels in a faint manner.

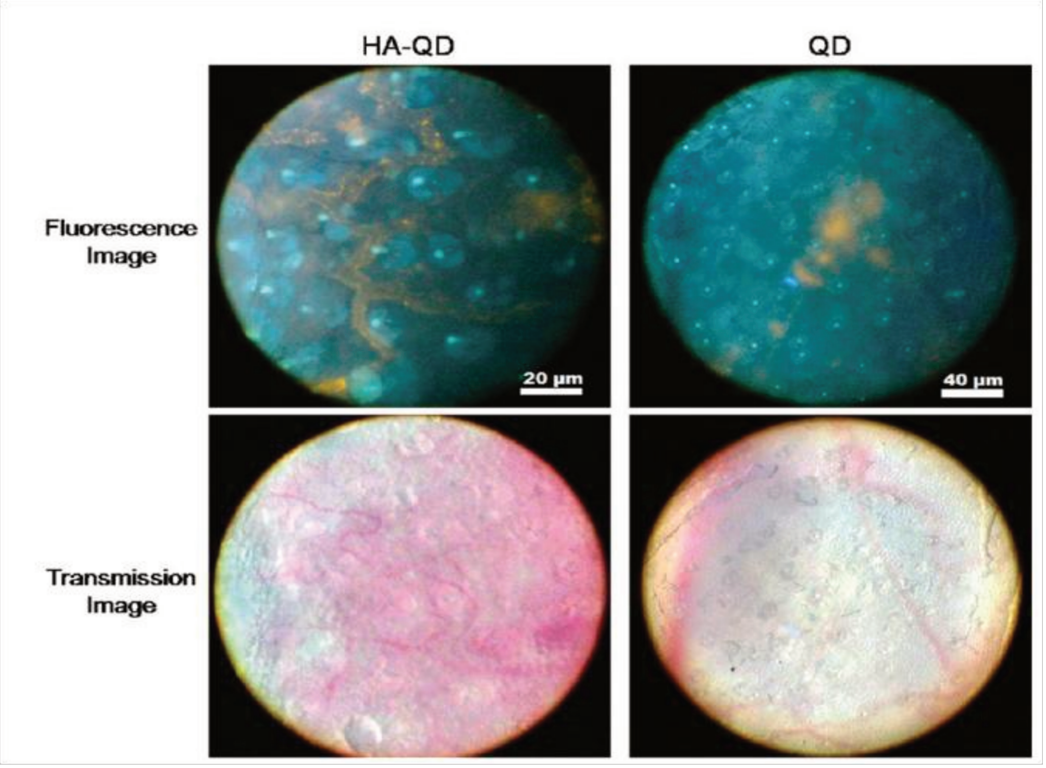

Figure 10 Fluorescence (top row) and transmission (bottom row) microscope images near the subcutaneous injection sites of 200 nM of hyaluronic acid-quantum dot conjugate (HA-QDs, ratio of QD/HA is 4:1) solution (left column) and unconjugated quantum dot (QD) solution (right column). Images are taken 30 min after the concurrent injections. Reproduced from [36].

The current research in QD production for bioimaging focuses on: 1) less toxic alternatives based on Cd-free QDs [22,52–54], 2) NIR emissions, 3) multimodal potential for diagnosis [54,55] and 4) multifunctional properties for theranostic applications [56,57]. The tendency in QD-based bioimaging is now the use of Ag_2S-QDs, since they have been reported to be fairly biocompatible non-cytotoxic NIR-emitters [22,58].

1.3.2 Noble metal nanoparticles

Studies on noble metal nanomaterials with interesting size-dependent electrical, optical, magnetic, and chemical properties have been intensively pursued, not only for their fundamental scientific interest, but also for their many technological applications [59,60].Specific features of such nanoparticles include excellent photostability, water-solubility, size-dependent colors, lack of swelling, sharp contrast, ease of characterization with Transmission Electron Microscopy

(TEM) or Scanning Electron Microscopy (SEM), and an established surface chemistry (often thiol-based) which is useful if targeted imaging or biosensing is desired.

In general, single gold or silver NPs display rather weak fluorescence and are not commonly used as imaging probes with a few exceptions including imaging of HeLa cells (gold NPs) and the adenocarcinomic human alveolar epithelial A549 cells (silver NPs) [61,62]. An alternative is the use of fluorescent metal nanoclusters (NCs), which have attracted considerable attention during the past decades. Fluorescent metal nanoclusters can be prepared by reduction of metal precursors or etching of large nanoparticles in the presence of strong stabilizers such as small thiol-molecules, polymers, and biomolecules. In contrast to the large Au or Ag nanoparticles, that have very low fluorescence emission, interestingly enough, when their size is further reduced to < 10 nm, the ultra-small nanoclusters possess different crystal structures and exhibit strong photoluminescence while their SPR property disappears. Nanoclusters consist of a few to tens of metal atoms and bridge the gap between molecules and nanoparticles displaying simultaneously the properties of both. Their novel optical, electronic, and catalytic activities make them very useful in ultrasensitive detection, biolabelling, bioimaging, and catalysis [63,64]. It should be pointed out that several excellent review papers have been dedicated to the metal NCs [63–67].

Regarding bioimaging, metal NCs possess an attractive set of features, such as ultrasmall size, good biocompatibility, brightness and photostability. In most cases the metal NCs are excited in the blue-green region and their large Stoke shifts can prevent spectral cross-talk and, thus, enhance the detection signal. Recently, a number of works have reported biological labeling and imaging applications based on fluorescent metal NCs. Wang et al. [68] proposed a galvanic replacement route to prepare fluorescent Au NCs using presynthesized and size-controlled Ag NCs as templates. The obtained Au NCs show strong fluorescence QYs (~10%) and good water- and bio-compatibility. The Au NCs were used as fluorescent probes for cellular marking in oral adenosquamous carcinoma CAL-27 cells and MC3T3-E1 normal cells, respectively. The results demonstrated that the particles were mostly found in the cell nucleus and were not only distributed in the cytosol.

Later, Wang et al. [69] reported a novel strategy for the synthesis of 2 nm-Au NCs and applied them for fluorescence imaging *in vivo* in nude mice. The fluorescent Au NCs emitting in the green region were spontaneously biosynthesized by cancerous cells (HepG2, human hepatocarcinoma cell line; K562, leukemia cell line) through Au(III) reduction inside the cells' cytosols, and finally concentrated around their nucleoli. Interestingly, this biosynthesis occurred only in the cancer cells and not in the noncancerous human embryo liver cells (L02) that were used as control cells. This observation has great potential to serve as a new strategy for specific fluorescent self-bio-marking of tumors due to the higher metabolic activity of these cells in contrast to normal cells, which opens up promising opportunities for biomedical applications requiring specific and sensitive imaging of malignancy without direct injection of vectorized fluorescent nanoparticles or other molecular probes.

Liu et al. [70] reported for the first time the synthesis of fluorescent Au NCs by using insulin as protecting ligand. The as-prepared insulin-Au NCs show good biocompatibility and retain the natural insulin bioactivity in lowering the blood glucose levels. The uptake efficiency of insulin-Au NCs by C2C12 cells may serve as a biomarker to distinguish the differentiated versus undifferentiated C2C12 myoblasts, since the differentiated ones overexpress on their surface insulin receptors that are correlated with malignancy. The confocal images presented in Figure 11 indicate that the red-emitting Au NCs are dispersed in the cytoplasm of the fully differentiated C2C12 mouse myoblasts. Moreover, in this study, the potential use of the fluorescent Au NCs in CT imaging was demonstrated.

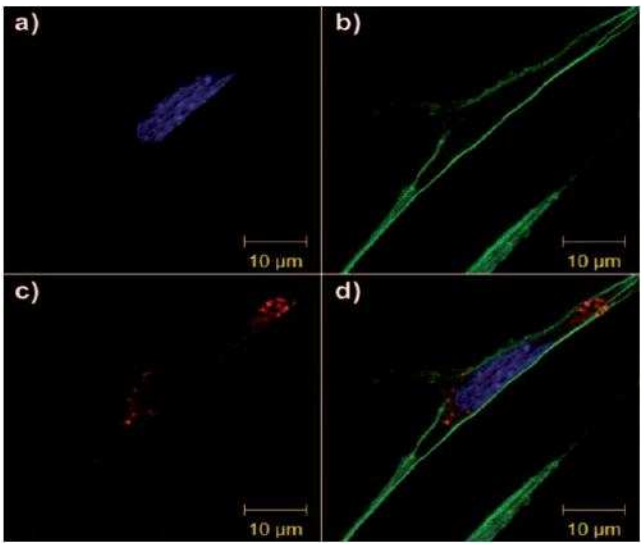

Figure 11 Microscopic observation of internalization of the insulin–Au NCs. Differentiated C2C12 myoblasts were treated with insulin–Au NCs for 2 h. a) Cell nucleus stained with 4',6-diamidino-2-phenylindole (DAPI, blue). b) Actin fiber stained with Alexa Fluor 488 phalloidin to confirm the cell boundary (green). c) Insulin–Au NCs exhibit red luminescence. d) Fluorescence image overlay of the three images. Reproduced from [70].

In a more recent example, Chattoraj et al. reported *in situ* generated fluorescent Au-NCs used for bioimaging of three human cancer cells, namely, lung, breast (Figure 12), and colon, by confocal microscopy [71]. The amount of Au-NCs in non-cancer cells is 20–40 times less than those in the corresponding cancer cells. The Au-NCs exhibited fluorescence maxima at 490–530 nm inside the cancer cells and have the potential of cancer diagnosis and therapy.

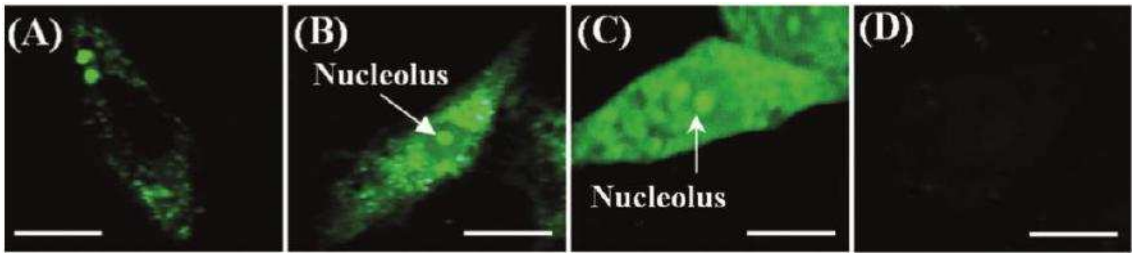

Figure 12 Confocal images of live breast cells stained by in situ generated Au-NCs. Confocal images of MCF7 (breast cancer cell line) at: A) 200 µM Au-NCs, B) 600 µM Au-NCs, and C) 2000 µM Au-NCs. Confocal images of MCF10A (control cell line) at D) 600 µM Au-NCs. The scale bar corresponds to 4 µm. Reproduced from [71].

There are a few obstacles that still need to be overcome regarding noble metal-based imaging such as the relatively low fluorescence QY, which is usually much less than that of QDs and many organic dyes, the polydispersity in size, which makes it very difficult to fundamentally

study the particle novel properties and mechanisms, the difficulty in modifying their surface in order to introduce other functions due to their ultra-small size and lower stability.

1.3.3 Upconversion nanoparticles

The phenomenon of upconversion is defined as a nonlinear optical process in which the sequential absorption of two or more photons leads to the emission of a single photon at a shorter wavelength (see section 1.2.4). The reported UCNPs are usually a rare earth (RE)-doped inorganic host matrix. The host matrix is required to have low lattice photon energies and most of those reported are oxide, halide, sulfide or oxysulfide. The doping RE ions (lanthanides) play roles as a sensitizer (Yb^{3+}) and an activator (Er^{3+}, Ho^{3+}, Tm^{3+}). The dopant is the emitter and additional doping with fluorophores is not needed. UCNPs can emit high-energy photons under NIR excitation [29,72,73]. The size of UCNPs is tunable, varying from 10 to 100 nm, and affects their quantum yields. The color of the emission of UCNPs is independent of the excitation wavelength, which is rather longwave (750–1000 nm). UCNPs with oleate capping, as-prepared by the most common synthetic routes, possess moderate brightness, but those modified with hydrophilic coatings are much less bright and their QYs hardly exceed 0.5% in aqueous media. Nevertheless, in few cases, QYs of 1–3% have also been reported. The seemingly poor QYs of UCNPs do not hamper their wide use in fluorescence bioimaging, since, in the case of UCNPs, images with high signal to noise ratios are obtained, due to their anti-Stokes emission behavior [29].

Since the discovery of the upconversion process in the 1960s, UCNPs have shown certain advantages in bioimaging [74–76]. The reasons are the following: (1) UCNPs minimize the photo-damage to cells and tissues; (2) NIR light exhibits high tissue penetration; (3) the emission locates in visible or NIR region, so the interference of background cell or tissue autofluorescence can be effectively avoided; (4) UCNPs show excellent photostability and low cytotoxicity as bioimaging agents; (5) They are weakly interacting with proteins and hardly attacked by the immunosystem; (6) They do not measurably swell in aqueous media. Although UCNPs are promising biocompatible NIR imaging agents that could replace QDs in some applications, their

wide use in bioimaging is still hampered by synthetic difficulties resulting in batch-to-batch differences in size and emission wavelengths.

Upconverting materials were first used in tissue imaging in 1999, where Zijlmans et al reported the first upconversion bio-imaging [77]. The authors observed low autofluorescence signal and no photobleaching of Y_2O_2S:Yb/Tm particles 200-400 nm in size upon excitation with a 980 nm-laser. Subsequently, two different upconverting compositions were tested for specific cell and tissue staining. These included green-emitting ytterbium/erbium (Y.Yb.Er)O_2S and blue-emitting ytterbium/thulium $(Y.Yb.Tm)_2O_2S$.

In another early cell-imaging application, Nyk et al. synthesized aqueous dispersible fluoride ($NaYF_4$) nanocrystals of about 20–30 nm size that were co-doped with the rare earth ions Tm^{3+} and Yb^{3+}, showing NIR-to-NIR (λ_{ex} = 975 nm, λ_{em} = 800 nm) upconversion for *in vitro* and *in vivo* photoluminescence imaging [78] (Figure 13). This NIR-to-NIR upconversion process demonstrated even deeper light penetration into the biological specimen and resulted in high contrast imaging due to the absence of background autofluorescence and decreased light scattering (inset Figure 13). These particles were used to image human pancreatic cancer cells (Panc 1) and mice using a Maestro fluorescence imaging system. MTS (3-(4,5-dimethylthiazol-2-yl)-5-(3-carboxymethoxyphenyl)-2-(4-sulfophenyl)-2H-tetrazolium) cell viability test showed no cytotoxicity for concentrations up to 2 mg/mL.

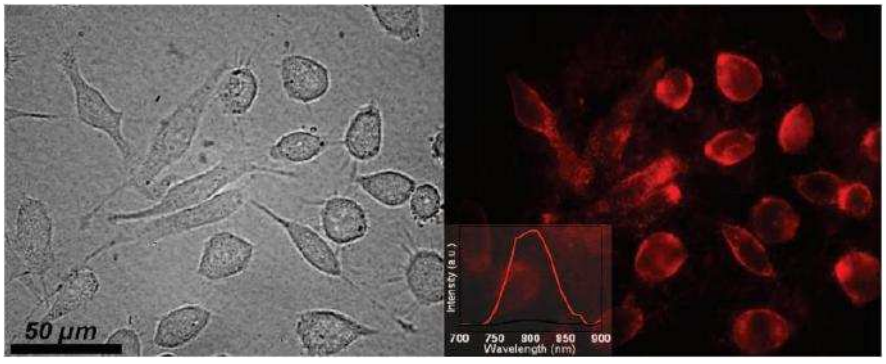

Figure 13 *In vitro* transmission (left) and PL (right) images of Panc 1 cells treated with UCNPs. Inset shows localized PL spectra taken from cells (red) and background (black). Reproduced from [78].

Achieving high QYs in water solutions is still a challenge and most synthetic protocols result in QYs< 1%. Recently, Liu et al.[79] synthesized water-soluble UCNPs based on triplet-triplet annihilation (TTA) by co-loading sensitizer (octaethylporphyrin Pd complex) and annihilator (9,10-diphenylanthracene) onto silica nanoparticles, whose upconversion QY could be as high as 4.5% in aqueous solution. The particles were found non-cytotoxic after 24 h of incubation with HeLa cells for concentrations up to 320 µg/mL using the MTT cell viability test. Subsequently, they were successfully applied in the *in vivo* imaging of lymph node in living mouse with an impressive signal-to-noise ratio (Figure 14). The high signal to noise ratios (SNRs) achieved *in vivo* (SNR=25) and *ex vivo* (SNR=49) render these particles a promising imaging tool for biomedical applications.

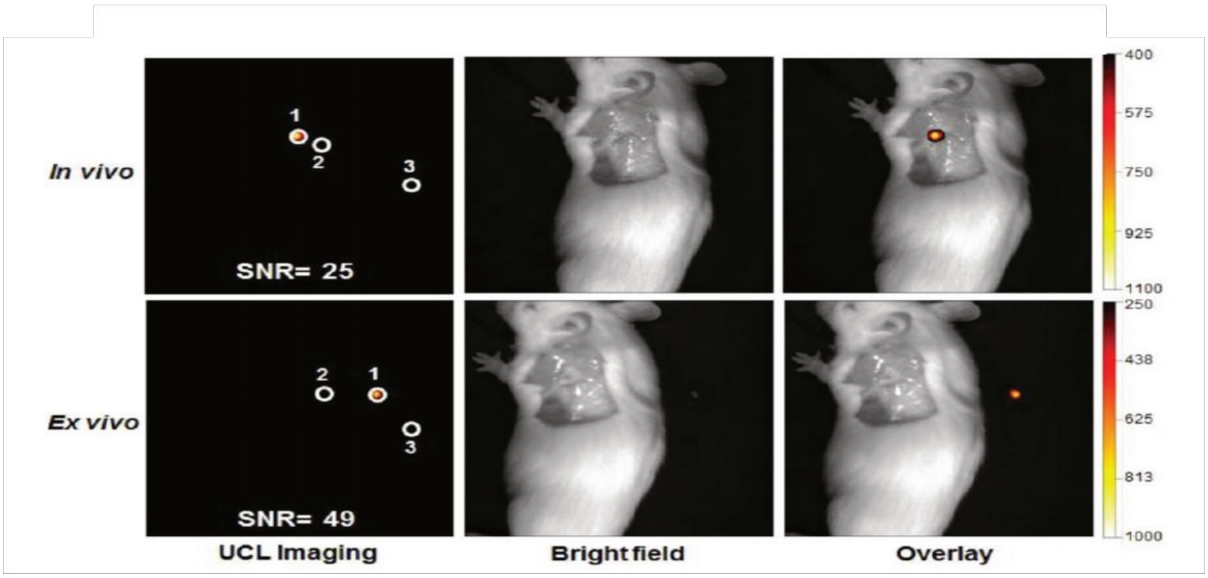

Figure 14 ***In vivo*** **and** ***ex vivo*** **upconversion luminescence lymphatic imaging at 30 min post injection of 20 µL of TTA-UCNP in paw. Impressive signal to noise ratios were achieved both** ***in vivo*** **and** ***ex vivo*****. Reproduced from** [79].

1.3.4 Semiconducting Polymer Dots

Very recently, semiconducting polymer dots (PDs) have emerged as a new class of promising fluorescent nanoprobes that exhibit good fluorescence brightness and photostability, high radiative rate and low cytotoxicity. PDs are nanoparticulate aggregates of π-conjugated organic semiconducting polymers such as those based on fluorene, phenylene, thiophene, and benzothiadiazole monomers and derivatives (Figure 15), typically in a glassy phase. To prepare

PDs, there are two main approaches. One is based on miniemulsion and the other is based on nanoprecipitation. In the miniemulsion approach, amphiphilic surfactant molecules are used to form water-miscible micelles that contain the hydrophobic semiconducting polymers. In comparison to the miniemulsion method, PDs prepared by nanoprecipitation are usually smaller in size and can be easier conjugated to biomolecules, such as streptavidin by covalent bonding for further biofunctionalization. For biological applications, a significant problem has yet to be addressed: control over their surface chemistry and conjugation to biological targeting ligands. Although research efforts involving silica or phospholipid encapsulation can result in composite particles with surface functional groups, many of the results reported so far on cellular labeling with PDs are presumably based on endocytosis, which is a far less effective and unspecific process compared to the established targeted labeling methods used with organic dyes or QDs [29,80–82].

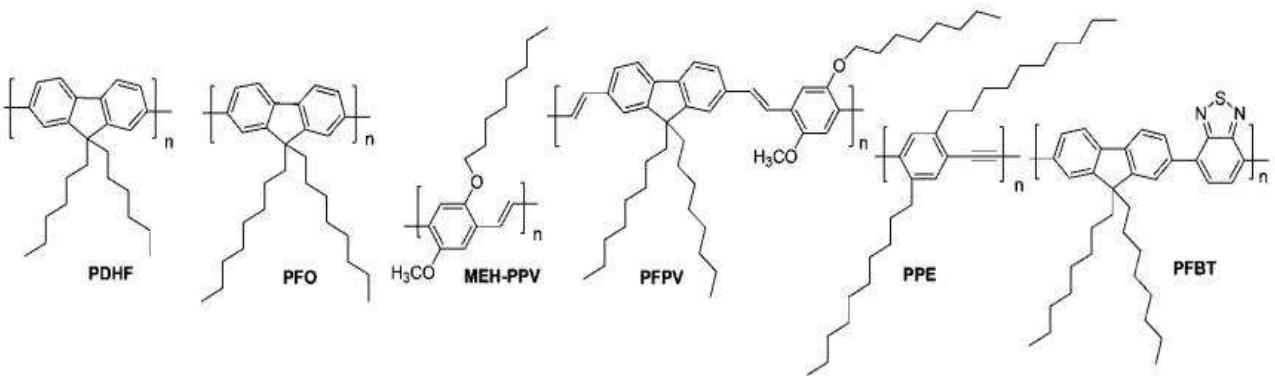

Figure 15 The structures of poly(9,9-dihexylfluorene) (PDHF), poly(9,9-dioctylfluorene) (PFO), poly[2-methoxy-5-(2-ethylhexyloxy)-1,4-phenylenevinylene] (MEH-PPV), poly[2-methoxy-5-(2-ethylhexyloxy)-2,7-(9,9-dioctylfluorene)] (PFPV), poly(p-phenylene ethynylene) (PPE), poly(9,9-dioctylfluorene-2,7-diyl-co-benzothiadiazole) (PFBT).

Doping with fluorophores is normally not necessary since the backbone of conjugated polymers behaves as an array of light harvesting units that exhibit a larger optical cross section compared to small organic molecule dyes. Despite the fact, many bibliographic examples exist where the PDs were doped with both molecular probes and other nanoparticles in order to form composite materials with new optical properties. PDs were doped with NIR fluorophores, QDs, or Eu(III) complexes with a spectrally narrow, red-shifted emission, and, in the case of Eu(III), long-lived excited states, which permitted time-gated measurements and cellular imaging with higher signal-to-noise ratios. In the aforementioned cases, PDs act as antennae that absorb the excitation light and efficiently transfer the excitonic energy to the dopant emitters, increasing their

brightness. Leaching of the dopant in these applications is a concern that needs further investigation [29,80–82].

Their intrinsic excellent optical characteristics make PDs new attractive materials for various optoelectronic applications, including light-emitting diodes, field-effect transistors, and photovoltaic devices [83,84] and promising fluorescent cellular propes for flow cytometry, blot-style assays, specific cellular, subcellular imaging, and *in vivo* imaging. In addition to that, their permeability and their hydrophobic interior serve as a combination that could be exploited in drug delivery applications, since, hydrophobic therapeutics can be loaded within the interior of the PD creating multifunctional materials with potential use in theranostic applications [80,82].

First used for bioimaging in 2008 [85], PDs have had a growth spurt over since. In this first bioimaging experiment, Wu et al. reported a size-controlled preparation of several new polymer dots with an approximate size of 5-15 nm and their photophysical characteristics relevant for bioimaging applications such as cellular imaging and single particle tracking. These new PDs showed enhanced performance in comparison to the previous reports in terms of quantum yield, radiative rate, and photostability. More precisely, nanoparticle absorption cross section of 10^{-13} cm^2 and quantum yields ~40% were demonstrated. Single particle imaging, photobleaching kinetics, and fluorescence saturation studies indicated much higher emission rates (10^8 s^{-1}) and practically no photoblinking of the PDs as compared to organic dyes or QDs. For the bioimaging experiment, the macrophages J774.A1 were incubated with 1 nM of different PDs suspensions (polyphenyleneether dots (PPE), poly(2-fluoro-1,4-phenylene vinylene) dots (PFPV), Polyfluorenebenzothiadiazole dots (PFBT) and Poly[2-methoxy-5-(2-ethylhexyloxy)-1,4-phenylenevinylene] dots (MEHPPV)) for 12 h and cellular uptake *via* endocytosis was observed (Figure 16).

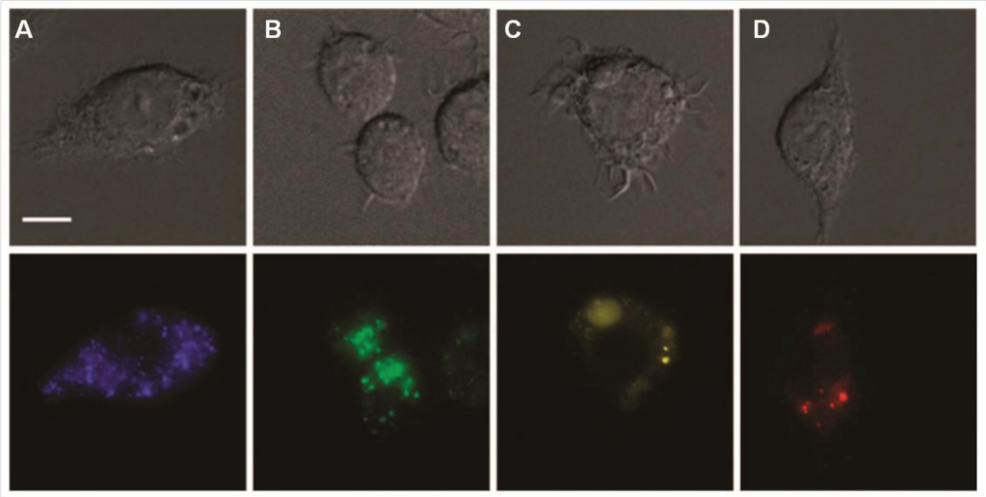

Figure 16 Differential interference contrast images (top), and fluorescence images (bottom) of macrophage cells labeled with: (A) polyphenylenether dots (PPE) (λ_{ex}=390 nm, λ_{em}=440 nm) , (B) poly(2-fluoro-1,4-phenylene vinylene) dots (PFPV) (λ_{ex}=445 nm, λ_{em}=510 nm), (C) Polyfluorenebenzothiadiazole dots (PFBT) (λ_{ex}=450 nm, λ_{em}=545 nm), and (D) Poly[2-methoxy-5-(2-ethylhexyloxy)-1,4-phenylenevinylene] dots (MEHPPV)(λ_{ex}=485 nm, λ_{em}=590 nm). Scale bar: 10 µm. Reproduced from [85].

Three years after their first bioimaging report, Wu et al. attempted this time living cell and *in vivo* targeted imaging [86]. The authors designed bioconjugated PD-based systems of approximately 15 nm size that consisted of donor–acceptor polymers for *in vivo* tumor targeting. PD–streptavidin probes were applied in order to label a specific cellular target, EpCAM, an epithelial cell-surface marker used for the detection of circulating tumor cells, on the surface of live MCF-7 human breast cancer cells and after the cells were incubated sequentially with a primary anti-EpCAM antibody and a biotinylated goat antimouse immunoglobulin G (IgG) secondary antibody. In addition, PDs were covalently conjugated to the CTX peptide that has strong affinity for tumors of neuroectodermal origin for specific brain tumor imaging in mice.

1.3.5 Carbonaceous materials

Carbon is commonly known as a black material, and, until recently, it was impossible to admit that it could be soluble in water and even show high fluorescence. However, the black material was associated with classical bulk carbon because, when carbon nanostructures are synthesized, their properties differ dramatically from these of the macroscopic material. Carbon nanomaterials can take several shapes and the best known and used in biology are: 1) fullerenes (C70 mainly),

2) carbon nanotubes (CNTs; single-walled and multi-walled), 3) nanodiamonds, 4) graphene (which is non-fluorescent), and the oxidized species graphene oxide, reduced graphene oxide, graphite oxide, 5) graphene quantum dots and 6) carbon dots (CDs), which were discovered recently. The main photoluminescence mechanisms of these carbonaceous materials are represented in Figure 17 together with their main biomedical applications. Several reviews covering the synthesis, optical properties and applications of these materials exist [87–90].

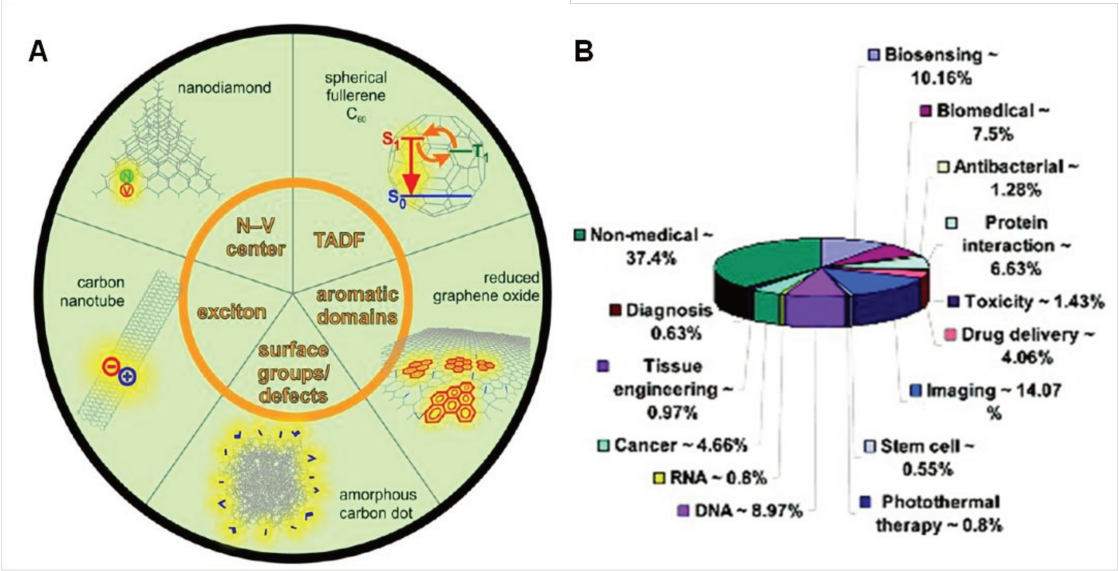

Figure 17 (A) Five representative known mechanisms of photoluminescence in nanosized carbon allotropes, and the respective allotropes in which each mechanism occurs. Reproduced from [87]. (B) Various applications of carbonaceous materials. 62.6% of their applications are biomedical in nature. Reproduced from [88].

1.3.5.1 Carbon dots

Carbon dots (CDs) can be defined as clusters of carbon atoms with diameters of typically 2 to 8 nm that also contain substantial fractions of oxygen and hydrogen if not nitrogen. CDs were discovered accidentally by Xu et al. in 2004 while purifying single-walled carbon nanotubes (SWCNTs) fabricated by arc-discharge methods [91]. Since then, CDs have been prepared from numerous organic materials and natural products containing carbon in various forms. Ammonium citrate, octadecylammonium citrate, and sodium 11-aminoundecanoate can be used as molecular precursors. In addition to these precursors, other small organic compounds, such as citric acid, boric acid, amino acid, glycerol, glucose, ethylene glycol, N-acetylcysteine, diamine,

and benzene have also been extensively used. Some natural sources, such as orange juice, banana juice, soy milk, meat, coffee, beer, egg, potato, sugar, bread, lysozyme, sucrose, starch, and grass have been studied to fabricate CDs. The synthesis of CDs can be divided into three basic steps: 1) synthesis of raw CDs; 2) passivation operations; and, 3) functionalization reactions. Raw CDs are not highly fluorescent [92] and chemical treatments of their surface, including oxidation of the surface carbons to carboxylic acid groups with nitric acid, doping the oxidized CDs with inorganic salts and capping the CDs with an organic polymer like polyethylene glycol polymer are needed in order to render them fluorescent. These operations are referred as passivation of CDs [93–96].

On the surface of the passivated CDs there are carboxyl moieties, which render CDs water-soluble and provide chemically reactive groups for further functionalization. CDs display both size and excitation wavelength dependent photoluminescence behavior, which make multiplexing by using CDs impossible. In addition, like all carbon nanoparticles in general, CDs can be single-photon and multi-photon excited [29]. Their ultrafine dimensions, tunable surface functionality, and the vast variety of simple, fast, and economic synthetic procedures available are some of the reasons for which CD emitters have found use in a wide range of applications, including chemical and biological sensing, bioimaging, drug delivery, photodynamic therapy, photocatalysis and electrocatalysis [93–96].

Regarding the cytotoxicity of CDs, results may vary depending on the synthetic route, the passivation and bioconjugation methods used for their production. Toxicity studies have been conducted by various research groups on different cell lines including 293 T human kidney cells, human hepatocellular liver carcinoma cell line HepG2, human breast cancer cell line MC-7 and colorectal adenocarcinoma HT-29 cells. While the reports still remain few, CDs appear to have low toxicity, with 80-90% cell viability obtained for concentrations around 500 μg/mL, which is much higher than the concentrations required for bioimaging [93]. A few negative points for their biological applications include the relatively complex procedures for their separation, purification and functionalization and their generally low quantum yields, which range from 5 to 45%. Although they do not measurably swell in aqueous solutions, aggregation is occasionally observed.

The first assessment of the bioimaging potential of CDs was presented by Sun et al in 2006 [92]. In this study, CDs were prepared via laser ablation of carbon materials followed by passivation with nitric acid, and with PEG1500N or poly-(propionylethylenimine-co-ethylenimine) (PPEI-EI). Subsequently, these CDs were used to label E. coli ATCC 25922 cells and to observe their cellular uptake by the heterogeneous human epithelial colorectal adenocarcinoma cell line Caco-2, using confocal microscopy (Figure 18). For E. coli ATCC 25922 cells labeling experiment, the cells were incubated with a solution of 0.1 mg/mL of CD-PEG1500N for 18 h, while for the Caco-2 cellular uptake experiment, cells were incubated with 0.5 mg/mL of the PPEI-EI-passivated CD for 1.5 h. The tunable emission of CDs depending on the excitation wavelength is illustrated in Figure 18.

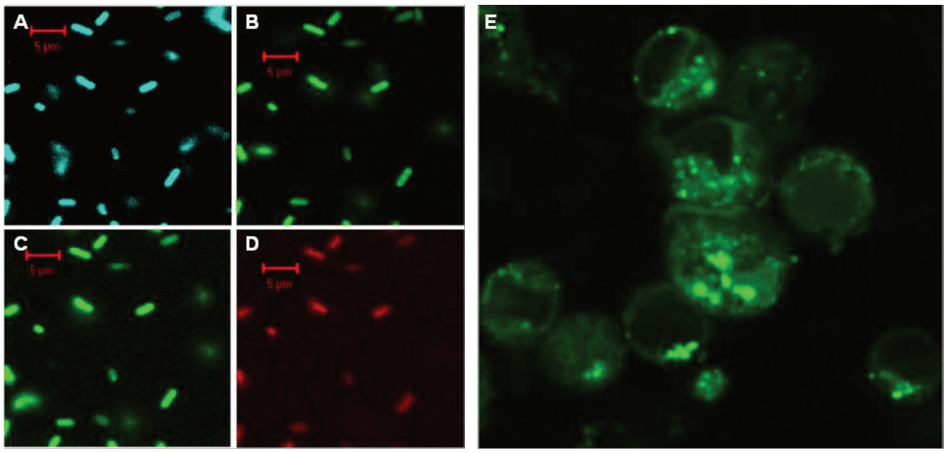

Figure 18 Confocal microscopy images of E. coli ATCC 25922 cells (A-D) and Caco-2 cells labeled with CDs (E). A) λex= 458 nm, detected with 475 nm long pass filter; B) λex= 477 nm, detected with 505 nm long pass filter; C) λex= 488 nm, detected with 530 nm long pass filter; and D) λex= 514 nm, detected with 560 nm long pass filter. Reproduced from [92].

Different passivation procedures lead to different material properties and thus different uptake and cytotoxicity in cells. In an attempt to investigate the potential of CDs as biocompatible fluorescent probes for targeting cancer cells *in vitro*, Li et al. [97] synthesized CDs passivated with three different polymers including: polyethylene glycol (PEG) (PEG1500N); a triblock copolymer, comprising poly(ethylenimide)-β-poly(ethylene glycol)-β-poly(ethylenimide) (PEI-PEG-PEI); and, 4-armed amine-terminated PEG (4-arm PEG). In order to functionalize them, the CDs were conjugated to the glycoprotein transferrin (80 kDa) that successfully targets the transferrin receptors overexpressed in cancer cells like HeLa. The functionalization of the CDs

did not change the fluorescent properties of the probe. After 2 h incubation, HeLa cells internalized the functionalized CDs more efficiently than the non-functionalized; and, the CDs passivated with PEG1500N and 4-arm PEG more than those passivated with PEI-PEG-PEI (Figure 19).

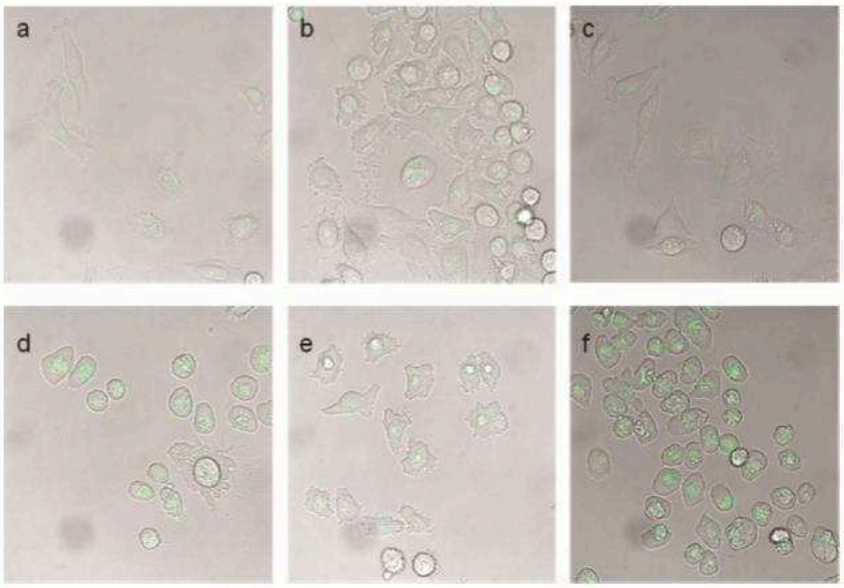

Figure 19 Carbon dots (a) CD-PEG1500N , (b) CD-PEI-PEG-PEI, (c) CD-4 arm PEG, (d) Transferin conjugated CD-PEG1500N (e) Transferin conjugated CD-PEI-PEG-PEI, and (f) Transferin conjugated CD-4 arm PEG with internalization after 2 h of incubation with HeLa cells. Photoluminescence (shown as green) and transmission images are merged. Reproduced from [97].

1.3.5.2 Nanodiamonds

The first nanodiamonds (NDs) were produced by detonating carbon-containing explosives in an oxygen-deficient environment to avoid carbon oxidation. Since then, a plethora of other methods of nanodiamond synthesis has been discovered, such as laser ablation, high-energy ball milling of diamond microcrystals grown at high static pressure and high-temperature, chemical vapor deposition, microplasma-assisted ND formation from ethanol vapor at atmospheric pressure, chlorination of carbides, ion irradiation of graphite, electron irradiation of carbon onions, and ultrasound cavitation [87,90,98].

Especially impressive are demonstrations of ND applications in the biomedical arena. The surface of NDs can be easily derivatized with a wide range of functional groups. These surface-functionalized NDs provide a versatile platform for bioconjugation with aptamers, peptides and proteins. Additionally, their biocompatibility and low cytotoxicity have made NDs useful as drug and gene delivery vehicles. NDs can also be used as light scattering labels due to the high refractive index and unique Raman signatures of the diamond material and NDs containing multicolour (blue, green and red) centres can be applied as markers for optical bioimaging [87,90,98].

Among a hundred colour centres listed in diamond, the negatively charged nitrogen-vacancy centre, $(N\text{-}V)^-$, is of particular interest to bioimaging since its emission is at the NIR window. The aforementioned centre absorbs at 560 nm and emits fluorescence at ~700 nm in the "transparent" NIR area. Moreover, it is very photostable, since no photobleaching is detected even under high-power excitation. However, the intrinsic amount of $(N\text{-}V)^-$ in NDs is very low and additional colour centres must be artificially created to form fluorescent nanodiamonds (FNDs) for bioimaging applications [87,90,98]. The excellent photostability of FNDs makes them an ideal tool for long-term, 3D imaging and tracking in living cells. Chang et al. proposed the use of FND as an advantageous non-photobleaching imaging probe in order to follow both fast (ms) and slow (h) events in cells. Figure 20A displays the bright-field and fluorescence images of a living HeLa cell after the uptake of 35 nm FNDs. The uptake of the FND particles is confirmed by axial sectioning of the cell and, with the use of a servo control system the authors were able to track the movement of a single particle inside the HeLa cell in 3D over a time period bigger than 200 s under a wide-field microscope (Figure 20B) [99].

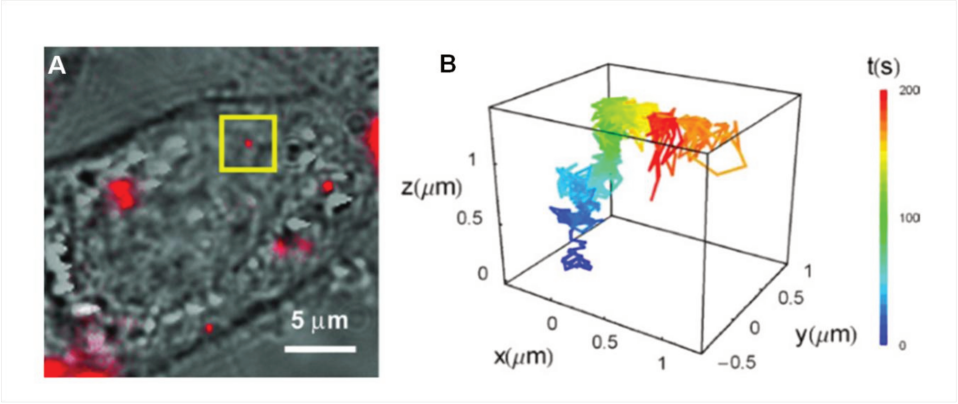

Figure 20 3D tracking of a single 35 nm FND in a live HeLa cell. A) Bright-field and epifluorescence merge images of the cell after FND uptake. B) Three-dimensional trajectory of a single FND inside the cell over a time span of 200 s. Reproduced from [99].

1.3.5.3 Graphene quantum dots

Graphene quantum dots (GQDs), are a kind of 0D material with characteristics derived from both graphene and CDs, which can be seen as incredibly small pieces of graphene [100–103]. By converting 2D graphene sheets into 0D GQDs, the GQDs exhibit new properties due to quantum confinement and edge effects, which are similar to the ones of CDs. Compared with organic dyes and QDs, GQDs are advantageous in terms of certain desired properties, such as high photostability against photobleaching and blinking, biocompatibility, and especially low cytotoxicity [100,101,103]. GQDs have a crystalline nature similar to graphene, as indicated by Raman spectroscopy, X-ray diffraction patterns and TEM results, which endows them with some of the properties of graphene [88] (Figure 21 A-F).

Regarding the preparation of GQDs, the synthetic methods include the cut-down of large graphene sheets, carbon nanotubes, carbon fibers or graphite into small graphene sheets or the use of benzene starting materials to build-up the GQDs. The average size of most synthesized GQDs ranges from 3 to 20 nm and they consist of no more than 5 layers of graphene sheets (~2.5 nm). The shape of most GQDs is circular and elliptical, but there are also triangular, quadrate and hexagonal dots as well [104,105]. The composite elements C, O and H and the surface groups such as carbonyl, carboxyl, hydroxyl and epoxy, of GQDs are similar to graphene [100–103].

Regarding their potential as cell imaging agents, GQDs are physically stable and free of heavy metal ions, which renders them excellent candidates for applications in the biological field. So far, the inherent toxicities of GQDs have been evaluated by cell-viability assays using cell lines like HeLa [106], the osteoblast precursor MC3T3 cell line [107] and the adenocarcinomic human alveolar basal epithelial cells A549 [108] and the results indicated that they possess excellent biocompatibility and low cytotoxicity. More precisely, negligible cytotoxicity was demonstrated at concentrations <0.5 mg/mL [106,107].

The most commonly imaged cell lines using GQDs are HeLa cells. Other cell lines used include dermal fibroblast cells, Chinese hamster ovary CHO-K1 cells, A549 cells, HEK293A cells, Madin-Darbycanine epithelial MDCK cells, human breast cancer T47D cells (Figure 21 G-J), MCF-7 cells, MC3T3cells, human osteosarcoma MG-63 cells. Tracking of stem cells over their lifecycle has also been demonstrated [109]. Graphene quantum dots show excitation wavelength (λ_{ex}=350-500 nm) dependent emissions.

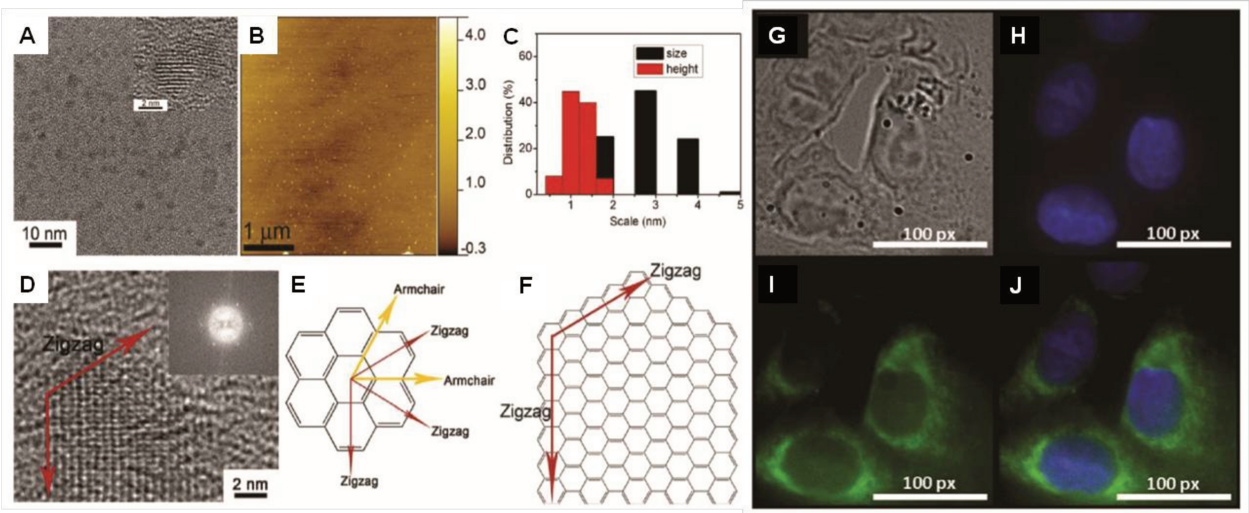

Figure 21 (A) TEM images of GQDs, inset of (A) is the HRTEM of GQDs. (B) AFM image of GQDs. (C) Size and height distribution of GQDs. (D) HRTEM image of the edge of GQD, inset is the 2D FFT of the edge in (D). (E) Schematic illustration showing the orientation of the hexagonal graphene network and the relative zigzag and armchair directions. (F) Schematic representation of the edge termination of the HRTEM image in (D). Fluorescence images of human breast cancer cells T47D after incubation with green GQDs for 4 h (G) phase contrast picture of T47D cells. (H) Individual nucleus stained blue with DAPI. (I) Agglomerated green GQDs surrounding each nucleus. (J) The overlay high contrast image of nucleolus stained with blue DAPI and GQDs (green) staining. Reproduced from [104].

1.3.5.4 Graphene oxides

Graphene is fundamentally one single layer of graphite; a layer of sp^2 bonded carbon atoms arranged in a honeycomb (hexagonal) lattice. Graphene as exfoliated from graphite, is hydrophobic, highly reactive and non biocompatible. Graphite oxide (GO) (formerly known as graphitic oxide or graphitic acid), a compound of carbon, oxygen, and hydrogen in different ratios, can be obtained by treating graphite with strong oxidizers. Upon oxidation to form GO, it becomes a hydrophilic material amenable to a host of biomedical applications. The C:O:H ratio, normally about 2:1:0.8, retains the layer structure of graphite with larger and irregular spacing.

Generally, GOs are synthesized by the Brodie, Staudenmaier, or Hummers methods. Presently, preparation strategies using variations of the Hummers method are mainly used for biomedical applications. Brodie and Staudenmaier, the first scientists to oxidize graphite over 100 years ago, used a combination of potassium chlorate ($KClO_3$) and nitric acid (HNO_3) to oxidize graphite, while the Hummers method involves treatment of graphite with potassium permanganate ($KMnO_4$) and sulphuric acid (H_2SO_4). Graphite salts made by intercalating graphite with strong acids, such as H_2SO_4, HNO_3, or $HClO_4$, have also been used as precursors for the oxidation of graphite [110].

Photothermal therapy (PTT) and photodynamic therapy (PDT) utilizing GO-based materials is an emerging modality in the treatment of cancer [111]. In PTT, a photothermal agent is employed for the selective local heating for healing abnormal cells or tissues; whereas, in PDT, the treatment occurs through a series of photochemical reactions triggered by photoactivated molecules called photosensitizers. Other studies demonstrate the use of GOs as antibacterial agents [112]. GO is also a promising material in drug delivery and bioimaging due to its intrinsic optical properties, large surface area, small size, economic production and to the non covalent interactions with aromatic ring molecules [113,114]. GOs do not need to be additionally doped with fluorophores and are very photostable. The decay times of fluorescence are in the order of nanoseconds. Their emission wavelength depends on the wavelength of excitation. Excitation in the UV (350–380 nm) often results in good brightness and blue fluorescence, but excitation wavelengths can be as

long as 650 nm and fluorescence then occurs in the near IR. The GO toxicity has been studied by several research groups, proving to be a biocompatible imaging agent [115–117].

Using the photoluminescence of GOs for cell bioimaging was first reported by Sun et al. in 2008 [113]. In this study, nanographene oxide (NGO) was PEGylated and subsequently conjugated with a B-cell specific antibody Rituxan (anti-CD20) in order to selectively recognize and bind to B-cell lymphoma cells. Doxorubicin (DOX) was loaded onto NGOs through π-π stacking; adding to the GOs a therapeutic functionality. The NGOs synthesized in this study were luminescent in the visible and NIR regions and were additionally used for cancer cell imaging. Another cell imaging study, demonstrated that the photoluminescence of transferrin-GOs is generally stronger than that of a conventional molecular dye like Fluorescein isothiocyanate (FITC) also conjugated to transferrin (Figure 22) [118]. Transferrin has been proven to be an efficient ligand for targeting cancer cells that overexpress on their surface transferrin receptors. With a two-photon microscopic system, the penetration depth can achieve 1 mm. A higher penetration depth should be achievable with an objective of longer working distance.

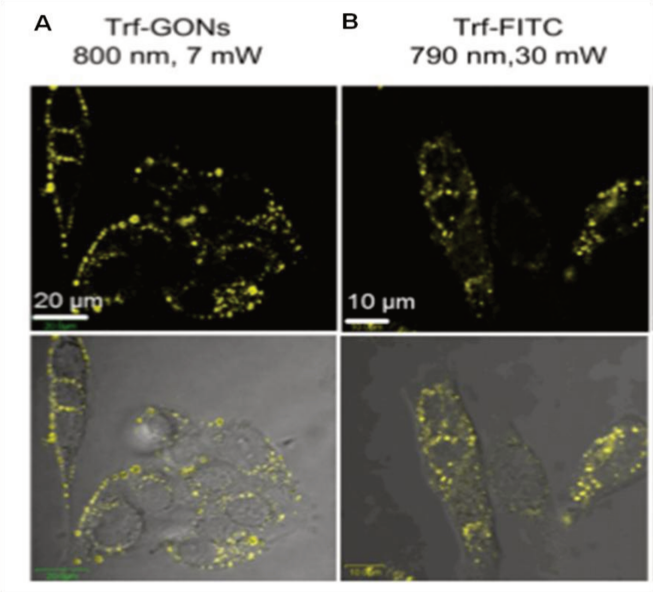

Figure 22 A comparison of the photoluminescence of (A) transferrin-GOs and (B) transferrin-FITC. Reproduced from [118].

Regarding fluorescence bioimaging, the two-photon photoluminescence of GOs is a very important property because of the low background signal and the higher penetration depth of

NIR light. Photoluminescence of GOs due to two-photon and three-photon absorption has been observed (like with most carbonaceous fluorescent materials) [119]. Qian et al. demonstrated the *in vivo* imaging of GOs in blood vessel of mouse ears with the use of two photon luminescence microscopy (λ_{ex}=810 nm) (Figure 23). In this study, one-photon luminescence was not observed, which was attributed to the absorption/scattering loss of 405 nm excitation in skin and blood. Two-photon luminescence microscopy was also used in the same study in order to image the GOs in a mouse brain and penetration depth of 300 μm was achieved.

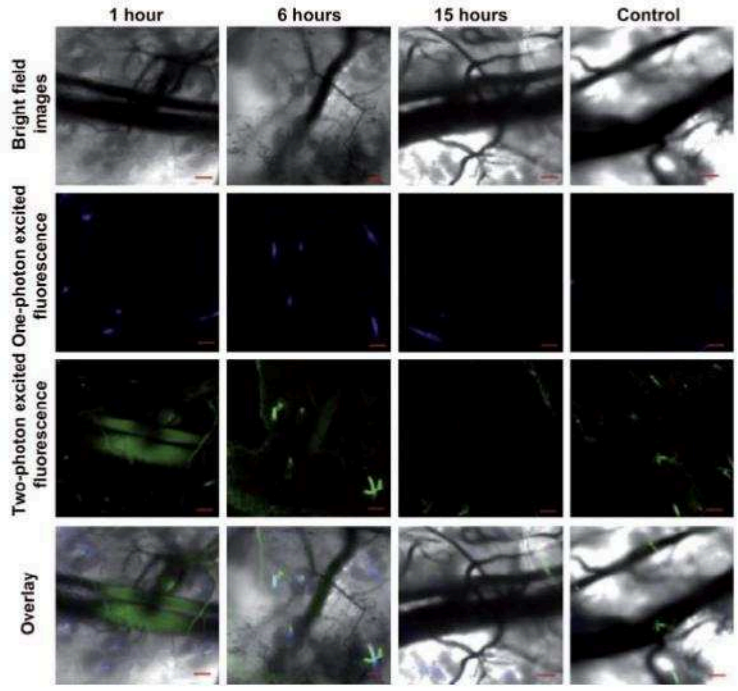

Figure 23 *In vivo* two-photon scanning and one-photon confocal luminescence imaging of intravenously injected GO nanoparticles in a blood vessel of a mice ear at various time points after injection. Reproduced from [119].

1.3.5.5 Single-walled and multi-walled Carbon Nanotubes

Carbon nanotubes (CNTs) are described as graphene sheets that are rolled into a cylindrical shape and have different electrical and optical properties depending on the axis about which they are rolled, which is called the chirality of the nanotube. The different CNT chiralities include the armchair structure, in which the C-C bonds are perpendicular to the tube axis; the zig-zag structure, in which the C-C bonds are parallel to the tube axis; and the chiral structure, in which

the C-C bonds lie at an angle with respect to the tube axis. CNTs are either single-walled (SWCNTs) with a diameter around 1-2 nm, or multi-walled (MWCNTs), which are composed of 2-30 concentric SWCNTs with an outer diameter ranging from 10 to 100 nm [87,90,120]. Some of the methods that are generally used to produce CNTs are arc-discharge, laser ablation, and chemical vapor deposition, including the high-pressure carbon monoxide (HiPCO) synthesis [87,90,120].

Since their discovery, CNTs have been particularly interesting because of their unique structural and chemical properties, including their high tensile strength, their high aspect ratio, and the capability to be chemically functionalized, while remaining relatively inert. This interest has led to their wide use in electronics [121–123], material composites [122,123], energy [122] and the biomedical field [87,90,120,124]. Within the emerging field of nanomedicine, CNTs have been investigated as drug delivery vectors, therapeutic agents exploiting microwave-, photo-, or radiofrequency-induced thermal effects, scaffolds for tissue engineering, and diagnostic imaging agents. Regarding the imaging modalities used with carbon nanotubes a lot of different techniques that rely on the intrinsic properties of CNTs have been applied. These techniques include Raman scattering, high optical and near infrared (NIR) absorbance and photoluminescence and photoacoustic imaging [87,90,120,122,124].

Regarding fluorescence imaging with NTs, they emit in the NIR but have low quantum yield and covalent functionalization would disrupt their structure. An interesting coating exchange method was developed in 2009 by Dai et al. in order to obtain biocompatible SWNTs with high QY. In their example, they demonstrated that sonicating single-walled carbon nanotubes with sodium cholate followed by surfactant exchange to form phospholipid-polyethylene glycol coated nanotubes produces bright and biocompatible *in vivo* imaging agents. In comparison to the traditional modification strategy in which SWNTs were directly sonicated in the PL–PEG solutions over a period of 15 min, the proposed coating exchange method prevents the damage and lost of QY of the SWNTs. *In vivo* whole-animal NIR-II fluorescence imaging of mice with intravenously injected SWNTs was realized for the first time. Low injection dose (17 mg/L) was sufficient to brightly visualize small tumor vessels beneath the thick skin [125].

Two years later, Welsher et al. used video-rate imaging in order to reveal the path of water soluble 200-500 nm in length SWNTs through mouse anatomy [126]. The inherit NIRII fluorescence of the particles was used for the particle monitoring and, as shown in Figure 24, the authors observed in real time the intravenously injected SWNTs reaching first the lungs and after several seconds the spleen and the liver. In an attempt to achieve further anatomical resolution, principle component analysis (PCA) was applied to the time series of images. PCA applied in this way has the ability to resolve features that are impossible to be distinguished in the raw images such as the pancreas.This study outlines the potential of NIR fluorescence imaging combined with PCA as a diagnostic tool.

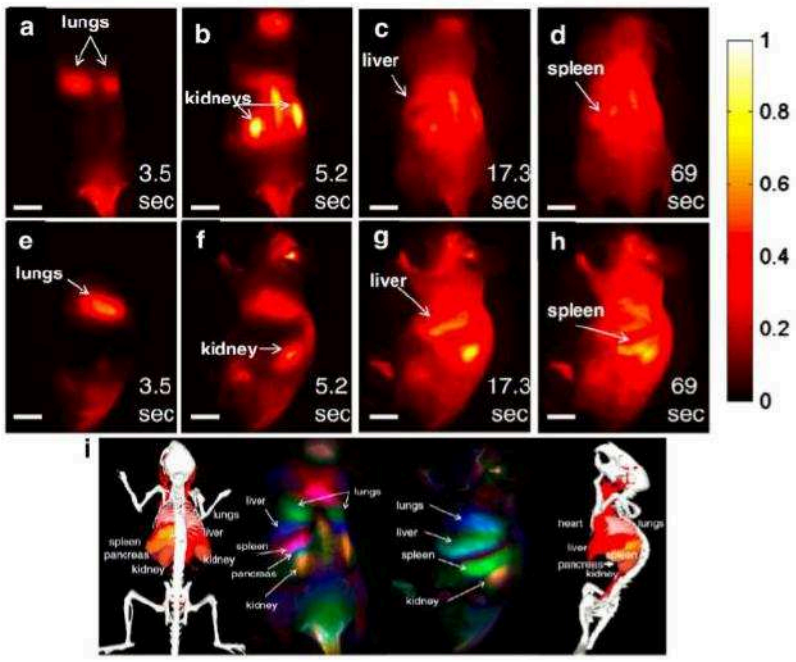

Figure 24 Video-rate NIR-II imaging of SWNTs in a live mouse.(a–h) Frames from video-imaging of a mouse injected with PEGylated SWNTs taken at different time points post-injection.(i). Dynamic contrast-enhanced imaging of the mouse injected with SWNTs through PCA.PCA images taken over the first 130 s following injection were performed by taking every 150 evenly spaced frames out of the 2000-frame dataset. Major features observed belong to the lungs ,liver ,kidney ,spleen and even the pancreas. Reproduced from [126].

1.3.6 Polymer-based nanoparticles

This section includes hydrophilic nanomaterials like nano-hydrogels, polyacrylamide polymers, polyurethanes, poly(hydroxyethylmethacrylamides) (pHEMA), poly (ethylene glycols) or special

polymers like Pluronic, that is a commercially available poly(ethylene glycol)-co-poly-ethyleneoxide) widely used in drug delivery [29]. It also includes hydrophobic materials like polystyrene and polyacrylonitrile nanoparticles. We can also include polyesters [127], as well as poly(lactic acid) (PLA) [128] and poly(lactic-co-glycolic acid) (PLGA) [129], "nature-based" polymers including proteins (human serum albumin for instance) [130], polypeptide constructions (poly(lysine), poly(glutamic acid) for example) [131] , saccharides (dextran, chitosan, cellulose) [132–134] and dendrimers [135–137].

Hydrophilic and hydrophobic, synthetic and natural polymers

Hydrogels are permeable to ions and hydrophilic organic species like amino acids or monosaccharides but not to bigger biomolecules such as proteins. Hydrophilic polymeric nanoparticles, depending on the cross-linking degree, can undergo substantial, ionic strength-dependent swelling in aqueous media; though water-aggregation is not commonly observed. The solubility and swellability of polymeric NPs depend on the cross-linking degree. NPs prepared from hydrogels are biocompatible, generally cell permeable (depending mainly on their charge and size), nontoxic, slowly excreted, rather quickly coated by the intracellular proteins and attacked by the immunosystem. Some of the polymers included in this category can be degraded by intracellular enzymes. Additional functionalities such as amino groups are better introduced by adding a functional monomer to the main monomer and then initiating the radical polymerization. In addition, several techniques are available for the preparation of organic polymer core–shell NPs. In order to render polymeric particles fluorescent, two major strategies exist: Fluorescent polymerizable monomers are added during the nanoparticle synthesis or the fluorophores are encapsulated inside or attached to the bare polymer particles (Figure 25). Fluorescent dopants tend to leach into the aqueous environment of the particle unless firmly retained, for example by electrostatic or covalent interactions [29].

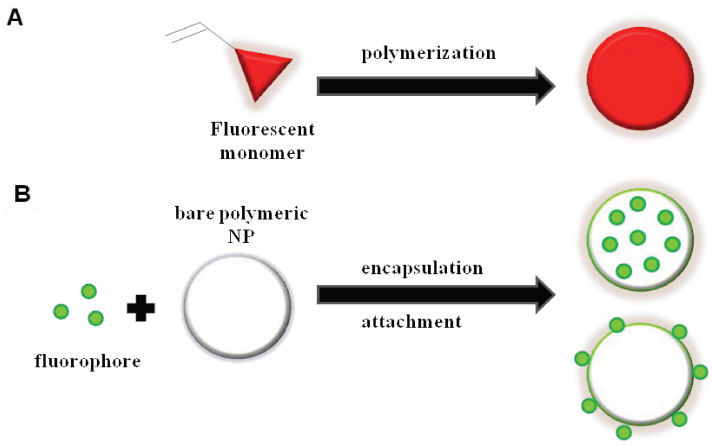

Figure 25 Two strategies toward fluorescent polymeric nanoparticles: (A) polymerization of fluorescent monomers; (B) encapsulating fluorophores inside or attaching fluorophores onto the bare polymeric nanoparticles.

On the other hand, hydrophobic materials like polystyrene nanoparticles (PS-NPs) can be doped with apolar fluorophores. For these materials, doping with lipophilic fluorophores is preferred because ionic probes are poorly soluble in hydrophobic NPs. PS-NPs are rather biocompatible, cell permeable, nontoxic, and their excretion is slow. If placed inside cells, they are only slowly coated by intracellular proteins and hardly attacked by the immunosystem. Functionalities like addition of amino groups are best introduced by the addition of co-reagents containing such groups to the monomer before starting emulsion polymerization. Post-modification and additional coatings are rather difficult. PS-NPs do not measurably swell in water and do not readily aggregate [29].

An advantage of using fluorescently labeled polymeric nanoparticles for bioimaging is their multifunctional capabilities. In a recent example, Wu et al prepared multifunctional chitosan–poly (methacrylic acid) (PMAA)–CdSe hybrid nanogels in an aqueous solution *via in-situ* immobilization of CdSe QDs (3.2–3.8 nm) into the chitosan–PMAA nanogels (Figure 26A) [138]. The hybrid nanogels could enter and illumine B16F10 cells, that serve as a mouse model for melanoma (Figure 26B), detect the pH changes, provide a pH-regulated release of the anticancer drug Temozolomide in the physiologically abnormal pH range of 5–7.4 that is found in the pathological zone, which provides potential for monitoring the anticancer drug-response and improving the therapeutic efficiency of the drugs. This example demonstrates the wide applicability and multifunctionality of polymeric nanoparticles for biomedical applications.

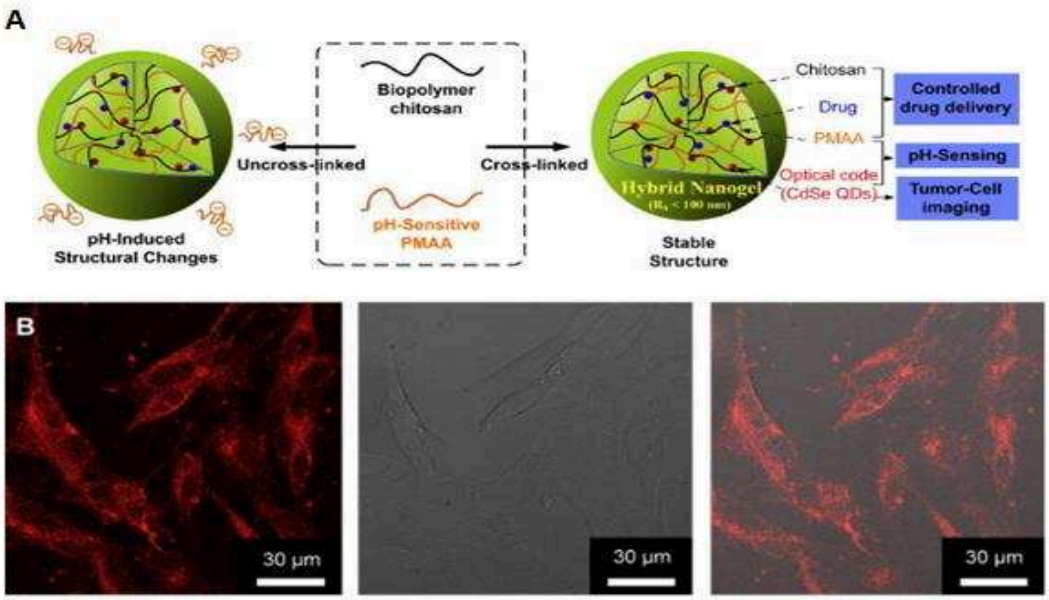

Figure 26 (A) Schematic representation of the concept for designing multifunctional chitosan–PMAA–CdSe hybrid nanogel and its potential extending applications in biomedical field. (B) Scanning confocal fluorescence (left), transmission (middle), and overlaid (right) images of mouse melanoma B16F10 cells upon staining with hybrid nanogels. Excitation wavelength = 496 nm. Reproduced from [138].

Dendrimers

Dendrimers are highly branched synthetic polymers that form spherical macromolecules which can be reliably synthesized to a specific physical size and in a highly reproducible manner. The name "dendrimer" originates from the Greek word "dendro", which means tree and refers to the tree-like structure of these molecules which "branch" outwards from their core molecule. Dendrimers can be divided in three distinct regions: the core, the interior (or branches) and the periphery (surface groups).

In 2004, Lee et al. observed that with a simple oxidation process, hydroxyl-terminated poly(amidoamine) (PAMAM) dendrimers emitted fluorescence in the blue region with high quantum yields [139]. Later, Shi et al. showed that PAMAM-stabilized Au NPs ~10 nm in size and produced by a weak reducing condition also exhibited blue fluorescence emission at 458 nm [140], which was attributed to the intrinsic fluorescence properties of the dendrimer stabilizers. By virtue of their intrinsic fluorescence, Lesniak et al. visualized by confocal microscopy various cell lines upon endocytosis of PAMAM-stabilized Ag NPs [141]. In another example, Al-Jamal et

al. synthesized a novel polylysine dendrimer that exhibited a weak but detectable fluorescence signal without further doping with additional fluorophores, and showed that intrinsically fluorescent dendrimers could be used to monitor their cellular uptake and trafficking within the cytoplasm by confocal microscopy (Figure 27) [142]. The aforementioned examples outline the importance of using the intrinsic fluorescence property of dendrimers in cellular imaging. However, the quantum yields of dendrimers are quite low, and most of the reported bioimaging examples are limited to the cell level.

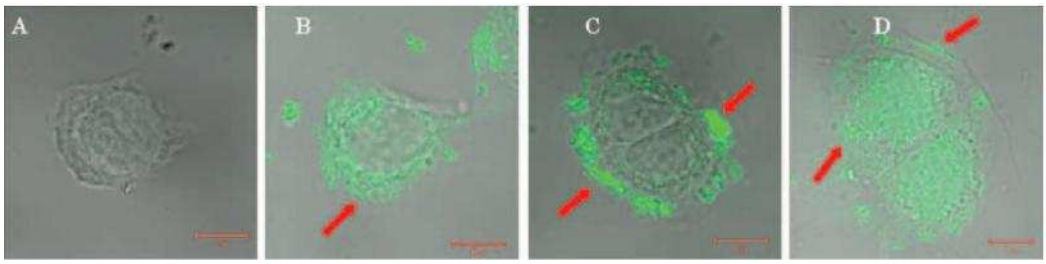

Figure 27 A time dependent uptake study of the dendrimer (green fluorescent) in fixed Caco-2 cells. Reproduced from [142].

In order to enhance the low intrinsic quantum yields of the dendrimers, additional doping with fluorescent dyes that are conjugated on their surface is performed [143]. Dendrimers are ideal nanoagents for theranostic applications. For example, PAMAM dendrimers functionalized with FITC as fluorescent probe, folic acid as a targeting ligand and different anticancer drugs have been applied for fluorescence imaging and simultaneous drug delivery *in vitro* and *in vivo* [143–145].

Apart from directly conjugating organic dyes or other dopants to the periphery of the dendrimers, fluorescent probes have also been loaded ino their interior using covalent interactions. For example, Amir et al. [146] introduced a novel and facile synthesis of orthogonally functionalized hybrid dendritic-linear delivery systems incorporating functional groups, both at their chain ends and internally, where two different fluorescent dyes were conjugated. More precisely, multiple coumarin units were loaded internally and a single FITC or Alexa647 dye was conjugated to the dendrimer periphery *via* an amide bond. This double labeling allows for the individual and simultaneous tracking of the dendritic scaffold and the payload in living cells (Figure 28B).

Exemplary, the coumarin release of the FITC-dendrimer was studied by confocal fluorescence microscopy using the B-16 melanoma cells (Figure 28A).

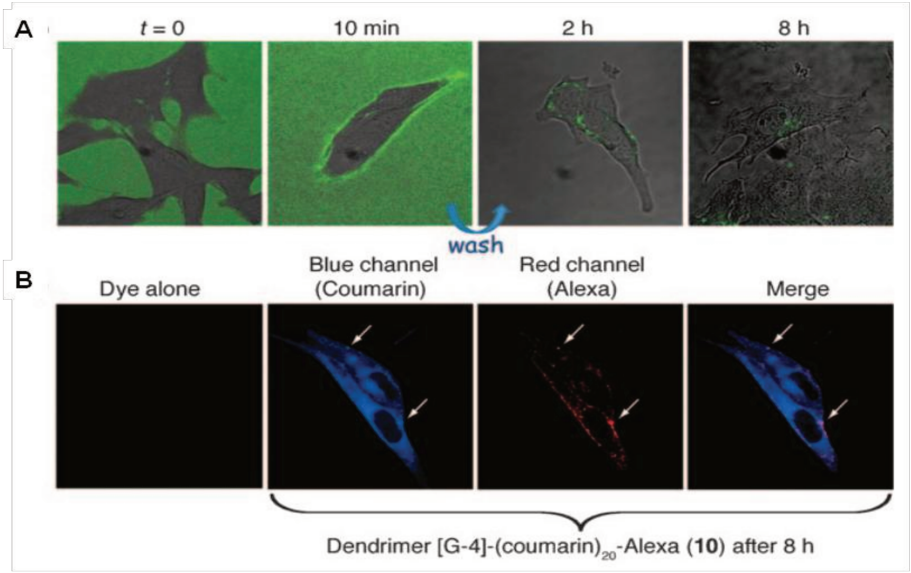

Figure 28 Subcellular confocal images of B-16 cells treated with (A) FITC-dendrimer (green) and (B) coumarin-Alexa 647-dendrimer (coumarin, blue; Alexa, red) at 8 h. Reproduced from [146].

1.3.7 Fluorescently Doped Silica nanoparticles

Silica nanoparticles (SiNPs) were among the first nanoparticles to be used in bioimaging. Functionalized fluorescent SiNPs are silica matrices combined with traditional organic fluorophores (or other dopants) or silica-coated fluorescent nanoparticles. The advantages of SiNPs include [29]:

1. SiNPs are extremely hydrophilic and easy to synthesize and separate.
2. Silica materials are biocompatible and non-toxic and, thus, cause little damage to living cells.
3. Silica materials are optically transparent and can let excitation and emission lights pass through without changing their characteristics.
4. SiNPs attach biomolecules effectively and can be easily modified with a variety of functional groups, such as poly(ethylene glycol) (PEG), hydroxyl (OH), carboxyl (COOH), phosphonate (CH_3HPO_2) and amine (NH_2) on their surface.

5. The silica matrix can encapsulate dyes and fluorescent nanoparticles without changing their optical character and the stability of the dye can be improved after being doped in the silica matrix.
6. The controllable particle size of SiNPs makes them suitable for application in *in vivo* bioimaging.

Spherical silica NPs are generally synthesized by one of two routes: reverse microemulsion or the Stöber method. The synthetic methods for the preparation of silica NPs have been reviewed [147,148]. The reverse micelle or water-in oil (w/o) microemulsion system is composed of a homogeneous mixture of water, oil, and surfactant molecules. Water nanodroplets form in the bulk oil phase, which then acts as a confined medium of nanoreactors for discrete particle formation. Polar and water-soluble dye molecules can be readily encapsulated into the silica NPs by this method because of the electrostatic attraction of the dye molecules to the negatively charged silica matrix. The aforementioned synthetic route produces in general monodisperse and highly uniform NPs. Nevertheless, a main drawback is that the fluorophores may leach out of the silica matrix. The use of surfactants necessitates extensive washing to remove the surfactant molecules before any biological application in order to avoid the disruption or lysis of the cell membranes. Alternatively, the Stöber method can be used for the synthesis of monodisperse silica particles with diameters ranging from 30 nm to 2 μm. In the Stöber process, silica particles are formed by the hydrolysis and condensation of siloxane precursors (for example tetraethylorthosilicate (TEOS)) in the presence of ethanol and ammonia. Using this method, a plethora of organic dye molecules can be incorporated within the silica matrix by covalent bonding. The procedure is carried out in two steps. First, the dye is chemically bound to an amine-containing silane agent (such as 3-aminopropyltriethoxysilane, APTES), and, second, APTES and TEOS are allowed to hydrolyze and co-condense and finally form dye-doped NPs [148].

In order to decrease photobleaching and thus enhance their bioimaging performance, intrinsically fluorescent nanomaterials have been coupled to SiNPs for cell imaging. As an example, human umbilical vein endothelial cell (HUVEC) staining highlighted the important advantage of dye-doped SiNPs compared to the free dye molecules in that silica matrix can protect the dye from

photobleaching, allowing for long-term live cell imaging. More precisely, as shown in Figure 29, complete photobleaching of cells stained with FITC alone occurs within 20 min of continued irradiation [149]. However, when FITC-doped SiNPs of 100 nm or 30 nm in size were used for cell staining the fluorescence signal was retained for longer times. In the case of the 100 nm FITC-doped SiNPs 60% of the fluorescence intensity retained after 20 min irradiation and 30 % after 60 min. The respective percentage of the fluorescence intensity retained in the case of the 30 nm particles was 52% and 17.2%.

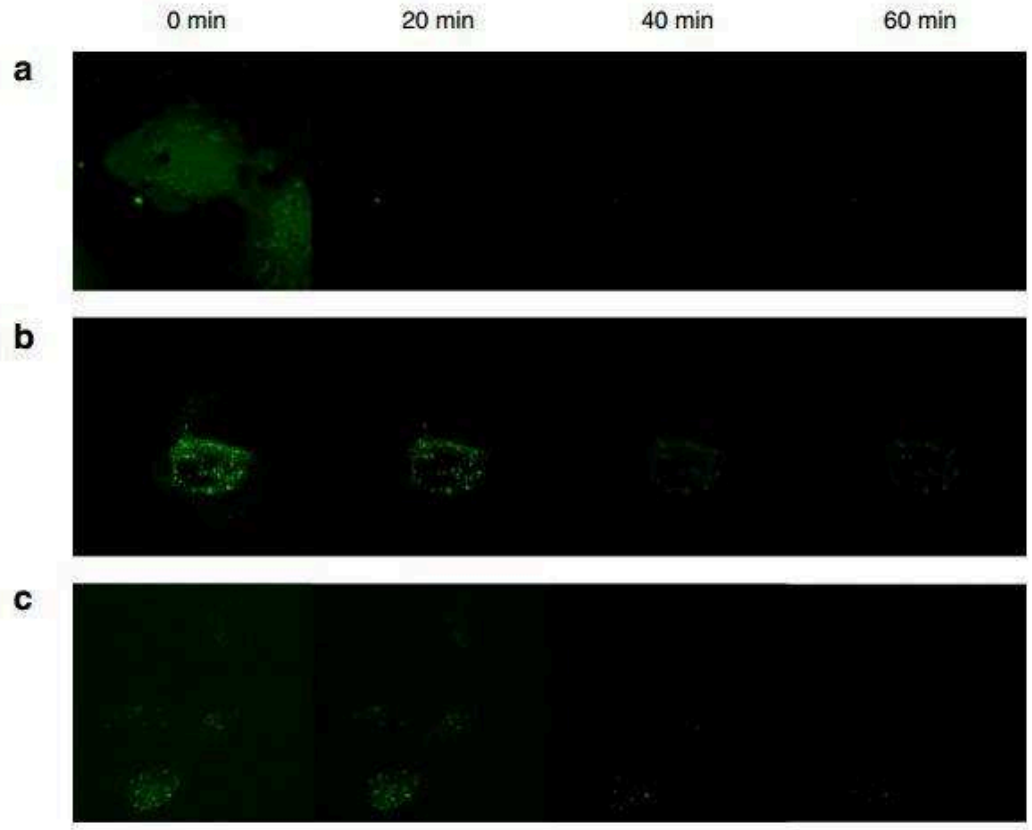

Figure 29 Confocal micrographs of continued irradiation of cells leading to photobleaching over a 1 h time scale. (A) FITC loaded HUVEC cells. (B) 30 nm fluorescent silica loaded cells. (C) 100 nm fluorescent silica loaded cells. Images are taken every 20 min and the photobleaching of pure FITC and FITC loaded nanomaterials are studied. Reproduced from [149].

In another example, Jun et al. synthesized highly sensitive QD-embedded SiNPs for selective tumor fluorescence imaging (Figure 30, A) [150]. In comparison to the single QDs, the QDs-embedded SiNPs showed ~200 times higher fluorescence intensity and increased uptake by HeLa cells (Figure 30, B). Single QDs and QDs-embedded SiNPs were used to label HeLa cells

and were subsequently transplanted in mice for long-term *in vivo* fluorescence cell tracking. The results indicated that even after 10 days of monitoring, the QDs-embedded SiNPs still possessed strong fluorescence signal (Figure 30, C), which implies that fluorescently doped SiNPs may have better photostability than free fluorophores and thus serve as powerful fluorescent tools for long-term imaging of living cells and tissues.

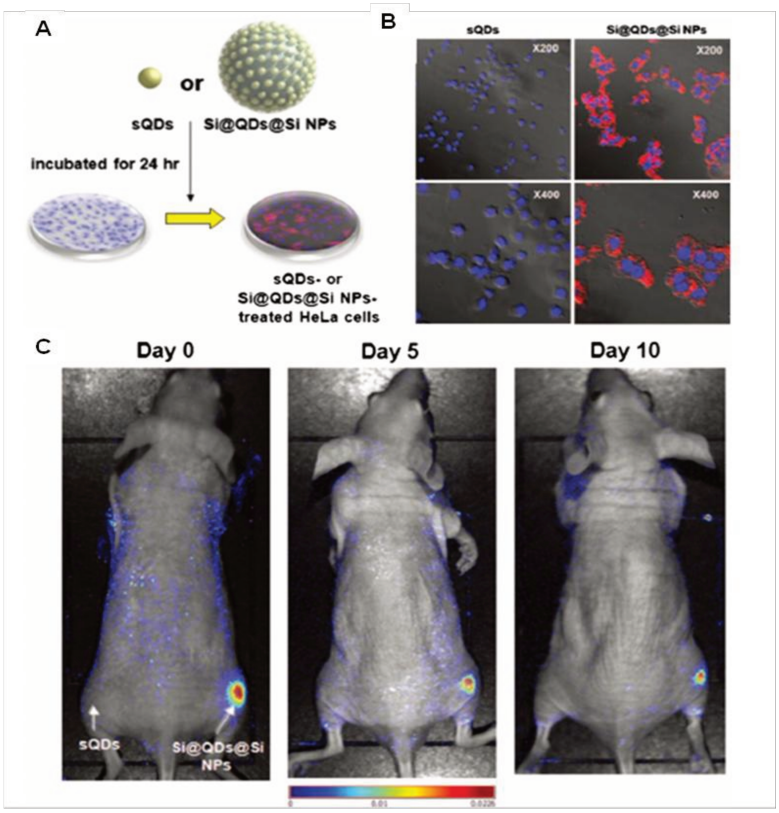

Figure 30 Cellular uptake *in vivo* of single QDs and QDs-embedded SiNP. (A) Illustration of QD or QDs-embedded SiNP labeling to HeLa cells; (B) Fluorescence images of QD- and QDs-embedded SiNP -uptaken cells (Red color: QD, blue color: DAPI). (C) Maestro *in vivo* fluorescence image of QD-labeled (left leg) and QDs-embedded SiNP -labeled (right leg) cell-transplanted mouse. Reproduced from [150].

1.4 Targeting strategies for bioimaging

Nowadays, two main targeting strategies exist in order to image malignant/diseased cells. The first one is the passive tumor targeting phenomenon that was first described in the literature over 20 years ago and is known as the enhanced permeability and retention (EPR) effect and the second is active targeting based on overexpressed cellular targets recognized by highly specific

targeting ligands. Such ligands include antibodies, aptamers, peptides, small molecules and, the recently applied, molecularly imprinted polymers (MIPs).

1.4.1 Passive targeting

In the case of passive targeting, the particles can just be added to the cells, tissues, or animals to be imaged by a certain modality. The particles serve to illumine the cells or diseased areas, and therefore are expected to show high brightness and light penetration depth, to be fairly biocompatible and non-cytotoxic. In principle, passive targeting occurs due to extravasation of the nanoparticles at the pathological sites where the microvasculature is leaky. Passive targeting of nanoparticles is mainly used to visualize tumors and inflamated tissues. Tumor vascular leakiness is due to the increased angiogenesis and the presence of cytokines and other vasoactive factors that enhance permeability (Enhanced Permeability and Retention effect). Tumor angiogenesis is characterized by vessels with irregular diameters and branching, and tumors lacking defining structures of vasculature such as arterioles, capillaries, or venules. Vascular endothelial growth factor (VEGF) and the angiopoietins are critical in regulating the balance between the leakiness associated with the defective endothelial linings of tumor vessels and vascular growth, maturation, and regression. Elevated levels of bradykinin result in vasodilatation and enhance the extravasation of large molecules and their retention in tumor sites. The majority of solid tumors exhibit a vascular pore cutoff size between 380 and 780 nm, although tumor vasculature organization is dependent on the tumor type, its development rate and microenvironment [151–153].

In order to achieve passive targeting with nanoparticles, they need to remain in the blood circulation for extended times so that there will be higher possibilities for the nanoparticles to pass by the diseased site. Bare nanoparticles usually have short circulation half-lives due to the natural defense mechanisms of the body, which eliminates them after opsonization by the mononuclear phagocytic system. For this reason, surface modifications that render the nanoparticles “invisible” to the immune system are desirable. A hydrophilic polymer such as polyethylene glycol (PEG) can be used for this purpose because it has low degree of

immunogenicity and antigenicity, chemical inertness of the polymer backbone, and availability of the terminal primary hydroxyl groups for derivatization.

Although passive targeting is very often used in clinical therapy and diagnosis, it suffers from certain limitations. Ubiquitously targeting cells within a tumor is not always feasible because some nanoparticles cannot diffuse efficiently and the random nature of the approach makes it difficult to control the process. The passive strategy is further limited because certain tumors do not show an EPR effect, and the permeability of vessels may not be the same throughout a single tumor. The majority of current nanoparticle-based cancer imaging research uses several other cellular targets found in specific types of cancer to more selectively visualize tumor tissues, which will be discussed in the following section [151–153].

1.4.2 Active targeting

1.4.2.1 Cellular targets for bioimaging

The list of the receptors that have been targeted for drug delivery or imaging is long with more targets being added as cancer research develops. Some of the most important receptors targeted in theranostic applications have been described in [154,155] and are presented below:

Somatostatin Receptors

Somatostatin receptors (SSTRs) are G protein-coupled receptors (GPCRs) with five distinct subtypes (SSTR1-SSTR5). SSTRs have been extensively targeted for cancer imaging and are over-expressed in various cancers such as neuroendocrine cancer, small-cell lung cancer, colorectal cancer, and breast cancer. Because endogeneous somatostatins (SST-14 and SST-28) have rather short *in vivo* half-lives (< 3 min) due to enzymatic degradation, many synthetic somatostatin analogues with enhanced resistance to *in vivo* enzymatic degradation have been developed, such as octreotide (D-Phe-cyclo(Cys-Phe-D-Trp-Lys-Thr-Cys)-Threol) and octreotate (D-Phe-cyclo(Cys-Phe-D-Trp-Lys-Thr-Cys)-Thr-OH). These two peptides have binding affinities in the low-nanomolar range to SSTR with longer plasma half-lives (~1.5 h).

Cholecystokinin-2 (CCK2) Receptor

Similar to somatostatin receptors, the CCK2 receptor is a member of the G protein-coupled receptors (GPCRs). CCK2 receptor is expressed in several cancers, such as medullary thyroid carcinomas, small-cell lung cancer, gastroenteropancreatic neuroendocrine, stromal ovarian cancer, astrocytomas, and gastrointestinal stromal cancer. The known peptides that bind to CCK2 include cholecystokinin, gastrin, and gastrin derivatives. CCK2 receptor targeted fluorescence imaging has not been extensively used [156].

Integrin Receptors

Tumor progression is largely dependent upon the growth of new blood vessels, a process called angiogenesis. Tumor angiogenesis is mediated by various protein receptors and enzymes, among which are integrin receptors, a family of heterodimeric transmembrane receptors. In mammals, 18 α and 8 β subunits of integrin receptors have been identified, which assemble into 24 different receptors. Among these 24 integrins, $\alpha_v\beta_3$, which is expressed in a number of cancers such as melanoma, glioblastoma, ovarian, prostate and breast cancer, is the most intensively targeted for cancer imaging. The most commonly used targeting ligand for $\alpha_v\beta_3$ is the RDG peptide.

Gastrin-Releasing Peptide (GRP) Receptor

Gastrin-releasing peptide (GRP) receptor has great potential as cancer-imaging target, because GRP receptor is massively overexpressed in breast, prostate, small cell lung, ovarian, gastrointestinal stromal and some endometrial cancers, whereas the expression levels in normal tissues are relatively low. The native GRP receptor ligand, bombesin , is a 14 amino acid peptide, in which the last eight residues are the most important for binding. This octapeptide, Gln-Trp-Ala-Val-Gly-His-Leu-Met is named bombesin, and its derivatives have been fluorescently labeled for in vivo cancer imaging.

Translocator Protein (TSPO) Receptor

The translocator protein (TSPO) (18 kDa), previously named peripheral benzodiazepine receptor (PBR), is a five transmembrane domain protein that is localized primarily in the outer mitochondrial membrane and is expressed predominantly in steroid-synthesizing tissues, including the brain. TSPO is significantly overexpressed in breast, prostate, colon, and brain

cancer, with protein expression linked to cancer progression and poor survival rates, suggesting that the protein is an attractive target for cancer imaging.

EGF Receptor

EGF receptor (170 kDa) is a transmembrane glycoprotein that is involved in the regulation of cell proliferation and promotes tumor invasion and metastasis. Over-expression of this receptor is associated with brain, breast, colon, lung, head, neck, ovarian, pancreas, prostate and skin cancer. Among the three well-known EGF receptor ligands, epidermal growth factor (EGF), amphiregulin (AR) and transforming growth factor- (TGF), EGF (a 6 kDa polypeptide) is the most widely used as the targeting moiety for cancer imaging. Besides EGF, anti-EGF receptor monoclonal antibodies are also commonly used to develop EGF receptor targeted fluorescent probes.

HER2

Similar to EGF receptor, HER2 is a transmembrane glycoprotein that is involved in cell survival, proliferation, angiogenesis and invasiveness. A number of cancers overexpress HER2, such as breast, ovarian, salivary glad, stomach, kidney, colon, prostate, urinary and non-small cell lung cancer. The levels of HER2 expression are associated with aggressiveness and poor prognosis. Although HER2 has no such natural ligands as EGF for EGF receptor, anti-HER2 antibodies have been labeled with various fluorescent dyes and nanoparticles for cancer imaging.

HER1

Activation of HER1 stimulates proliferation, protection from apoptosis, dedifferentiation and cancer migration. It can be found overexpressed in many solid tumors like colorectal, lung, head and neck. Like in the case of HER2, antibodies are the most popular targeting ligands.

Nucleolin

Nucleolin, a eukaryotic nucleolar phosphoprotein, is involved in the synthesis and maturation of ribosomes. The protein is located mainly in dense fibrillar regions of the nucleolus and has been found overexpressed on the surface of cancer cells. In most cases, the AS1411 aptamer is used for targeting nucleolin.

Folate Receptor (FR)

Folate receptor (FR) is a 38-40 kDa glycosylphosphatidylinositol (GPI)-linked membrane glycoprotein. While FR expression is low to absent in most normal tissues except for choroid plexus and placenta, high FR expression is observed in various types of cancers, such as ovarian, cervix, brain, head and neck, lung, kidney and endometrium cancer. This high tumor/normal tissue FR expression ratio qualifies FR as a good cancer-imaging target. In addition, the FR ligand, folic acid, has high binding affinity in the picomolar range and has carboxylate group that can be easily coupled to signaling molecules. Moreover, folate conjugates bind to FR and get cleared from non-target sites rapidly. Therefore, FR has become an attractive target for in vivo cancer imaging.

Transferrin Receptor (TFR)

Transferrin-receptor (TFR) regulates iron uptake and delivery into the cells as demanded by metabolic needs. TFRs represent suitable targets for early cancer diagnosis, as the receptor has been qualitatively described for various cancers, presumably due to malignant transformation of normal cells. The native TFR ligand, transferrin, is an 80 kDa glycoprotein and serves as a good targeting moiety for TFR targeted cancer imaging [118].

Disialoganglioside (GD2)

GD2 is a disialoganglioside expressed on tumors of neuroectodermal origin, including human neuroblastoma and melanoma, with highly restricted expression on normal tissues, principally to the cerebellum and peripheral nerves in humans.The relatively tumor specific expression of GD2 makes it a suitable target for immunotherapy with monoclonal antibodies or with artificial T cell receptors.

Chemokine receptor

The chemotactic cytokines called chemokines are a superfamily of small secreted cytokines that were initially characterized through their ability to prompt the migration of leukocytes. Attention has been focused on the chemokine receptors expressed on cancer cells because cancer cell migration and metastasis show similarities to leukocyte trafficking. CXC chemokine receptor 4 (CXCR4) was first investigated as a chemokine receptor that is associated with lung metastasis

of breast cancers. Recently, CXCR4 was reported to be a key molecule in the formation of peritoneal carcinomatosis in gastric cancer. The selective interaction between the stromal cell-derived factor-1 (SDF-1) and the chemokine receptors CXCR4 and CXCR7 has been exploited for targeted imaging.

Epithelial cell adhesion molecule (EpCAM)

Epithelial cell adhesion molecule (EpCAM) is a transmembrane glycoprotein mediating Ca^{2+}-independent homotypic cell–cell adhesion in epithelia. EpCAM is also involved in cell signaling, migration, proliferation, and differentiation. It is overexpressed in many solid tumors like colorectal, lung, head and neck. Anti-EpCAM antibodies have been used for imaging and drug delivery applications.

Sugar receptors

Polysaccharides like hyaluronan, proteoglycans, glycoproteins, glycosphingolipids and their receptors are involved in cell-cell communication and signaling and are overexpressed in several tumor types or viral infections. For example, galactose has been found to have high affinity for asialoglycoprotein receptors found on hepatocytes. Mannose can be used in targeting dendritic cells, which highly express mannose receptors. Hyaluronic acid functionalized nanoparticles have also been used in order to target the overexpressed CD44 (hyaluronan receptor) or the hyaluronidases. Dendritic cell-specific intercellular adhesion molecule-3-grabbing nonintegrin (DC-SIGN) is a popular C type lectin on the surface of dendritic cells that can be targeted by highly mannosylated or Lewis-type glycan structures. Conversely, lectins, which are a class of proteins that regulate bioadhesion and cell recognition, have been used as a mean to target glycan structures.

CD20

B-lymphocyte antigen CD20 or CD20 is an activated-glycosylated phosphoprotein expressed on the surface of all B-cells beginning at the pro-B phase (CD45R+, CD117+) and progressively increasing in concentration until maturity. Its function is uncertain, while it most probably is involved in the regulation of transmembrane Ca^{2+}. It is overexpressed in all B-cell NHL, pre-B cells but not in stem cells. It is usually targeted by anti-CD20 antibodies.

1.4.2.2 Targeting ligands for bioimaging

The most popular targeting ligands for bioimaging consist of antibodies, aptamers, peptides and small molecules [151,152,157]. Molecularly imprinted polymers (MIPs), also dubbed "synthetic antibodies", are proposed in the end of this section as a new cell-targeting ligand [158].

Antibodies

Antibodies (Abs) are large, Y-shaped glycoproteins that belong to the immunoglobulin superfamily. They are mostly produced by plasma cells and are used by the immune system to identify pathogens, including bacteria, viruses or other harmful substances. Antibodies recognize a unique molecule of this "harmful agent", called antigen, via the Fab's variable region. Each tip of the Y-shape of an antibody contains a paratope that is specific for one particular epitope on the antigen, allowing these two structures to bind with high precision.

Antibodies were the first targeting ligands for bioimaging due to their high specificity and the availability of many different and well-established antibodies in the biomedical research field. Nowadays, monoclonal antibodies (mAbs) are routinely used as the major nanoparticle targeting ligand. However, many studies point out long blood circulation times and slow tumor accumulation as two main drawbacks that limit their potential clinical application. For this reason, production of imaging probes using smaller antibody fragments (for example Fab′, scFv, and $F(ab')^2$) has become a common practice (Figure 31). In addition, combinations of these smaller antibody fragments have been constructed for optimized pharmacokinetics profiles. These include diabodies (divalent $sc(Fv)^2$ or trivalent $[sc(Fv)^2]^2$), minibodies that consists of two scFv fragments genetically linked to a CH_3 domain, and triabodies created through genetically linking two scFv to an Fc fragment. Antibody fragments often display enhanced pharmacokinetics profiles when compared to antibodies, attributed to their shortened serum half-life and faster tumor accumulation [159].

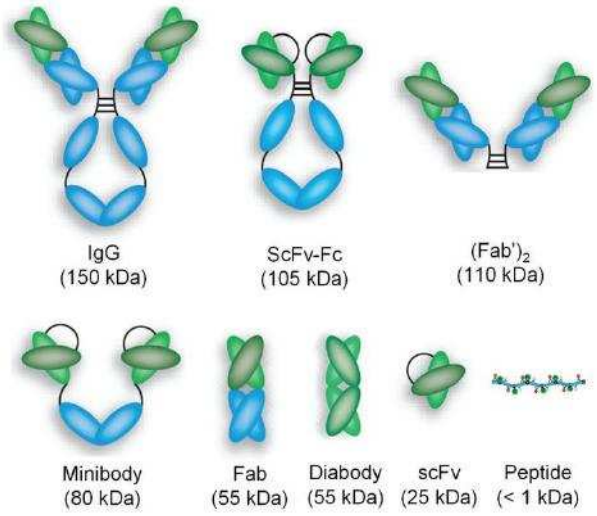

Figure 31 Intact antibodies and a variety of antibody fragments available. Reproduced from [160].

A review of describing antibody-guided nanoparticles from 2003 to 2012 reveals that most targeting antibodies are monoclonal and mostly of murine origin, though some antibodies from other species, and polyclonals from rabbit, have been applied, as well as some chimeric and humanized antibodies. The majority of these antibodies target the extracellular domains of cell surface proteins, which is logical considering their intended application as *in vivo* targeted nanoparticles. The most prevalent examples are mAbs routinely utilized in the treatment of cancers with upregulated epidermal growth factor receptors [157]. These antibodies have been successfully conjugated to a variety of nanoparticles, from QDs, metallic NPs (for example AuNPs, SPIONs etc.), polymers (for example PLGA, chitosan etc.) and liposomes, to silica NPs. However, the majority of the conjugation techniques employed lack directionality due to the presence of multiple reactive functional groups on antibodies, yielding heterogeneous antibody orientations on the nanoparticles.

Antibody targeting with nanoparticles faces several major challenges. First of all, the immunogenicity and purity of antibodies are still sources of concern, especially since murine antibodies are widely used. The body can perceive these types of antibodies as foreign proteins and clear them. Successful antigen binding is not always feasible, since the mAb must have high target specificity and affinity and both the linker and the NPs, must not perturb this desired specificity. In addition, regarding the conjugation step, the Ab-NP linkage must be highly

efficient and site-specific and the mAb-NP conjugate linker must be stable during the time of the particle circulation. Antibody production and isolation are also difficult, laborious and costly procedures which lead many researchers to explore the use of alternative targeting ligands, such as the ones detailed in the following sections.

Aptamers

Since their development in 1990 by Szostak's [161] and Gold's groups [162], aptamers have successfully existed as a separate class of targeting ligands. Aptamers are short single-stranded nucleic acids (RNA or DNA) that can form secondary and tertiary structures capable of specifically binding proteins or other cellular targets; they are essentially a chemical equivalent of antibodies. Specific aptamers for a target are selected from an initial oligonucleotide library through a combinatorial chemistry technique named SELEX (Figure 32). Systematic evolution of ligands by exponential enrichment (SELEX) is a combinatorial chemistry technique in molecular biology for producing oligonucleotides of either single-stranded DNA or RNA that specifically bind to a target ligand or ligands. The process begins with the synthesis of a very large oligonucleotide library consisting of randomly generated sequences of fixed length flanked by constant 5' and 3' ends that serve as primers. For a randomly generated region of length *n*, the number of possible sequences in the library is 4^n (*n* positions with four possibilities (A,T,C,G) at each position). The sequences in the library are exposed to the target ligand - which may be a protein, a small organic compound or even whole cells - and those that do not bind the target are removed. The bound sequences are eluted and amplified by PCR to prepare for subsequent rounds of selection in which the stringency of the elution conditions is increased to identify the tightest-binding sequences. Normally, the Kds between aptamers and their targets are from μM to pM.

Aptamers are very suitable ligands for nanoparticle targeting. It is possible to synthesize aptamers with a specific functional moiety at the one end of the nucleic acid strand, such as a carboxylate, amino, sulfhydryl or aldehyde. In addition, aptamers are typically non-immunogenic and non-cytotoxic and can be adequately modified to achieve higher stability in blood circulation. They can be selected *in vitro* and *in vivo*, and be repeatedly and reversibly denatured

without losing their recognition ability. The ability to chemically synthesize aptamers results in small batch variations. Moreover, since their production is not dependent on animals or their immune response, aptamers can be selected for a variety of targets even if they are weak antigens. The aptamer size is much smaller than the one of antibodies, allowing them to bind clefts, binding sites, and enzymatic active sites, which is difficult in the case of antibodies.

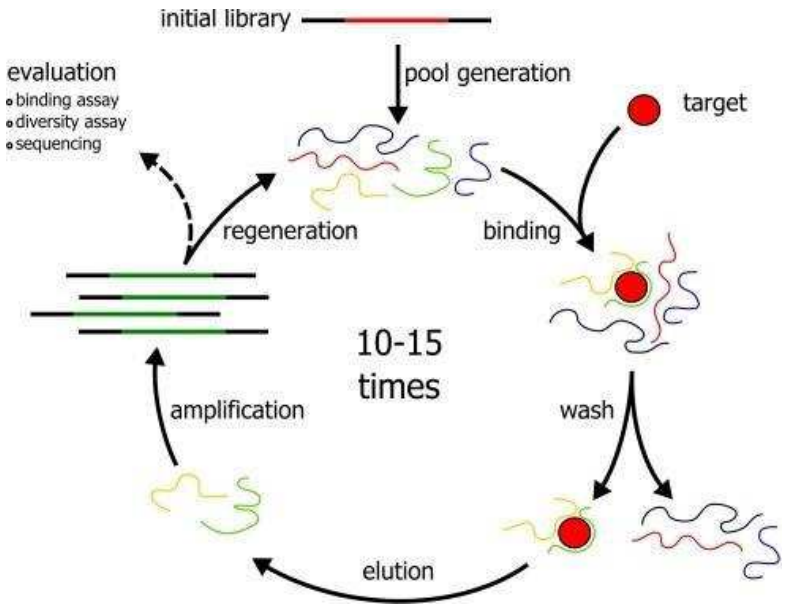

Figure 32 Schematic outline of the general SELEX procedure. Reproduced from [163].

Aptamers are very suitable ligands for nanoparticle targeting. It is possible to synthesize aptamers with a specific functional moiety at the one end of the nucleic acid strand, such as a carboxylate, amino, sulfhydryl or aldehyde. In addition, aptamers are typically non-immunogenic and non-cytotoxic and can be adequately modified to achieve higher stability in blood circulation. They can be selected *in vitro* and *in vivo*, and be repeatedly and reversibly denatured without losing their recognition ability. The ability to chemically synthesize aptamers results in small batch variations. Moreover, since their production is not dependent on animals or their immune response, aptamers can be selected for a variety of targets even if they are weak antigens. The aptamer size is much smaller than the one of antibodies, allowing them to bind clefts, binding sites, and enzymatic active sites, which is difficult in the case of antibodies.

However, degradation by nucleases has been the main barrier to *in vivo* aptamer-targeted nanoparticle applications. Attempts at translating RNA aptamers for use as therapeutics have focused on replacement of the nuclease-susceptible 2'-hydroxyl RNAs with other moieties. RNAs containing 2'-fluoro and 2'-Omethyl pyrimidines, which can be generated by in vitro transcription with an appropriate T7 RNA polymerase mutant, have known partial resistance to nucleases [157].

According to reviewed studies (2004-2012) that used aptamers as nanoparticle targeting ligands, all of them applied aptamers to cell surface biomarkers and used either DNA (62%), unmodified RNA (17%), or modified RNA (21%). Compared to numerous RNA nucleases, there are relatively fewer DNases in vivo. DNA aptamers do, however, suffer from characteristics that can complicate their in vitro selection via SELEX, such as the formation of hard to manage G-tetrads [157].

In all the aforementioned reviewed studies, aptamers were facilely conjugated to a variety of nanoparticles. The main potential advantages of using aptamers over antibodies are their small size (15 kDa), low immunogenicity, and easy scale-up preparation. Up to now, more than 200 aptamers have been isolated and Pegaptanib, a VEGF165 targeted aptamer, was approved by the FDA in 2004 for the treatment of neovascular macular degeneration. Another commonly used that targets nucleolin, AS141 is currently in phase II of clinical trials.

Peptides

Peptide-based targeting ligands can be identified by many different methods. Most commonly, they are gleaned from the binding regions of proteins for the target of interest. In these cases, peptide libraries are often synthesized in order to delineate the optimal peptide sequence, and may utilize single amino acid mutations in order to fully understand the binding of the resulting peptide to its binding partner.

Another commonly used method for peptide discovery for a specific target is phage display, first developed in 1985 by Smith [164]. Phage display is a screening tool for peptides, allowing the

selection of peptide sequences with increased affinities to a specific target of choice. The phage display system is a cyclic selection process similar to SELEX, where the purified target molecules or specific cell types are incubated with a randomized library of peptide sequences displayed on bacteriophage capsids. Some peptides bind to the target protein, and nonspecific binders are washed away with the specific binders eluted. Binding peptide sequences-bacteriophages are collected, which infect E. Coli and are amplified, followed by additional cycles of selection.

There have been numerous publications using peptides to functionalize nanoparticles during the past decade. Studies from 2011-2012 using peptides as targeting ligands predominantly utilized ligands discovered via phage display. Some used natural peptides, such as EGF, CANF, and Angiopep-2. About 30% of reviewed papers used cyclic peptides, though this percentage is influenced by the popularity of the RGD peptide as a targeting ligand to $\alpha_v\beta_3$ integrin [157].

To date, there have been many studies using peptide-NPs conjugates *in vitro* for example, targeting protein kinase CK2, glioma, FGF receptor and other cellular targets. In comparison to antibodies, peptides possess certain advantages, such as lack of immunogenicity and facile synthesis at lower costs than antibodies. However, peptides incur also certain disadvantages, such as lower target affinities (K_d ~ 10^{-4}-10^{-6} M), increased chance of non-specific binding, higher potential of proteolytic cleavage, glomerular transit, varying toxicities and differential effects on cell signaling that can result to allergic sensitization.

Small Molecules

Vitamin B9 (folic acid) is the most commonly used small molecule targeting ligand and has been intensively investigated for several clinical applications. Folic acid is a high affinity ligand of the endogenous folate receptor (K_d ~10^{-9} M), which is a biomarker in many types of cancer. Presently, several therapeutic agents have been coupled with folic acid for tumor-selective theranostics such as chemotherapeutic agents, oligonucleotides, gene therapy vectors, radiotherapeutic agents, MRI and radioimaging contrast agents, drug-carrying liposomes and

nanoparticles. As reported, folic-acid conjugated nanoparticles can be actively internalized via receptor-mediated endocytosis and directed towards cancer cells.

Sigma receptors are also upregulated in many cancer types. Benzamides (anisamide, in particular), are demonstrated sigma receptor ligands and, therefore, can functionalize nanoparticles towards sigma receptor-positive cells and tissues. In addition, vitamin B12 (riboflavin) plays an important role in cellular metabolism, and the riboflavin carrier protein is overexressed in cells with high metabolic activity such as cancer or endothelial cells. Consequently, flavin mononucleotide, an endogenous RCP ligand can be used to target the aforementioned cells.

Carbohydrates, which generally interact weakly with some cell surface receptors, can also serve as small molecule targeting ligands. Carbohydrates allow for nanoparticle glycotargeting, which is based on the endogenous lectin interactions with carbohydrates. A main drawback of this targeting strategy is that glycotargeting often requires multiple interacting carbohydrates to obtain sufficiently strong binding. One typical example is the asialoglycoprotein receptor (ASGP-R) which is present only on hepatocytes at a high density of ~500.000 receptors per cell and readily binds carbohydrates like arabinose, galactose, mannose, which can consequently serve as effective liver-targeted imaging or drug delivery systems.

Molecularly Imprinted Polymers

Tailor-made molecularly imprinted polymers (MIPs) are promising synthetic receptor materials that have been known and applied in bioanalytical and biosensing applications for more than 40 years [165] but it is only till recently that they found application in bioimaging of cells and tissues [166]. Molecular imprinting is based on a templating process at the molecular level. Monomers carrying functional groups self-assemble around a template molecule (the target or a derivative), followed by copolymerization with cross-linking monomers, which results in the formation of a polymeric mold around the template. Subsequent removal of the template reveals three-dimensional binding sites in the polymer that are complementary to the template in size, shape and position of the functional groups. MIPs exhibit binding affinities and specificities

comparable to those of antibodies. Their use as antibody mimics was first proposed by Mosbach's group and they are now sometimes referred to as “plastic antibodies”. In contrast to antibodies, their production is reproducible, relatively fast and economic, and no animals are necessary. Moreover, they are physically and chemically stable and are not degraded by proteases, nucleases or denatured by solvents like in the case of antibodies, peptides and aptamers [158]. Thus, MIPs have a great potential in providing a robust, specific and biocompatible imaging tool that reveals the location and distribution of cellular targets in/on the cells. This would lead to a better insight of the tremendously diverse biological processes in which these molecules are involved during cancer and disease. MIPs functionalized with different fluorophores including organic dyes [167], quantum dots [168], or other fluorescent materials like upconverting nanoparticles [169] or carbon dots [170] have already been reported and successfully applied in bioanalytical or biosensing applications; thus, a wide variety of ready-to-apply protocols of nanoparticle functionalization suitable for targeted imaging with MIPs is already available. In addition, MIPs could easily provide multimodal and multifunctional imaging platforms. Last but not least, their size, biocompatibility and hydrophilicity can be tuned according to the application and the specific cellular target.

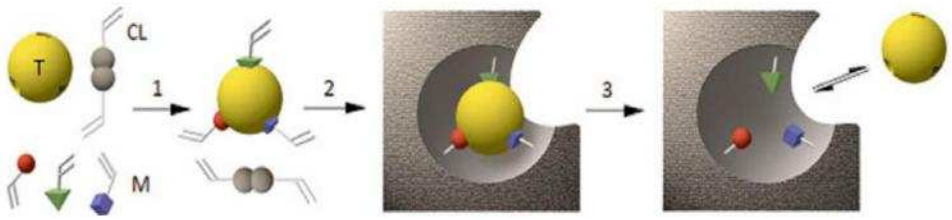

Figure 33 General principle of molecular imprinting. A molecular template (T) is mixed with functional monomers (M) and a cross-linker (CL) resulting in the formation of a self-assembled complex (1). The polymerization of the resulting system produces a rigid structure bearing imprinted sites (2). Finally removal of the template liberates cavities that can specifically recognize and bind the target molecule (3). Reproduced from [158].

Our group was the first to describe targeted cell and tissue imaging using MIPs as recognising ligands [166]. Fluorescently-labeled MIP particles were applied for bioimaging of fixed and living human keratinocytes, to localize hyaluronan and sialylation sites [166,168,171]. Very recently, Sellergren's group coated silica cores with a MIP shell containing nitrobenzoxadiazole as a fluorescent reporter group, to target sialic acid (SA) on cell surface glycans [172]. Liu’s group

reported SA-imprinted silica nanoparticles for surface enhanced Raman scattering imaging of cancer cells and tissues [173] as well as FITC-labeled silica particles with a shell imprinted with SA, fucose or mannose to image these monosaccharides, overexpressed on cancer cells [174]. The application of MIPs for bioimaging will extensively be discussed in Chapter 3.

1.5 Conclusion

Nanoparticles have made an impressive "debut" in the biomedical arena with applications ranging from intraoperative fluorescence imaging to drug delivery, photothermal and photodynamic therapy. Regarding fluorescent bioimaging, there is a demand for reliable fluorescent labels and high-performance recognition ligands. The ideal nano-imaging agent should have low cytotoxicity, high bio- and water-compatibility, high quantum yield, suitable size for a given application, photostability and to be easily synthesized and functionalized. In this chapter, an overview of the most commonly applied nanoparticles for bioimaging is provided and all the important aforementioned aspects are discussed. To date, several targeting strategies have been developed in order to distinguish healthy from diseased cells. The most commonly used targeting ligands, including antibodies and antibody fragments, aptamers, peptides and small molecules have been presented. Their pros and cons have extensively been discussed and in order to overcome some of their intrinsic disadvantages for bioimaging applications, like quick degradation by proteases or nucleases or high synthetic cost and sophisticated biofunctionalization steps, for the first time, molecularly imprinted polymers are proposed as a smart alternative targeting strategy. A review in recent literature reveals that the most used nanoparticles in fluorescent bioimaging are QDs and UCNPs, while the most chosen targeting methods involve the use of antibodies or antibody fragments (Table1 ANNEX 1). In the next chapters, the synthetic methodologies for obtaining water compatible MIPs for sugar acids will be discussed and the fluorescent bioimaging application of these MIPs targeting the glycosylations on and in keratinocyte cells and tissues will be demonstrated.

1.6 References

[1] L. Mazzola, *Nat. Biotechnol.* **2003**, *21*, 1137–1143.

[2] T. Tsuzuki, *Int. J. Nanotechnol.* **2009**, *6*, 567.

[3] K. Brindle, *Nat. Rev. Cancer* **2008**, *8*, 94–107.

[4] D. Artemov, N. Mori, R. Ravi, Z. M. Bhujwalla, *Cancer Res.* **2003**, *63*, 2723–2727.

[5] P. M. Winter, S. D. Caruthers, A. Kassner, T. D. Harris, L. K. Chinen, J. S. Allen, E. K. Lacy, H. Zhang, J. D. Robertson, S. A. Wickline, et al., *Cancer Res.* **2003**, *63*, 5838–43.

[6] M. Zhao, D. A. Beauregard, L. Loizou, B. Davletov, K. M. Brindle, *Nat. Med.* **2001**, *7*, 1241–4.

[7] J. W. M. Bulte, D. L. Kraitchman, *NMR Biomed.* **2004**, *17*, 484–499.

[8] E. Terreno, D. D. Castelli, A. Viale, S. Aime, *Chem. Rev.* **2010**, *110*, 3019–3042.

[9] L. K. Ott, *Shielding from Harm: The MRI Screening tool—The First Line of Defense in MRI Safety*, **2015**.

[10] G. Liney, *MRI in Clinical Practice*, Springer, London, **2006**.

[11] C. Barsanti, F. Lenzarini, C. Kusmic, *World J. Diabetes* **2015**, *6*, 792–806.

[12] S. M. Ametamey, M. Honer, P. A. Schubiger, *Chem. Rev.* **2008**, *108*, 1501–16.

[13] W. A. W. Kalender, *Phys. Med. Biol.* **2006**, *51*, R29–R43.

[14] G. K. von Schulthess, H. C. Steinert, T. F. Hany, *Radiology* **2006**, *238*, 405–422.

[15] B. A. Kaufmann, J. R. Lindner, *Curr. Opin. Biotechnol.* **2007**, *18*, 11–16.

[16] V. Ntziachristos, *Nat. Methods* **2010**, *7*, 603–614.

[17] M. Y. Berezin, S. Achilefu, *Chem. Rev.* **2010**, *110*, 2641–2684.

[18] R. S. Dothager, K. Flentie, B. Moss, M.-H. Pan, A. Kesarwala, D. Piwnica-Worms, *Curr. Opin. Biotechnol.* **2009**, *20*, 45–53.

[19] R. Weissleder, V. Ntziachristos, *Nat. Med.* **2003**, *9*, 123–128.

[20] Q. Liu, W. Feng, T. Yang, T. Yi, F. Li, *Nat Protoc* **2013**, *8*, 2033–2044.

[21] S. Gao, D. Chen, Q. Li, J. Ye, H. Jiang, C. Amatore, X. Wang, R. Weissleder, Y. L. Wang, J. J. Chen, et al., *Sci. Rep.* **2014**, *4*, 11–18.

[22] Y. Zhang, G. Hong, Y. Zhang, G. Chen, F. Li, H. Dai, Q. Wang, *ACS Nano* **2012**, *6*, 3695–3702.

[23] N. Hoogerbrugge, Y. J. L. Kamm, P. Bult, K. M. Landsbergen, E. M. H. F. Bongers, H. G.

Brunner, H. J. Bonenkamp, J. A. de Hullu, M. J. L. Ligtenberg, C. Boetes, *Ann. Oncol.* **2008**, *19*, 655–9.

[24] P. W. Wiest, J. A. Locken, P. H. Heintz, F. . Mettler, *Semin. Ultrasound, CT MRI* **2002**, *23*, 402–410.

[25] J. G. Elmore, K. Armstrong, C. D. Lehman, S. W. Fletcher, *JAMA* **2005**, *293*, 1245–56.

[26] C. E. S. Hoogstins, Q. R. J. G. Tummers, K. N. Gaarenstroom, C. D. de Kroon, J. B. M. Z. Trimbos, T. Bosse, V. T. H. B. M. Smit, J. Vuyk, C. J. H. van de Velde, A. F. Cohen, et al., *Clin. Cancer Res.* **2016**, *22*, 2929–38.

[27] M. Koch, V. Ntziachristos, *Annu. Rev. Med.* **2016**, *67*, 153–64.

[28] G. M. van Dam, G. Themelis, L. M. A. Crane, N. J. Harlaar, R. G. Pleijhuis, W. Kelder, A. Sarantopoulos, J. S. de Jong, H. J. G. Arts, A. G. J. van der Zee, et al., *Nat. Med.* **2011**, *17*, 1315–1319.

[29] O. S. Wolfbeis, *Chem. Soc. Rev.* **2015**, *44*, 4743–4768.

[30] W. Chan, D. J. Maxwell, X. Gao, R. E. Bailey, M. Han, S. Nie, *Curr. Opin. Biotechnol.* **2002**, *13*, 40–46.

[31] U. Resch-Genger, M. Grabolle, S. Cavaliere-Jaricot, R. Nitschke, T. Nann, *Nat. Methods* **2008**, *5*, 763–775.

[32] X. Wang, X. Ren, K. Kahen, M. A. Hahn, M. Rajeswaran, S. Maccagnano-Zacher, J. Silcox, G. E. Cragg, A. L. Efros, T. D. Krauss, *Nature* **2009**, *459*, 686–689.

[33] B. Mahler, P. Spinicelli, S. Buil, X. Quelin, J.-P. Hermier, B. Dubertret, *Nat. Mater.* **2008**, *7*, 659–664.

[34] K. D. Wegner, N. Hildebrandt, *Chem. Soc. Rev.* **2015**, *44*, 4792–4834.

[35] M. Green, M. Green, *Semiconductor Quantum Dots*, Royal Society Of Chemistry, Cambridge, **2014**.

[36] C. Wang, X. Gao, X. Su, *Anal. Bioanal. Chem.* **2010**, *397*, 1397–1415.

[37] E. Oh, R. Liu, A. Nel, K. B. Gemill, M. Bilal, Y. Cohen, I. L. Medintz, *Nat. Nanotechnol.* **2016**, *11*, 479–486.

[38] C. E. Bradburne, J. B. Delehanty, K. Boeneman Gemmill, B. C. Mei, H. Mattoussi, K. Susumu, J. B. Blanco-Canosa, P. E. Dawson, I. L. Medintz, *Bioconjug. Chem.* **2013**, *24*, 1570–83.

[39] V. Brunetti, H. Chibli, R. Fiammengo, A. Galeone, M. A. Malvindi, G. Vecchio, R.

Cingolani, J. L. Nadeau, P. P. Pompa, W. A. Hild, et al., *Nanoscale* **2013**, *5*, 307–317.

[40] K.-T. Yong, W.-C. Law, R. Hu, L. Ye, L. Liu, M. T. Swihart, P. N. Prasad, J. M. Bruchez, M. Moronne, P. Gin, et al., *Chem. Soc. Rev.* **2013**, *42*, 1236–1250.

[41] M. Bruchez, M. Moronne, P. Gin, S. Weiss, A. P. Alivisatos, *Science* **1998**, *281*, 2013–6.

[42] W. C. Chan, S. Nie, *Science* **1998**, *281*, 2016–8.

[43] F. Pinaud, X. Michalet, L. A. Bentolila, J. M. Tsay, S. Doose, J. J. Li, G. Iyer, S. Weiss, *Biomaterials* **2006**, *27*, 1679–1687.

[44] J. M. Klostranec, W. C. W. Chan, *Adv. Mater.* **2006**, *18*, 1953–1964.

[45] A. M. Smith, H. Duan, A. M. Mohs, S. Nie, *Adv. Drug Deliv. Rev.* **2008**, *60*, 1226–1240.

[46] D. Geißler, N. Hildebrandt, *Anal. Bioanal. Chem.* **2016**, *408*, 4475–4483.

[47] X. Wu, H. Liu, J. Liu, K. N. Haley, J. A. Treadway, J. P. Larson, N. Ge, F. Peale, M. P. Bruchez, *Nat. Biotechnol.* **2002**, *21*, 41–46.

[48] W. Cai, D.-W. Shin, K. Chen, O. Gheysens, Q. Cao, S. X. Wang, S. S. Gambhir, X. Chen, *Nano Lett.* **2006**, *6*, 669–76.

[49] M. V. Yezhelyev, A. Al-Hajj, C. Morris, A. I. Marcus, T. Liu, M. Lewis, C. Cohen, P. Zrazhevskiy, J. W. Simons, A. Rogatko, et al., *Adv. Mater.* **2007**, *19*, 3146–3151.

[50] S. Kim, Y. T. Lim, E. G. Soltesz, A. M. De Grand, J. Lee, A. Nakayama, J. A. Parker, T. Mihaljevic, R. G. Laurence, D. M. Dor, et al., *Nat. Biotechnol.* **2004**, *22*, 93–97.

[51] S. H. Bhang, N. Won, T.-J. Lee, H. Jin, J. Nam, J. Park, H. Chung, H.-S. Park, Y.-E. Sung, S. K. Hahn, et al., *ACS Nano* **2009**, *3*, 1389–98.

[52] I. C. Serrano, G. Stoica, E. Palomares, L. Hu, Z. W. Mao, C. Y. Gao, D. Peer, J. M. Karp, S. Hong, O. C. Farokhzal, et al., *RSC Adv.* **2016**, *6*, 31210–31213.

[53] E. Yaghini, H. D. Turner, A. M. Le Marois, K. Suhling, I. Naasani, A. J. MacRobert, *Biomaterials* **2016**, *104*, 182–191.

[54] X. Liu, G. B. Braun, H. Zhong, D. J. Hall, W. Han, M. Qin, C. Zhao, M. Wang, Z.-G. She, C. Cao, et al., *Adv. Funct. Mater.* **2016**, *26*, 267–276.

[55] L. Jing, K. Ding, S. V. Kershaw, I. M. Kempson, A. L. Rogach, M. Gao, *Adv. Mater.* **2014**, *26*, 6367–6386.

[56] F. Ye, Å. Barrefelt, H. Asem, M. Abedi-Valugerdi, I. El-Serafi, M. Saghafian, K. Abu-Salah, S. Alrokayan, M. Muhammed, M. Hassan, *Biomaterials* **2014**, *35*, 3885–3894.

[57] Y.-L. Wu, H. Yin, F. Zhao, J. Li, *Adv. Healthc. Mater.* **2013**, *2*, 297–301.

[58] P. Jiang, C.-N. Zhu, Z.-L. Zhang, Z.-Q. Tian, D.-W. Pang, *Biomaterials* **2012**, *33*, 5130–5135.

[59] C. M. Cobley, J. Chen, E. C. Cho, L. V. Wang, Y. Xia, *Chem. Soc. Rev.* **2011**, *40*, 44–56.

[60] S. Guo, E. Wang, *Nano Today* **2011**, *6*, 240–264.

[61] H. He, C. Xie, J. Ren, *Anal. Chem.* **2008**, *80*, 5951–7.

[62] I. Sur, D. Cam, M. Kahraman, A. Baysal, M. Culha, *Nanotechnology* **2010**, *21*, 175104.

[63] L. Shang, S. Dong, G. U. Nienhaus, *Nano Today* **2011**, *6*, 401–418.

[64] Y. Z. Lu, W. Q. T. Chen, G. Schmid, M. Baumle, M. Geerkens, I. Helm, C. Osemann, T. Sawitowski, A. Roucoux, J. Schulz, et al., *Chem. Soc. Rev.* **2012**, *41*, 3594.

[65] S. Choi, R. M. Dickson, J. Yu, S. Wennmalm, S. M. Simon, S. A. Patel, C. I. Richards, J. C. Hsiang, R. M. Dickson, C. I. Richards, et al., *Chem. Soc. Rev.* **2012**, *41*, 1867–1891.

[66] H. Qian, M. Zhu, Z. Wu, R. Jin, *Acc. Chem. Res.* **2012**, *45*, 1470–9.

[67] Y.-C. Shiang, C.-C. Huang, W.-Y. Chen, P.-C. Chen, H.-T. Chang, R. Kubo, T. G. Schaaff, G. Knight, M. N. Shafigullin, R. F. Borkman, et al., *J. Mater. Chem.* **2012**, *22*, 12972.

[68] C. Wang, Y. Wang, L. Xu, X. Shi, X. Li, X. Xu, H. Sun, B. Yang, Q. Lin, *Small* **2013**, *9*, 413–20.

[69] J. Wang, G. Zhang, Q. Li, H. Jiang, C. Liu, C. Amatore, X. Wang, *Sci. Rep.* **2013**, *3*, 1157.

[70] C.-L. Liu, H.-T. Wu, Y.-H. Hsiao, C.-W. Lai, C.-W. Shih, Y.-K. Peng, K.-C. Tang, H.-W. Chang, Y.-C. Chien, J.-K. Hsiao, et al., *Angew. Chemie Int. Ed.* **2011**, *50*, 7056–7060.

[71] S. Chattoraj, M. A. Amin, S. Mohapatra, S. Ghosh, K. Bhattacharyya, *ChemPhysChem* **2016**, *17*, 61–68.

[72] M. Haase, H. Schäfer, *Angew. Chemie Int. Ed.* **2011**, *50*, 5808–5829.

[73] F. Wang, X. Liu, F. Auzel, J. F. Suyver, A. Aebischer, D. Biner, P. Gerner, J. Grimm, S. Heer, K. W. Krämer, et al., *Chem. Soc. Rev.* **2009**, *38*, 976.

[74] J. Zhou, Z. Liu, F. Li, R. Weissleder, M. J. Pittet, J. Cheon, J. H. Lee, J. Xie, G. Liu, H. S. Eden, et al., *Chem. Soc. Rev.* **2012**, *41*, 1323–1349.

[75] S. A. Hilderbrand, F. Shao, C. Salthouse, U. Mahmood, R. Weissleder, P. L. A. M. Corstjens, S. Li, M. Zuiderwijk, K. Dardos, W. R. Abrahms, et al., *Chem. Commun.* **2009**, *152*, 4188.

[76] L. Cheng, C. Wang, Z. Liu, M.-F. Joubert, F. Auzel, T. Sandrock, H. Scheife, E. Heumann, G. Hube, E. Downing, et al., *Nanoscale* **2013**, *5*, 23–37.

[77] H. J. Zijlmans, J. Bonnet, J. Burton, K. Kardos, T. Vail, R. S. Niedbala, H. J. Tanke, *Anal. Biochem.* **1999**, *267*, 30–36.

[78] M. Nyk, R. Kumar, T. Y. Ohulchanskyy, E. J. Bergey, P. N. Prasad, *Nano Lett.* **2008**, *8*, 3834–3838.

[79] Q. Liu, T. Yang, W. Feng, F. Li, *J. Am. Chem. Soc.* **2012**, *134*, 5390–5397.

[80] C. Wu, D. T. Chiu, *Angew. Chemie Int. Ed.* **2013**, *52*, 3086–3109.

[81] J. Pecher, S. Mecking, *Chem. Rev.* **2010**, *110*, 6260–6279.

[82] D. Tuncel, H. V. Demir, *Nanoscale* **2010**, *2*, 484–94.

[83] R. H. Friend, R. W. Gymer, A. B. Holmes, J. H. Burroughes, R. N. Marks, C. Taliani, D. D. C. Bradley, D. A. Dos Santos, J. L. Brdas, M. Lgdlund, et al., *Nature* **1999**, *397*, 121–128.

[84] S. Günes, H. Neugebauer, N. S. Sariciftci, *Chem. Rev.* **2007**, *107*, 1324–1338.

[85] C. Wu, B. Bull, C. Szymanski, K. Christensen, J. McNeill, *ACS Nano* **2008**, *2*, 2415–2423.

[86] C. Wu, S. J. Hansen, Q. Hou, J. Yu, M. Zeigler, Y. Jin, D. R. Burnham, J. D. McNeill, J. M. Olson, D. T. Chiu, *Angew. Chem. Int. Ed. Engl.* **2011**, *50*, 3430–4.

[87] O. Kozák, M. Sudolská, G. Pramanik, P. Cígler, M. Otyepka, R. Zbořil, *Chem. Mater.* **2016**, *28*, 4085–4128.

[88] H. Y. Mao, S. Laurent, W. Chen, O. Akhavan, M. Imani, A. A. Ashkarran, M. Mahmoudi, *Chem. Rev.* **2013**, *113*, 3407–3424.

[89] C. N. R. Rao, A. K. Sood, K. S. Subrahmanyam, A. Govindaraj, *Angew. Chem. Int. Ed. Engl.* **2009**, *48*, 7752–77.

[90] G. Hong, S. Diao, A. L. Antaris, H. Dai, *Chem. Rev.* **2015**, *115*, 10816–10906.

[91] X. Xu, R. Ray, Y. Gu, H. J. Ploehn, L. Gearheart, K. Raker, W. A. Scrivens, *J. Am. Chem. Soc.* **2004**, *126*, 12736–12737.

[92] Y.-P. Sun, B. Zhou, Y. Lin, W. Wang, K. A. S. Fernando, P. Pathak, M. J. Meziani, B. A. Harruff, X. Wang, H. Wang, et al., *J. Am. Chem. Soc.* **2006**, *128*, 7756–7.

[93] S. N. Baker, G. A. Baker, *Angew. Chem. Int. Ed. Engl.* **2010**, *49*, 6726–44.

[94] H. Li, Z. Kang, Y. Liu, S.-T. Lee, X. Y. Xu, R. Ray, Y. L. Gu, H. J. Ploehn, L. Gearheart,

K. Raker, et al., *J. Mater. Chem.* **2012**, *22*, 24230.

[95] J. C. G. Esteves Da Silva, H. M. R. Gonçalves, *Trends Anal. Chem.* **2011**, *30*, 1327–1336.

[96] S. Y. Lim, W. Shen, Z. Gao, *Chem. Soc. Rev.* **2014**, *44*, 362–381.

[97] Q. Li, T. Y. Ohulchanskyy, R. Liu, K. Koynov, D. Wu, A. Best, R. Kumar, A. Bonoiu, P. N. Prasad, *J. Phys. Chem. C* **2010**, *114*, 12062–12068.

[98] A. S. Barnard, *Analyst* **2009**, *134*, 1751–64.

[99] Y.-R. Chang, H.-Y. Lee, K. Chen, C.-C. Chang, D.-S. Tsai, C.-C. Fu, T.-S. Lim, Y.-K. Tzeng, C.-Y. Fang, C.-C. Han, et al., *Nat. Nanotechnol.* **2008**, *3*, 284–288.

[100] J. Shen, Y. Zhu, X. Yang, C. Li, Y. Wang, L. Chen, A. P. Alivisatos, A. Priyam, D. E. Blumling, K. L. Knappenberger, et al., *Chem. Commun.* **2012**, *48*, 3686.

[101] S. Zhu, S. Tang, J. Zhang, B. Yang, S. Empedocles, M. Bawendi, X. Michalet, F. F. Pinaud, L. A. Bentolila, J. M. Tsay, et al., *Chem. Commun.* **2012**, *48*, 4527.

[102] Z. Zhang, J. Zhang, N. Chen, L. Qu, H. W. Kroto, J. R. Heath, S. C. O'Brien, R. F. Curl, R. E. Smalley, S. Iijima, et al., *Energy Environ. Sci.* **2012**, *5*, 8869.

[103] L. Li, G. Wu, G. Yang, J. Peng, J. Zhao, J.-J. Zhu, H. W. Kroto, J. R. Heath, S. C. O'Brien, R. F. Curl, et al., *Nanoscale* **2013**, *5*, 4015.

[104] J. Peng, W. Gao, B. K. Gupta, Z. Liu, R. Romero-Aburto, L. Ge, L. Song, L. B. Alemany, X. Zhan, G. Gao, et al., *Nano Lett.* **2012**, *12*, 844–849.

[105] S. Kim, S. W. Hwang, M.-K. Kim, D. Y. Shin, D. H. Shin, C. O. Kim, S. B. Yang, J. H. Park, E. Hwang, S.-H. Choi, et al., *ACS Nano* **2012**, *6*, 8203–8.

[106] F. Jiang, D. Chen, R. Li, Y. Wang, G. Zhang, S. Li, J. Zheng, N. Huang, Y. Gu, C. Wang, et al., *Nanoscale* **2013**, *5*, 1137.

[107] S. Zhu, J. Zhang, S. Tang, C. Qiao, L. Wang, H. Wang, X. Liu, B. Li, Y. Li, W. Yu, et al., *Adv. Funct. Mater.* **2012**, *22*, 4732–4740.

[108] Y. Sun, S. Wang, C. Li, P. Luo, L. Tao, Y. Wei, G. Shi, L. A. Ponomarenko, F. Schedin, M. I. Katsnelson, et al., *Phys. Chem. Chem. Phys.* **2013**, *15*, 9907.

[109] K. L. Schroeder, R. V. Goreham, T. Nann, *Pharm. Res.* **2016**, 1–21.

[110] S. S. Nanda, G. C. Papaefthymiou, D. K. Yi, *Crit. Rev. Solid State Mater. Sci.* **2015**, *40*, 291–315.

[111] W. Zhang, Z. Guo, D. Huang, Z. Liu, X. Guo, H. Zhong, *Biomaterials* **2011**, *32*, 8555–8561.

[112] W. Hu, C. Peng, W. Luo, M. Lv, X. Li, D. Li, Q. Huang, C. Fan, *ACS Nano* **2010**, *4*, 4317–4323.

[113] X. Sun, Z. Liu, K. Welsher, J. T. Robinson, A. Goodwin, S. Zaric, H. Dai, *Nano Res.* **2008**, *1*, 203–212.

[114] Z. Liu, J. T. Robinson, X. Sun, H. Dai, *J. Am. Chem. Soc.* **2008**, *130*, 10876–10877.

[115] T. Nezakati, B. G. Cousins, A. M. Seifalian, *Arch. Toxicol.* **2014**, *88*, 1987–2012.

[116] Y. Chang, S.-T. Yang, J.-H. Liu, E. Dong, Y. Wang, A. Cao, Y. Liu, H. Wang, *Toxicol. Lett.* **2011**, *200*, 201–210.

[117] V. C. Sanchez, A. Jachak, R. H. Hurt, A. B. Kane, *Chem. Res. Toxicol.* **2012**, *25*, 15–34.

[118] J.-L. Li, H.-C. Bao, X.-L. Hou, L. Sun, X.-G. Wang, M. Gu, *Angew. Chem. Int. Ed. Engl.* **2012**, *51*, 1830–4.

[119] J. Qian, D. Wang, F.-H. Cai, W. Xi, L. Peng, Z.-F. Zhu, H. He, M.-L. Hu, S. He, *Angew. Chemie Int. Ed.* **2012**, *51*, 10570–10575.

[120] M. I. Sajid, U. Jamshaid, T. Jamshaid, N. Zafar, H. Fessi, A. Elaissari, *Int. J. Pharm.* **2016**, *501*, 278–299.

[121] D. N. Futaba, K. Hata, T. Yamada, T. Hiraoka, Y. Hayamizu, Y. Kakudate, O. Tanaike, H. Hatori, M. Yumura, S. Iijima, *Nat. Mater.* **2006**, *5*, 987–94.

[122] R. H. Baughman, A. A. Zakhidov, W. A. de Heer, *Science* **2002**, *297*, 787–92.

[123] M. De Volder, S. Tawfick, R. Baughman, A. J. Hart, *Science* **2013**, *339*, 535–9.

[124] A. Eatemadi, H. Daraee, H. Karimkhanloo, M. Kouhi, N. Zarghami, A. Akbarzadeh, M. Abasi, Y. Hanifehpour, S. W. Joo, *Nanoscale Res. Lett.* **2014**, *9*, 393.

[125] K. Welsher, Z. Liu, S. P. Sherlock, J. T. Robinson, Z. Chen, D. Daranciang, H. Dai, *Nat. Nanotechnol.* **2009**, *4*, 773–780.

[126] K. Welsher, S. P. Sherlock, H. Dai, *Proc. Natl. Acad. Sci.* **2011**, *108*, 8943–8948.

[127] B. Nottelet, V. Darcos, J. Coudane, *Eur. J. Pharm. Biopharm.* **2015**, *97*, 350–370.

[128] A. Schädlich, H. Caysa, T. Mueller, F. Tenambergen, C. Rose, A. Göpferich, J. Kuntsche, K. Mäder, *ACS Nano* **2011**, *5*, 8710–20.

[129] E. R. Swy, A. S. Schwartz-Duval, D. D. Shuboni, M. T. Latourette, C. L. Mallet, M. Parys, D. P. Cormode, E. M. Shapiro, *Nanoscale* **2014**, *6*, 13104–12.

[130] V. M. Alexander, K. Sano, Z. Yu, T. Nakajima, P. L. Choyke, M. Ptaszek, H. Kobayashi, *Bioconjug. Chem.* **2012**, *23*, 1671–9.

[131] M. Liu, X. Zhang, B. Yang, L. Liu, F. Deng, X. Zhang, Y. Wei, *Macromol. Biosci.* **2014**, *14*, 1260–7.

[132] Y. Ge, Y. Zhang, S. He, F. Nie, G. Teng, N. Gu, *Nanoscale Res. Lett.* **2009**, *4*, 287–295.

[133] T. Dai, S. Zhou, C. Yin, S. Li, W. Cao, W. Liu, K. Sun, H. Dou, Y. Cao, G. Zhou, *Biomaterials* **2014**, *35*, 8227–8235.

[134] S. Dong, M. Roman, *J. Am. Chem. Soc.* **2007**, *129*, 13810–13811.

[135] C. C. Lee, J. A. MacKay, J. M. J. Fréchet, F. C. Szoka, *Nat. Biotechnol.* **2005**, *23*, 1517–1526.

[136] A.-M. Caminade, D. Yan, D. K. Smith, E. Buhleier, W. Wehner, F. Vögtle, D. A. Tomalia, H. Baker, J. Dewald, M. Hall, et al., *Chem. Soc. Rev.* **2015**, *44*, 3870–3873.

[137] S. Svenson, D. A. Tomalia, *Adv. Drug Deliv. Rev.* **2012**, *64*, 102–115.

[138] W. Wu, J. Shen, P. Banerjee, S. Zhou, *Biomaterials* **2010**, *31*, 8371–8381.

[139] W. I. Lee, Y. Bae, A. J. Bard, *J. Am. Chem. Soc.* **2004**, *126*, 8358–8359.

[140] X. Shi, T. R. Ganser, K. Sun, L. P. Balogh, J. R. Baker, *Nanotechnology* **2006**, *17*, 1072–1078.

[141] W. Lesniak, A. U. Bielinska, K. Sun, K. W. Janczak, X. Shi, J. R. Baker, L. P. Balogh, *Nano Lett.* **2005**, *5*, 2123–2130.

[142] K. T. Al-Jamal, P. Ruenraroengsak, N. Hartell, A. T. Florence, *J. Drug Target.* **2006**, *14*, 405–412.

[143] I. J. Majoros, A. Myc, T. Thomas, C. B. Mehta, J. R. Baker, *Biomacromolecules* **2006**, *7*, 572–579.

[144] T. P. Thomas, I. J. Majoros, A. Kotlyar, J. F. Kukowska-Latallo, A. Bielinska, A. Myc, J. R. Baker, *J. Med. Chem.* **2005**, *48*, 3729–35.

[145] J. F. Kukowska-Latallo, K. A. Candido, Z. Cao, S. S. Nigavekar, I. J. Majoros, T. P. Thomas, L. P. Balogh, M. K. Khan, J. R. Baker, *Cancer Res.* **2005**, *65*, 5317–24.

[146] R. J. Amir, L. Albertazzi, J. Willis, A. Khan, T. Kang, C. J. Hawker, *Angew. Chemie Int. Ed.* **2011**, *50*, 3425–3429.

[147] S.-H. Wu, C.-Y. Mou, H.-P. Lin, C. T. Kresge, M. E. Leonowicz, W. J. Roth, J. C. Vartuli, J. S. Beck, T. Yanagisawa, T. Shimizu, et al., *Chem. Soc. Rev.* **2013**, *42*, 3862.

[148] L. Wang, W. Zhao, W. Tan, *Nano Res.* **2008**, *1*, 99–115.

[149] S. Veeranarayanan, A. C. Poulose, S. Mohamed, A. Aravind, Y. Nagaoka, Y. Yoshida, T.

Maekawa, D. S. Kumar, *J. Fluoresc.* **2012**, *22*, 537–48.

[150] B.-H. Jun, D. W. Hwang, H. S. Jung, J. Jang, H. Kim, H. Kang, T. Kang, S. Kyeong, H. Lee, D. H. Jeong, et al., *Adv. Funct. Mater.* **2012**, *22*, 1843–1849.

[151] M. K. Yu, J. Park, S. Jon, *Theranostics* **2012**, *2*, 3–44.

[152] J. R. McCarthy, J. Bhaumik, M. R. Karver, S. Sibel Erdem, R. Weissleder, *Mol. Oncol.* **2010**, *4*, 511–28.

[153] O. M. Koo, I. Rubinstein, H. Onyuksel, *Nanomedicine* **2005**, *1*, 193–212.

[154] J. D. Byrne, T. Betancourt, L. Brannon-Peppas, *Adv. Drug Deliv. Rev.* **2008**, *60*, 1615–26.

[155] M. Bai, D. J. Bornhop, *Curr. Med. Chem.* **2012**, *19*, 4742–58.

[156] E. Laabs, M. Béhé, S. Kossatz, W. Frank, W. A. Kaiser, I. Hilger, *Invest. Radiol.* **2011**, *46*, 196–201.

[157] A. D. Friedman, S. E. Claypool, R. Liu, *Curr. Pharm. Des.* **2013**, *19*, 6315–29.

[158] K. Haupt, A. V Linares, M. Bompart, B. T. S. Bui, *Top. Curr. Chem.* **2012**, *325*, 1–28.

[159] A. L. Nelson, *MAbs* **2010**, *2*, 77–83.

[160] H. Hong, J. Sun, W. Cai, *Biomark. Insights* **2008**, *3*, 435–451.

[161] A. D. Ellington, J. W. Szostak, *Nature* **1990**, *346*, 818–822.

[162] C. Tuerk, L. Gold, *Science* **1990**, *249*, 505–10.

[163] T. Schütze, B. Wilhelm, N. Greiner, H. Braun, F. Peter, M. Mörl, V. A. Erdmann, H. Lehrach, Z. Konthur, M. Menger, et al., *PLoS One* **2011**, *6*, e29604.

[164] G. P. Smith, *Science* **1985**, *228*, 1315–7.

[165] K. Haupt, K. Mosbach, *Chem. Rev.* **2000**, *100*, 2495–2504.

[166] S. Kunath, M. Panagiotopoulou, J. Maximilien, N. Marchyk, J. Sänger, K. Haupt, *Adv. Healthc. Mater.* **2015**, *4*, 1322–1326.

[167] X.-A. Ton, B. Tse Sum Bui, M. Resmini, P. Bonomi, I. Dika, O. Soppera, K. Haupt, *Angew. Chemie Int. Ed.* **2013**, *52*, 8317–8321.

[168] M. Panagiotopoulou, Y. Salinas, S. Beyazit, S. Kunath, L. Duma, E. Prost, A. G. Mayes, M. Resmini, B. Tse Sum Bui, K. Haupt, *Angew. Chemie - Int. Ed.* **2016**, *55*, 8244–8.

[169] S. Beyazit, S. Ambrosini, N. Marchyk, E. Palo, V. Kale, T. Soukka, B. Tse Sum Bui, K. Haupt, *Angew. Chemie - Int. Ed.* **2014**, *53*, 8919–8923.

[170] S. Xu, H. Lu, *Biosens. Bioelectron.* **2016**, *85*, 950–956.

[171] M. Panagiotopoulou, S. Kunath, P. X. Medina-Rangel, K. Haupt, B. Tse Sum Bui,

Biosens. Bioelectron. **2016**, DOI 10.1016/j.bios.2016.07.080.

[172] S. Shinde, Z. El-Schich, A. Malakpour, W. Wan, N. Dizeyi, R. Mohammadi, K. Rurack, A. Gjörloff Wingren, B. Sellergren, *J. Am. Chem. Soc.* **2015**, *137*, 13908–12.

[173] D. Yin, S. Wang, Y. He, J. Liu, M. Zhou, J. Ouyang, B. Liu, H.-Y. Chen, Z. Liu, S. Nie, et al., *Chem. Commun.* **2015**, *51*, 17696–17699.

[174] S. Wang, D. Yin, W. Wang, X. Shen, J.-J. Zhu, H.-Y. Chen, Z. Liu, P. Chakravarty, E. O. Serebrovskaya, M. Ogawa, et al., *Sci. Rep.* **2016**, *6*, 22757.

[175] J. Li, Y. Dai, S. Wang, C. Han, K. Xu, *Sensors Actuators B Chem.* **2016**, *232*, 1–8.

[176] Abdullah-Al-Nahain, J.-E. Lee, I. In, H. Lee, K. D. Lee, J. H. Jeong, S. Y. Park, *Mol. Pharm.* **2013**, *10*, 3736–3744.

[177] Z. Su, H. Shen, H. Wang, J. Wang, J. Li, G. U. Nienhaus, L. Shang, G. Wei, *Adv. Funct. Mater.* **2015**, *25*, 5472–5478.

ANNEX 1

Table 1 provides an examplary summary of the cellular targets, targeting strategies and nanoparticles applied in fluorescent bioimaging as presented in this chapter:

Table 1 Cellular targets and the targeting strategies applied for fluorescent bioimaging using nanoparticles.

Cellular target	Cell line/*in vivo*	Targeting ligand	Nanoparticle	PMID [Reference]
EGFR	Cervical cancer cells	Anti-EGFR anibody	Au NPs	18590338 [61]
	Epidermoid carcinoma cells	EGF	QDs	20024999
	Oral squamous carcinoma cells/ Mice	Anti-EGFR antibody	QDs	21980236
	Epidermoid carcinoma cells	Anti-EGFR antibody	Polymeric NPs (Fluorospheres ®)	23273065
Nucleolin	Cervical cancer cells	AS1411 aptamer	Ag NCs	[175]
	Cervical cancer cells	AS1411 aptamer	GQDs-SiNPs	26524192
CD44	Adenocarcinomic human alveolar basal epithelial cells/ Mice	Hyaluronic acid	GQDs	24007260 [176]
	Mouse liver cells, Rat liver stellate cells, Liver hepatocellular carcinoma cells	Hyaluronic acid	QDs	20518553

αvβ3	Human primary glioblastoma cells	RGD peptide	SiNPs	26960989
	Cervical cancer cells	RGD peptide	GQDs	[177]
	Melanoma cells, Human primary glioblastoma cells, Mice	RGD peptide	QDs	16608262 [48]
CD20	T-lymphoblastoid cells, B-lymphocyte cells	Anti-CD20 antibody	GOs	20216934 [113]
	B-cells	Anti-CD20 antibody	QDs-chitosan NPs	24956063
	Chronic lymphocytic leukemia cells	Anti-CD20 antibody	Polymeric NPs (Cy5.5 dye)	26124662
Transferin-receptor	Cervical cancer cells	Transferin	CDs	[97]
	Cervical cancer cells	Transferin	QDs	9748158 [42]
EpCAM	Human colon adenocarcinoma cells	Anti-EpCAM antibody	UCNPs@SiNPs	27119593
	Breast cancer cells	Anti-EpCAM antibody	Pdots	20929226
HER2	Breast cancer cells	Anti-Her2 antibody	QDs	12459735 [47]
	Breast cancer cells	Anti-Her2 antibody	UCNPS@SiNPs	19420539
Folate receptor	Human colon adenocarcinoma cells	Folic acid	UCNPs@SiNPs	19420539
	Ovarian carcinoma cells	Folic acid	UCNPs@SiNPs	23562047
	Breast cancer cells	Folic acid	QDs	20965282

Passive targeting	Mice Pig	Passive targeting	QDs	14661026 [50]
Hyaluronic acid	Keratinocyte cells	MIPs	QDs	27238424 [168]
	Keratinocyte cells	MIPs	Polymeric NPs (Rhodamine B)	25880918, 27481167 [166,171]
Sialylated proteins	Human prostate cancer cells	MIPs	Polymeric NPs (nitrobenzoxadiazole)	26414878 [172]
	Liver hepatocellular carcinoma cells, Breast cancer cells	MIPs	Polymeric NPs (Fluorescein isothiocyanate)	26948803 [174]

Table 2 provides an examplary summary of nanoparticles used for multimodal bioimaging, targeted bioimaging combined with drug delivery/gene therapy and a combination of photodynamic (PDT)/ photothermal (PTT) therapy and imaging.

Table 2 Representative examples of nanoparticles for use in multimodal imaging, combined imaging and drug release/gene delivery and combined imaging and photodynamic (PDT)/photothermal (PTT) therapy. Adapted from [29].

Methods and materials	PMID
Polymer-functionalized NIR fluorescent dyes on magnetic NPs for optical bioimaging and MRI.	23869722
^{18}F-Labeled magnetic upconversion NPs prepared via rare-earth cation-assisted ligand assembly for trimodal imaging (fluorescence, MRI and PET).	21384900
Bimodal magnetic resonance (MRI) and fluorescence imaging of intracranial glioblastoma using NP of the type $NaYF_4$:Yb,Tm,Gd@oleate and a surface modified with HS-PEG-NH_2.	24397730
Fluorescently doped SiNPs for use in bimodal (PET and fluorescent) imaging of lymph nodes.	23138852
Upconversion NPs coated with mesoporous silica for imaging and PDT.	19598161
Upconversion NPs in mesoporous silica used for plasmon-enhanced luminescence imaging and NIR light triggered drug release.	24521281
Urethane-doped biodegradable photoluminescent polymers; typical size 100 nm; obtained by nanoprecipitation; loaded with the drug 5-fluorouracil.	23465824
Magnetic resonance and fluorescence imaging of doxorubicin-loaded and dextrane coated NPs.	20599526
LaF_3:Yb,Tm coated with SiO_2 for folic acid-directed targeting of cancer cells; bimodal imaging by upconversion luminescence and X-ray computer tomography.	23134318
Rare-earth functionalized reduced graphene oxide for tracking and photothermal killing of drug-resistant bacteria.	24327351

CHAPTER 2

Synthesis and Characterization of MIPs for Sugar Acids

2.1 Introduction

As a new class of synthetic receptors, molecularly imprinted polymers (MIPs) have shown great performance in many biochemical applications because of their specific recognition ability, high stability, and ease of preparation. The molecular imprinting concept has arisen from the ambition to prepare biomimetic materials with selective molecular recognition sites such as those of natural enzymes and antibodies. The synthesis of such artificial receptors has thus attracted increasing interest from various research fields, e.g. chromatography [1] solid-phase extraction [2], catalysis [3], and sensors [4]. In this chapter, the synthetic approaches for obtaining water-compatible MIPs for the recognition of sugar acids in aqueous environments will be discussed.

Molecular imprinting has been realized in three different ways through the non-covalent, covalent and semi-covalent (or hybrid) approaches. The non-covalent imprinting approach was pioneered by Mosbach and co-workers [5]. This approach is more like the interactions occurring between biomolecules in nature. Functional and crosslinking monomers are copolymerised in the presence of a template (the imprint molecule) in a suitable solvent. The template can be the target molecule or a derivative thereof. The functional monomers initially form a complex with the template and after polymerisation, the monomer-template assembly is held in position by the highly crosslinked three-dimensional rigid structure. Subsequent removal of the imprint molecule leaves cavities with a size, shape and chemical functionality complementary to the template. In this way, a molecular memory is introduced into the polymer that is now capable of selectively binding the target with affinities comparable to natural receptors.

Alternatively, monomers can be covalently coupled to the imprint molecule, thus a polymerizable imprint molecule derivative is synthesized. Covalent imprinting was primarily developed by Wulff and co-workers [6]. Owing to its greater stability, covalent imprinting yields a more homogeneous population of binding sites. The key for successful covalent imprinting is the choice of the covalent linkage which connects functional monomer with template. However, the number of covalent bonds which fulfill the requirements of stability and reversibility is small. The covalent bonds include boronic acid esters, Schiff bases, ketals and sulfide bonds. This is why, MIPs use more frequently protocols based on the non-covalent approach, which is more

flexible concerning the choice of functional monomers. A "semi-covalent" approach has been described by Whitcombe combining the advantages of both methods; a covalent linkage between template and functional monomer is generated during synthesis and non-covalent binding is used for the rebinding step [7].

Synthesizing water-compatible MIPs still remains a challenge, despite many efforts in the past two decades to make MIPs recognize selectively target molecules in aqueous environments or more complex biological matrices. The conventionally developed MIPs are normally only compatible with organic solvents, and they mostly fail to show specific template binding in aqueous solutions, which significantly limits their practical application in such areas as molecularly imprinted sorbent assays, biomimetic sensors, and biotechnology. The incompatibility of the MIPs with aqueous environments is suspected to be due to the following two reasons: 1) The use of water to substitute organic solvents can considerably weaken such non-covalent interactions as hydrogen bonding and electrostatic forces between the template molecules and binding cavities of the MIPs, thus resulting in their lower molecular recognition ability in the aqueous solutions; 2) It is well known that hydrophobic effects are very strong in water. The hydrophobicity of the typical MIPs and small organic molecules (normally used as templates) are largely enhanced in aqueous solutions in comparison with that in organic solvents, which will greatly increase the nonspecific hydrophobic interactions between the MIPs and templates, leading to large nonspecific template binding [8].

Recently, much research has been devoted to address the issue of water incompatibility of the MIPs. Some of the MIPs synthesized by the conventional imprinting approaches in organic solvents or in a mixture of water-containing solvents as porogen can then be used in aqueous solvents [9–12]. Other approaches include the development of water-compatible MIPs based on: 1) stoichiometric non-covalent template-monomer complexes [13–16], 2) hydrophobic effect-driven recognition with the use of cyclodextrin based monomers [17–19], 3) metal coordination-driven recognition [20] and 4) the use of surface post-modification by either introducing hydrophilic functional groups onto the MIP surfaces by chemical modification or by grafting hydrophilic polymer layers onto MIP surfaces via conventional free or living (controlled) radical polymerization [21,22]. In this chapter, emphasis will be given in the use of stoichiometric

monomers, since it is the method that we applied for the synthesis of the MIPs described in this chapter in order to render them water-compatible.

2.1.1 Stoichiometric Non-Covalent Template–Monomer Complexes

As mentioned above, in aprotic solvents of low polarity, recognition between the template molecule and the functional monomer relied mainly on electrostatic interactions in addition to hydrogen bonding. For example, if the template has an acidic functional group (carboxylate, phosphonate), basic functional monomers, available commercially, like vinylpyridine and *N*,*N*-diethylaminoethyl methacrylate, can be employed. However, these interactions are weak and, hence, a large excess of functional monomer (at least fourfold) is used in order to ensure a sufficiently high degree of complexation with functional groups of the template for effective imprinting to occur. This leads to a substantial number of non-specific binding sites. But, if the association constant between template and functional monomer is high enough ($K_a \geq 10^3$ M^{-1}; for comparison, the K_a of hydrogen bonds, electrostatic interactions between carboxylic acids and basic nitrogen and electrostatic interactions between carboxylic acids and basic nitrogen with additional hydrogen bonds are respectively around 1.7, 3.3, and 30 M^{-1} in acetonitrile) [23], they will completely bind to each other in a 1:1 molar ratio. With this procedure, non-specific binding sites are not produced in the polymer.

For this purpose, a series of functional monomers bearing strong interacting groups towards the templates have been rationally designed and synthesized, such as N,N'-diethyl-4-vinyl-benzamidine [13,24–26], 9-(guanidinomethyl)-10-vinylanthracene [14], 1,3-disubstituted ureas (e.g., 1-(3,5-bis(trifluoromethyl)phenyl)-3-(4-vinylphenylurea)) [15], 5-(4‴-vinyl)benzyloxy-1,3-bis[2′-(3″,3″,4″,4″-tetramethyl-2″,5″-dioxaborolanyl) phenylcarbomoyl] benzene and 2-(4-vinylphenyloxy)-3,5,6-trichlorobenzoquinone [16]. They could form rather stable complexes with specific templates in polar solvents through stoichoimetric non-covalent interactions, thus leading to MIPs with specific molecular recognition in aqueous media.

Wulff and co-workers were the first to develop a series of host monomers bearing an amidine group [13,24–26], such as N,N'-diethyl-4-vinyl- benzamidine 1 (Figure 1a) which can form strong

electrostatic interactions with carboxylates, phosphonates and phosphates (5×10^3 $M^{-1} < K_a < 10^6$ M^{-1}). For example, enantioselective MIPs were prepared by targeting the oxyanions of N-terephthaloyl-D-phenylglycine **2** with monomer **1** in tetrahydrofuran (THF). The binding here was strong enough to provide quantitative rebinding in methanol [13]. Though rebinding behavior in water was not demonstrated, it is highly likely that strong specific interactions would also prevail in this medium, since there has been a precedent involving amidine moieties from the template pentamidine and carboxyl moieties from the monomer MAA that interact very strongly and specifically in water-based solutions (Figure 1b) [27].

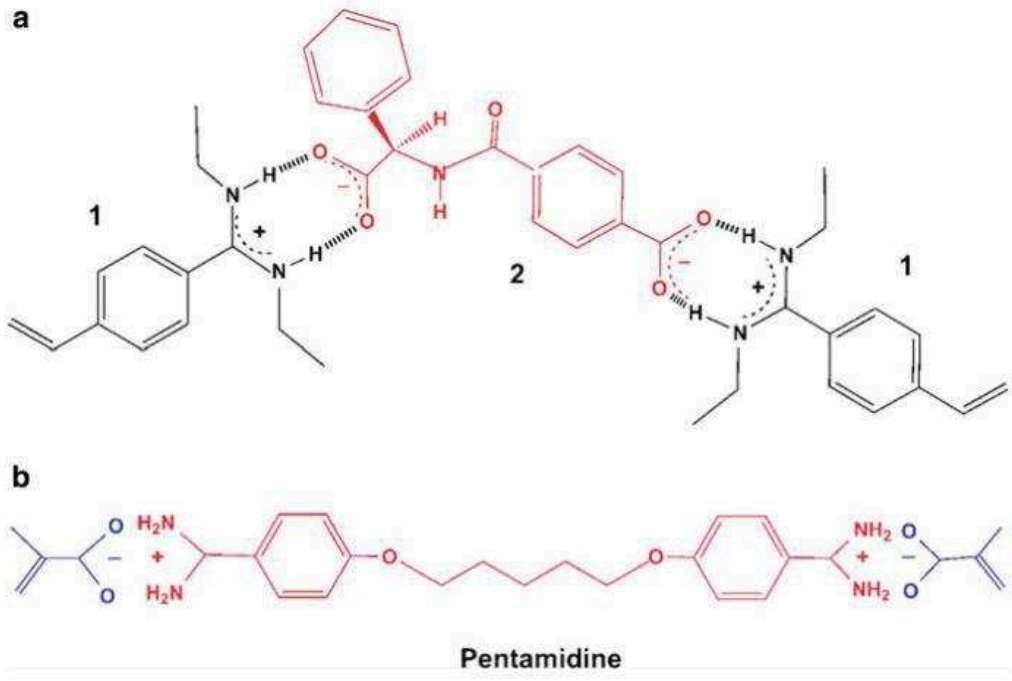

Figure 1 Complexes formed (a) between amidine groups in the functional monomer N,N'-diethyl- 4-vinyl-benzamidine and carboxyl groups in the imprinting template N-terephthaloyl-D- phenylglycine [24] and (b) between amidine groups in the imprinting template pentamidine and carboxyl groups in the functional monomer methacrylic acid [27]. Reproduced from [28].

Whitcombe and coworkers [16] synthesized two functional monomers, one is a derivative of a boron-containing receptor **3** and the other is a quinone **4** to react respectively with the carboxylate and the amino groups of the antibiotic ampicillin **5** (Figure 2). The association constant of the polymerizable boronic acid-containing receptor with ampicillin carboxylate in a 1:1 complex was determined to be 2,800 M^{-1} (in d_3-acetonitrile).

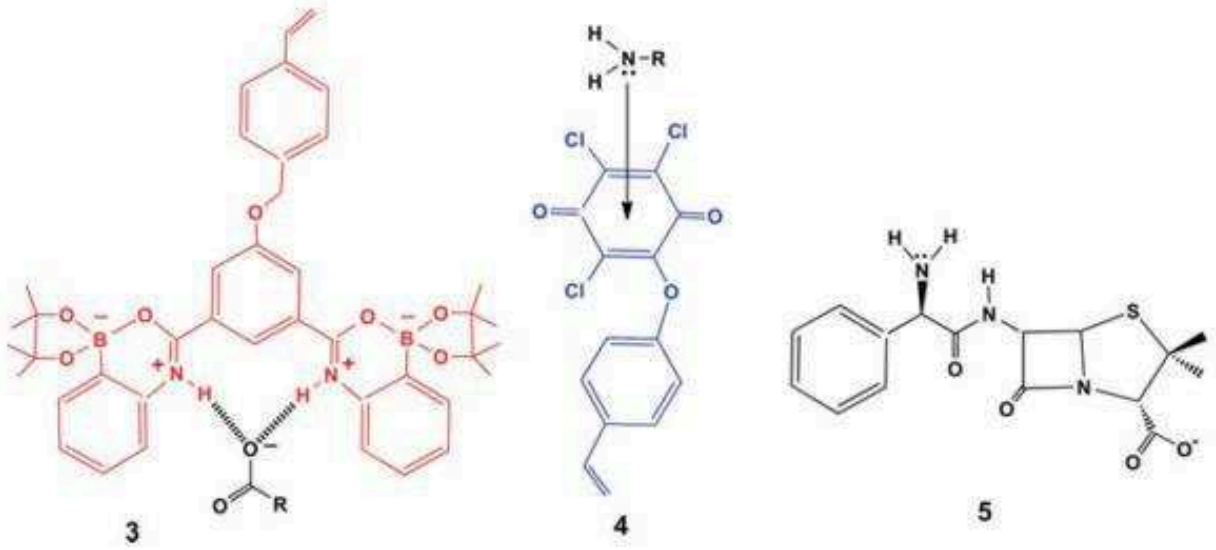

Figure 2 Monomers (3 and 4) for the stoichiometric complexation of ampicillin (5). Reproduced from [28].

Binding of the amino group in ampicillin with the electron-deficient quinone occured through N–π interactions and the K_a of a 2:1 complex was estimated to be >30,000 M^{-1} (in d_6- DMSO). The polymers prepared with ampicillin carboxylate and these monomers in a 1:1:1 ratio in DMSO demonstrated efficient binding of ampicillin, as compared to the non-imprinted polymer, in aqueous buffer solutions. These two new functional monomers show the high potential of imprinting of a target carrying carboxyl and amino groups which are common to many other antibiotics, amino acids, peptides, nucleotides, and alkaloids, and therefore could be generalized to the imprinting of these bioactive compounds and give rise to polymers which would have high specificities and selectivities in aqueous media.

Verboom and coworkers prepared a polymerizable anthracene type functional monomer with a guanidine group (Figure 3A) [14]. The ^{1}H NMR dilution experiments gave binding association constants (K_a values) of 1.2×10^5 and 1.4×10^5 M^{-1} for the 1:1 complex of this functional monomer with ammonium acetate and tetrabutylammonium acetate in deuterated methanol, respectively, which indicated the formation of very strong non-covalent interactions between the

guanidine group and acetate. In addition, its complexation with different carboxylates in ethanol induced significant changes in fluorescene. These results demonstrated that the aforementioned functional monomer is highly suitable for the synthesis of fluorescent MIPs with molecular recognition in aqueous environments.

A series of urea-based vinyl monomers were synthesized for stoichiometric oxyanion recognition [15]. One of these urea-based monomers, 1-(4-vinylphenyl)-3-(3,5-bis(trifluoromethyl) phenyl)urea **6**, was employed stoichiometrically with the template penicillin G **7** (Figure 3B) for the preparation of a MIP to extract penicillin G and its beta-lactam derivatives from aqueous samples. The K_a between this monomer and tetrabutylammonium benzoate is 8,820 M^{-1} (in d_6-DMSO). The MIP was synthesized in acetonitrile as porogen and the loading of the antibiotics was done in HEPES buffer where the development of strong stoichiometric electrostatic interactions between the carboxylate groups of the antibiotics and the urea moiety of the monomer allowed for retention. The clean-up was achieved simply by percolating the loading buffer containing 10% CH_3CN: all non-specific interactions were eliminated, as monitored on the NIP, leaving the specific interactions untouched as judged by the high recoveries of the analytes during elution [29].

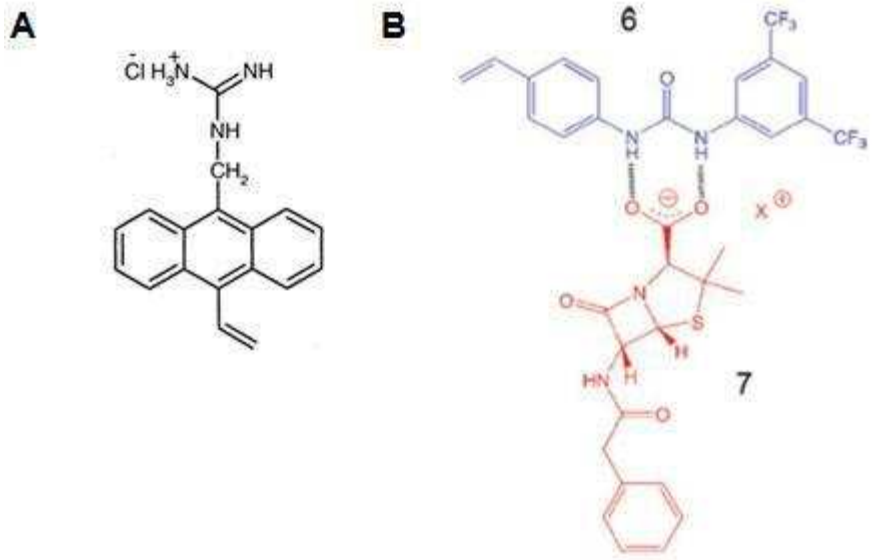

Figure 3 (A) 9-(Guanidinomethyl)-10-vinylanthracene functional monomer used in [14] .(B) Urea-based functional monomer (6) for the complexation of penicillin G (7). Reproduced from [28].

A complementary method to reduce the hydrophobically driven nonspecific binding of the MIP towards the template molecule in aqueous solutions is by increasing the surface hydrophilicity of the MIPs. To this end, some hydrophilic functional monomers (e.g., acrylamide, 2-hydroxyethyl methacrylate (HEMA)), cross-linkers (e.g., poly(ethylene glycol) diacrylate, *N*,*N*′-methylene bisacrylamide, *N*,*N*′-ethylene bisacrylamide, and pentaerythritol triacrylate (PETA) have been employed in the molecular imprinting systems to prepare hydrophilic MIPs.

Regarding the imprinting of sugar acids, many researchers have opted for the preparation of water compatible MIPs targeting sialic acid both with the covalent and the non-covalent approaches. In the case of covalent imprinting, boronate-based monomers such as 4-vinylphenylboronic acid are employed. Boronic acids covalently react with diols in the relative affinity order: *cis*-1,2-diols > 1,3 diols >> *trans*-1,2 diols, forming reversible boronate esters. Several examples of water compatible MIPs prepared using boronic acids as functional monomers will be discussed in Chapter 3 [30–33]. Regarding non-covalent imprinting of sialic acid, Takeuchi and coworkers were the first to employ monomers with basic functionality such as 4-vinylpyridine and *N*,*N*,*N*-trimethylaminoethyl methacrylate chloride in order to target the carboxyl group of sialic acid [34,35]. In the first case, a ratio of 1:1:28 between sialic acid:4-vinylpyridine:EGDMA was applied, while in the second case the authors used a ratio of 1:1:7.7:20 between sialic acid:*N*,*N*,*N*-trimethylaminoethyl methacrylate:2-hydroxyethyl methacrylate:EGDMA. Dimethylformamide (DMF) was used as porogen and the polymerizations were UV-initiated at 4^{o} C. The recognition abilities of the polymers were evaluated in the first case in an acetonitrile:water mixture (4:1) and in the second case in phosphate buffer, where an IF~2 was demonstrated [34].

In the present chapter, we aimed for the non-covalent synthesis of water-compatible molecularly imprinted polymers using the stoichiometric monomers: 1-(4-vinylphenyl)-3-(3,5-bis(trifluoromethyl)phenyl) urea (UREA) or a polymerizable benzamidine, (4-acrylamidophenyl)(amino)methaniminium acetate (AB), for the ultimate goal of the application as imaging agents specific for hyaluronan and sialylation sites on cells and tissue. To this end, the dye rhodamine and two InP/ZnS QDs, emitting in the green and in the red regions were used as fluorescent probes. Since molecular imprinting of entire biomacromolecules like

polysaccharides or proteins is challenging, we opted for what is commonly called the "epitope approach", which was inspired by nature [36,37] (Figure 4). The monosaccharides, glucuronic acid (GlcA) and N-acetylneuraminic acid (NANA) were imprinted in DMSO, and the resulting MIPs were able to bind these molecules if present and accessible, as the terminal units on larger oligosaccharides or proteoglycans (see Figure 3 Chapter 3). In addition, the epitope approach was a good alternative to the direct imprinting of these large molecules to avoid some difficulties that may accompany their use as templates such as the need of purification or their low-abundance and high cost. High molecular-weight templates may become entrapped or covalently bound to the polymer matrix. Furthermore, the large imprinted sites may be seen as general nanopores able to bind a range of smaller molecules, resulting in reduced selectivity.

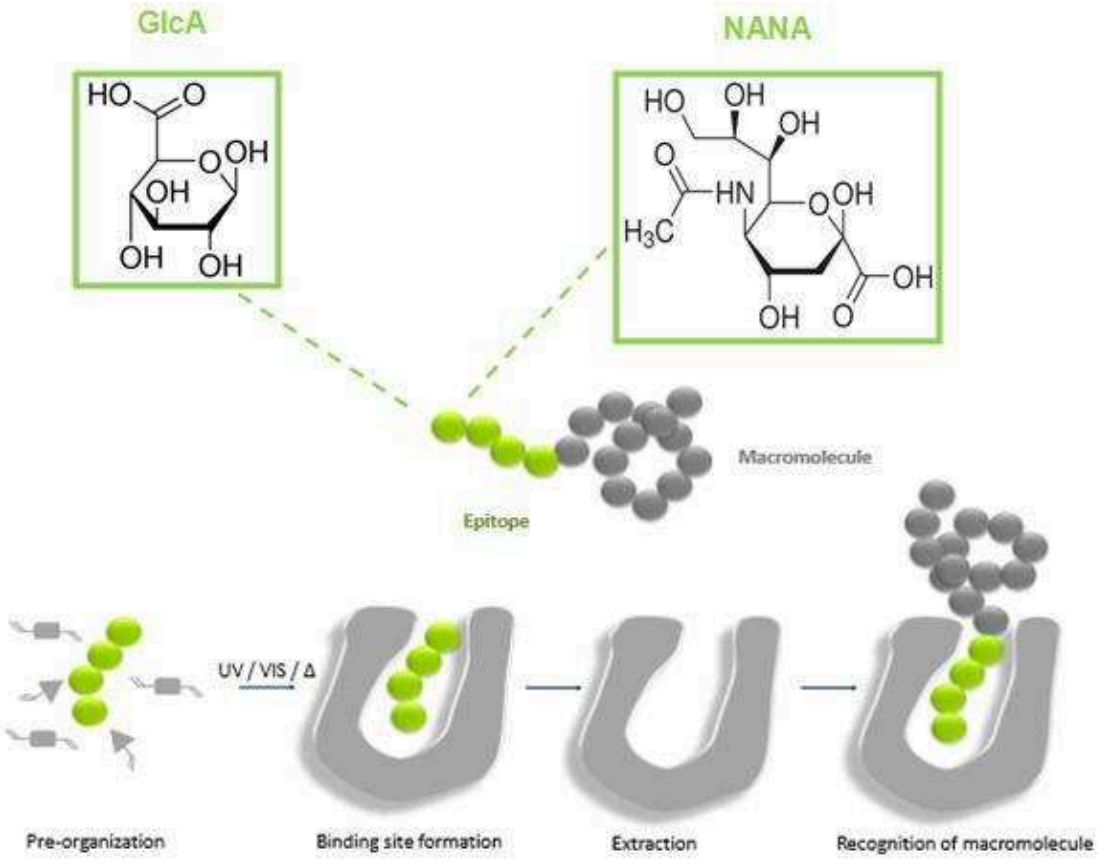

Figure 4 Schematic representation of the epitope approach in order to target glycosylations with MIPs using GlcA and NANA as epitopes.

2.2 Results and Discussion

2.2.1 Targeting sugar acids with MIPs prepared by precipitation polymerization

UREAMIP

A series of urea-based functional monomers was synthesized by Hall et al. [15], of which the 1-(4-vinylphenyl)-3-(3,5-bis(trifluoromethyl)phenyl)urea (UREA) (Figure 3B) proved to have the highest association constant (K_a =8,820M^{-1}) with tetrabutylammonium benzoate in DMSO-d_6. The first report of the use of urea-based monomers for the recognition of oxoanionic carbohydrates comes from Ambrosini et al., who used urea-based monomers to develop specific imprinted materials against glucuronide residues [38]. They used substituted glucuronides (tetraacetylated and 1-O-dodecyl) to improve the molecule solubility in porogenic solvents more compatible with molecular imprinting, such as THF, acetonitrile and chloroform and achieved a high imprinting factor in acetonitrile in the presence of a base (pentametylpiperidine) to reduce nonspecific binding. Although recognition in aqueous environment was not reported in this example, the water-compatibility of urea-based MIPs has been demonstrated in several other examples where selective recognition and extraction of antibiotics from water samples was possible [29,39,40].

In our first attempts to prepare MIPs for GlcA, UREA was employed as a stoichiometric functional monomer, phenyl-β-D-glucuronic acid monohydrate was used as template and the porogen was ACN:DMSO (4:1). The binding behavior of the UREAMIP was assessed with both equilibrium binding studies in ACN+1%TEA using radiolabeled GlcA and fluorescence measurements using the fluorescent analogue 4-methylumbelliferyl-β-D-glucuronide (MUG) (λ_{ex}= 315 nm, λ_{em}= 380 nm) (see the calibration curve of MUG in ANNEX 2, Figure 1). The structures of the template, functional monomer and fluorescent analogue used in this study are presented in Figure 5.

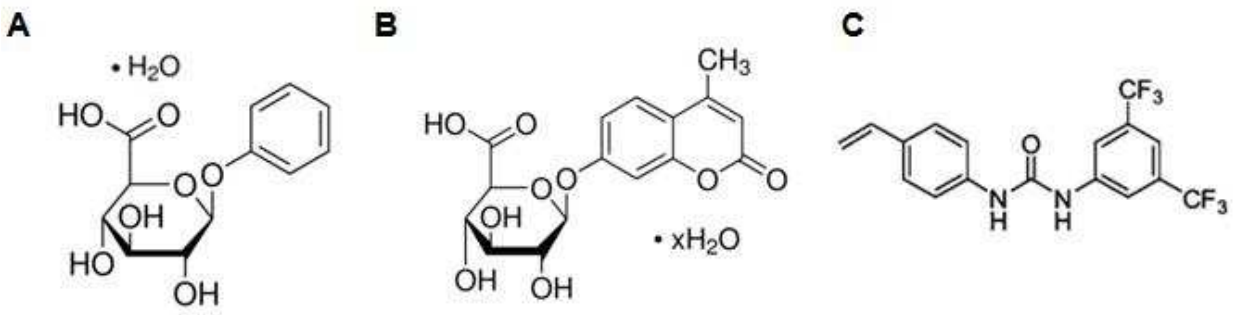

Figure 5 Chemical structures of: (A) phenyl-β-D-glucuronic acid monohydrate, (B) MUG and (C) UREA.

TEA serves as a base to deprotonate GlcA [15,41] and its presence is essential to induce specific binding, in accord with previous reports of MIPs imprinted with salicylic acid using the UREA monomer. As observed in Figure 6 significant specificity was obtained in ACN+1%TEA. The binding in aqueous conditions was also assessed. Both MIP and NIP demonstrated low binding and no specificity in 100 mM HEPES buffer, pH 7.5, or in ACN:100 mM HEPES buffer, pH 7.5 (50:50), the conditions used for the recognition of other carboxyl anions, namely, enrofloxacin and penicillin G [39,40].

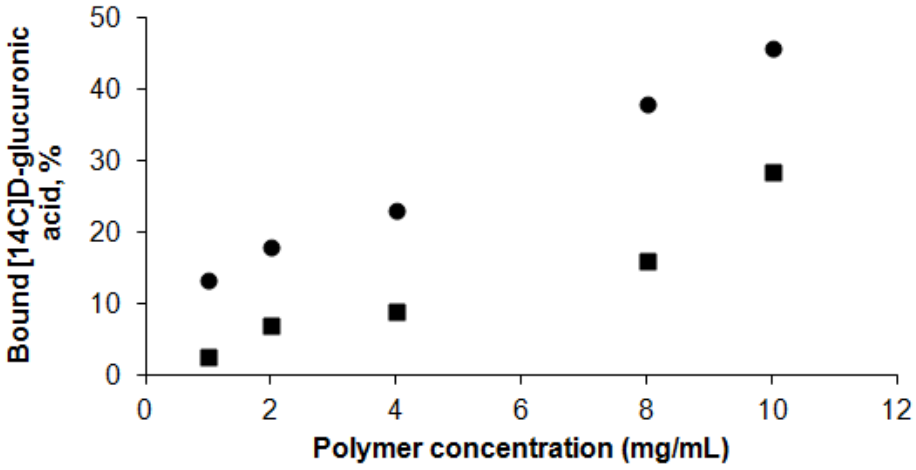

Figure 6 Equilibrium binding isotherms in ACN+1%TEA of [14C]D-glucuronic acid to UREANIP (squares) and UREAMIP(circles) .

Fluorescence measurements using 5 µM MUG were employed in order to test other aqueous conditions (Figure 7). In 90% water, there was no binding at all for both MIP and NIP; the addition of water to the ACN+1% TEA mixture seems to hamper the binding of the fluorescent analogue MUG. Although the best specificity can be achieved by the addition of 8% water, the binding capacity unfortunately was lower.

Despite their lower performance in aqueous conditions, the MIPs were assessed in a mixture of methanol:water (1:30), the medium used for cell imaging experiments. High aggregation was observed, rendering these particles unsuitable for further bioimaging. Therefore, other polymer compositions were tested.

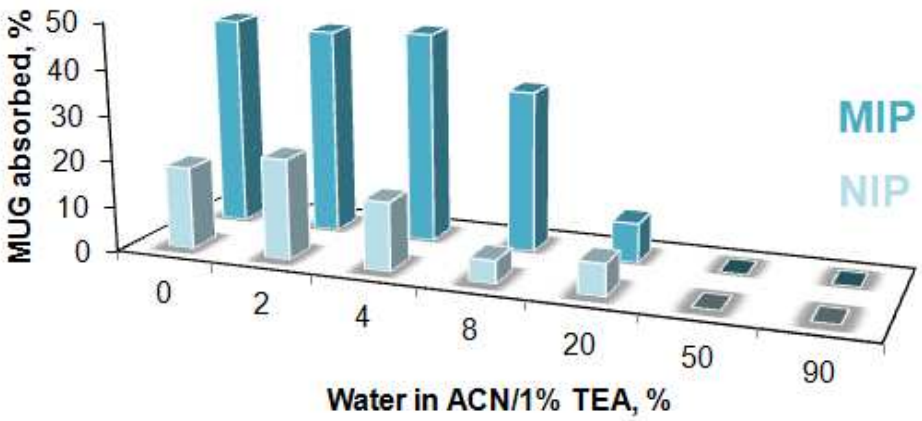

Figure 7 Influence of water on the binding behaviour of MUG (5 µM) to 10 mg UREAMIP and UREANIP polymers in ACN + 1% TEA. Data are means from two independent experiments.

ABMIPs

Recently, we showed that MIPs prepared with an unsubstituted amidine monomer, (4-acrylamidophenyl)(amino)methaniminium acetate (AB), could selectively capture molecules bearing carboxylic acid moieties in very complex media such as human sweat [42]. The stoichiometry between AB and the –COOH template, as determined by ^{1}H NMR spectroscopy

analysis was 1:1, with a high binding constant K_a of 9.4×10^3 M^{-1} in CD_3OD:D_2O (4:1). These results demonstrated the feasibility of preparing highly selective molecularly imprinted binding sites for recognition in complex aqueous media, using this amidinium monomer, which can form stoichiometric interaction with a high binding constant for carboxyl groups. AB was thus chosen for the preparation of MIPs against sugar acids since it appears to be a promising tool for the synthesis of highly selective MIPs for a wide range of not only carboxylate but also phosphate, phosphonate and possibly sulfate-based biological molecules.

^{1}H NMR studies

The stoichiometry and the strength of the interaction between the templates GlcA and NANA and the functional monomer AB were determined by chemical shift analysis using the method of continuous variation (Job plot) [43] and titration [44]. These studies were done in DMSO and methanol:water (4:1), the solvents used for preparing the ABMIPs.

Job's and titration method

Job's method, or the method of continuous variations, was proposed by Job in 1928. The method allows determining the quantitative relationships among substances (stoichiometry) in the system. In general, the experimental procedure includes the preparation of a series of solutions of two different compounds in the way that the total molar concentration of the two binding partners is held constant but their mole fractions are varied. Then the change in observable signal is plotted against the mole fraction of one of the components. An extremum indicates the stoichiometry of the complex. The mole ratio method or titration method provides the information about the complex stability. Herein, the total concentration of one partner (**A**) is held constant whereas the concentration of another component (**B**) is gradually varied. By plotting observable signal against variable amounts of the complexing agent, the association constant (K_a) can be determined.

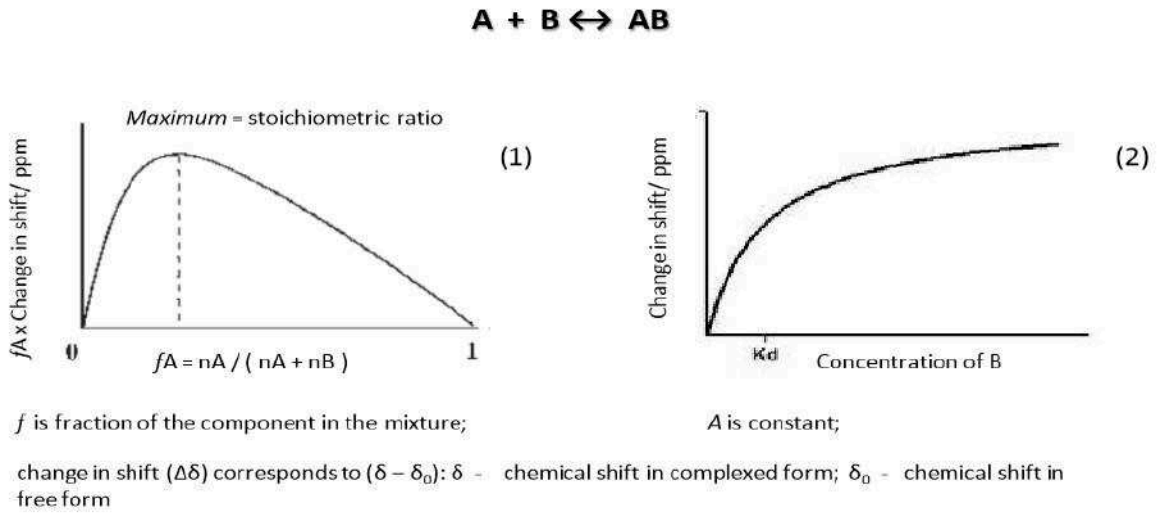

Figure 8 Representation of Job's (1) and the mole ratio (2) methods.

Interaction between AB and the templates

The assignment of GlcA, NANA and AB resonances was deduced from ^{1}H – ^{13}C HSQC (Heteronuclear Single Quantum Correlation) and ^{1}H – ^{1}H COSY (Correlation Spectroscopy) spectra (see ANNEX 2, Figures 2-5). In all experiments, the free and the template-bound monomer forms are in fast exchange on the NMR timescale in the sense that a single (weighted) averaged chemical shift is observed.

The cyclic forms of carbohydrates can exist in two forms, α and β, based on the position of the substituent at the anomeric center (Figure 9). The two forms are sometimes described as "anomers" since they are isomers at the anomeric center. The anomeric center is the carbon derived from the carbonyl carbon (the ketone or aldehyde functional group) of the open-chain form of the carbohydrate molecule. In an aqueous solution, the α and β anomers will quickly equilibrate to an equilibrium mixture of the two forms, a process called anomerization. For example, in aqueous solution for D-glucopyranoside, the β anomer is the more stable anomer and thus found in excess.

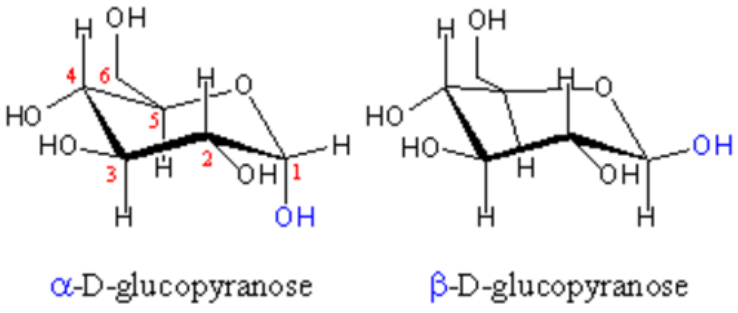

Figure 9 The two anomeric forms, α and β of D-glucopyranose.

For the NMR studies, in the case of GlcA, the chemical shift difference (Δδ), due to complexation, of the H5 of the α form of the template (Figure 10A) was followed as a function of mole fraction of the template in the Job plot and as a function of the monomer/template concentration for titration experiments, respectively. The H5 proton was selected because it showed the greatest chemical shift difference among all protons.

For NANA, the proton $H3^{eq}$ is the one which shows the greatest chemical shift difference among all protons of NANA. Overlay of the $H3^{eq}$ and $H3^{ax}$ resonances rendered difficult the measurement of the chemical shift difference induced by complex formation for the Job plot at 0.7, 0.8 and 0.9 template mole fraction.

For the Job plot, solutions of GlcA, NANA and AB, at a constant concentration of 10 mM were prepared with the template mole fraction, varying from 0 to 1 by steps of 0.1. Association constants were determined by titrating an increasing amount of AB into a constant amount of GlcA or NANA. Stock solutions of 40 mM AB were added (from 0 to 2 equivalents) to a fixed 10 mM concentration of template. The Job plots of both the templates support a 1:1 equilibrium and the titration data fitted by a 1:1 binding isotherm by non-linear regression lead to an overall high association constants K_a of 7.1 x 10^3 M^{-1} for GlcA (Figure 10A) and K_a of 41 x 10^3 M^{-1} for NANA (Figure 10B) ($\beta 11 = K_a$ where K_a is the association constant.).

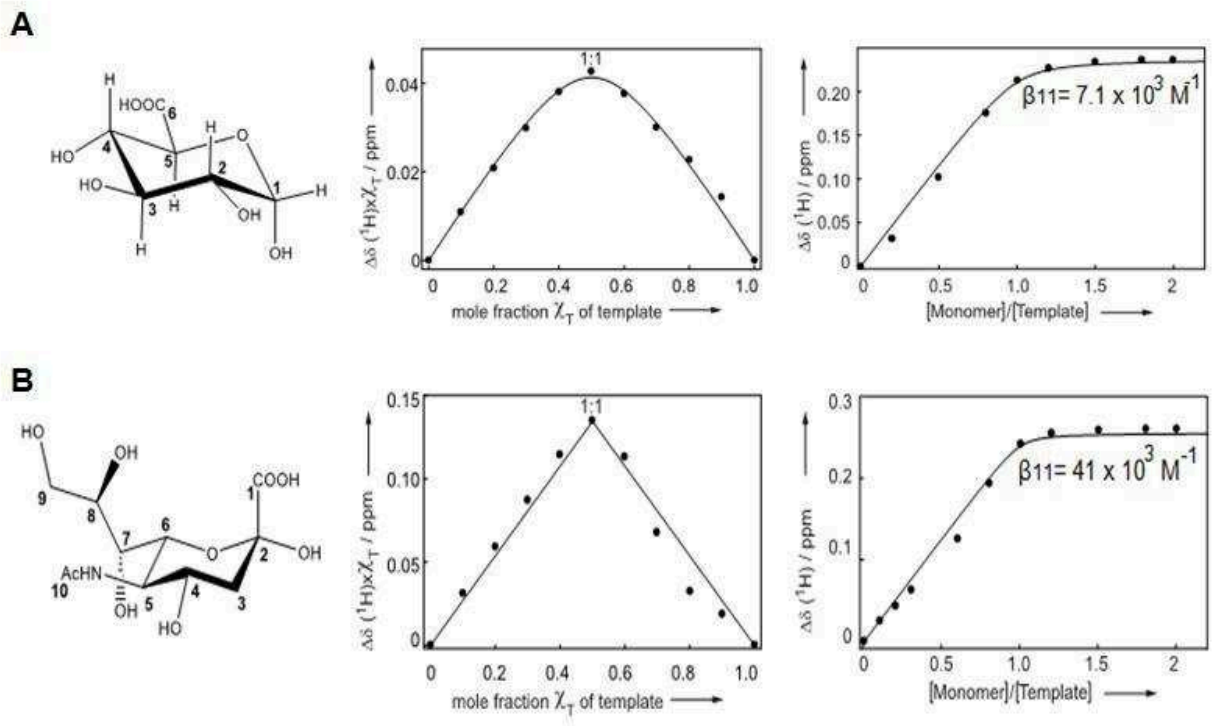

Figure 10 ^{1}H NMR Job plot and titration of (A) GlcA and (B) NANA with AB in DMSO-d_6 at 25 °C. (A) The chemical shift difference (Δδ) of the H5 proton of the α form of GlcA was measured and is represented with full circles. From left to right: Molecular structure of the α form of GlcA and atoms number related to the NMR studies; Job plot data (circles) and non-linear regression (line) analysis show a maximum at a mole fraction of 0.5 supporting a 1:1 stoichiometry of the complex monomer-template; titration data (circles) and non-linear regression (line) analysis lead to an overall association constant K_a of 7.1 x 10^3 M^{-1}. (B) The chemical shift difference (Δδ) of the $H3^{eq}$ proton of the template was measured and is represented with full circles. From left to right Molecular structure of NANA and atoms number related to the NMR studies; Job plot data (circles) and non-linear regression (line) analysis show a strong maximum at a mole fraction of 0.5 supporting a 1:1 stoichiometry of the complex monomer-template; titration data (circles) and non-linear regression (line) analysis lead to an overall association constant K_a of 41 x 10^3 M^{-1}.

The Job plots of both the templates were also obtained for the same experiment in MeOD/D_2O. In this case the data also support a 1:1 equilibrium and the titration data fitted by a 1:1 binding isotherm by non-linear regression lead to an overall high association constants K_a of 4.4 x 10^3 M^{-1} for GlcA (Figure 11A) and K_a of 36 x 10^3 M^{-1} for NANA (Figure 10B) (β11 = K_a where K_a is the association constant.).

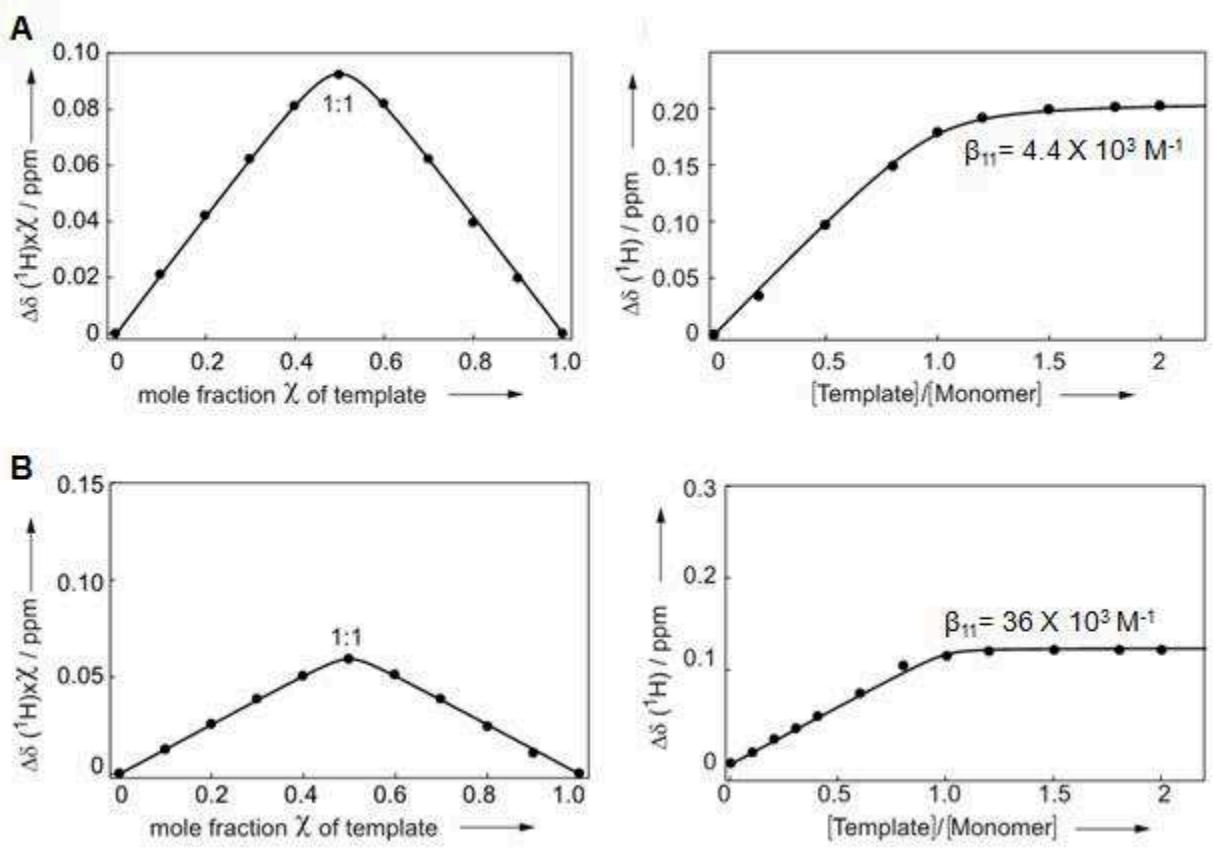

Figure 11 ^{1}H NMR Job plot and titration of (A) GlcA and (B) NANA with AB in MeOD/D_2O at 25 °C. (A) The chemical shift difference (Δδ) of the H5 proton of the α form of GlcA was measured and is represented with full circles. From left to right: Job plot data (circles) and non-linear regression (line) analysis show a maximum at a mole fraction of 0.5 supporting a 1:1 stoichiometry of the complex monomer-template; titration data (circles) and non-linear regression (line) analysis lead to an overall association constant K_a of 4.4 x 10^3 M^{-1}. (B) The chemical shift difference (Δδ) of the $H3^{eq}$ proton of the template was measured and is represented with full circles. From left to right: Job plot data (circles) and non-linear regression (line) analysis show a strong maximum at a mole fraction of 0.5 supporting a 1:1 stoichiometry of the complex monomer-template; titration data (circles) and non-linear regression (line) analysis lead to an overall association constant K_a of 36 x 10^3 M^{-1}.

Synthesis and characterization of AB polymers

For the synthesis protocol of the AB polymers against GlcA, a design of experiments approach coupled with a multi-objective optimization method was used to obtain the best polymer out of a repertoire of synthesized polymers and to predict the polymer composition with the best binding properties. An optimal glucuronic acid binding polymer composition was found with 0.65mol% of initiator and a 1:3:20 ratio of template:co-functional monomer:cross-linker plus 1 equivalent of the stoichiometric monomer AB [45]. Having these results in mind, MIPs for GlcA and NANA without any fluorescent labeling, were first synthesized and their binding performances evaluated

by equilibrium binding studies. Precipitation polymerization in two different porogens, MeOH:water (4:1) and DMSO, was assessed. AB and MAM were used as functional monomers and EGDMA as crosslinker, with a molar ratio template:AB:MAM:EGDMA of 1:1:3:20. MAM was added to provide hydrogen bonding interactions with the template and to render the MIP more hydrophilic to prevent aggregation in the aqueous cell imaging medium. The proposed complex formed between the functional monomers and the templates is presented in Figure 12.

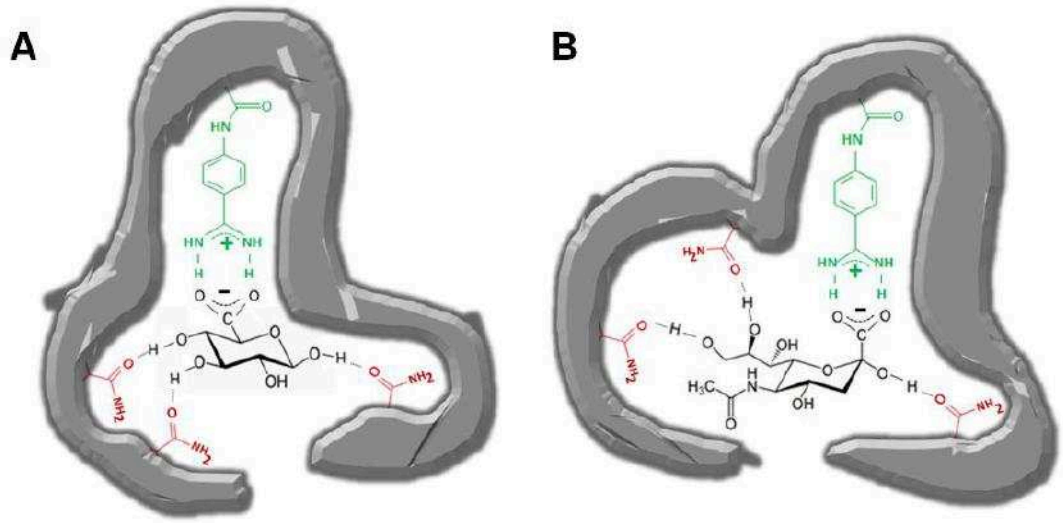

Figure 12 Proposed complex formed between the functional monomers methacrylamide (red), 4acrylamidophenyl)(amino)methaniminium acetate (AB) (green) and the templates (A) N-acetylneuraminic acid and (B) glucuronic acid (black).

The recognition properties of the polymers were evaluated by radioligand equilibrium binding assays in water. First, synthesis of an ABMIPGlcA in MeOH:water (4:1) was applied since imprinting in alcohol:water mixtures of this ratio has shown high specificities and selectivities in our research group [42]. Indeed, as shown in Figure 13, this polymerization protocol led to significant specific binding in water. Unfortunately, the obtained particles exhibited polydispersity and aggregation in aqueous environments and thus proved to be unsuitable for targeted cell imaging applications (Figure 15B). On the contrary, the ABMIPs synthesized in DMSO targeting GlcA and NANA were both specific towards their respective template as the binding with the control non-imprinted polymer was lower (Figure 14).

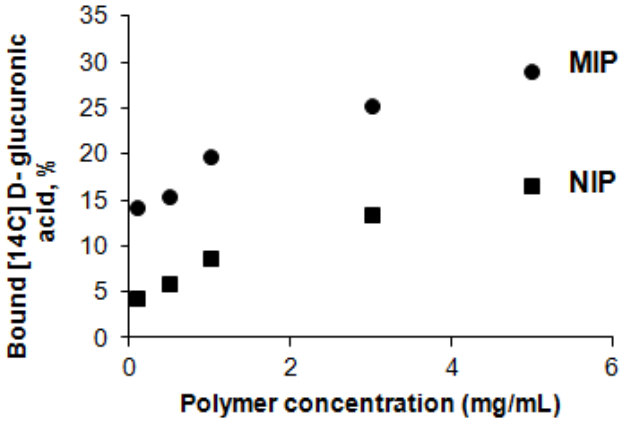

Figure 13 Equilibrium binding isotherms in water of [^{14}C]D-glucuronic to ABMIPGlcA synthesized in MeOH:water (4:1). Data are means from 2 indipendent experiments.

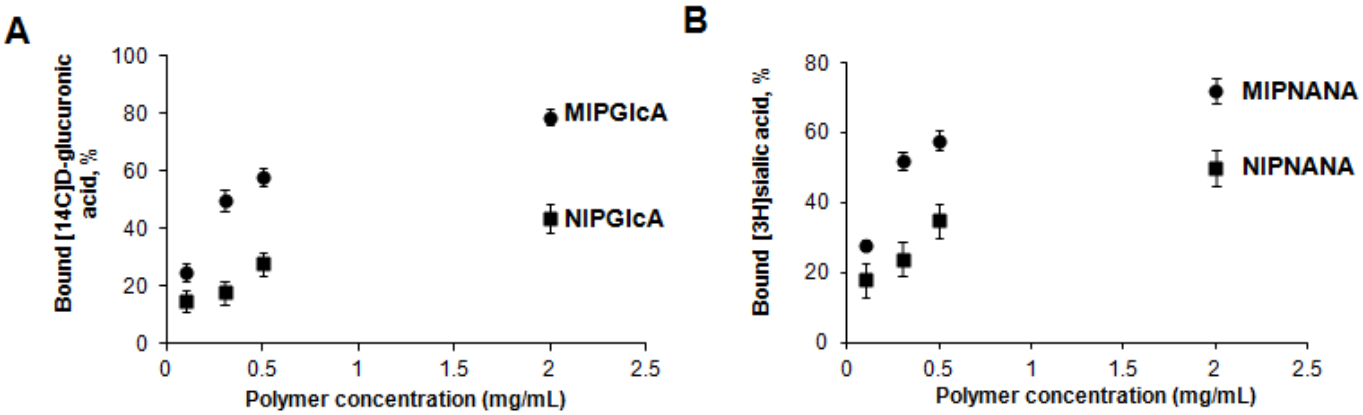

Figure 14 Equilibrium binding isotherms in water of: A) [^{14}C]D-glucuronic to AB-MIPGlcA and B) [^{3}H]sialic acid to AB-MIPNANA.

These particles, in contrast to the ones synthesized in MeOH:water (4:1) exhibited monodispersity with a size of ~400 nm and no aggregation phenomena were observed when applied in cell culture medium (Figure 15A).

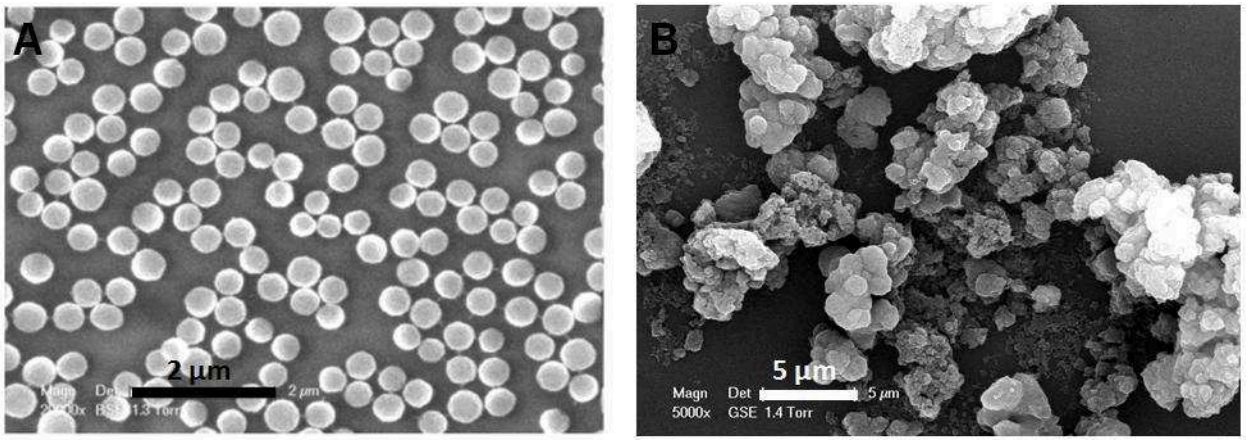

Figure 15 SEM images of: (A) ABMIPGlcA synthesized in DMSO and (B) ABMIPGlcA synthesized in MeOH:water (4:1).

To further evaluate the selectivity of the MIPs synthesized in DMSO, competitive binding assays at equilibrium were performed. A fixed amount of MIPGlcA was incubated with radiolabeled glucuronic acid (225 nM) or MIPNANA was incubated with radiolabeled sialic acid (0.5 nM), in the presence of varying amounts of other sugar molecules present on the glycocalix or structurally related compounds at concentrations between 0.1 nM and 100 µM (Figure 16). The solvent chosen for the competitive binding studies was methanol:water (1:9), which is closer in composition to the one used for cell preparation and fixation before imaging (see Chapter 3). The values of IC_{50} (the concentrations of non-labeled GlcA or NANA required to displace 50% of the radioligand) for MIPGlcA and MIPNANA respectively, determined from a nonlinear regression fit, were 495 nM and 4500 nM. Moreover, the two MIPs exhibited negligible affinity for all of the competitors, and very little cross-reactivity is observed between GlcA and NANA, thus confirming their selectivity for their target (Table 1).

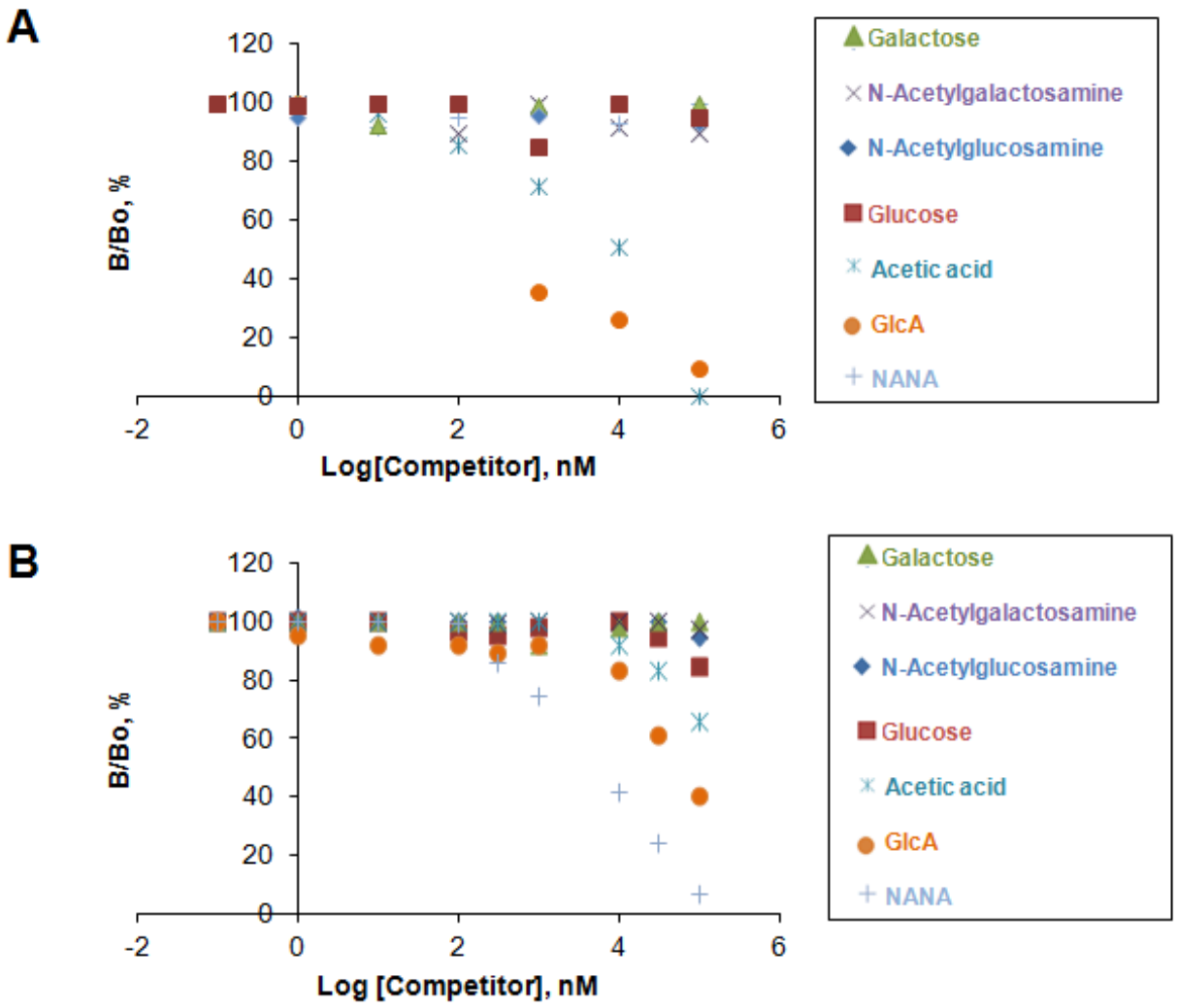

Figure 16 Inhibition of binding radiolabeled glucuronic acid (A) or sialic acid (B) on 0.3 mg/mL of the respective MIPs by competing ligands in methanol:water (1:9). B/B0 is the ratio of the amounts of radioactive glucuronic acid bound in the presence and absence of displacing ligand. Values represent the mean from three independent experiments.

Table 1 Cross-reactivity of the MIPs with various competitors, as determined by the competitive radioligand binding experiments (data from Figure 16).

Competitor	Structure	Cross-reaction MIPGlcA, %	Cross-reaction MIPNANA, %
Glucuronic acid	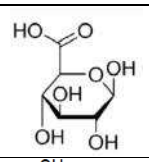	100	9
N-Acetylneuraminic acid	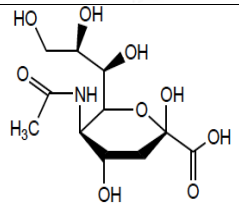	< 1	100
Acetic acid	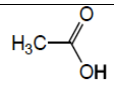	3	4
Glucose	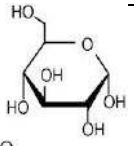	< 1	< 1
N-Acetylglucosamine	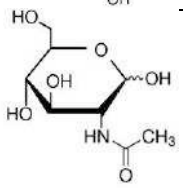	< 1	< 1
Galactose	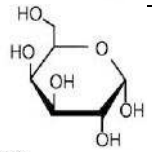	< 1	< 1
N-Acetylgalactosamine	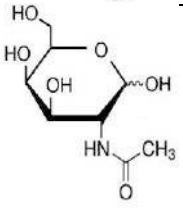	< 1	< 1

Therefore, these MIPs if labeled with fluorescent tags would constitute powerful selective recognition tools for cell labeling and imaging. For this purpose, MIPs were either labeled with the dye rhodamine or with QDs.

Labeling with rhodamine B

Fluorescent dye moieties were incorporated into the polymer matrix by adding a polymerizable rhodamine (λ_{em}=570 nm) derivative to the prepolymerization mixture. Its molar ratio with respect to the other monomers was optimized to maximize the fluorescence intensity of the particles (optimal ratio 1:0.05, AB: rhodamine). Higher dye content resulted in lower brightness due to reabsorption or energy transfer. Particles with diameters of 400 nm, with a good monodispersity were obtained (Figure 17A). This particle size was chosen to avoid possible internalization of the particles, so as to target the extracellular hyaluronan and sialylation sites. The fluorescence intensities of the MIP and NIP particles were determined with a spectrofluorimeter and were found to be similar with less than 10% deviation (Figure 17B), which was taken into account later on for quantification in microscopic images (See Chapter 3). Their binding characteristics were similar to those of unlabeled polymers.

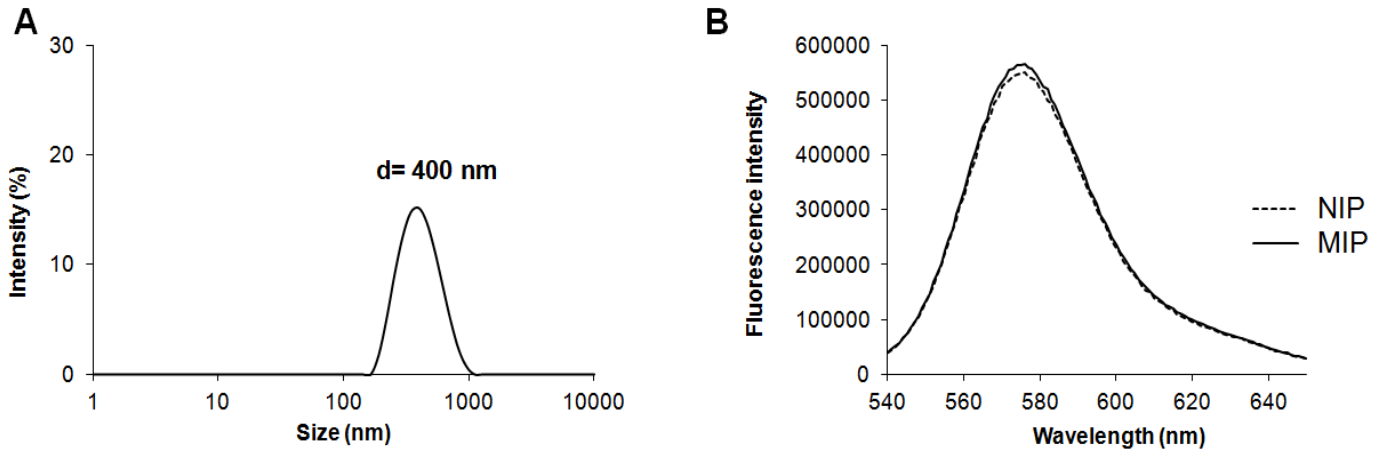

Figure 17 (A) Size distribution of MIPGlcA as measured by dynamic light scattering in water; (B) Fluorescence emission spectra of rhodamine-MIPGlcA and rhodamine-NIPGlcA, λex=540 nm).

Labeling with InP/ZnS QDs

Fluorescent semiconductor nanocrystals, so-called quantum dots (QDs), have unique optical and electronic properties: size-tunable light emission, high signal brightness with reduced photobleaching, long-term photostability, and possible multiplexing due to narrow, symmetric,

and well-resolved emission spectra. They have broad absorption spectra which enable simultaneous excitation of multiple QDs by a common excitation wavelength. QD nanocrystals are generally synthesized in apolar solvents and are hydrophobic. Substantial progress in surface chemistry for rendering them soluble in aqueous media has been the key to their biocompatibility and functionalization for the coupling of specific affinity ligands (antibodies, nucleic acids, peptides). Different QD-solubilization strategies have been devised, including ligand exchange with small monodentate or polydentate thiol-containing molecules and encapsulation by a layer of amphiphilic polymers, polysaccharides, or proteins, silica shells, and phospholipid micelles [46,47].

In this section we propose a novel versatile solubilization and functionalization strategy, which consists of creating a stable and robust hydrophilic cross-linked polymer coating directly on QDs by photopolymerization using the particles as individual internal light sources. This coating strategy was first employed in our group for the functionalization of UCNPs and then further adapted for the coating of QDs [48]. Green- and red-emitting InP/ZnS QDs, hereafter referred to as green-QDs and red-QDs, which are less toxic than cadmium-based QDs, were employed. Emitted fluorescent light from green (550 nm) or red QDs (660 nm), when excited with a UV lamp (365 nm), locally photopolymerizes a thin polymer shell on the surface of the QDs, thus yielding core–shell nanoparticles (Figure 18).

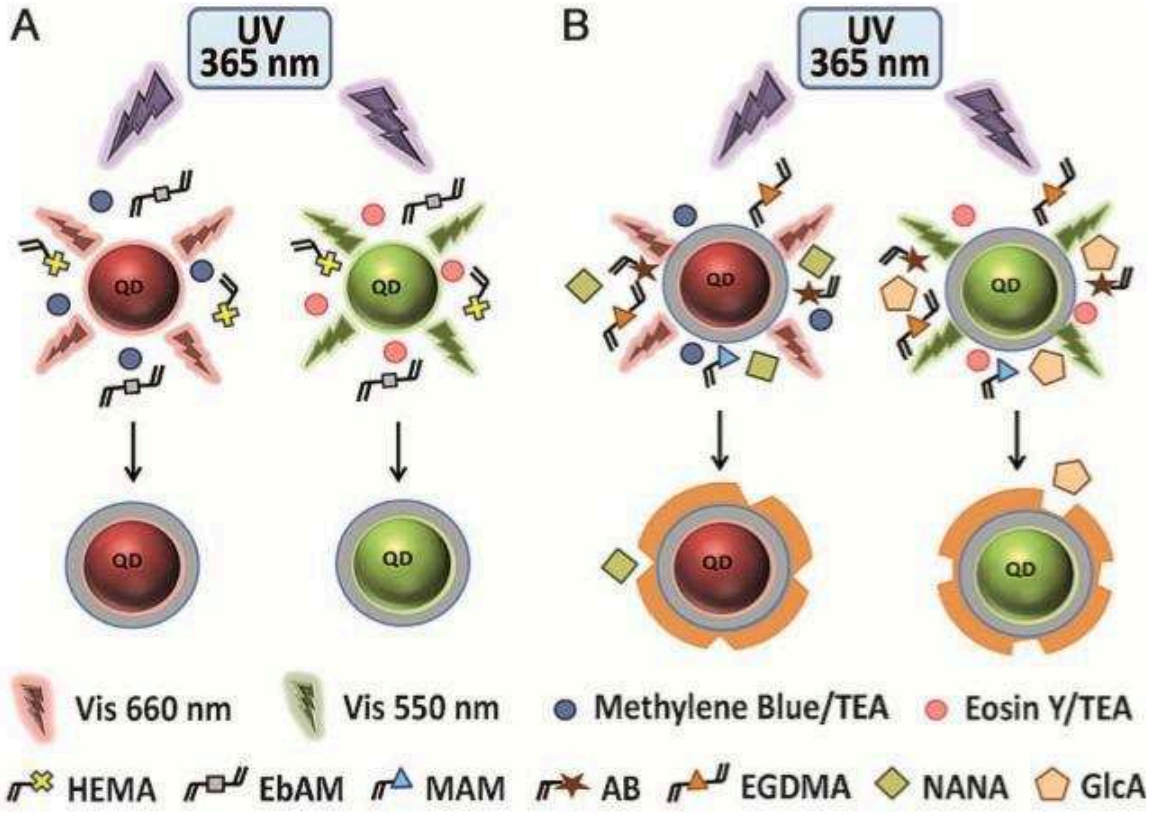

Figure 18 (A) Red or green light emitted from InP/ZnS quantum dots excited by UV irradiation is used to synthesize a polymeric shell in situ around the particles by photopolymerization. Methylene blue/triethylamine (TEA) are used as the initiator system for red-QDs and eosin Y/ TEA for green-QDs. (B) A second shell of MIP is synthesized by reinitiation in the presence of functional and cross-linking monomers and a molecular template (GlcA or NANA).

Since emission from QDs is weak as compared to direct light, polymerization is confined to the QD surface; however, appropriate initiator systems must be used. More precisely, initiator systems comprising of eosin Y/triethylamine (TEA) and methylene blue/TEA were used in the case of the green and the red QDs respectively. The emission wavelength of the QD must overlap with the absorption wavelength of the initiator, and the latter must not be activated by the UV light (Figure 19). Preliminary experiments confirmed that these requirements are met in the systems described.

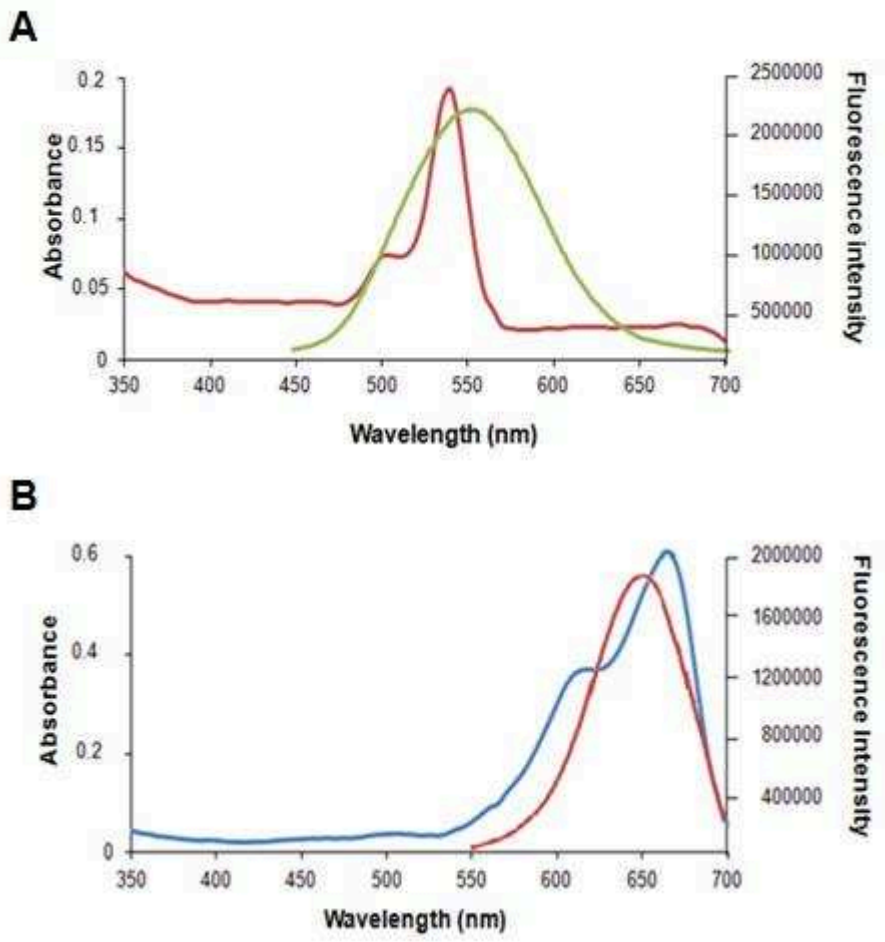

Figure 19 Emission spectra (λex = 365 nm) in DMSO:toluene (1:1) of: A) green-QDs (green) showing an overlapping with the absorbance of eosin Y (red) in the visible region; B) of red-QDs (red) showing an overlapping with the absorbance of methylene blue (blue), in the visible region.

At the same time, we verified that there was no self-initiated polymerization, a phenomenon frequently observed in the presence of numerous monomers and under lower-wavelength UV light [49] (see Chapter 4). For this, polymerization of a mixture of 2-hydroxyethyl methacrylate (HEMA) and N,N'-ethylenebis(acrylamide) (EbAM) was studied with the initiators eosin Y/TEA and methylene blue/TEA, in the presence and the absence of green-QDs or red-QDs respectively, in order to show that the initiator was not activated by the UV light used for QD excitation. The reaction was initiated by UV irradiation and after 2 h, some cloudiness was observed in the vials containing QDs and none in the control vial. To make sure that there were polymers, the content from both vials was sedimented by centrifugation. Where QDs were

present, a polymer sediment was visible whereas in the control vial, no polymerization was observed (Figure 20).

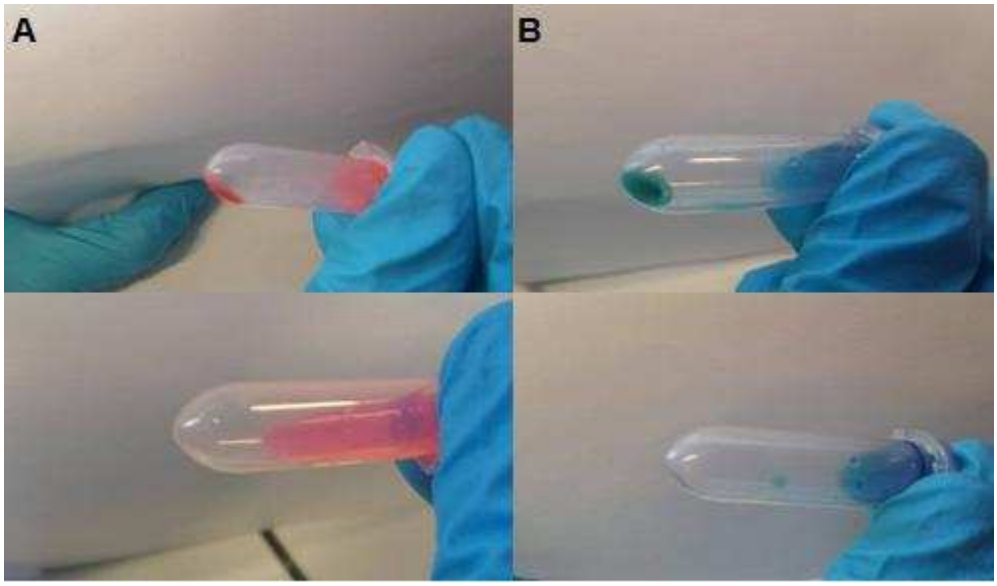

Figure 20 Polymerization of a mixture of HEMA and EbAM in the presence (up) and the absence (down) of green (A) and red (B) QDs after 2 h of UV irradiation.

Additional verification was done by irradiating the above mixture without green- or red-QDs with a 525-nm or a 630-nm LED light source respectively (the wavelength of emission of the QDs) for 2 h, in which case polymer formation was observed.

Coating of green-QDs

A water-compatible shell was synthesized around the green-QDs by using the hydrophilic monomers 2-hydroxyethyl methacrylate (HEMA) and N,N'-ethylenebis(acrylamide) (EbAM), the initiator couple eosin Y/triethylamine (TEA), and green-QDs in toluene:dimethyl sulfoxide (DMSO; 1:1). This shell stabilizes the QDs for their further conjugation in polar solvents. Its presence (HEMA-QDs) was confirmed by transmission electron microscopy (TEM) (Figure 21) and dynamic light scattering (DLS) (Figure 24).

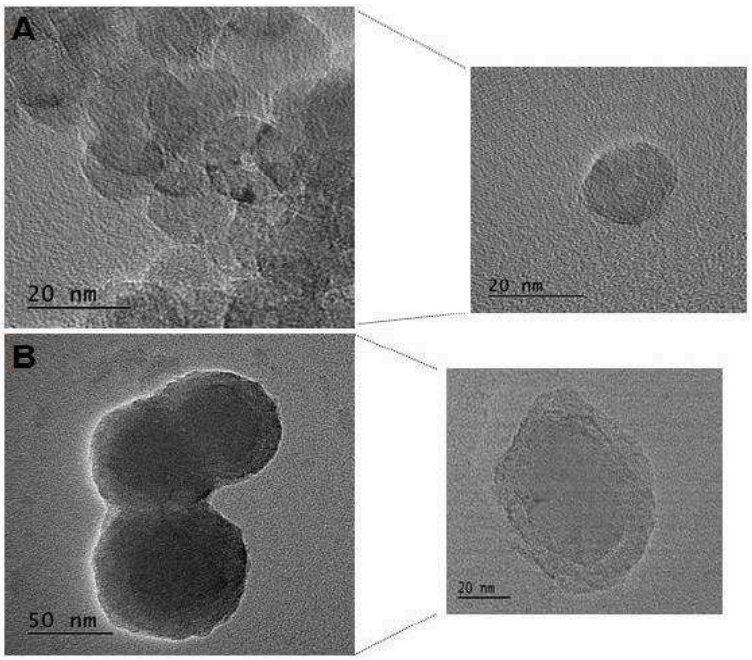

Figure 21 Evidence for the formation of a polymer shell around greenQDs. A) TEM images of bare QDs and B) HEMA-QDs.

Further evidence was provided by another experiment, in which propargyl acrylamide was added to the polymerization mixture described above. The resulting propargyl-functionalized shell was then labeled with azidofluorescein by click chemistry. Fluorescein (λ_{ex}=495 nm) was incorporated, as shown by the emission spectrum of the core–shell particles (Figure 22).

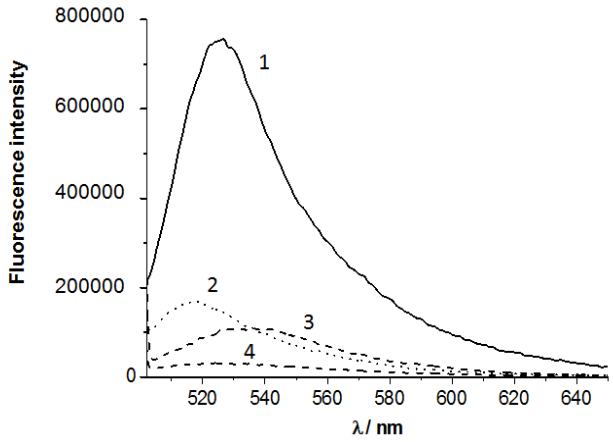

Figure 22 Emission spectra (λex=495 nm) of propargyl-functionalized QDs before (4) and after fluorescein labeling (1). The presence of fluorescein (λem=525 nm) was clearly visible after labeling, whereas in control experiments with bare QDs, no fluorescein was seen before (2) or after labeling (3).

Apart from fluorescence measurements, the presence of the propargyl-shell was verified with TEM, scanning transmission electron microscopy (STEM) images and DLS measurements (Figure 23).

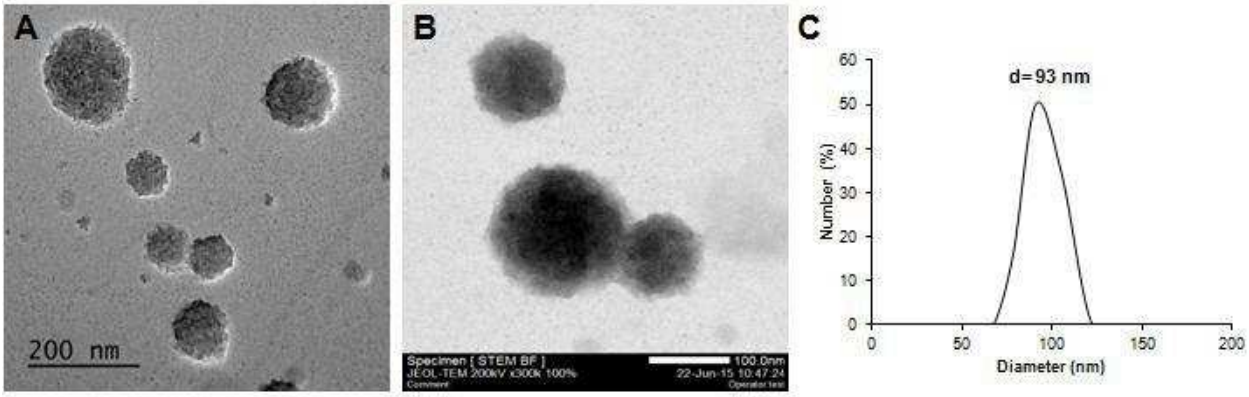

Figure 23 Evidence for the formation of a propargyl-shell around green QDs. A) TEM images B) STEM images and C) DLS measurements.

A MIP was photopolymerized on top of the first HEMA-shell again by using green light emitted by the QDs. The HEMA-QD particles were resuspended in DMSO and the second shell (MIPGlcA-QDs) was obtained by irradiation with UV light using a MIP-precursor mixture containing GlcA, AB, methacrylamide (MAM), ethylene glycol dimethacrylate (EGDMA), and eosin/TEA. MAM was added to provide hydrogen-bonding interactions with GlcA and to render the MIP more hydrophilic to prevent aggregation in the aqueous cell-imaging medium. A control non-imprinted polymer (NIP) was prepared in the same way but without the addition of GlcA. The successful introduction of this second shell was verified after photobleaching by DLS measurements (Figure 24).

The specificity of MIPGlcA-QDs was evaluated by equilibrium binding assays with [^{14}C]D-glucuronic acid in water. MIPGlcA bound more glucuronic acid than NIPGlcA (Figure 25), thus indicating the creation of imprinted sites.

Coating of red-QDs

To prove the versatility of our method for functionalizing QDs, commercially available red-QDs emitting at 660 nm were tested. Methylene blue/TEA was used for initiation to ensure spectral overlap between QD emission and initiator absorption (Figure 19B). A HEMA/EbAM shell was grafted around the QDs, followed by a MIPNANA shell, by the same procedure as described for green-QDs. The polymers were then photobleached to eliminate any methylene blue fluorescence. The increase in size of the QDs after coating was verified by DLS measurements (Figure 24B).

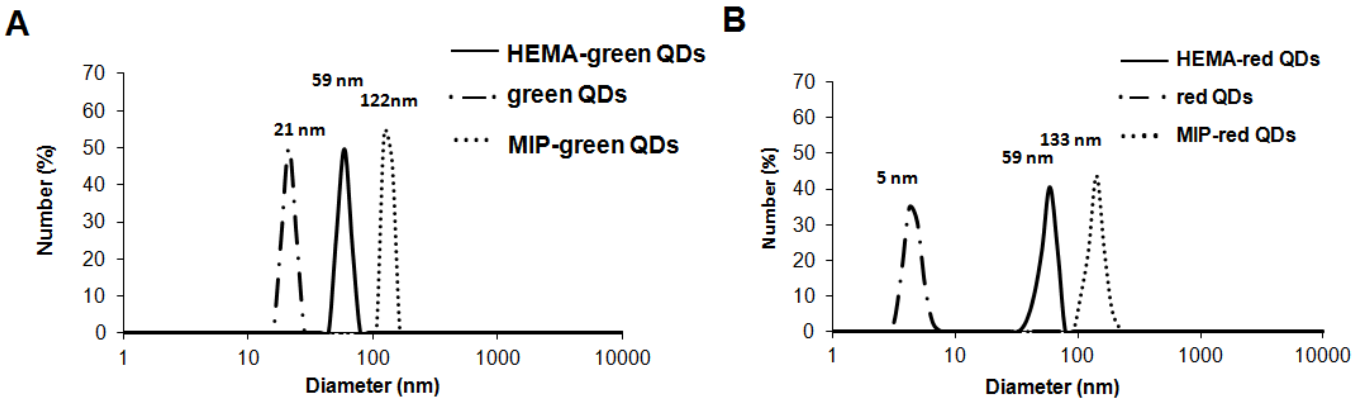

Figure 24 Size distribution as measured by DLS of bare QDs (dotted line), HEMA-QDs (solid line), and MIP-QDs (dashed line) for the coating of (A) green and (B)red QDs.

The specificity of MIPNANA-QDs was evaluated by equilibrium binding assays with [^{3}H]sialic acid in water. MIPNANA bound more sialic acid than NIPNANA (Figure 25), thus indicating the creation of imprinted sites.

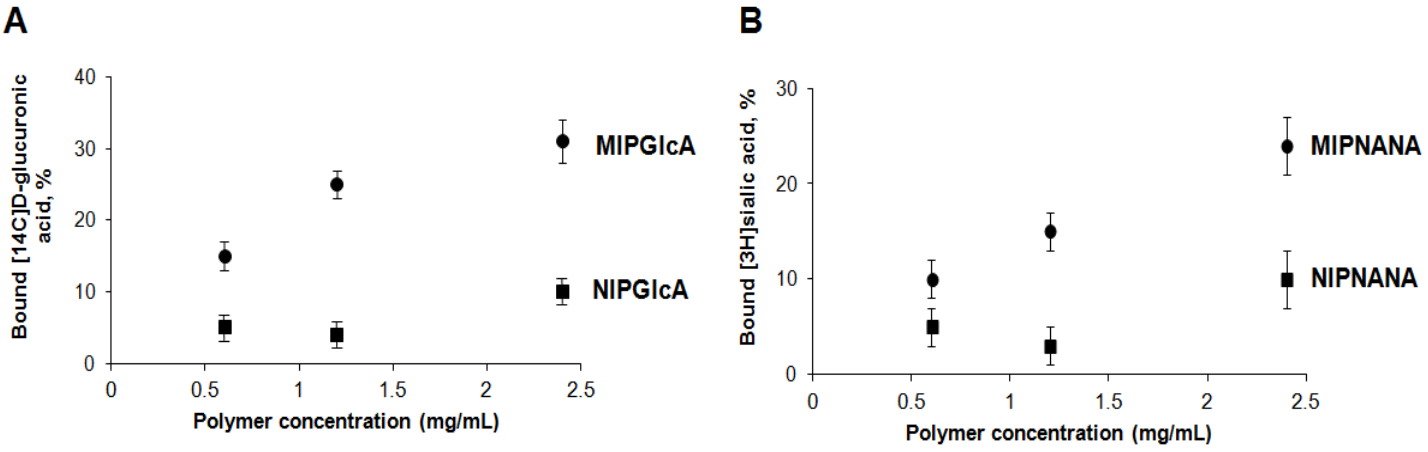

Figure 25 Equilibrium binding isotherms in water of: (A) [^{14}C]D-glucuronic to MIPGlcA-QDs and (B) [^{3}H]sialic acid to MIPNANA-QDs.

2.3 Materials and Methods

2.3.1 Reagents and Materials

All chemicals and solvents were of analytical grade and purchased from Sigma-Aldrich (St-Quentin Fallavier, France) or from VWR International (Fontenay-sous-Bois, France), unless otherwise stated. Anhydrous solvents were used for MIPs synthesis. 2,2'-azobis(2,4-dimethylvaleronitrile) (ABDV) was from DuPont Chemicals (Wilmington, USA). Phenyl-β-D-glucuronic acid monohydrate was from Biosynth. The 1-(4-vinylphenyl)-3-(3,5-bis(trifluoromethyl)phenyl) urea (UREA) monomer was kindly provided by Dr. Hall (Medway School of Pharmacy, UK). D-[6-^{14}C]glucuronic acid (specific activity: 55 mCi/mmole, activity: 0.1 mCi/mL) and [6-^{3}H]sialic acid (specific activity 20 Ci/mmole, activity 0.1 mCi/mL) were from Biotrend Chemikalien GmbH (Koln, Germany). Radioactivity was measured in the presence of scintillation liquid (Ultra Gold, PerkinElmer) with a liquid scintillation counter (Beckman LS-6000 IC). Photobleaching of the initiator dyes trapped inside the polymer particles after polymerization was done by irradiating with a fluorescent tube 18 W (MAZDAFLUOR, UK). Polymer suspensions prepared by ultrasonicating with the microtip of a Branson Sonifier 250. Water was purified using a Milli-Q system (Millipore, Molsheim, France). ^{1}H NMR spectra were recorded on a Bruker 400 MHz spectrometer. Fluorescence measurements were performed

on a FluoroLog-3 spectrofluorimeter (Horiba Jobin Yvon, Longjumeau, France). UV-Vis absorbance was measured on a Cary 60 UV-Vis spectrophotometer (Agilent Technologies). QDs were excited at 365 nm with a UV-lamp (VILBER LOURMAT, 6 W). The LED 525 (120 mW, 240 mA) and the LED 630 (140 mW, 240 mA) used in the study were supplied by ROITHNER LASERTECHNIK. Transmission electron microscopy (TEM) images were captured using a JEOL JEM-2100F. The TEM grid was a 300 mesh carbon-coated copper grid from AGAR Scientific (Stansted, U.K.). Dynamic light scattering (DLS) analysis was performed on a Zeta-sizer NanoZS (Malvern Instruments Ltd., Worcestershire, UK) at 25 °C.

2.3.2 Preparation of UREA-MIPGlcA

0.125 mmol of the template phenyl-β-D-glucuronic acid monohydrate (Figure 5) were weighed in a 20 mL glass vial and incubated with 0.5 mmol of triethylamine (TEA) in 10 mL of acetonitrile: dimethylsulfoxide (4:1) for 30 min. Subsequently 0.125 mmol of the functional monomer 1-(4-vinylphenyl)-3-(3,5-bis(trifluoromethyl)phenyl) urea (UREA), 2.5 mmol ethylene glycol dimethacrylate (EGDMA) and 0.026 mmol ABDV were added. The vials were sealed with an airtight septum and the mixture was purged with nitrogen for 10 min under ice. The polymerization was thermally initiated at 48 °C for 18 h. As a control, non-imprinted polymers were synthesized in the same way but in the absence of the template molecule. The polymer particles were transferred to 50 mL polypropylene centrifuge tubes and washed on a tube rotator (SB2, Stuart Scientific), 3 times with methanol: acetic acid (9:1) followed by 3 times with a methanol:0.1 M NH_4OH mixture, twice with water and twice with methanol. The particles were dried overnight under vacuum.

Equilibrium binding assays of UREA-MIPGlcA

The binding properties of the UREA polymers towards GlcA in a mixture of ACN+1% TEA were evaluated by equilibrium binding experiments. MIPs and NIPs in a polymer concentration of 30 mg/mL were suspended in ACN+1% TEA in a sonicating bath. From this stock suspension, increasing amounts of polymer particles were pipetted in separate 2-mL polypropylene microcentrifuge tubes. After addition of 100 µL radiolabeled glucuronic acid (225

pmol, 12 nCi) the final volume was adjusted to 1 mL with ACN+1% TEA and the mixture was incubated overnight on a tube rotator. The samples were centrifuged at 30,000 *g* for 15 min and a 500 µL aliquot of the supernatant was pipetted into a scintillation vial that contained 4 mL of scintillation liquid. The amount of free radioligand was measured with a liquid scintillation counter and the amount of radiolabeled analyte bound to the polymer particles was calculated by subtracting the amount of the unbound analyte from the total amount of the analyte added to the mixture.

Effect of water addition on the binding properties of UREAMIP-GlcA

The binding properties of the UREAMIP towards the fluorescent analogue of GlcA, MUG (Figure 5) in a mixture of ACN+1% TEA containing different amounts of water were evaluated by fluorescence measurements. A fixed polymer concentration of 10 mg/mL in ACN+1% TEA and a final MUG concentration of 5 µM MUG were incubated overnight in ACN+1% TEA containing concentrations of water ranging from 0% up to 90%. The samples were subsequently centrifuged at 30,000 *g* for 15 min and a 500 µL aliquot of the supernatant was transferred in a glass cuvette. Fluorescence measurements were performed and the amount of the MUG bound was calculated by subtracting the amount of the unbound analyte from the total amount of the analyte added to the mixture.

2.3.3 Synthesis of 4-acrylamidophenyl)(amino)methaniminium acetate (AB)

4-acrylamidophenyl)(amino)methaniminium chloride was first synthesized. 34 g (0.25 mol) of sodium acetate trihydrate was dissolved in 200 mL of water and 2 g (9.6 mmol) of 4-aminobenzamidine dihydrochloride was added. The solution was cooled to < 5 °C in an ice bath and 4 mL (49 mmol) of acryloyl chloride was added dropwise. The reaction was left to proceed for 1 h. The pH was then adjusted to 4.0 with hydrochloric acid (37%) and precipitation was observed. After filtration, the precipitate was redissolved in 100 mL of water at 40 °C. Hydrochloric acid was again added this time to pH 1.0 and the product was left overnight to crystallize at 4 ^{o}C. The crystals were collected by filtration and dried in an oven maintained at 50 °C. The yield of 4-acrylamidophenyl)(amino)methaniminium chloride was 60%. ^{1}H NMR (400

MHz, DMSO-d_6): 10.56 (s, 1H), 8.99 (s, 4H), 7.84 (d, 2H), 7.81 (d, 2H), 6.48 (d, 1H), 6.31 (dd, 1H), 5.82 (s, 1H). 4-acrylamidophenyl)(amino)methaniminium chloride was then converted to 4-acrylamidophenyl)(amino)methaniminium acetate as the acetate ion is more readily exchangable with the template's carboxylate. Therefore 1.0 g of 4-acrylamidophenyl)(amino)methaniminium chloride was suspended in 100 mL of saturated sodium acetate solution and stirred overnight. The product was collected by filtration, washed with water to eliminate residual sodium acetate and dried at 50 °C. The yield of 4-acrylamidophenyl)(amino)methaniminium acetate, which we term AB in the text, was 60 %. ^{1}H NMR (400 MHz, DMSO-d_6):10.56 (broad s, 5H), 7.84 (d, 2H), 7.78 (d, 2H), 6.48 (dd, 1H), 6.31 (dd, 1H), 5.82 (dd, 1H), 1.70 (s, 3H).

2.3.4 ^{1}H NMR studies

Interaction between AB and the templates GlcA and NANA

The assignment of GlcA, NANA and AB resonances was deduced from ^{1}H – ^{13}C HSQC (Heteronuclear Single Quantum Correlation) and ^{1}H – ^{1}H COSY (Correlation Spectroscopy) spectra (see ANNEX 2, Figures 2-5). The stoichiometry and the strength of the interaction between the templates and AB were determined by chemical shift analysis using the method of continuous variation (Job plot) and titration. In all experiments, the free and the template-bound monomer forms are in fast exchange on the NMR timescale in the sense that a single (weighted) averaged chemical shift is observed. For the Job plot, solutions of the templates and AB, at a constant concentration of 10 mM were prepared with the template mole fraction, $\chi_T = \frac{[T]}{\{T\}+[M]}$, varying from 0 to 1 by steps of 0.1. The total volume of each sample was 700 µL. Association constants were determined by titrating an increasing amount of AB into a constant amount of the templates GlcA and NANA. Stock solutions of 40 mM AB were prepared and added (from 0 to 2 equivalents) to a fixed 10 mM concentration of template. For all the data presented in this work (Job and titration experiments), the non-linear regression analysis was done using a home-written Mathematica program.

2.3.5 Preparation of ABMIPs

0.022 mmol of GlcA (or 0.022 mmol of NANA) and 0.022 mmol of the functional monomer (4-acrylamidophenyl)(amino)methaniminium acetate (AB), were incubated for 1 h in 1 mL DMSO. This mixture was then transferred to a 4 mL glass vial containing 0.066 mmol methacrylamide (MAM), 0.423 mmol EGDMA, 0.0055 mmol ABDV (stock solution of 3.4 mg ABDV in 1300 µL DMSO from which 524 µL was pipetted into the vial) and 270 µL DMSO. The vials were sealed with an airtight septum and the mixture was purged with nitrogen for 5 min under ice. The polymerization was thermally initiated at 48 °C for 18 h. As a control, non-imprinted polymers were synthesized in the same way but in the absence of the template molecule. The polymer particles were transferred to 50 mL polypropylene centrifuge tubes and washed on a tube rotator (SB2, Stuart Scientific), 3 times with methanol: acetic acid (9:1) followed by 3 times with a (7:3) mixture of 100 mM NH_3 (in water): methanol, twice with water and 3 times with methanol. The particles were dried overnight under vacuum.

Rhodamine-labeled MIPs were prepared as described above by additionally incorporating polymerizable rhodamine B (PolyFluor 570) at a ratio 0.05:1 (rhodamine B: AB), to the polymerization mixture. ABMIPs were also prepared using a mixture of methanol:water (4:1) as porogen by applying exactly the same amounts and methods described in the aforementioned polymerization protocol.

Equilibrium binding assays of ABMIPs

The binding properties of the AB polymers towards GlcA and NANA in water were evaluated by equilibrium binding experiments. MIPs and NIPs synthesized in DMSO were suspended in water in a sonicating bath in a polymer concentration of 5 mg/mL. From this stock suspension, increasing amounts of polymer particles were pipetted in separate 2-mL polypropylene microcentrifuge tubes. After addition of either radiolabeled glucuronic acid (225 pmol, 12 nCi) or sialic acid (500 fmol, 10 nCi), the final volume was adjusted to 1 mL with water and the mixture was incubated overnight on a tube rotator. The samples were centrifuged at 30,000g for 15 min and a 500 mL aliquot of the supernatant was pipetted into a scintillation vial that

contained 4 mL of scintillation liquid. The amount of free radioligand was measured with a liquid scintillation counter and the amount of radiolabeled analyte bound to the polymer particles was calculated by subtracting the amount of the unbound analyte from the total amount of the analyte added to the mixture.

For the MIPs and NIPs synthesized in the mixture of methanol:water (4:1), higher concentrations of polymer were used and a polymer stock suspension of 15 mg/mL was prepared. The binding properties of these MIPs were evaluated in a similar way as described above for the polymers synthesized in DMSO.

Competitive binding assays

For selectivity studies, monosaccharides on the glycocalix or molecules having similar structures to the analytes GlcA and NANA were added to the equilibrium binding assays to compete with the radioactive analytes. Competitive binding assays were performed on non-labeled MIP-GlcA and MIP-NANA synthesized in DMSO in a similar way to the binding studies described above but in methanol: water (1:9). Stock solutions of GlcA, NANA, acetic acid, glucose, N-acetylglucosamine, galactose and N-acetylgalactosamine (2 mM) were prepared in water. The competitors were added at concentrations ranging from 0.1 nM to 100 µM, in order to compete with 0.5 nM [6-^{3}H]sialic acid or 0.225 µM D- [6-^{14}C]glucuronic acid in the binding assays, with a constant amount of 0.3 mg of MIP per vial.

2.3.6 Experiments with green-QDs

Synthesis of green-QDs

Indium chloride (0.1 mmol), stearic acid (0.1 mmol), hexadecylamine (0.2 mmol) and zinc undecylenate (0.1 mmol) were added to 1-octadecene (2 mL). The mixture was repeatedly evacuated and refilled with nitrogen to provide a water-free and oxygen-free reaction atmosphere, then heated to 270 °C with stirring. On reaching 270 °C, 1 mL of 0.1 M tris(trimethylsilyl) phosphine in 1-octadecene was rapidly injected. The mixture was held at 240

°C for 20 min, then cooled to room temperature. The flask was opened and zinc diethyldithiocarbamate (0.2 mmol) and zinc undecylenate (0.2 mmol) were added. The mixture was re-evacuated and placed under nitrogen, then heated to 180 °C for 10 min and 240 °C for 20 min. The reaction was cooled to room temperature, then 4 mL toluene added and the solution centrifuged at 2200 *g* for 5 min. The clear QD solution was poured off and ethanol added until the QDs precipitated. The mixture was centrifuged at 2200 *g* for 15 min. The supernatant was removed and the QDs were resuspended in toluene. Precipitation with ethanol was repeated 3 times to ensure the removal of synthetic residues. Finally the QDs were resuspended in toluene and stored at 4 °C in the dark until use.

Verification that polymerization is initiated by the emitted visible light from the QDs and not by UV light

Polymerization of a mixture of 2-hydroxyethyl methacrylate (HEMA) and N,N'-ethylenebis(acrylamide) (EbAM) was studied with the initiator eosin Y (see mechanism below), in the presence and the absence of green-QDs, in order to show that the initiator was not activated by the UV light used for QD excitation. In a 4 mL glass vial containing 16.4 mg (0.097 mmol) of EbAM, 26.5 µL (0.22 mmol) of HEMA and 100 µg green-QDs (100 µL from a 1 mg/mL solution diluted from a stock (5 mg/mL) in toluene), were added 300 µL DMSO:toluene (1:1), 20 µL of eosin Y (10 mM in DMSO:toluene (1:1)) and 10 µL of TEA (72 mM in DMSO:toluene (1:1)). The vial was sealed with an air-tight septum and the mixture was purged with nitrogen for 2 min. A control vial was prepared in the same way but without the addition of QDs. The reaction was initiated by irradiation at 365 nm with a UV lamp placed at ~2 cm from the vials. After 2 h of reaction, some cloudiness was observed in the vial containing QDs and none in the control vial. To make sure that there were polymers, the content from both vials was transferred to 2 mL polypropylene microcentrifuge tubes and the contents were sedimented by centrifugation for 15 min at 17500 *g*. Where QDs were present, a polymer sediment was visible whereas in the control vial, no polymerization was observed.

Additional verification was done by irradiating the above mixture without QDs with a 525-nm LED light source (the wavelength of emission of the QDs) for 2 h. Polymer particles were now formed that could be sedimented by centrifugation. These results not only indicate that the

polymerization is initiated by the fluorescence light and not by the UV light, but also that at this UV wavelength no self-initiated polymerization occurs, a phenomenon frequently observed in the presence of numerous monomers and under lower-wavelength UV light [49].

Mechanism of photoinitiation by dyes

Photoinitiation by eosin Y or methylene blue-triethylamine (TEA).

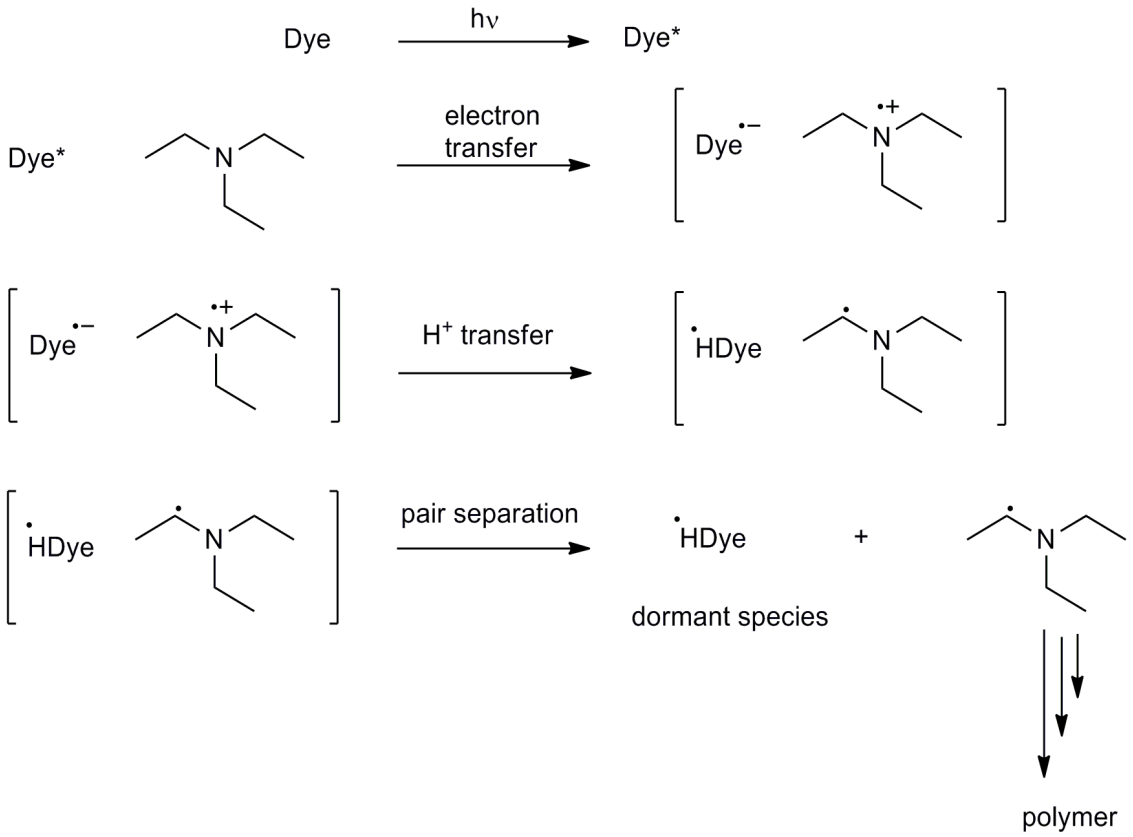

Synthesis of HEMA-QDs

In a 4 mL glass vial containing 16.4 mg (0.097 mmol) of EbAM, 26.5 µL (0.22 mmol) of HEMA and 100 µg green-QDs (100 µL from a 1 mg/mL solution diluted from a stock (5 mg/mL) in toluene), were added 300 µL DMSO:toluene (1:1), 20 µL of eosin Y (10 mM in DMSO:toluene (1:1)) and 10 µL of TEA (72 mM in DMSO:toluene (1:1)). The vial was sealed with an air-tight septum and the mixture was purged with nitrogen for 2 min. Polymerization was initiated by

irradiation at 365 nm with a UV lamp placed at ~2 cm from the vials. After 2 h of reaction, the content was transferred to 2 mL polypropylene microcentrifuge tubes. Subsequently, 500 µL of DMSO:toluene (1:1) was added and the HEMA-QD particles were ultrasonicated, then sedimented by centrifugation for 15 min at 17,500 *g*. The particles were washed 4 times with 800 µL DMSO:toluene (1:1) and twice with water. Eosin Y trapped inside the particles was photobleached overnight with a fluorescent tube. Finally, the nanoparticles were dried overnight under vacuum.

Synthesis of propargyl acrylamide (PA)-QDs

PA-QDs were prepared in the same way as described for HEMA-QDs except that the polymerization mixture contained additionally 23.8 mg (0.219 mmol) PA, synthesized as described below.

Synthesis of propargyl acrylamide

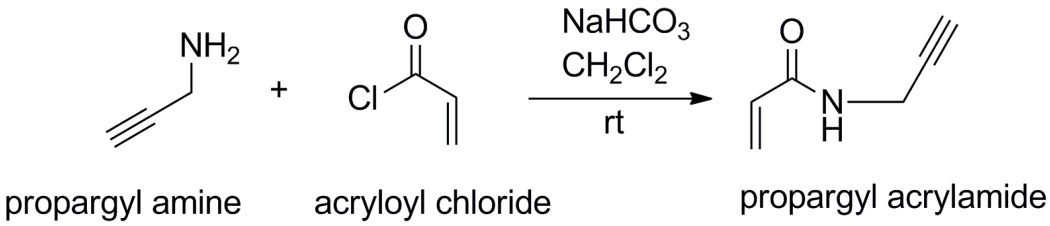

1.83 mL (28.57 mmol) of propargylamine and 2.4 g (28.57 mmol) of sodium bicarbonate were dispersed in 12.5 mL of anhydrous dichloromethane and cooled down to 0 °C. 2.31 mL (28.57 mmol) acryloyl chloride in 7 mL anhydrous dichloromethane was then added dropwise under vigorous stirring. The reaction was left overnight at room temperature (rt) with vigorous stirring, after which the mixture was washed twice with brine and water and dried over magnesium sulphate. The solvent was removed under vacuum and the resulting oily product was purified by column chromatography on silica with n-hexane/ethyl acetate (1:2) elution system. ^{1}H NMR (400 MHz, $CDCl_3$): δ (ppm) = 6.25 (m, 3H), 4.11 (d, 2H,), 2.23 (s, 1H).

Fluorescence labeling of PA-QDs with FITC-N_3

PA-QDs were ultrasonicated for 1 min to give a well dispersed solution. 25 µL of FITC-N_3 (see synthesis below), 440 µL of water, 10 µL of 100 mM $CuSO_4.5H_2O$ and 50 µL of 100 mM sodium ascorbate were then added. The mixture was stirred in the dark for 24 h at room temperature. The nanoparticles were collected by centrifugation (15 min, 17500 *g*), washed repeatedly with acetonitrile:water (1:1) until no fluorescein was detected in the supernatant, monitored by fluorescence spectroscopy of FITC. The particles were dispersed in 1 mL water. The fluorescence spectra before and after click conjugation were recorded.

Synthesis of FITC-N_3

FITC-N_3 was prepared by reacting FITC isomer I with an excess of 11-azido-3,6,9-trioxaundecan-1-amine. Briefly, FITC isomer I (10 mg, 0.0256 mmol) and 11-azido-3,6,9-trioxaundecan-1-amine (92 µL, 0.46 mmol) were dissolved in 108 µL of DMSO in a glass vial. The mixture was stirred at room temperature in the dark for 24 h, before it was diluted in 1.9 mL of acetonitrile:water (1:1) to give a stock solution of FITC-N_3.

Synthesis of MIPGlcA-QDs

5.46 mg (0.022 mmol) of AB (see synthesis above) and 4.27 mg (0.022 mmol) glucuronic acid (GlcA) were incubated for 1 h in 1 mL DMSO. Following the pre-incubation step, the contents of the vial were transferred to a 4 mL glass vial containing HEMA-QDs. Subsequently, 80 µL (0.423 mmol) of EGDMA, 5.62 mg (0.066 mmol) MAM, 20 µL of eosin Y (10 mM) and 10 µL of TEA (72 mM) were added. The same procedure was followed in the absence of the template, for the synthesis of the NIP. The vials were sealed with an air-tight septum and the mixture was purged with nitrogen for 2 min. The polymerization was initiated by irradiation at 365 nm with a UV lamp. After 2 h of reaction, the content was transferred to 2 mL polypropylene microcentrifuge tubes and the particles were washed 3 times with methanol:acetic acid (9:1) followed by 3 times with 100 mM NH_3:methanol (7:3), twice with water and 3 times with

methanol. Eosin Y trapped inside the particles was photobleached overnight with a fluorescent tube. The particles were dried overnight under vacuum.

Equilibrium binding assay of MIPGlcA-QDs

MIPGlcA-QDs particles (4,8 mg/mL) were suspended in water in a sonicating bath. From this stock suspension, increasing amounts of polymer particles ranging from 0.6-2.4 mg/mL were pipetted in separate 2-mL polypropylene microcentrifuge tubes. After addition of radiolabeled glucuronic acid (225 pmol, 12 nCi), the final volume was adjusted to 1 mL with water and the mixture was incubated overnight on a tube rotator. The samples were centrifuged at 30,000 *g* for 15 min and a 500 µL aliquot of the supernatant was pipetted into a scintillation vial that contained 4 mL of scintillation liquid (Ultra Gold, PerkinElmer). The amount of free radioligand was measured with a liquid scintillation counter and the amount of radiolabeled analyte bound to the particles was calculated by subtracting the amount of the unbound analyte from the total amount of the analyte added to the mixture, determined from zero-polymer blanks.

2.3.7 Experiments with red-QDs

Verification that polymerization is initiated by the emitted visible light from the QDs and not by UV light

The same procedure as described for green-QDs was adopted except that methylene blue instead of eosin Y and a 630-nm LED light source were employed.

Synthesis of HEMA-QDs and MIPNANA-QDs

For red HEMA-QDs, the same procedure was adopted as described above for the green-QDs except that methylene blue was used instead of eosin Y.
MIPNANA-QDs were synthesized as described for MIPGlcA-QDs except that GlcA was substituted by NANA and eosin Y by methylene blue.

Equilibrium binding assay of MIPNANA-QDs

A similar procedure as described above for the assay of MIPGlcA-QDs was employed except that radiolabeled sialic acid (500 fmol, 10 nCi) was used instead of radiolabeled glucuronic acid (225 pmol, 12 nCi), giving similar CPM (counts per min) values in the assays.

2.4 Conclusions

Molecularly imprinted polymers (MIPs) have been gaining all the more popularity in the field of biochemical analytics with applications in chromatography, solid-phase extraction, catalysis and sensing. One drawback in comparison to their natural counterparts is the inherent water incompatibility of the MIPs prepared by the conventional methods. In order to address this issue, two stoichiometric monomers, UREA and AB, whicn can form strong stoichiometric interactions with –COOH groups, were used with the ultimate goal of targeting glycosylation sites present on and in the cells. Since imprinting of polysaccharides poses difficulties such as the need of purification or the low abundance and high cost of the templates and the generation of large imprinted sites which may be seen as general nanopores able to bind a range of irrelevant smaller molecules resulting in lower selectivities, we opted for the "epitope" approach by using the monosaccharides GlcA and NANA as the imprinting templates. Although the UREAMIPs had high binding capacity when used in ACN, specific recognition in water was not achieved and the particles showed high aggregation. On the contrary, MIPs using AB as functional monomer demonstrated high specificity and selectivity in aqueous environments. Two ABMIPs were synthesized using MAM as comonomer and EGDMA as cross-linker in a mixture of methanol:water or in DMSO. The latter resulted in monodispersed particles of ~400 nm size, characteristics desirable for targeted cell imaging of the glycocalix. The polymers were further labeled either with an organic dye (Rhodamine B) or with QDs, in order to be used as specific targeting ligands for fluorescent cell imaging. For the coating of the QDs, a novel versatile solubilization and functionalization strategy was proposed, which consists of creating polymer shells directly on QDs by photopolymerization using the particles as individual internal light sources. Green- and red-emitting InP/ZnS QDs were employed forming successfully a HEMA shell and on top a MIP shell for GlcA and NANA respectively. The obtained ~120 nm-particles

could serve as intracellular imaging agents. Biolabeling and bioimaging of human skin cells and tisssues with fluorescent MIPs will be described in Chapter 3.

2.5 References

[1] M. Kempe, K. Mosbach, *J. Chromatogr. A* **1995**, *694*, 3–13.

[2] B. Tse Sum Bui, K. Haupt, *Anal. Bioanal. Chem.* **2010**, *398*, 2481–2492.

[3] G. Wulff, *Chem. Rev.* **2002**, *102*, 1–28.

[4] Y. Fuchs, O. Soppera, K. Haupt, *Anal. Chim. Acta* **2012**, *717*, 7–20.

[5] R. Arshady, K. Mosbach, *Macromol. Chem. Phys.* **1981**, *182*, 687–692.

[6] G. Wulff, A. Sarhan, *Angew. Chemie Int. Ed.* **1972**, *11*, 341–344.

[7] M. J. Whitcombe, M. E. Rodriguez, P. Villar, E. N. Vulfson, *J. Am. Chem. Soc.* **1995**, *117*, 7105–7111.

[8] H. Zhang, *Polymer (Guildf).* **2014**, *55*, 699–714.

[9] L. I. Andersson, *Anal. Chem.* **1996**, *68*, 111–117.

[10] H. Bengtsson, U. Roos, L. I. Andersson, *Anal. Commun.* **1997**, *34*, 233–235.

[11] K. Haupt, A. Dzgoev, K. Mosbach, *Anal. Chem.* **1998**, *70*, 628–631.

[12] H. Sun, F. Qiao, *J. Chromatogr. A* **2008**, *1212*, 1–9.

[13] G. Wulff, K. Knorr, *Bioseparation* **2001**, *10*, 257–76.

[14] H. Zhang, W. Verboom, D. N. Reinhoudt, *Tetrahedron Lett.* **2001**, *42*, 4413–4416.

[15] A. J. Hall, P. Manesiotis, M. Emgenbroich, M. Quaglia, E. De Lorenzi, B. Sellergren, *J. Org. Chem.* **2005**, *70*, 1732–1736.

[16] C. Lubke, M. Lubke, M. J. Whitcombe, E. N. Vulfson, *Macromolecules* **2000**, *33*, 5098–5105.

[17] S. A. Piletsky, H. S. Andersson, I. A. Nicholls, *J. Mol. Recognit.* **1998**, *11*, 94–7.

[18] S.-H. Song, K. Shirasaka, Y. Hirokawa, H. Asanuma, T. Wada, J. Sumaoka, M. Komiyama, *Supramol. Chem.* **2010**, *22*, 149–155.

[19] T. Hishiya, M. Shibata, M. Kakazu, H. Asanuma, M. Komiyama, *Macromolecules* **1999**, *32*, 2265–2269.

[20] B. R. Hart, K. J. Shea, *J. Am. Chem. Soc.* **2001**, *123*, 2072–2073.

[21] P. Manesiotis, C. Borrelli, C. S. A. Aureliano, C. Svensson, B. Sellergren, C. Alexander, H. S. Andersson, L. I. Andersson, R. J. Ansell, N. Kirsch, et al., *J. Mater. Chem.* **2009**, *19*, 6185.

[22] S. Beyazit, B. Tse Sum Bui, K. Haupt, C. Gonzato, *Prog. Polym. Sci.* **2016**, DOI 10.1016/j.progpolymsci.2016.04.001.

[23] G. Wulff, A. Biffis, *Molecular Imprinting with Covalent or Stoichiometric Non-Covalent Interactions. In Molecularly Imprinted Polymers. Man-Made Mimics of Antibodies and Their Applications in Analytical Chemistry*, Elsevier, **2000**.

[24] G. Wulff, R. Schönfeld, *Adv. Mater.* **1998**, *10*, 957–959.

[25] G. Wulff, T. Gross, R. Schonfeld, *Angew. Chemie - Int. Ed.* **1997**, *36*, 1961–1964.

[26] A. G. Strikovsky, D. Kasper, M. Grün, B. S. Green, J. Hradil, G. Wulff, *J. Am. Chem. Soc.* **2000**, *122*, 6295–6296.

[27] B. Sellergren, *Anal. Chem.* **1994**, *66*, 1578–1582.

[28] K. Haupt, A. V Linares, M. Bompart, B. T. S. Bui, *Top. Curr. Chem.* **2012**, *325*, 1–28.

[29] J. L. Urraca, M. C. Moreno-Bondi, A. J. Hall, B. Sellergren, *Anal. Chem.* **2007**, *79*, 695–701.

[30] S. Shinde, Z. El-Schich, A. Malakpour, W. Wan, N. Dizeyi, R. Mohammadi, K. Rurack, A. Gjörloff Wingren, B. Sellergren, *J. Am. Chem. Soc.* **2015**, *137*, 13908–12.

[31] S. Wang, D. Yin, W. Wang, X. Shen, J.-J. Zhu, H.-Y. Chen, Z. Liu, P. Chakravarty, E. O. Serebrovskaya, M. Ogawa, et al., *Sci. Rep.* **2016**, *6*, 22757.

[32] D. Yin, S. Wang, Y. He, J. Liu, M. Zhou, J. Ouyang, B. Liu, H.-Y. Chen, Z. Liu, S. Nie, et al., *Chem. Commun.* **2015**, *51*, 17696–17699.

[33] Z. El-Schich, M. Abdullah, S. Shinde, N. Dizeyi, A. Rosén, B. Sellergren, A. G. Wingren, *Tumour Biol.* **2016**, DOI 10.1007/s13277-016-5280-y.

[34] A. Kugimiya, J. Matsui, T. Takeuchi, *Mater. Sci. Eng. C* **1997**, *4*, 263–266.

[35] A. Kugimiya, H. Yoneyama, T. Takeuchi, *Electroanalysis* **2000**, *12*, 1322–1326.

[36] A. M. Bossi, P. S. Sharma, L. Montana, G. Zoccatelli, O. Laub, R. Levi, *Anal. Chem.* **2012**, *84*, 4036–4041.

[37] A. Rachkov, N. Minoura, *Biochim. Biophys. Acta* **2001**, *1544*, 255–66.

[38] S. Ambrosini, M. Serra, S. Shinde, B. Sellergren, E. De Lorenzi, *J. Chromatogr. A* **2011**, *1218*, 6961–9.

[39] E. Benito-Peña, J. L. Urraca, B. Sellergren, M. C. Moreno-Bondi, *J. Chromatogr. A* **2008**, *1208*, 62–70.

[40] J. L. Urraca, A. J. Hall, M. C. Moreno-Bondi, B. Sellergren, *Angew. Chemie - Int. Ed.* **2006**, *45*, 5158–5161.

[41] B. Li, J. Xu, A. J. Hall, K. Haupt, B. Tse Sum Bui, *J. Mol. Recognit.* **2014**, *27*, 559–65.

[42] S. Nestora, F. Merlier, S. Beyazit, E. Prost, L. Duma, B. Baril, A. Greaves, K. Haupt, B. Tse Sum Bui, *Angew. Chemie - Int. Ed.* **2016**, *55*, 6252–6256.

[43] J. S. Renny, L. L. Tomasevich, E. H. Tallmadge, D. B. Collum, *Angew. Chemie - Int. Ed.* **2013**, *52*, 11998–12013.

[44] P. Thordarson, J.-M. Lehn, D. J. Cram, C. J. Pedersen, C. J. Pedersen, R. M. Izatt, J. H. Rytting, D. P. Nelson, B. L. Haymore, J. J. Christensen, et al., *Chem. Soc. Rev.* **2011**, *40*, 1305–1323.

[45] S. Kunath, N. Marchyk, K. Haupt, K.-H. Feller, *Talanta* **2013**, *105*, 211–218.

[46] K. D. Wegner, N. Hildebrandt, *Chem. Soc. Rev.* **2015**, *44*, 4792–4834.

[47] W. Chan, D. J. Maxwell, X. Gao, R. E. Bailey, M. Han, S. Nie, *Curr. Opin. Biotechnol.* **2002**, *13*, 40–46.

[48] S. Beyazit, S. Ambrosini, N. Marchyk, E. Palo, V. Kale, T. Soukka, B. Tse Sum Bui, K. Haupt, *Angew. Chemie - Int. Ed.* **2014**, *53*, 8919–8923.

[49] M. Panagiotopoulou, S. Beyazit, S. Nestora, K. Haupt, B. Tse Sum Bui, *Polymer (Guildf).* **2015**, *66*, 43–51.

2.6 ANNEX 2

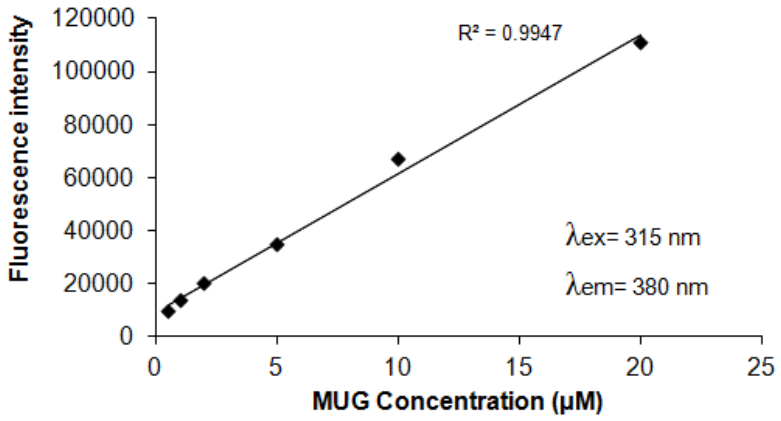

Figure 126 Calibration curve of MUG in ACN.

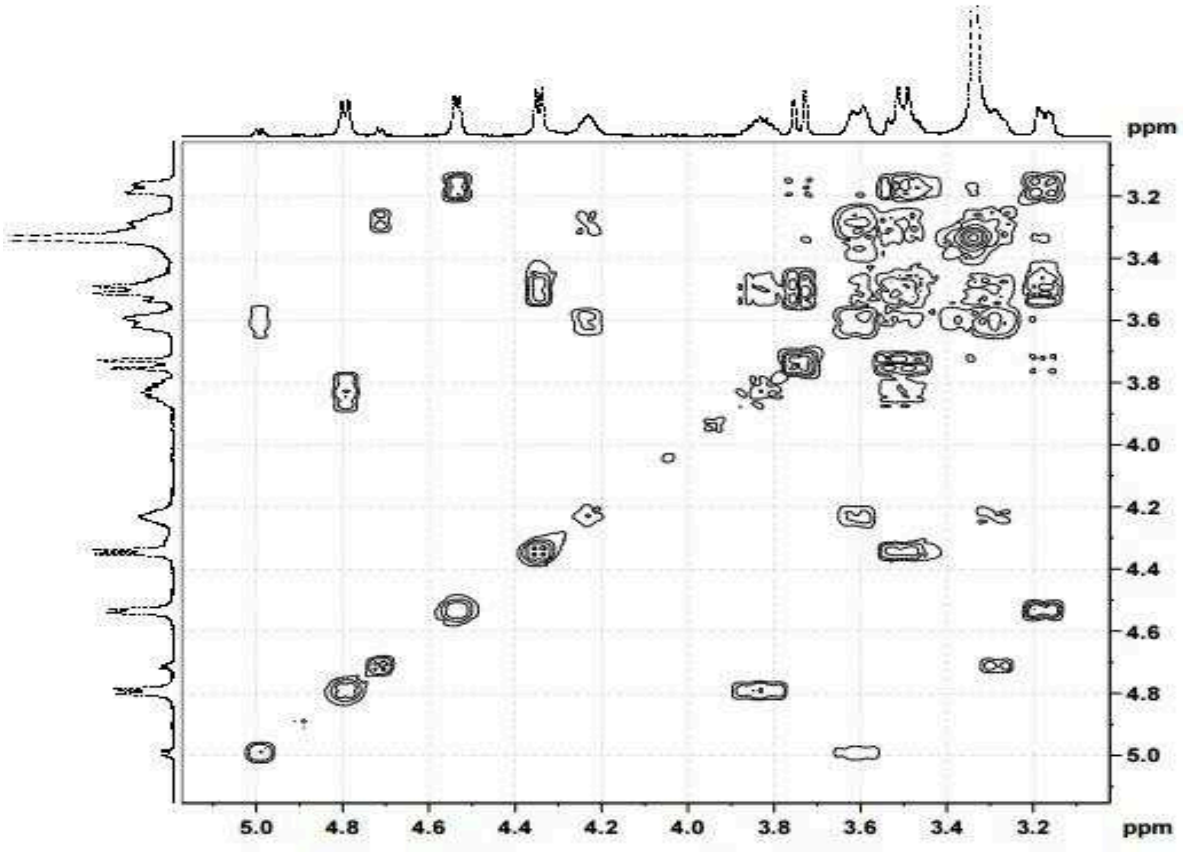

Figure 227 ^{1}H-^{1}H Correlation Spectroscopy (COSY) spectrum used for the assignment of NANA resonances in DMSO-d_6.

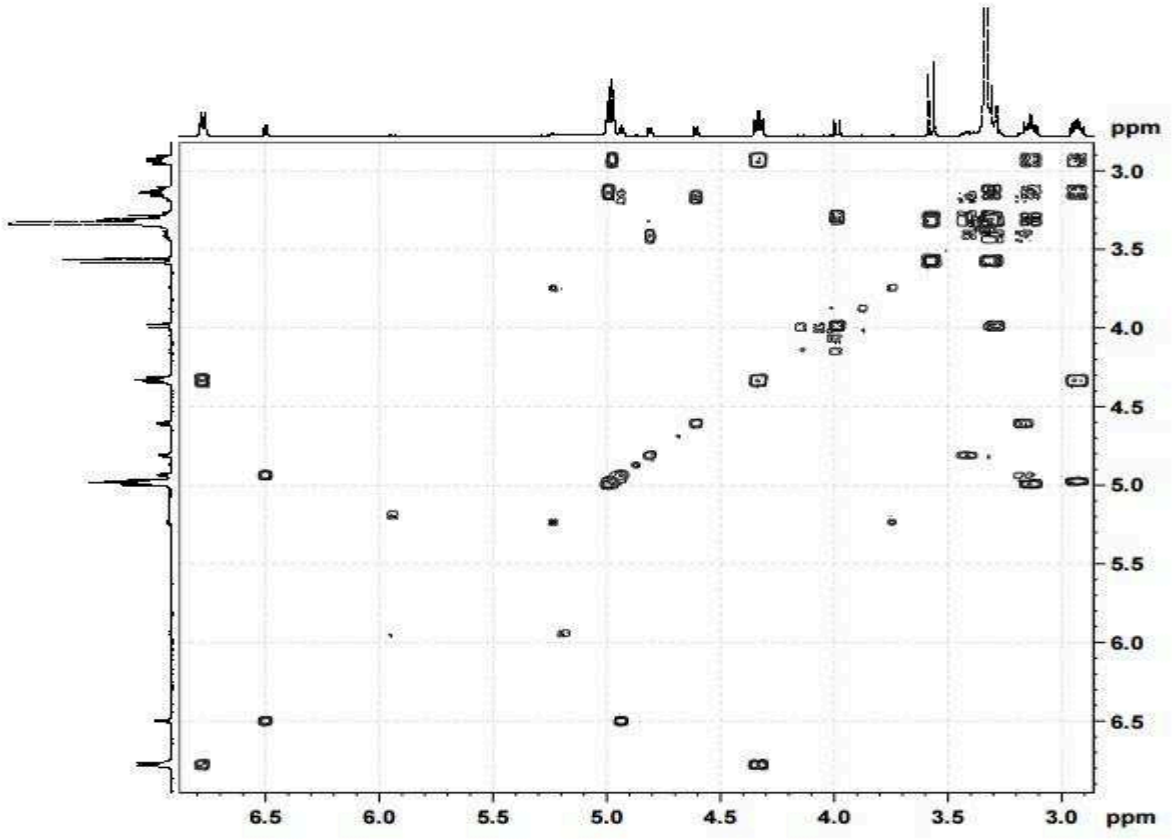

Figure 3 ^{1}H-^{1}H Correlation Spectroscopy (COSY) spectrum used for the assignment of GlcA resonances in DMSO-d_6

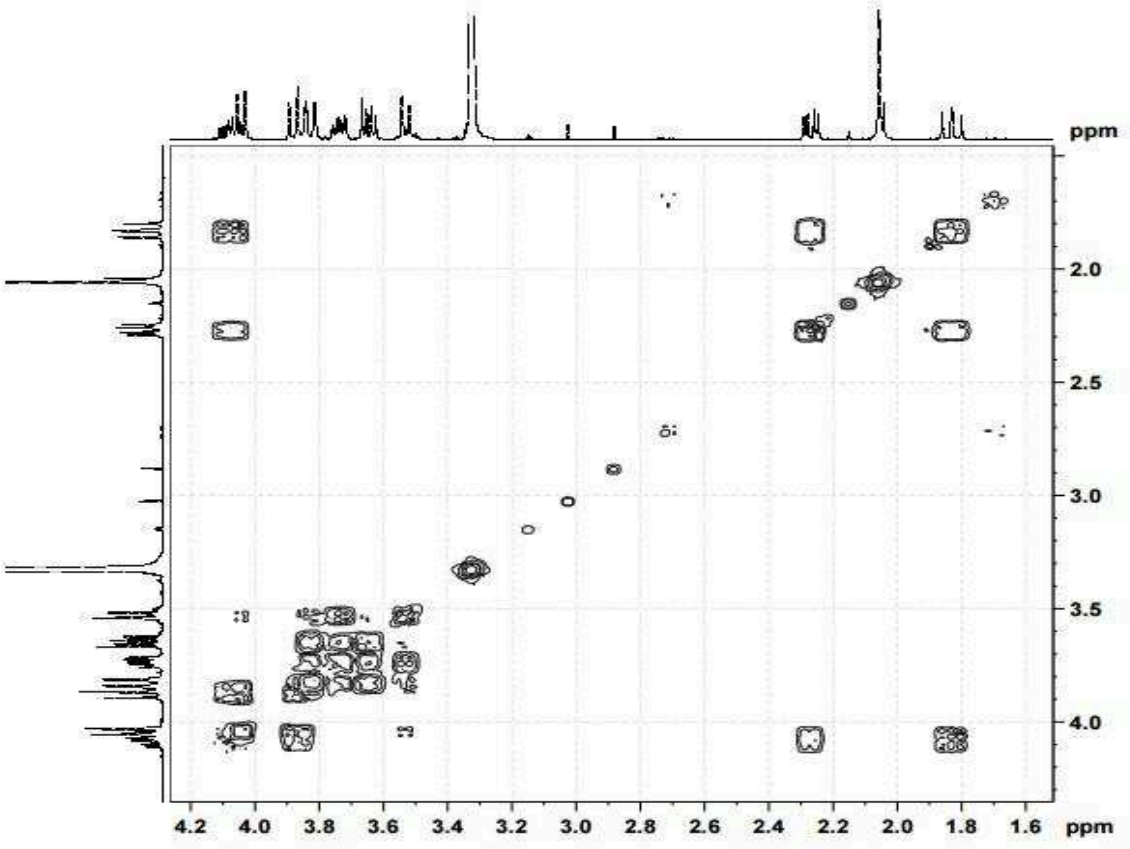

Figure 428 ^{1}H-^{1}H Correlation Spectroscopy (COSY) spectrum used for the assignment of NANA resonances in MeOD/D_2O

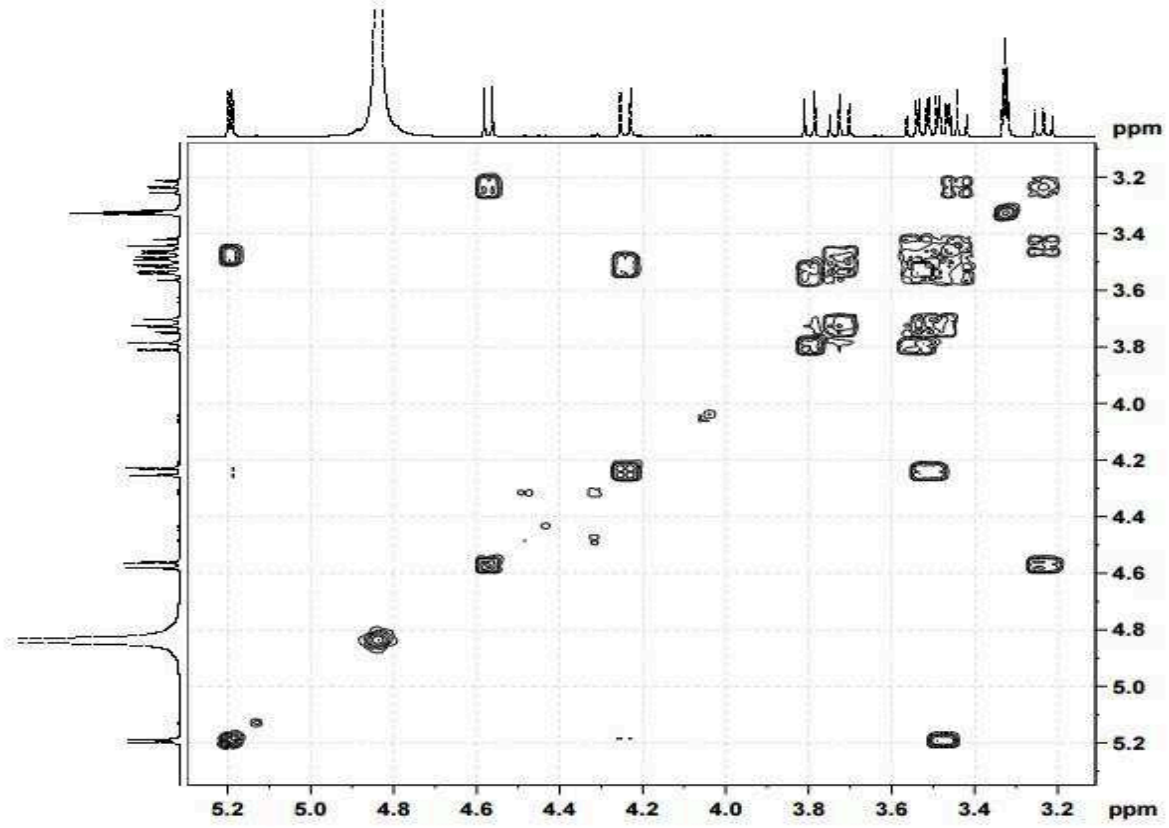

Figure 529 ^{1}H-^{1}H Correlation Spectroscopy (COSY) spectrum used for the assignment of GlcA resonances in MeOD/D_2O

CHAPTER 3

Cell and Tissue Imaging with Molecularly Imprinted Polymers

3.1 Introduction

Glycosylation in biology refers mainly to the enzymatic process that attaches glycans to proteins and is a form of co-translational and post-translational modification that the majority of proteins synthesized in the endoplasmic reticulum undergo [1–3]. Glycosylation is critical for a wide range of biological processes in health and disease [4,5] and therefore, glycosylation sites on the cell surface are of great interest, since altered glycosylation levels or distributions are indicators of pathological conditions like viral infection or malignancy. Recent advances in glycobiology and cancer research have defined the key processes underlying aberrant glycosylations with sialic acids or hyaluronan in cancer and its consequences [6–9]. Among others, overexpressed glycosylations have been associated with tumor growth, escape from apoptosis, metastasis formation and resistance to therapy.

Generally, for imaging the glycome, lectins and antibodies are the most commonly applied targeting ligands. Lectins are naturally occurring glycan-binding proteins that have been widely used for the detection and enrichment of glycoconjugates [10,11]. Lectins are able to recognize structures as varied as the monosaccharides sialic acid [12] and fucose or higher-order structures such as the conserved core region of N-glycans and the sialyl-Tn tumor antigen, a short O-glycan containing a sialic acid residue linked to GalNAcα-O-Ser/Thr that serves as cancer biomarker [13]. However, lectins typically have low affinities (K_d ~10^{-4}-10^{-2} M) for their glycan epitope and require multivalency for high-avidity binding. Moreover, lectins are generally tissue-impermeable, often toxic and lack specificity [14]. For these reasons, the utility of lectins for imaging in living systems is limited, although they have been widely used to visualize glycans *ex vivo*. The use of lectins to probe specific glycans on cultured cell lines is well precedented [15]. Lectins have enabled the visualization of different glycans on tissue sections or whole-mount specimens at discrete time points in mouse, chick, and fly embryogenesis, as well as in the mature mouse thymus, rat endothelial vasculature, and human kidney [13] Table 1 Most commonly used lectins and their binding specificities.Table 1 lists the most commonly used lectins and their binding specificities.

Table 1 Most commonly used lectins and their binding specificities. DBA: Dolichos Biflorus Agglutin; PNA: Peanut Agglutin; SBA: Soybean Agglutin; VVA: Vicia Villosa Lectin; WGA: Wheat Germ Agglutin; ConA: Concanavalin A; Gal: galactose; GlcNAc: N-acetylglucosamine; Glc: glucose; Man: mannose; GalNAC: N-acetylgalactosamine

Lectin	Source	Binding specificity	Targets
DBA	*Dolichos biflorus*	α-GalNAc	O-glycans
Jacalin	*Artocarpus integrifolia*	α-Gal,α-GalNAc, Galβ1-3GalNAc, Sialyl-Galβ1-3GalNAc, GlcNAcβ1-3GalNAc	O-glycans
PNA	*Arachis hypogaca*	Galβ1-3GalNAc, α-Gal, β-Gal	O-glycans
SBA	*Glycine max*	α-GalNAc, βGalNAc, α-Gal, β-Gal	O-glycans
VVA	*Vicia villosa*	α-GalNAc, GalNAcα1-6Gal, GalNAcα1-3Gal	O-glycans
WGA	*Triticum vulgare*	β-GlcNAc, sialic acid	O- and N-glycans and chitin
ConA	*Canavalia ensiformis*	α-Man, α-Glc, α-GlcNAc	N-glycans

Like lectins, antibodies generated against glycan structures enable the visualization of these molecules. Since the polysaccharides involved in the glycosylation procedure have a highly conserved simple composition and are ubiquitously expressed in all animals that have a developed immune system, they are so-called weak antigens. Therefore, production of antibodies that specifically recognize them is naturally difficult [16–18]. Like lectins, antibodies are also tissue-impermeant, and most antibodies generated against glycan epitopes are of the low-affinity IgM subtype. Despite the fact, there are some well-characterized commercially available monoclonal antibodies that bind distinct epitopes on heparan and chondroitin sulfate, as well as sialyl Lewis x, sulfoadhesin, and O-linked N-acetylglucosamine (O-GlcNAc) among others [13]. Regarding *in vivo* imaging, only one report exists where a glycan-specific antibody was used. In this study, Licha et al. [19] succeeded in visualizing the peripheral lymph node endothelial glycan termed sulfoadhesin in mice by using the MECA-79 antibody.

Boronic acids are also important ligands for specific recognition and isolation of *cis*-diol-containing biomolecules such as saccharides, nucleosides and glycoproteins. Boronic acids covalently react with *cis*-diols to form five or six-membered cyclic esters in an alkaline aqueous solution, while the cyclic esters dissociate when the medium is changed to acidic pH [20].

Phenylboronic acid tags have recently been used, in conjugation with QDs, for the specific fluorescent imaging of sialic acids [21]. Although the authors claim high selectivity towards sialic acids, as indicated by reduced staining when a competitive assay with free sialic acid is applied or when staining of sialidase treated cells is performed, we believe that this method cannot be applied for the selective sialic acid imaging on the cell surface, due to the plethora of other free sugar structures available for recognition on the cell glycocalix.

In this context, tailor-made molecularly imprinted polymers (MIPs) are promising synthetic receptor materials for imaging the glycosylation sites. The work described in this chapter constitutes the first cell imaging example using MIPs labeled with the organic dye rhodamine or with QDs as fluorescent targeting ligands and will extensively be described in the following sections. Very recently, several other groups have started applying the molecular imprinting technology for cell imaging applications targeting the glycome. These bioimaging examples are presented below.

Sellergren's group developed MIPs targeting cell surface glycans based on sialic acid imprinted core-shell nanoparticles using nitrobenzoxadiazole (NBD) fluorescent reporter groups [22] (Figure 1A). Imprinting was achieved using a hybrid approach combining reversible boronate ester formation between p-vinylphenylboronic acid and sialic acid, cationic amine functionalities and a urea-based monomer as a binary hydrogen bond donor targeting the carboxylic acid and OH functionalities. The monomers were grafted from 200 nm RAFT modified silica core particles using ethyleneglycol dimethacrylate (EGDMA) as crosslinker. When applied in cells, the particles selectively stained the different cell lines, including prostate cancer cells DU145 and PC3 and the leukemic cells Jurkat, in correlation with the sialic acid expression level. The selectivity of the staining was further verified by enzymatic cleavage of sialic acid and by cell staining using a FITC labeled sialic acid selective lectin. The reported MIPs displayed high affinities for their target in methanol/water mixtures ($K = 6.6 \times 10^5\ M^{-1}$ in 2% water, $5.9 \times 10^3\ M^{-1}$ in 98% water) but were in loosely aggregated form. The same MIPs were very recently applied for an extended screening of sialic acid expression in four different chronic lymphocytic leukemia (CLL) cell lines (HG3, CI, Wa-osel, and AIII) [23] (Figure 1B).

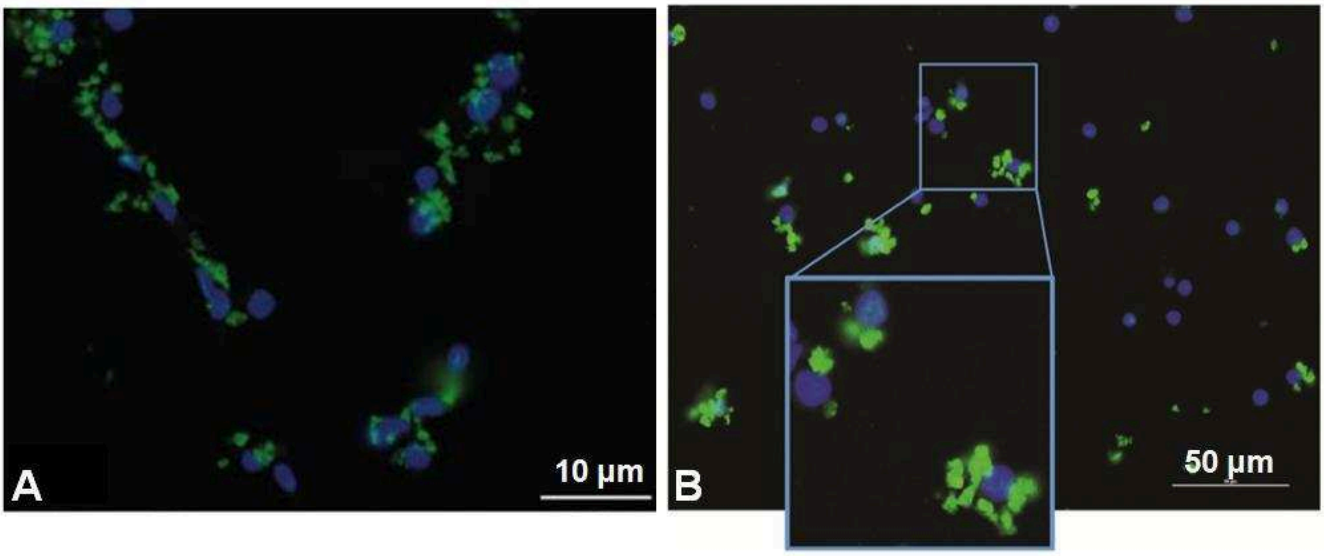

Figure 1 Confocal microscopy images for the localization of the SA-MIP in (A) DU145 cells and (B) HG3 cells. Reproduced from [22,23].

Yin et al. employed Raman-active silver nanoparticles as signal reporting cores that were coated with an imprinted boronate thin shell layer targeting sialic acid [24]. Healthy human hepatic cells and hepatocarcinoma cells (HepG-2) were imaged in this study to prove the selectivity of the polymers. HepG-2 cells showed a SERS signal much stronger than the one obtained for the control cells, proving the specific binding of the MIPs to the sialic acid terminal moieties on the cell surface.

The same group presented very recently monosaccharide-imprinted fluorescent nanoparticles for selective imaging of cancer cells [25] (Figure 2). FITC-doped silica NPs were first synthesized as a fluorescent core and further functionalized with a monosaccharide-imprinted silica layer by the boronate affinity oriented surface molecular imprinting. The monosaccharides sialic acid, fucose and mannose were imprinted and the obtained MIPs were able to specifically recognize their targets and to differentiate cancer cells from normal cells. Fluorescence imaging of human hepatoma carcinoma cells (HepG-2) over normal hepatic cells (L-02) and mammary cancer cells (MCF-7) over normal mammary epithelial cells (MCF-10A) by these NPs was demonstrated. The selectivity of the MIPs towards their targets was further verified by boronate affinity sandwich assay and by enzymatic treatment with sialidase, fucosidase or mannosidase. Control staining using FITC-labelled lectins, including *Sambucus nigra* lectin, *Ulex europaeus* agglutinin

I and *Lens culinaris* agglutinin for the recognition of sialic acid, fucose and mannose respectively was also performed.

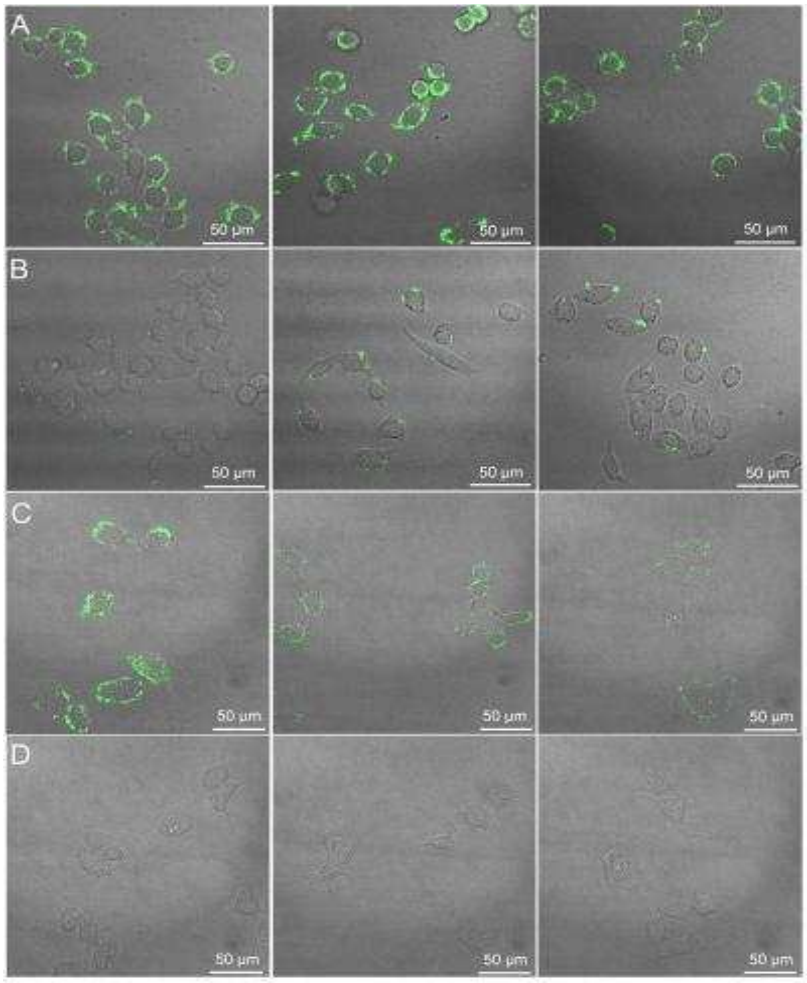

Figure 2 Confocal fluorescence imaging of (A)HepG-2 cells , (B) L-02 cells ,(C) MCF-7 cells and (D MCF-10A cells after staining with different monosaccharide-imprinted NPs. Columns from left to right: SA, fucose and mannose-imprinted NPs. The concentration of the NPs was 200 µg/mL.

In this chapter, we describe a thorough study of imaging human keratinocytes with MIPs labeled with the organic dye rhodamine or quantum dots of different colors, targeting GlcA and NANA that were described in Chapter 2. NANA is the predominant sialic acid (SA) found in mammalian cells. Keratinocytes were chosen as a model for this study because they overexpress on their surface, hyaluronan (a natural and linear polysaccharide consisting of repeating units of N-acetyl-D-glucosamine and D-glucuronic acid) and other glycosylations. Thus if GlcA and NANA are present and not sterically hindered, as for instance at the terminal end of hyaluronan,

proteoglycans or glycoconjugates, they would be recognized and labeled. NANA is reported to be located extracellularly, at the end of sugar chains of sialylated proteins and sphingolipids on the glycocalix, whereas GlcA, apart from being extensively found in hyaluronan is also present in some proteoglycans such as chondroitin sulfate, heparan sulfate and dermatan sulfate, though in lower proportions (Figure 3). Quantification and localization studies were performed using fluorescence microscopy. In addition, we showed that multiplexed cell targeting and imaging is possible both on fixed and living cells. Skin tissue imaging was also performed, enlarging the application field of MIPs in biomedical and histological imaging. To this goal, cell viability studies for the concentrations of the particles used in the imaging experiments were carried out. Finally, the versatility of our targeting technique was proved by imaging the chronic leukemia cell line KU812.

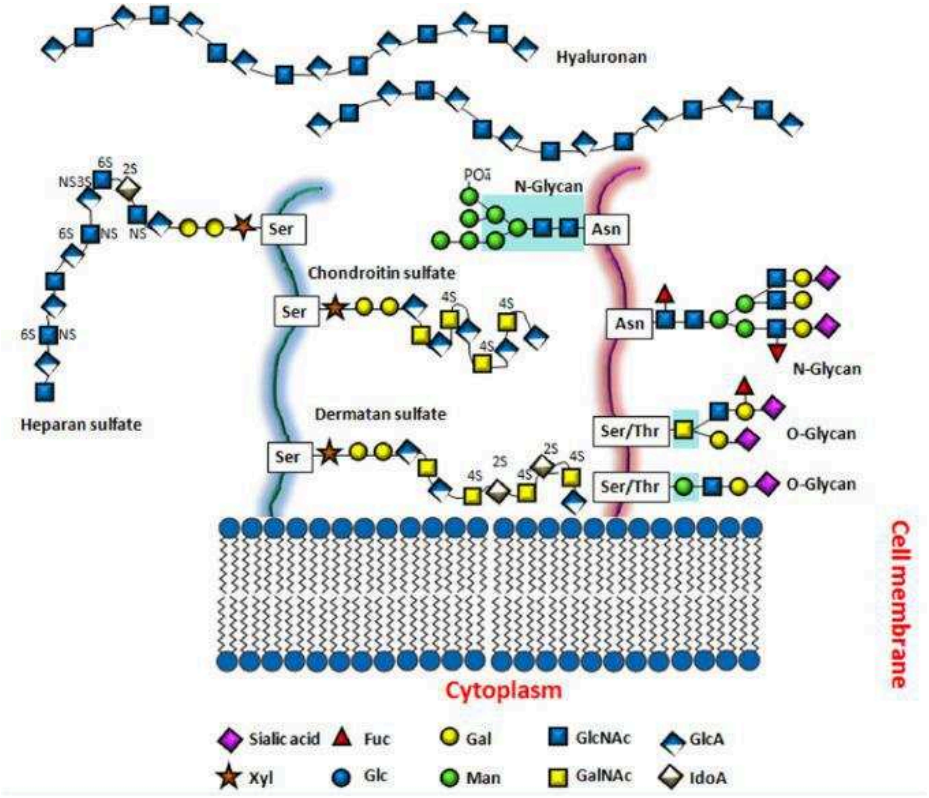

Figure 3 The glycocalyx is a cell-coat structure of glycans and glycoconjugates that surrounds the cell membranes. Glucuronic acid (GlcA) is found extensively in hyaluronan and in smaller proportions, in dermatan sulfate, chondroitin sulfate and heparan sulfate while N-acetylneuraminic acid (sialic acid) is found at the terminal end of glycoproteins. Fuc: fucose; Gal: galactose; GlcNAc: N-acetylglucosamine; Xyl: xylose, Glc: glucose; Man: mannose; GalNAC: N-acetylgalactosamine; IdoA: iduronic acid.

3.2 Results and Discussion

3.2.1 Optimization of the cell imaging protocol

A standard immunostaining protocol was adapted and optimized to the application of MIPs for cell imaging in order to localize and quantify hyaluronan or sialic acid on and in the keratinocyte cells HaCaT. The protocol with the different steps is shown in Figure 4. Each step was carefully designed in order to eliminate phenomena like high background fluorescence and particle aggregation.

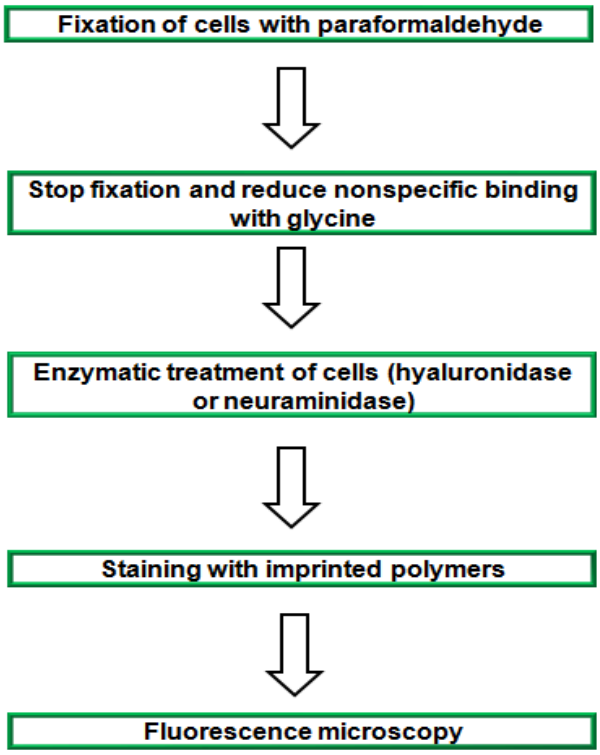

Figure 4 Protocol for cell staining with molecularly imprinted polymers.

Several types of chemical fixatives are used in modern cell biology and histology, including cross-linking fixatives like aldehydes, precipitating fixatives like alcohols, oxidizing agents like osmium tetroxide (mostly used for electron microscopy sample preparation), mercurials like B-5 and Zenker's fixative, picrates and HEPES-glutamic acid buffer-mediated organic solvent

protection effect (HOPE) fixative. For our protocol, cross-linking fixation with paraformaldehyde as fixative was chosen because of its simplicity and low cost. In addition, paraformaldehyde fixation results in low background fluorescence.

When fixatives react and cross-link with protein molecules, lots of free aldehyde groups remain. These cell/tissue-bound free aldehyde groups will bind covalently with any amino group offered to them, including terminal and side-chain (lysine) amino groups of proteins being used as histochemical reagents, which means all antibodies, all lectins and all enzymes. Thus, even a highly specific monoclonal primary antibody may bind at sites that contain basic proteins but not the antigen of interest. This is why, aldehyde blocking is necessary. A commonly used blocking reagent is Bovine Serum Albumin (BSA) because it is cheap and easily found in biochemical laboratories. Another way to achieve aldehyde blocking is by feeding them with small-molecule amines such as glycine. Both blocking reagents were tested with HaCaT cells and glycine-based blocking was adapted for our staining protocol because it did not induce aggregation to the MIP particles, as observed with BSA-based blocking.

An (optional) additional step, to confirm the specificity of the MIP staining, is enzymatic treatment with hyaluronidase or neuraminidase. Hyaluronidase hydrolyzes the endo-N-acetylhexosaminic bonds of hyaluronan, thus eliminating terminal glucuronic acid groups and generating terminal N-acetylglucosamine on the cell surface, and neuraminidase eliminates terminal sialic acid residues.

The final step is the incubation with MIP or NIP particles as a control. The spatial distribution of the fluorescently-labeled MIPs on the cells was determined by epifluorescence microscopy. Among the MIPs characterized in Chapter 2, the ones using AB and MAM as functional monomers synthesized in DMSO were used for further imaging experiments, because of their monodispercity and homogeneous particle distribution on the cells (unlike the other MIPs tested), their suitable size to target the extracellular matrix and their high affinity towards the targets. Localization of these particles on the cells was determined by confocal microscopy.

3.2.2 Quantitive imaging of fixed cells using rhodamine-labeled MIPs

Application of the optimized cell imaging protocol resulted in nicely distributed particles on the surface of the cells (Figure 5). Although hyaluronan and to a lesser extend sialic acid terminal moieties can also be found intracellularly, the rhodamine-labeled MIPGlcA and MIPNANA, due to their large size (~400 nm) were exclusively found extracellularly, targeting the overexpressed glycosylations in the glycocalix. Image analysis revealed that MIPGlcA and MIPNANA had respectively 44% and 48% more binding to the cells than their corresponding NIPs (Figure 6).

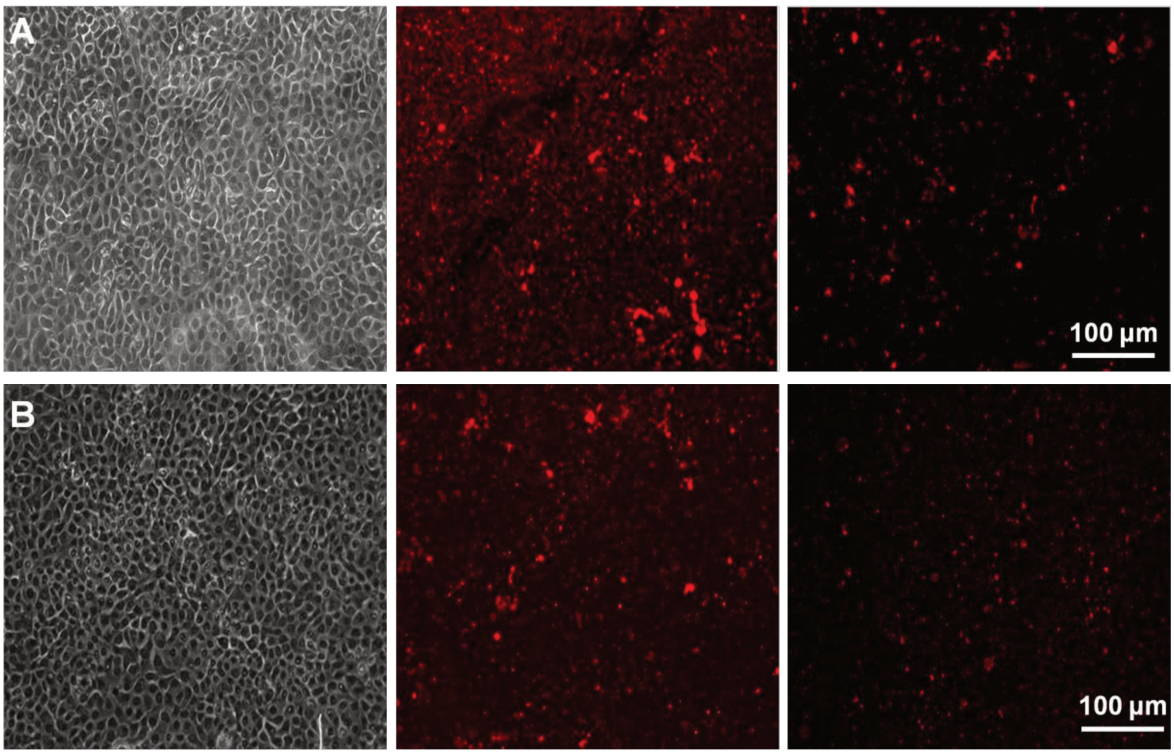

Figure 5 Representative epifluorescence microscopy images of: (A) rhodamine-MIPGlcA and (B) rhodamine-MIPNANA. From left to right: phase contrast image, cells stained by MIP, cells enzymatically (hyaluronidase or neuraminidase) treated and stained by MIP.

The relatively high binding of the non-imprinted polymers is due to the presence in these particles of randomly distributed aminidinium groups from the functional monomer AB (K_{aGlcA}=7.1 x 10^3 M^{-1}, K_{aNANA} = 41 x 10^3 M^{-1} as deduced from ^{1}H NMR in DMSO-d_6). It should be stressed, though, that the NIP binding does not reflect the extent of nonspecific binding of the MIP, since in the MIP the amidine groups are located in specific binding sites. The NIP was only

used to confirm the molecular imprinting effect. Thus, these results illustrate the specificity of the binding of GlcA-imprinted polymer particles to hyaluronan and NANA-imprinted particles to sialylation sites on human keratinocytes.

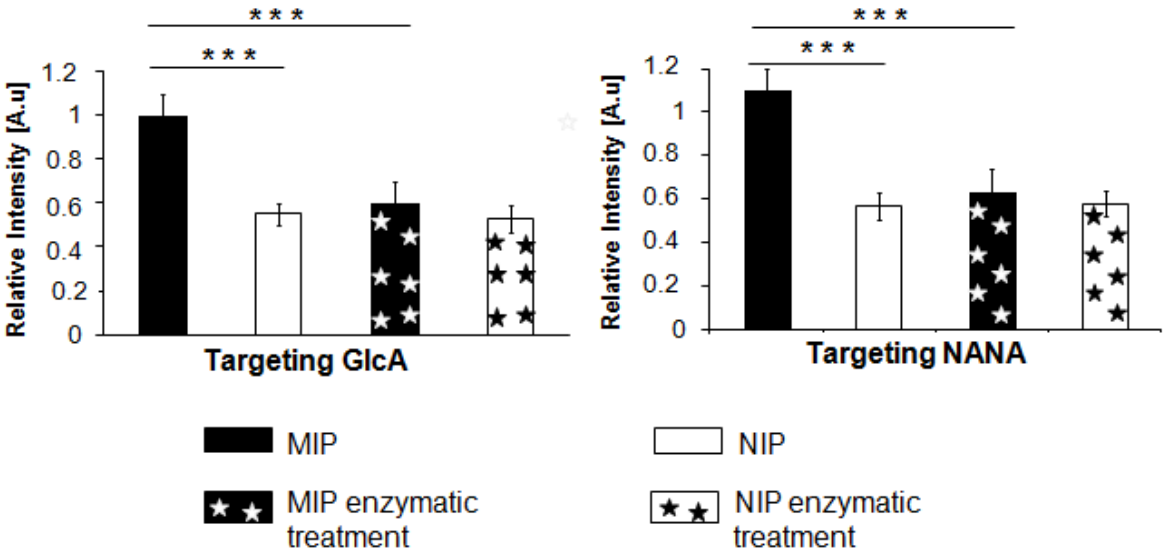

Figure 6 Relative fluorescence intensities of HaCaT cells after imaging with rhodamine-MIPs (black) and rhodamine-NIPs (white), with and without enzymatic treatment, n=4 independent replicates with quadruplicates for each experiment. Error bars represent the standard deviation. Mean values of MIP and NIP for normal cells, and of MIP for normal cells and MIP of enzymatically-treated cells, are significantly different at 99.9% confidence (p<=0.001*).**

After enzymatic treatment with hyaluronidase or neuraminidase, there was no significant difference anymore between MIPs and NIPs, thus confirming the specific labeling of the MIPs for their targets (Figure 6). These results are comparable to those obtained with a reference method where staining was done with a biotinylated hyaluronic acid binding protein (HABP) [17], coupled with fluorescein isothiocyanate-labeled straptavidin in the place of rhodamine-MIPGlcA [26] (Figure 7). This reference method was applied using the same protocol as with MIPs, except for the solvent that was changed to PBS buffer for better stability of the protein. The nucleus was stained with DAPI to study the localization of the protein under the same conditions as with the MIP. It can be seen that in the absence of enzymatic treatment, there are areas with a heterogeneous distribution of hyaluronan, some cells carrying less hyaluronan than others, which is consistent with the observations with the MIPs (Figure 5) and with the literature [27]. As

described above with MIPs, enzymatic treatment with hyaluronidase was performed prior to HABP staining as a control. The quantitative analysis of the images revealed a significant (52%) reduction in the fluorescence signal of hyaluronidase treated versus untreated cells. A similar control for sialic acid labeling was not performed because the lectins commonly used for the sialic acid staining, recognize also N-acetyglucosamine and N-acetylgalactosamine, thus highly selective staining cannot be obtained.

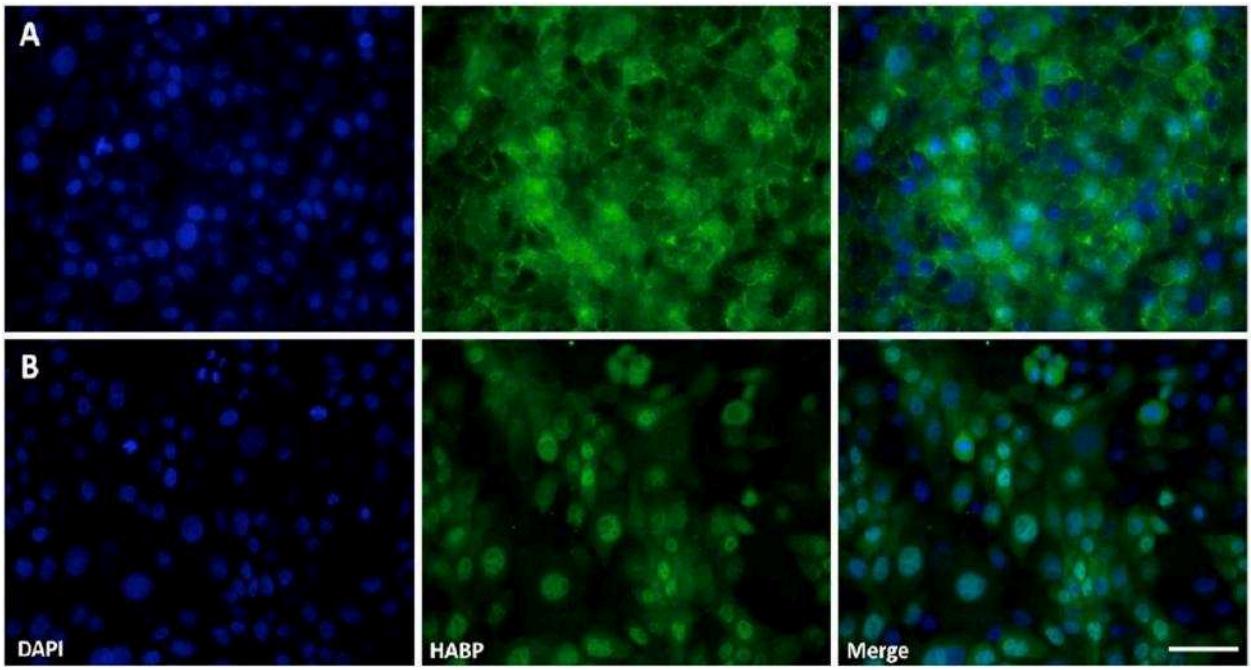

Figure 7 Localization of hyaluronan on confluent HaCaT cells that were fixed and stained with a FITClabeled hyaluronic acid binding protein (HABP). The nucleus was stained with DAPI. (A) Untreated and (B) hyaluronidase-treated samples. Scale bar: 50 µm.

3.2.3 Quantitive imaging of fixed cells using MIP-QDs

For quantitative cell-imaging with the MIP-QDs on human keratinocytes, the same optimized immunostaining protocol as described for the rhodamine-labeled MIPs was applied (Figure 8). MIPGlcA-QDs and MIPNANA-QDs showed 42% and 48% more binding to the cells than their respective NIP-QDs (Figure 9). The specificity of the MIP staining was confirmed by hyaluronidase or neuraminidase treatment, which resulted in the same fluorescence profile as staining by the NIP (~40% reduction for both MIPGlcA-QDs and MIPNANA-QDs) (Figure 8).

Thus, these results illustrate the specificity of the binding of GlcA-imprinted polymer particles to hyaluronan and NANA-imprinted particles to sialic acids on human keratinocytes.

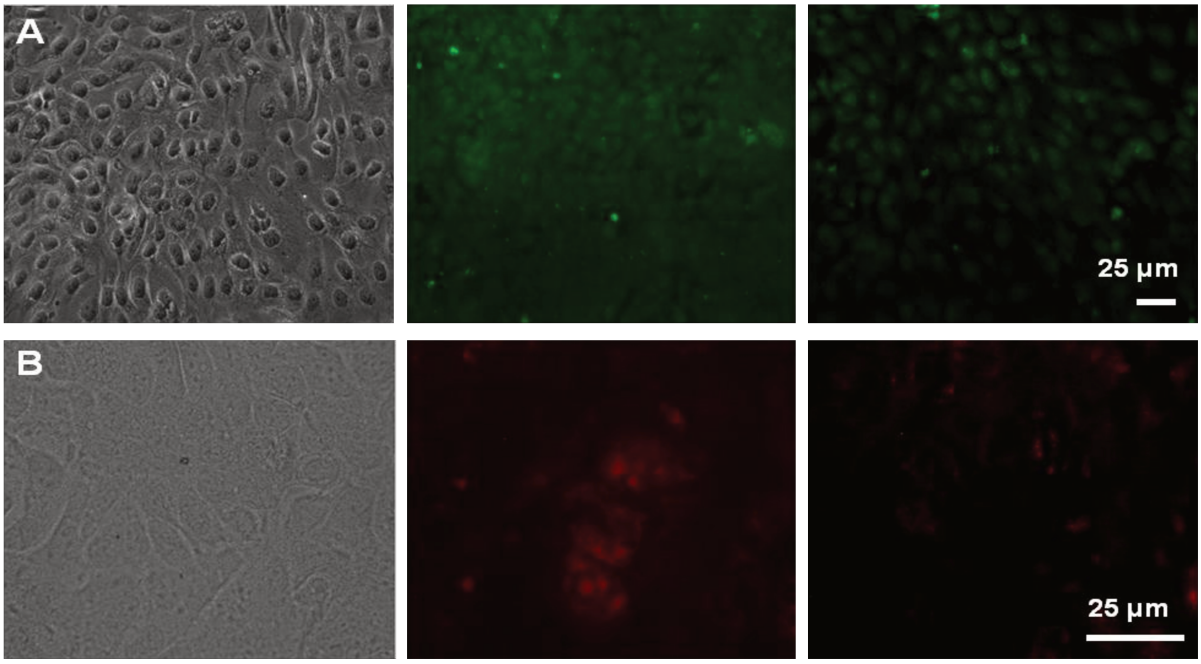

Figure 8 Representative epifluorescence microscopy images of: (A) MIPGlcA-QDs and (B) MIPNANA-QDs. From left to right: phase contrast image, cells stained by MIP, cells enzymatically (hyaluronidase or neuraminidase) treated and stained by MIP.

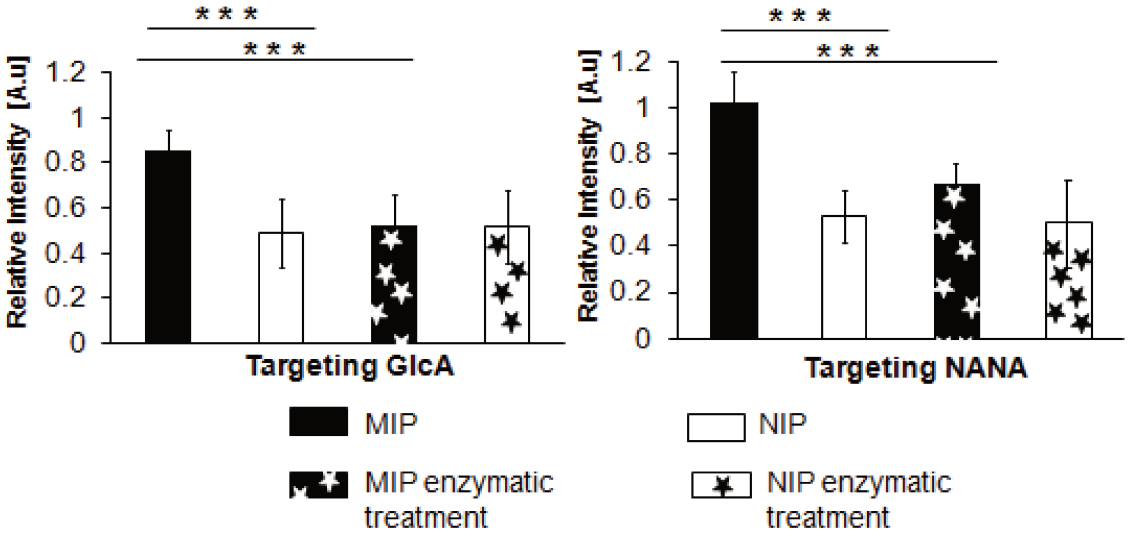

Figure 9 Relative fluorescence intensities of HaCaT cells after imaging with MIP-QDs (black) and NIP-QDs (white), with and without enzymatic treatment, n=4 independent replicates with quadruplicates for each experiment. Error bars

represent the standard deviation. Mean values of MIP and NIP for normal cells, and of MIP for normal cells and MIP of enzymatically-treated cells, are significantly different at 99.9% confidence ($p \leq 0.001$*).**

3.2.4 Localization studies using confocal microscopy

Confocal microscopy was used to study the distribution of MIPs along the z-axis, with additional labeling of the nucleus and in some cases of the membrane (Figure 10). In the cases of the MIPs prepared by precipitation polymerization, the red rhodamine labeled MIP particles are localized only on the cell surface due to specific binding to hyaluronan and sialylations (Figure 10 A,C). Extracellular labeling is achieved because the size of the particles is large enough to avoid internalization. Our experiment also shows that MIP staining can be easily coupled with other staining methods without interference or loss of specificity.

On the other hand, the MIPGlcA-QDs (green) were localized extracellularly, pericellularly, and intracellularly, even within the nucleus in some cases (Figure 10B). Nuclear staining, due to the distribution of hyaluronan in nuclear clefts, has been reported previously [27]. MIPNANA-QDs (red) were localized mainly extra- and pericellularly (Figure 10D), in accord with the localization of terminal sialic acids in human cells [22,28]. Since selective labeling and imaging could be achieved by the individual fluorescent MIP-QDs, it was interesting to prove the flexibility of our cell staining protocol by applying it for multiplexing with the two different colored MIP-QDs. This study demonstrates for the first time the potential of MIPs when conjugated to quantum dots of different emission colors as a versatile multiplexed imaging tool without compromising the selectivity towards their target analytes (Figure 10E).

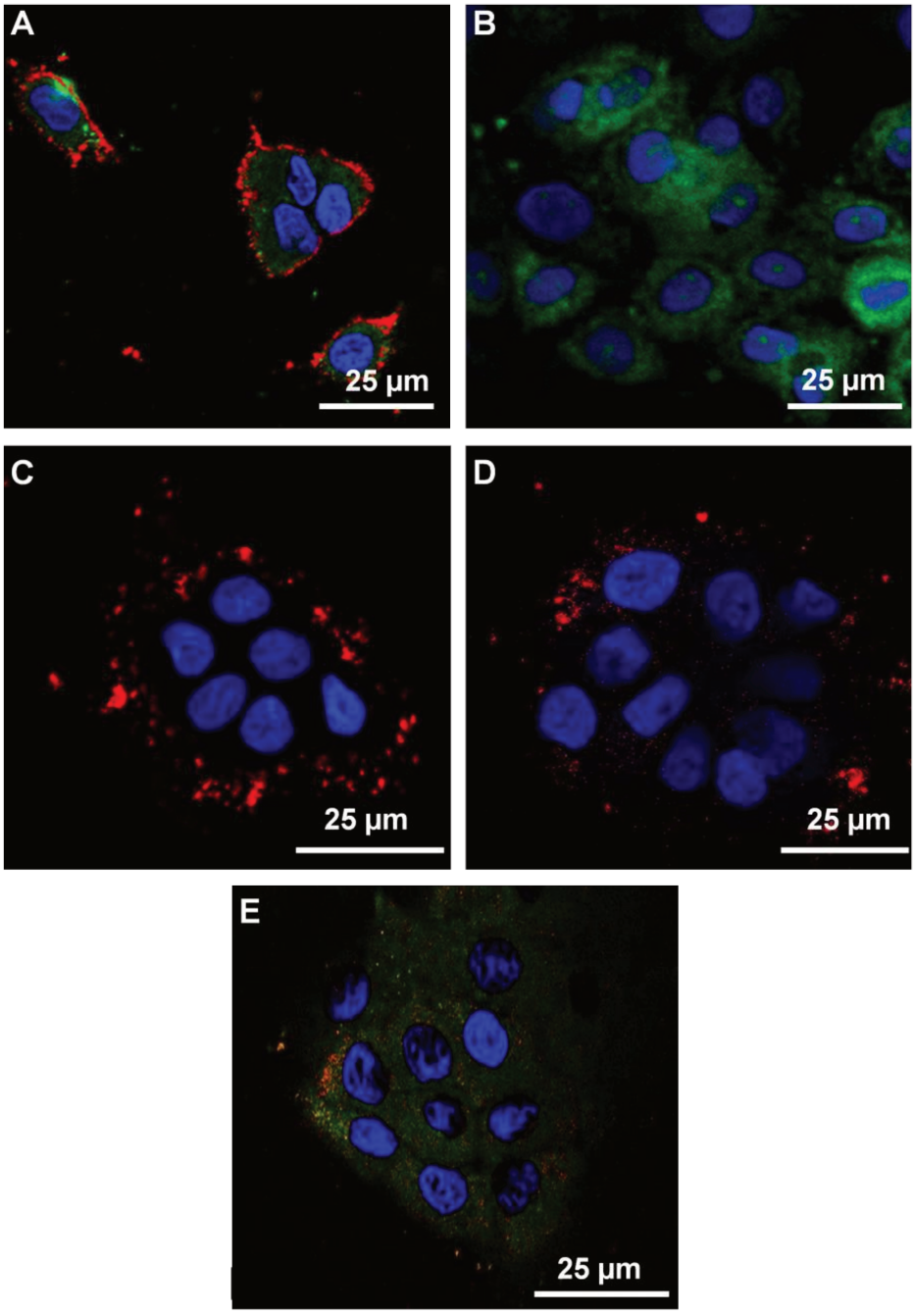

Figure 10 Confocal images for the localization of (A) Rhodamine-MIPGlcA (red); (B) MIPGlcA-QDs (green); (C) Rhodamine-MIPNANA (red); (D) MIPNANA-QDs (red) and E) Multiplexed cell imaging with MIPGlcA-QDs and MIPNANA-QDs. Nuclear staining was performed with DAPI and membrane staining in (A) was performed with DiO.

3.2.5 Cancer cell imaging

Cancer is characterized by abnormal cell growth, spread and invasion to other organs, which can have a fatal outcome. In 2012, more than 10 million deaths due to cancer were reported and several types of cancer including colon, breast, liver and stomach are figuring in the WHO lists describing the 10 leading causes of death in middle and high income societies (Figure 11) [29]. Successful cancer treatment is still a subject of extensive biomedical research and early diagnosis is the key for a positive outcome. For this, imaging modalities such as MRI, PET, CT and US are employed. Optical imaging can be a useful asset to cover for the disadvantages of the current diagnostic methods, although till now, intraoperative imaging can only be used to remove surface tumors due to the limited light penetration depth. In order to show that our cell staining protocol could serve as a versatile staining tool and be successfully adapted for tumor detection, imaging of the chronic leukemia cell line KU812 was performed. High serum levels of both hyaluronan and sialylated proteins have been reported to have a prognostic impact in leukemia [30,31].

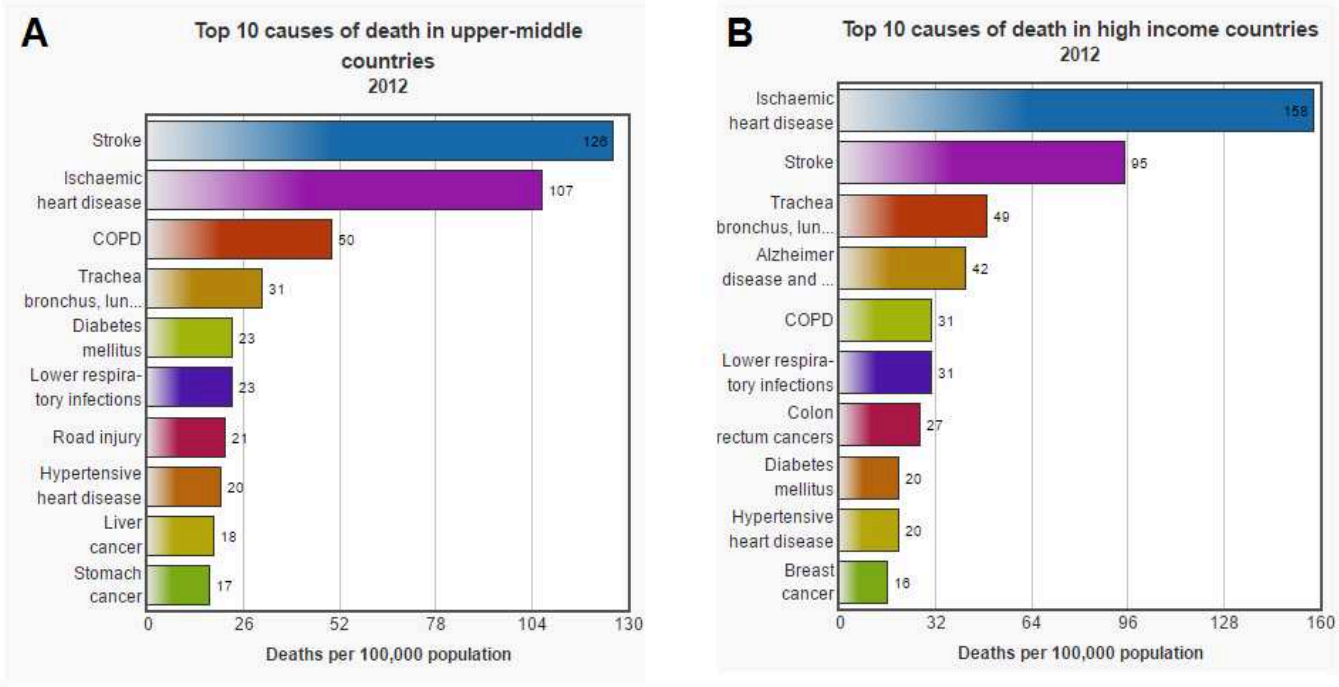

Figure 11 The 10 leading causes of death by country income group in 2012 according to WHO. (A) Upper-middle income countries. (B) High income countries. Reproduced from [29]

Leukemia includes a group of blood cell cancers that usually begin in the bone marrow and result in high numbers of abnormal white blood cells, which are not fully developed and are called leukemia cells. Common symptoms include pain in bones or joints, bleeding and bruising problems, feeling weak or tired, fever, and being prone to infections. These symptoms occur due to the lack of normal blood cells. Diagnosis is made either by blood tests or by bone marrow biopsy. The exact cause of leukemia remains unknown but both inherited and environmental (non-inherited) factors are believed to be involved [32]. Risk factors include smoking, ionizing radiation and some chemicals such as benzene. There are four main types of leukemia: acute lymphoblastic leukemia (ALL), acute myeloid leukemia (AML), chronic lymphocytic leukemia (CLL) and chronic myeloid leukemia (CML). According to WHO, in 2012, leukemia developed in 352,000 people globally and caused 265,000 deaths [29].

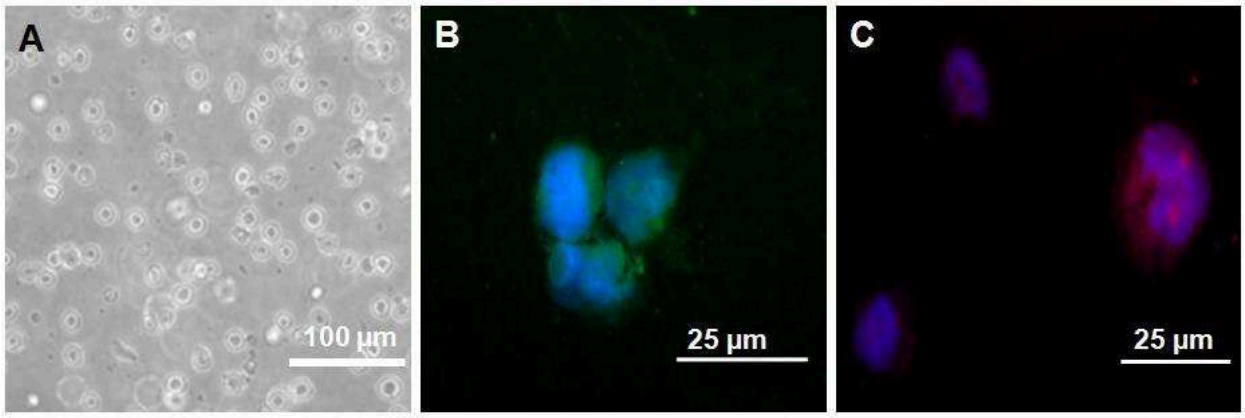

Figure 12 Representative epifluorescence microscopy images of KU812 cells: (A) Phase contrast; (B) cells labeled with MIPGlcA-QDs (green) and (C) cells labeled with MIPNANA-QDs (red). Cell nucleus was stained with DAPI (blue).

As demonstrated in Figure 12, staining of the CML cell line KU812 was successful for both hyaluronan and sialic-acid terminating moieties, proving the versatility of our MIP-staining method to practically any cell line overexpressing these two biomarkers.

3.2.6 Live cell imaging

It would be hard to argue that live-cell imaging has not changed our view of biology. The past 10 years have seen an explosion of interest in imaging cellular processes, down to the molecular level. There are now many advanced techniques being applied to live cell imaging in order to provide critical insight into the fundamental nature of cellular and tissue function, especially due to the rapid advances that are currently being witnessed in fluorescent protein and synthetic fluorophore technology. The evolution in fluorescent probes makes it now possible to tag and image cellular structures and macromolecular complexes over a broad range of sizes. It is possible to capture very rapid cellular events such as signaling or imaging and tracking multiple fluorophores over time and depth [33,34].

The need and benefits of documenting dynamic cellular and sub-cellular processes in real or near real-time in order to understand the several biological processes, have been understood for a long time. The limitations of population averaging, the ability to obtain real-time measurements, and to obtain data from in vivo systems has led to an increased use of live-cell imaging. The organisms or cell types along with the questions being addressed when live cell imaging is applied are vast. Some examples of live cell imaging include temperature dependency of drug-induced events in neurons [35], fast imaging of zebra fish [36], monitoring molecular interaction [37] and how viral replication in cells occurs [38].

While the benefits and need for live-cell imaging is well appreciated, the need to ensure cellular health is not. It is crucial when performing such experiments that cell viability is at the forefront of any measurement to ensure that the physiological and biological processes that are under investigation are not altered in any way. The conditions applied for live cell imaging should not cause cell apoptosis or necrosis and phototoxicity due to long imaging procedures should also be taken into account. This is why before performing live cell imaging, the cell viability is verified using the commonly used MTT test. The principles of MTT and of other related tetrazolium salt-based cell viability assays are shortly described.

Cell viability tests

The biocompatibility of an unknown nanomaterial depends on several different parameters, such as the cell lines employed, the exposure times applied, the interaction mechanism with the cells, together with the size, shape, functionality and concentration of the nanoparticles tested. In light of this, a complete toxicological study should take into account all the aforementioned factors to fully characterise a novel nanomaterial. For an accurate result, several viability tests should be performed on different cell lines and exposure times.

MTT and related tetrazolium salts

The reduction of the tetrazolium dyes is based on NAD(P)H-dependent oxidoreductase enzymes present in the cytoplasmic matrix of the cells [39]. Therefore, reduction of MTT and other tetrazolium dyes depends on the cellular metabolic activity due to the NAD(P)H flux. Different assay conditions, such as different metabolic rates depending on the cell line used or the mechanism of the reduction of the tetrazolium dyes (intracellularly in the cases of MTT and MTS or extracellularly in the case of WSTs), can alter the amount of the formazan crystals produced without really affecting the cell viability.

MTT (3-(4,5-dimethylthiazol-2-yl)-2,5-diphenyltetrazolium bromide), an initially yellow tetrazole compound, gets reduced to purple formazan in living cells [39] (Figure 13). A solubilization step, most commonly with DMSO, is needed in order to dissolve the purple formazan crystals and the absorbance of the obtained colored solution is measured at a certain wavelength, usually between 500 and 600 nm, by a spectrophotometer.

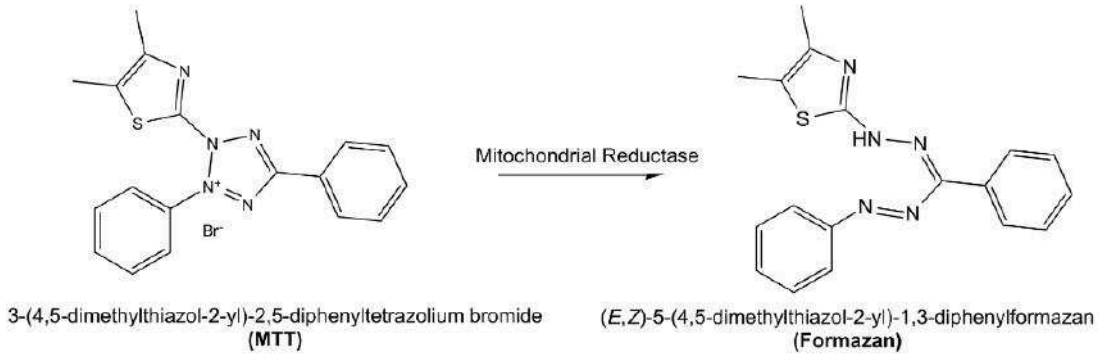

Figure 13 MTT, a yellow tetrazole compound, is reduced to purple formazan crystals in living cells.

Recently, water-soluble tetrazolium salts have been presented as alternatives to MTT: they were developed by introducing positive or negative charges and hydroxy groups to the phenyl ring of the tetrazolium salt, or with sulfonate groups added directly or indirectly to the phenyl ring. Such tests include: XTT (2,3-bis-(2-methoxy-4-nitro-5-sulfophenyl)-2H-tetrazolium-5-carboxanilide), MTS (3-(4,5-dimethylthiazol-2-yl)-5-(3-carboxymethoxyphenyl)-2-(4-sulfophenyl)-2H-tetrazolium) and WSTs (Water-soluble Tetrazolium salts). These tests can be used as water-compatible alternatives whenever there is a need to avoid the final solubilization step required in the MTT assay.

In our study, before imaging living cells, MIP NPs were analysed by the MTT assay. $CdCl_2$ was used as a positive control to induce cell death. The results show that the MIPs do not reduce the viability of keratinocytes incubated for 24 h up to a concentration of 0.027 mg mL^{-1} (Figure 14). Furthermore, the cell morphology was not influenced by the presence of the polymer particles as indicated in Figure 16. Thus, imaging of living cells could be further performed. In order to remove any background signal, the plate was divided in four sections: 1) blank wells containing medium only, 2) untreated control cells, 3) MIP NPs in medium only and 4) cells treated with MIP NPs.

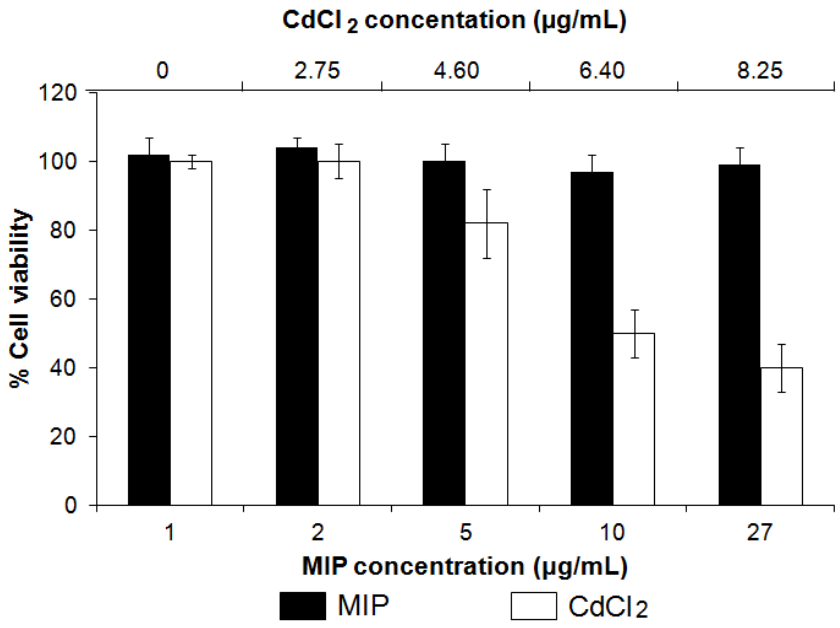

Figure 14 Cell viability (MTT) assay in cell culture medium with MIPGlcA and $CdCl_2$ serving as a positive control. Results were obtained from 2 independent experiments from different days with 8 replications each, error bars represent the standard deviation.

Live cell imaging using rhodamine-labeled MIPs

After the assessment of the cytotoxicity of the MIPs with the MTT assay for the polymer concentrations previously used for imaging, MIPGlcA and MIPNANA, labeled with rhodamine B were applied for imaging living cells. Alterations in glycosylations have been found to regulate cell cycle progression and cytokinesis; more specifically, enhanced glycosylation has been associated to certain phases of the cell cycle like mitosis [40,41]. Figure 16 A and B show that some cells seem to be more brightly stained by the MIPs. This could correspond to the G2 or mitosis phases indicating the presence of more glycosylation sites. Hence, imaging in live cells with our MIPs could help to correlate glycosylation activity with cell growth. For visualization purposes, Figure 15 demonstrates the aforementioned stages of the cell cycle.

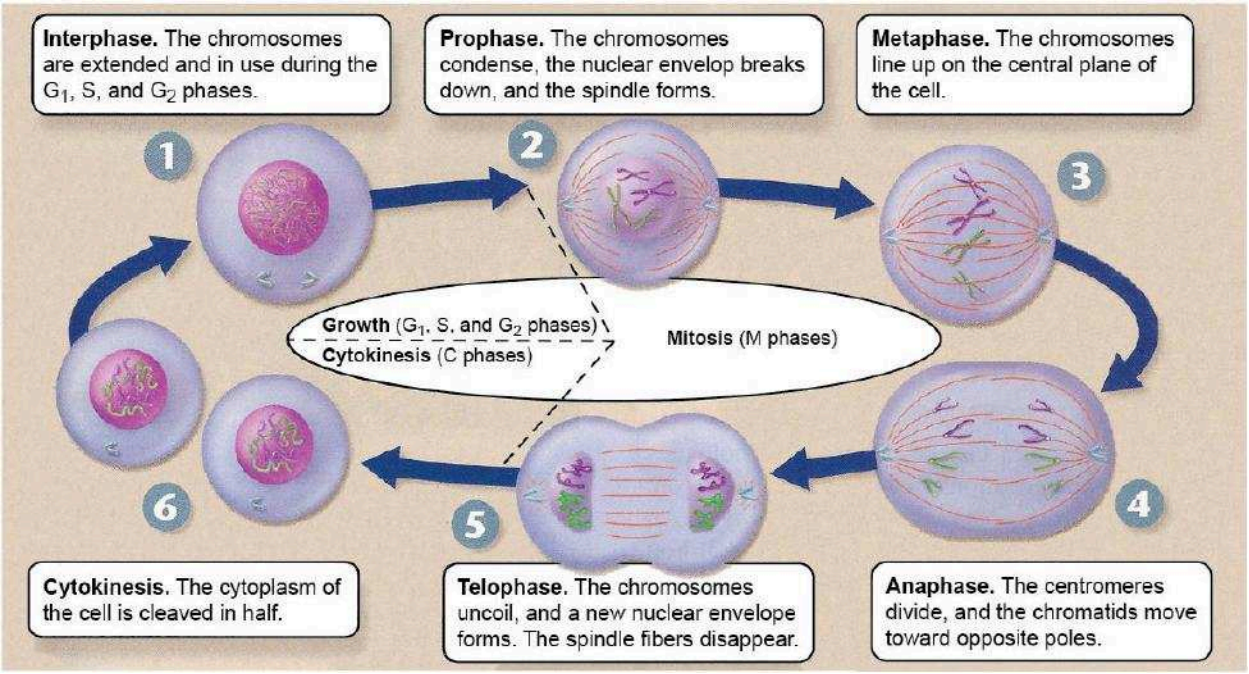

Figure 15 The cell cycle is the life cycle of a cell. At the end of the cell cycle, after mitosis has taken place, the parent cell no longer exists; it has given rise to two daughter cells. There are two phases in the cell cycle, *interphase* and *mitosis*. Mitosis is the technical term for the division of the chromosomes. *Cytokinesis*, when the cell itself actually splits, is the division of the cytoplasm. ©The McGraw-Hill Companies

Furthermore, the polymer particles are stable and do not seem to aggregate in the culture medium. The vital keratinocytes were incubated for 90 min with the MIP suspensions in cell culture medium. Figure 16 shows that the binding of the polymer particles is limited to areas where cells were present, indicating specific binding to hyaluronan or sialic acid. Thus, imaging of live cells is possible; this paves the way to real-time imaging of changes in hyaluronan or sialic acid within the cells. Multiplexed live cell imaging of the overexpressed polysaccharides could provide some information on the levels of the extracellular and intracellular glycosylations during the cell cycle. MIPGlcA-QDs (green) and rhodamine-MIPNANA (red) were used to demonstrate multiplexed staining in living cells.

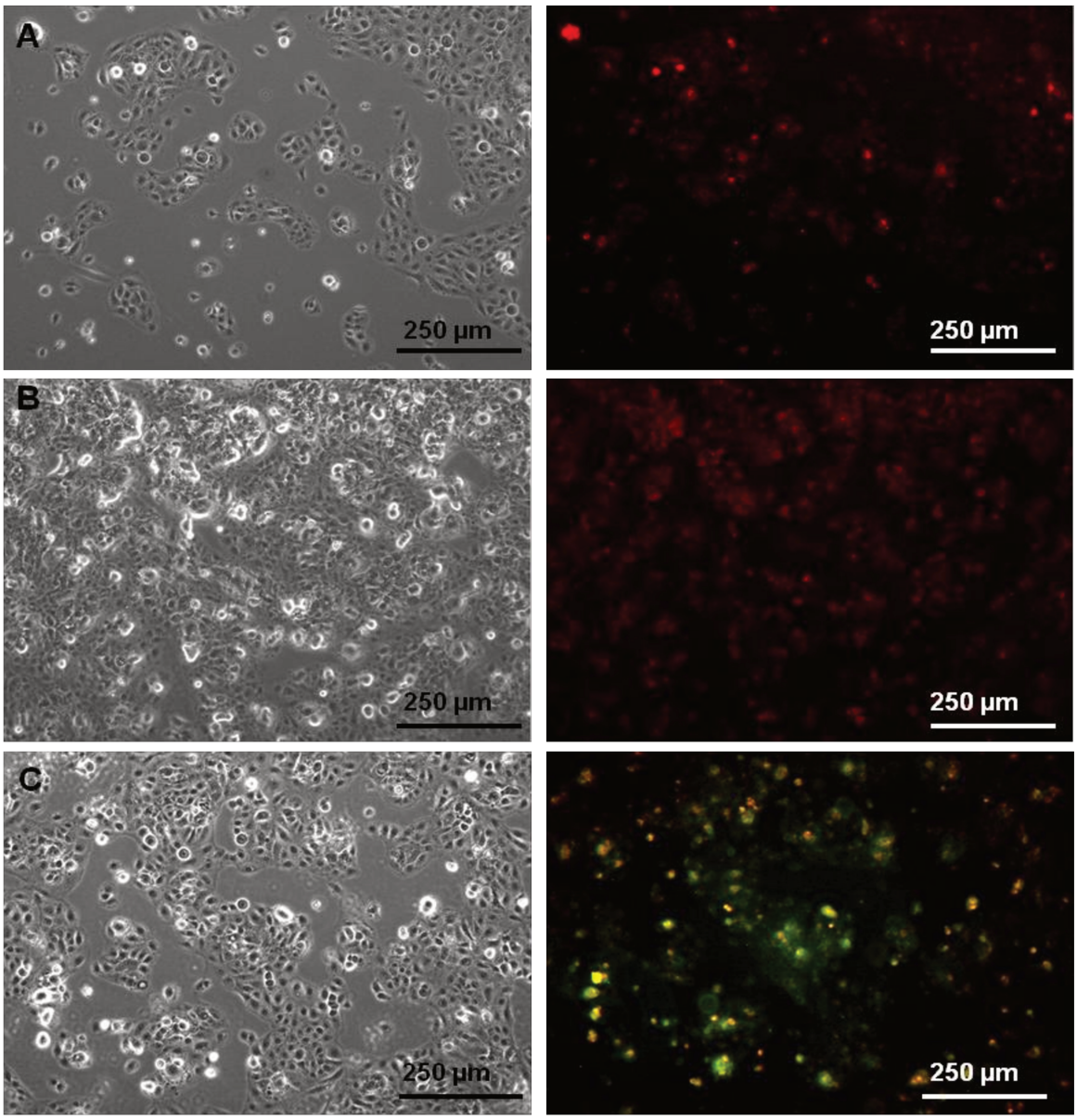

Figure 16 Vital keratinocytes grown on cover slips and stained with (A) rhodamine-MIPGlcA; (B) rhodamine-MIPNANA and (C) MIPGlcA-QDs (green) and rhodamine-MIPNANA (red) for simultaneous dual targeting and imaging (right) with their corresponding phase contrast (left).

3.2.7 Tissue imaging

Skin is the largest and one of the most important organs in human body since it prevents harmful substances from entering, and provides a protection-shield against the outer environment. It accounts for 15% of the body weight and 70% is made up of water. Its 7 layers consist of: epidermis (which is composed of 5 sublayers), dermis, and hypodermis (Figure 17). Epidermis is

the outer layer, no thicker than a sheet of paper and serves as an outer protection-shield. Dermis is the thick middle layer and makes up most of the skin. It contains collagen and elastin fibers that provide strength, structure and elasticity. Finally, the hypodermis layer mainly consists of fat and is the source of nerves and blood vessels as well as the roots of the hair follicles, sebaceous glands and sweat glands.

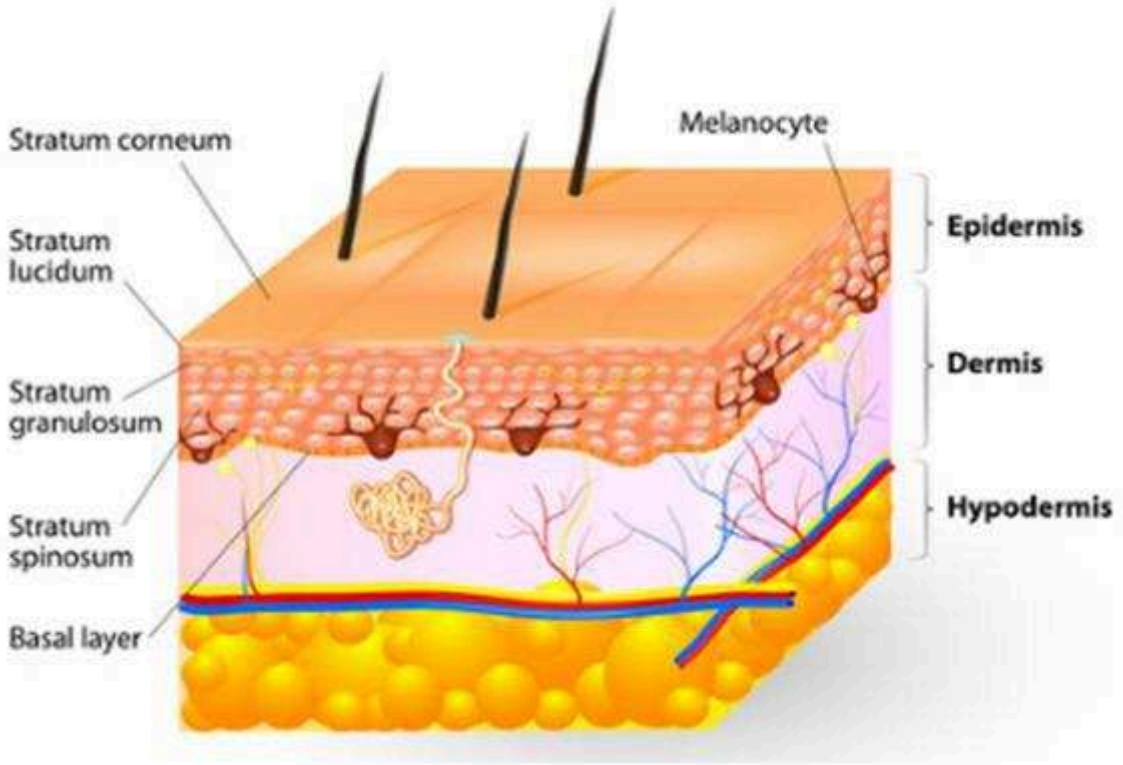

Figure 17 The layers of human skin. Image reproduced from Shutterstock.

According to the literature, the highest concentration of hyaluronan is found in the papillary dermis and the basal layer of the epidermis (stratum basale). Medium concentrations of hyaluronan are also expected in the spinous cell layer (stratum spinosum) and lowest ones for stratum granulosum, stratum lucidum and stratum corneum.

Molecularly imprinted polymers were applied to human skin specimen to establish their usefulness for tissue imaging. Human skin specimen were sliced, immobilized on microscope slides, fixed with acetone and stained with MIPs imprinted with glucuronic acid (Figure 18,19).

As demonstrated in Figure 18, MIPs bound to the skin tissue are mainly localized in the basal layer of the epidermis and the papillary dermis. Lower amounts of imprinted polymer particles can be found in the cornified and granular cell layer and even lower amounts in the spinous cell layer.

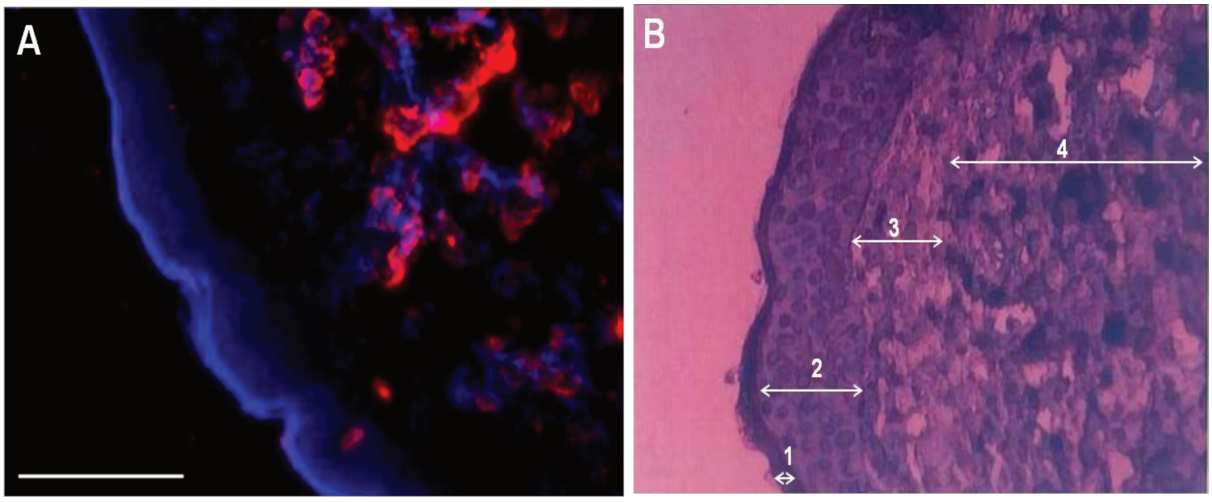

Figure 18 For the localization of the Rhodamine-MIPGlcA confocal microscopy images (A) and hematoxylin-eosin staining (B) were compared. In (B): 1 is the stratum granulosum, stratum lucidum and stratum corneum; 2 is the spinous cell layer; 3 is the basal cell layer (stratum basale) and 4 is the papillary dermis. Hematoxylin stains blue the cell nucleus and eosin stains red the cytoplasm. Scale bar: 100 µm.

This is in good agreement with the reports in the literature [42–44] on hyaluronan localization, and also with the results obtained with FITC-labeled HABP applied to tissue samples from the same batch and prepared in the same way (Figure 19). Only the localization of HABP in the spinous cell layer is slightly higher than that of MIPs. However, the shape and structure of the hyaluronan exposing regions of cells are very similar with both imaging methods. Again it should be noted that MIP staining could be easily coupled with two other dyes, DAPI and DiO, without interferences.

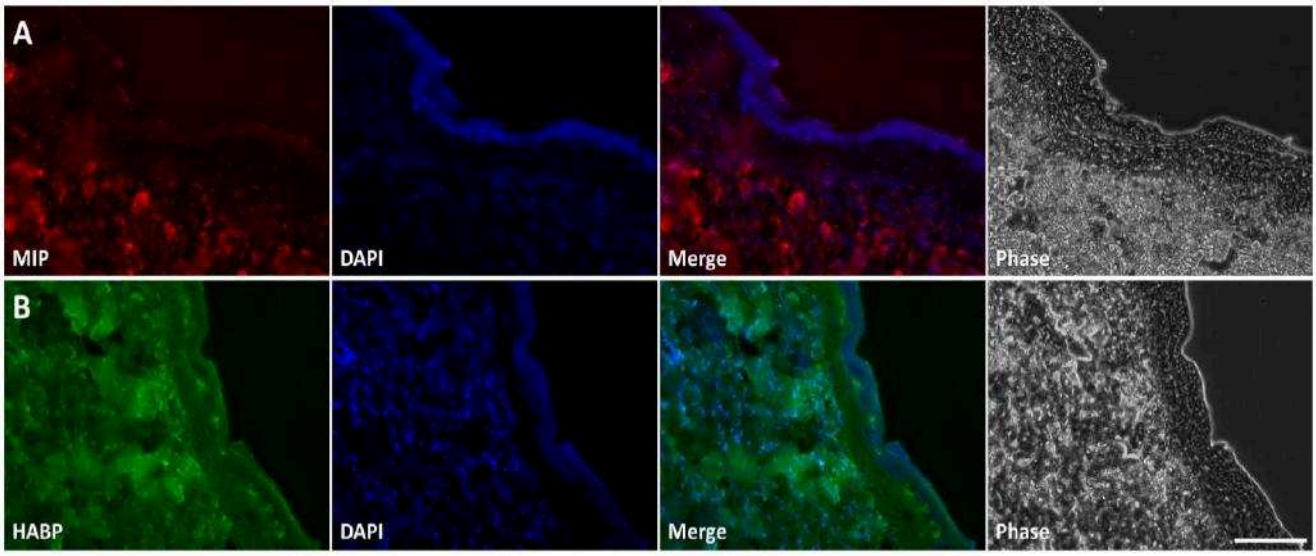

Figure 19 Human skin specimens stained with (A) rhodamine-MIPGlcA and B) FITC-labeled hyaluronic acid binding protein (HABP). Scale bar: 100 µm.

3.3 Materials and Methods

3.3.1 Reagents and Materials

All chemicals and solvents were of analytical grade and purchased from Sigma-Aldrich (St-Quentin Fallavier, France) or from VWR International (Fontenay-sous-Bois, France), unless otherwise stated. Glycine and paraformaldehyde (PFA) were from Applichem. Hyaluronic acid binding protein (HABP) was from Merck. Methacryloxyethyl thiocarbonyl rhodamine B (PolyFluor 570) was purchased from Polysciences Inc. (Warrington, USA). HaCaT cells were obtained from Cell Lines Service (Eppelheim, Germany). KU812 cells were obtained from the American Tissue Culture Collections (ATCC) (Virginia, USA). Glass cover slips, cell culture flasks (crystal-grade polystyrene), 12 well-plates (crystal-grade polystyrene), penicillin/streptomycin, Dulbecco's Modified Eagle Medium (DMEM), Roswell Park Memorial Institute 1640 (RPMI-1640) medium, fetal bovine serum (FBS), 0.4% Trypan Blue, 0.25% trypsin/ethylenediaminetetraacetic acid (EDTA) were from Thermo Scientific (Illkirch, France). Microscope slides for cell samples were from Roth Sochiel E. U. R. L. (Lauterbourg, France). Polymer suspensions were ultrasonicated with the microtip of a Branson Sonifier 250. Water was

purified using a Milli-Q system (Millipore, Molsheim, France). Skin tissue specimens were provided by Jörg Sänger (Institute of Pathology Bad Berka, Germany).

3.3.2 Cell culture

Human adult low calcium high temperature (HaCaT) cells were cultured in DMEM-high glucose with 10% FBS and 1% penicillin/streptomycin medium, hereafter referred as cell culture medium in the text, at 37 °C, 5% CO_2 and 100% humidity. Cells were passaged when confluent using 0.25% trypsin/EDTA in PBS buffer. For biochemical assays and microscopic studies, the cells were cultured in 12-well plates (well diameter 22.1 mm) equipped with round glass cover slips (diameter 12 mm). 100 µL of 1 x 10^5 suspended HaCaT cells were pipetted onto each cover slip. After 3 h of incubation, 2 mL of medium was added to the cells. Afterwards, they were left to grow to confluency for 48–60 h. Human chronic myelogenous leukemia cells KU812 were cultured in RPMI-1640 medium with 10% FBS and 1% penicillin/streptomycin at 37 °C, 5% CO_2 and 100% humidity. Fresh medium was added every 2-3 days with removal of the old medium by centrifugation and subsequent resuspension at 3 x 10^5 viable cells/mL.

Cell counting

Cell counting was performed using a disposable hemocytometer. Confluent cells were collected and centrifuged for 5 min at 400 *g*. Then the cell pellet was resuspended in 5 mL of culture medium and the cell suspension was transferred to a 50 mL conical polypropylene centrifuge tube. Subsequently, 15 mL culture medium were added in order to get a final volume of 20 mL. Before the cells get the time to sediment, 500 µL of the cell suspension was transferred into an Eppendorf tube. In another Eppendorf tube, 400 µL of 0.4 % Trypan Blue was pipetted and 100 µL of the previous cell suspension was added. Afterwards, 100 µL of the Trypan Blue-treated cells were pipetted into the well of the counting chamber of the hemocytometer. A microscope with a 10x magnification objective was used and the live, unstained cells were counted using a hand tally counter (living cells are impermeable to Trypan Blue). To obtain the number of viable cells/mL in the original cell suspension, the average cell count from each of the sets of the 16

corner squares of the hemocytometer was calculated and then multiplied by 10^4. This number was further multiplied by 5 to correct for the 1:4 dilution from the Trypan Blue addition.

3.3.3 Sample preparation and cell fixation for epifluorescence and confocal microscopy imaging

Each cover slip with confluent HaCaT cells in 12-well plates was washed 3 times with 2 mL PBS and fixed at room temperature for 10 min in 600 μL paraformaldehyde (3% w/v) in PBS. To stop fixation, each cell sample was incubated 3 times with 1 mL 20 mM glycine in PBS for 20 min at room temperature and finally they were washed 3 times with 2 mL PBS. After fixation, the cells were incubated for 90 min with 600 μL hyaluronidase (sheep testis) (75 U) or neuraminidase (Arthrobacter ureafaciens) (25 U) solution in PBS at 37 °C (positive control) or left in PBS without enzyme (untreated samples). The cells were then washed 3 times with 1 mL methanol: water (1:30) and then incubated with either 1 mL of a sonicated polymer suspension of 0.06 mg/mL MIPGlcA-QDs or MIPNANA-QDs or 0.027 mg/mL rhodamine MIPGlcA or rhodamine MIPNANA, in methanol: water (1:30) at 37 °C for 90 min. Afterwards, each fixed cell layer was washed 3 times with 1 mL methanol: water (1:30) and then mounted for fluorescence microscopy imaging on a microscope slide with 5 μL mounting medium. The mounting medium consisted of 0.5 mL water, 0.5 mL 1 M Tris HCl buffer pH 8 and 9 mL glycerol. For the staining of the cell nucleus, a stock solution of 1 mg/mL 4′,6-diamidin-2-phenylindol (DAPI) in water was diluted 10 times with mounting media. 5 μL from that solution was placed on a microscope slide to mount the cells on cover slips. After 3 min, the image capture took place.

To fix the KU812 cells, in a cell suspension of 2 x 10^6 cell/mL, an equal amount of 3% (w/v) paraformaldehyde in PBS was added to create a 1 x 10^6 cell/mL suspension and the cells were incubated for 10 min at room temperature. Then, clean cover slips were placed in the buckets of a swing bucket centrifuge (Whatman paper was used to soak any cell solution that fell from the cover slips) and were spotted with a few microliters of the cell suspension and centrifuged at low speed. The staining of the KU812 cells was performed in a similar way to the HaCaT cell staining.

3.3.4 Staining with hyaluronic acid binding protein

HaCaT cells were grown on cover slips and fixed in 3% (w/v) paraformaldehyde in PBS. Enzymatic treatment with hyaluronidase was performed when needed. Afterwards, 25 µg hyaluronic acid binding protein (HABP) from a stock solution (50 µg HABP in 1% BSA, 0.05 % Tween 20 in PBS) was diluted in 5 mL PBS. From that, 800 µL per cell sample were used to incubate at 4 °C overnight. After that, the cells were rinsed 3 times with PBS and incubated with 0.2 U streptavidin-FITC in PBS per cell sample at 4 °C for 30 min, followed by 3 times rinsing with PBS. After that, the samples were mounted with 10 µL mounting media on glass microscope slides for fluorescence microscopy imaging. All samples were prepared in duplicate per experiment (n = 2). Each experiment was repeated at least 3 times.

3.3.5 MIP incubation on live cell samples

Rhodamine-labeled

HaCaT cells were grown on cover slips to confluency in duplicate as described above. Afterwards, they were washed 3 times with PBS and 3 times with cell culture medium and incubated with 1 mL of a 0.027 mg/mL rhodamine-MIPs suspension in cell culture medium at 37 °C for 90 min. Then, the samples were washed 3 times with cell culture medium and mounted on microscopy slides for imaging.

Multiplexed imaging

For multiplexed imaging, the cells were prepared as described above and incubated with suspensions of 1 mL of 0.027 mg/mL rhodamine-MIPNANA and 1 mL of 0.06 mg/mL MIPGlcA-QDs in cell culture medium at 37 °C for 90 min. Then, the samples were washed 3 times with cell culture medium and mounted on microscopy slides for imaging.

Cytotoxicity testing

Cell viability in presence of MIPs was determined using the MTT assay. The MTT assay is a colorimetric assay for assessing the metabolic activity of living cells. These enzymes reduce the tetrazolium dye 3-(4,5-dimethylthiazol-2-yl) 2,5-diphenyltetrazolium bromide (MTT) to form insoluble formazan, which has a purple color. HaCaT cells were grown to confluency as described above. After trypsinisation, the cells were diluted with cell culture medium to 15,000 cells, which were seeded in each well of a 96-well plate. After 24 h, cells were incubated with MIP (1–27 µg/mL) or $CdCl_2$ (0–8.25 µg/mL) for 24 h in cell culture medium. Dissolution of the blue crystals of MTT was achieved by DMSO and Sorensen's buffer. Cell viability was determined by dividing the absorbance obtained for treated cells by that of the untreated controls.

3.3.6 Tissue Imaging

Adult skin specimens were collected by autopsy in the Institute of Pathology Bad Berka. The samples were sliced in 8 µm thick sections in a cryostat, transferred to adhesive microscope slides, dried and fixed for 10 min with cold acetone (-10 °C). The sections were then washed 3 times with PBS. Afterwards, the tissue samples were either incubated with a rhodamine-MIPGlcA suspension or with HABP. The sample preparation for MIP staining included 3 washing steps with 1 mL methanol/water (1:30) and an incubation step with 1 mL of a tip-sonicated rhodamine-MIPGlcA suspension of 0.027 mg/mL polymer in methanol/water (1:30) at 37 °C for 90 min. Afterwards, each tissue sample was washed 3 times with 1 mL methanol/water (1:30) and then mounted for fluorescence microscopy imaging with a cover slip and 20 µL mounting medium containing 100 µg/mL DAPI. The sample preparation for HABP included the addition of 5 µg HABP in 1 mL PBS to each of the tissue samples. Incubation took place at 4 °C overnight. Then, the tissue samples were rinsed 3 times with cold PBS and incubated with 0.2 U streptavidin-FITC in PBS at 4 °C for 30 min and subsequently rinsed 3 times with cold PBS. After that, the samples were mounted with 20 µL mounting media containing 100 µg/mL DAPI and covered with a cover slip for fluorescence microscopy imaging. All tissue specimens were at least prepared in four replications (n = 4).

Hematoxylin-eosin staining

Adult skin specimens were prepared as previously mentioned: The samples were sliced in 8 µm thick sections in a cryostat, transferred to adhesive microscope slides, dried and fixed for 10 min with cold acetone (-10 °C). The sections were then washed 3 times with PBS. Afterwards, the tissues were stained in a hematoxylin Meyer's solution by dipping them till covered and incubating them for 15 min. Afterwards, the samples were washed with tap water till they turn to blue for about 20 min and incubated for 1 min in alcoholic eosin. Further washing in 100% ethanol was performed and subsequently in xylene till the samples get clear. After that, the samples were mounted with 20 µL mounting media and used for microscopy. With the hematoxylin-eosin staining the nuclei appear blue and the cytoplasm red.

3.3.7 Fluorescence image capturing and analysis

Epifluorescence images were captured with a Leica DMI 6000B microscope, filter set A4, L5, TX2, N PLAN L 20.0 x 0.40 DRY, HCX PL FLUOTAR 40.0 x 0.60 DRY, HCX FLUOTAR 63.0 x 0.70 DRY and HCX FLUOTAR 100.0 x 1.30 OIL objectives with 20x, 40x, 63x and 100x magnification. Images were captured using exactly the same settings concerning light intensity and exposure time in 16-Bit Tiff format. Only confluent cell layers were examined for quantification studies and when quantitative analysis was carried out, nuclear staining was not performed. From each sample, at least 4 images were captured with the Leica Application Suite (LAS) software and each cell sample was at least prepared in quadruplicate. All fluorescence intensities were determined with Image J (National Institute of Health, USA, version 1.45s). For image analysis, prior background subtraction was necessary in order to determine the fluorescence signal coming from the particles. As a control for the background signal, samples with fixed cells were used and the average background signal at 4 different areas of each gray value image was subtracted prior to quantification. Furthermore, a slight difference in the fluorescence intensity from MIP and NIP particles was corrected during the quantification using Image J. Confocal microscopy images were captured with a Zeiss LSM 710, AxioObserver. A Plan-Apochromat 63x/1.40 Oil DIC M27 objective and 405 nm, 488 nm and 543 nm lasers were used for all images.

3.4 Conclusion

In biology, glycosylation refers mainly to the enzymatic process for the attachment of glycans to proteins and is critical for a wide range of biological processes in health and disease, since altered glycosylation levels are indicators of pathological conditions like malignancy. Generally, for imaging the glycome, lectins and antibodies are mostly employed. Nevertheless, lectins and antibodies against sugars are generally tissue-impermeable and might lack specificity. In this context, tailor-made molecularly imprinted polymers are promising synthetic receptor materials for imaging the glycosylation sites. The work described in this chapter constitutes the first cell imaging example using MIPs as recognition ligands. More precisely, we have synthesized molecularly imprinted polymers, either labeled with the fluorescent organic dye Rhodamine or with QDs (see Chapter 2), for selectively targeting and imaging hyaluronan and sialylated glycosylation sites on/in human keratinocytes. A standard immunostaining protocol was successfully adapted for MIP staining on fixed cells. It is worth noting that the MIP protocol is more advantageous as it is straightforward and does not require primary and secondary antibodies. Simultaneous dual-color imaging of the cells with two MIP-coated QDs of different emission colors (red for targeting the sialic acid moiety and green for targeting the glucuronic acid of hyaluronan) was also demonstrated, proving the versatility of our method. Moreover, the MIPs were not cytotoxic for the low concentrations required for bioimaging and could be applied to live cell labeling, which opens the way to the possibility of real-time imaging of glycosylation level and distribution in the cells. Nevertheless, in order to render MIPs generally applicable in biomedicine, where toxicity of the polymerization precursors is a matter of concern, special attention needs to be paid to the choice of the monomers, solvent, template and initiator. In Chapter 4, a “greener” initiator-free MIP synthesis is proposed. In the present chapter, successful tissue imaging was also demonstrated and the MIPs were located in the basal layer of the epidermis and the papillary dermis, results that are in accord with the literature and with the control staining using HABP. In addition, staining of the chronic leukemia cell line KU812 was also performed, proving the potential of MIPs in cancer theranostics. This kind of synthetic receptors is a powerful bioimaging tool that can also behave as a targeted drug delivery device or a specific blocking agent on cells and tissues.

3.5 References

[1] K. W. Moremen, M. Tiemeyer, A. V Nairn, *Nat. Rev. Mol. Cell Biol.* **2012**, *13*, 448–62.

[2] R. G. Spiro, *Glycobiology* **2002**, *12*, 43R–56R.

[3] F. Bard, J. Chia, *Trends Cell Biol.* **2016**, *26*, 379–88.

[4] K. Ohtsubo, J. D. Marth, *Cell* **2006**, *126*, 855–67.

[5] P. M. Rudd, T. Elliott, P. Cresswell, I. A. Wilson, R. A. Dwek, P. Cresswell, M. Sugita, H. A. Chapman, B. Manoury, S. A. Porcelli, et al., *Science* **2001**, *291*, 2370–6.

[6] V. C. Hascall, A. K. Majors, C. A. De La Motte, S. P. Evanko, A. Wang, J. A. Drazba, S. A. Strong, T. N. Wight, *Biochim. Biophys. Acta* **2004**, *1673*, 3–12.

[7] N. M. Varki, A. Varki, *Lab. Invest.* **2007**, *87*, 851–7.

[8] S. Seton-Rogers, *Nat. Rev. Cancer* **2012**, *12*, 228–228.

[9] C. Büll, M. A. Stoel, M. H. den Brok, G. J. Adema, *Cancer Res.* **2014**, *74*, 3199–204.

[10] N. Sharon, *J. Biol. Chem.* **2007**, *282*, 2753–64.

[11] H. Ghazarian, B. Idoni, S. B. Oppenheimer, *Acta Histochem.* **2011**, *113*, 236–247.

[12] F. Lehmann, E. Tiralongo, J. Tiralongo, *Cell. Mol. Life Sci.* **2006**, *63*, 1331–54.

[13] S. T. Laughlin, C. R. Bertozzi, *Proc. Natl. Acad. Sci.* **2009**, *106*, 12–17.

[14] H. Ohba, R. Bakalova, *Cancer Chemother. Pharmacol.* **2003**, *51*, 451–8.

[15] S. Carlsson, M. C. Carlsson, H. Leffler, *Glycobiology* **2007**, *17*, 906–12.

[16] A. Kawamura, I. Kijima-Suda, M. Sugimoto, M. Itoh, K. Takada, K. Tomita, T. Ogawa, Y. Nagai, *Biochim. Biophys. Acta* **1990**, *1033*, 201–6.

[17] C. A. de la Motte, J. A. Drazba, *J. Histochem. Cytochem.* **2011**, *59*, 252–7.

[18] E. Sterner, N. Flanagan, J. C. Gildersleeve, *ACS Chem. Biol.* **2016**, *11*, 1773–1783.

[19] K. Licha, N. Debus, S. Emig-Vollmer, B. Hofmann, M. Hasbach, D. Stibenz, S. Sydow, M. Schirner, B. Ebert, D. Petzelt, et al., *J. Biomed. Opt.* **2005**, *10*, 41205.

[20] T. D. James, M. D. Phillips, S. Shink, in *Boronic Acids Sacch. Recognit.*, Royal Society Of Chemistry, Cambridge, **2006**, pp. 3–176.

[21] A. Liu, S. Peng, J. C. Soo, M. Kuang, P. Chen, H. Duan, *Anal. Chem.* **2011**, *83*, 1124–1130.

[22] S. Shinde, Z. El-Schich, A. Malakpour, W. Wan, N. Dizeyi, R. Mohammadi, K. Rurack,

A. Gjörloff Wingren, B. Sellergren, *J. Am. Chem. Soc.* **2015**, *137*, 13908–12.

[23] Z. El-Schich, M. Abdullah, S. Shinde, N. Dizeyi, A. Rosén, B. Sellergren, A. G. Wingren, *Tumour Biol.* **2016**, DOI 10.1007/s13277-016-5280-y.

[24] D. Yin, S. Wang, Y. He, J. Liu, M. Zhou, J. Ouyang, B. Liu, H.-Y. Chen, Z. Liu, S. Nie, et al., *Chem. Commun.* **2015**, *51*, 17696–17699.

[25] S. Wang, D. Yin, W. Wang, X. Shen, J.-J. Zhu, H.-Y. Chen, Z. Liu, P. Chakravarty, E. O. Serebrovskaya, M. Ogawa, et al., *Sci. Rep.* **2016**, *6*, 22757.

[26] S. Kunath, M. Panagiotopoulou, J. Maximilien, N. Marchyk, J. Sänger, K. Haupt, *Adv. Healthc. Mater.* **2015**, *4*, 1322–1326.

[27] S. P. Evanko, W. T. Parks, T. N. Wight, *J. Histochem. Cytochem.* **2004**, *52*, 1525–35.

[28] L. M. Steirer, G. R. Moe, *PLoS One* **2011**, *6*, e27249.

[29] *http://www.who.int/en/* **2012**.

[30] P. S. Patel, S. G. Adhvaryu, B. R. Baxi, *Int. J. Biol. Markers* **1991**, *6*, 177–82.

[31] N. Abd, E. Maksoud, H. M. Ragab, M. M. Abd, E. Latif, S. Abdalla, *J. Am. Sci.* **2010**, *6*, 423–432.

[32] J. J. Hutter, R. Schulze-Rath, G. Hammer, M. Blettner, L. Kheifets, R. Shimkhada, X. Shu, J. Perentesis, W. Wen, L. Alderton, et al., *Pediatr. Rev.* **2010**, *31*, 234–41.

[33] M.-H. Sung, J. G. McNally, *Wiley Interdiscip. Rev. Syst. Biol. Med.* **2011**, *3*, 167–182.

[34] D. J. Stephens, V. J. Allan, *Science* **2003**, *300*, 82–6.

[35] W.-Y. Cheng, W.-L. Hsu, H.-H. Cheng, Z.-H. Huang, Y.-C. Chang, *Anal. Biochem.* **2009**, *386*, 105–12.

[36] P. J. Keller, A. D. Schmidt, A. Santella, K. Khairy, Z. Bao, J. Wittbrodt, E. H. K. Stelzer, *Nat. Methods* **2010**, *7*, 637–642.

[37] R. N. Day, F. Schaufele, *Mol. Endocrinol.* **2005**, *19*, 1675–86.

[38] E. M. Campbell, T. J. Hope, *Trends Microbiol.* **2008**, *16*, 580–7.

[39] T. Mosmann, *J. Immunol. Methods* **1983**, *65*, 55–63.

[40] C. F. Chou, M. B. Omary, *J. Biol. Chem.* **1993**, *268*, 4465–72.

[41] S. P. Evanko, T. N. Wight, *J. Histochem. Cytochem.* **1999**, *47*, 1331–42.

[42] R. Tammi, J. A. Ripellino, R. U. Margolis, M. Tammi, *J. Invest. Dermatol.* **1988**, *90*, 412–414.

[43] C. Wang, M. Tammi, R. Tammi, *Histochemistry* **1992**, *98*, 105–12.

[44] E. Papakonstantinou, M. Roth, G. Karakiulakis, *Dermatoendocrinol.* **2012**, *4*, 253–8.

CHAPTER 4

Initiator-free Synthesis of Molecularly Imprinted Polymers by Polymerization of Self-initiated Monomers

4.1 Introduction

The immense potential of nanotechnology in electronics, renewable energy, biomedical applications, food and agriculture, cosmetics and healthcare is evident. As discussed in the previous chapters, MIPs as a new biorecognition tool have drawn particular attention, showing an exponential increase in the number of papers and patents related to the field each year (Figure 1). The recent progress presented in this thesis proves that MIPs, as an innovative, cheap and robust alternative to their natural counterparts such as antibodies, peptides and aptamers, have a very promising future with great potential development in the food industry [1], theranostics and pharmaceutics [2–4], fields where their application has been little explored up till now.

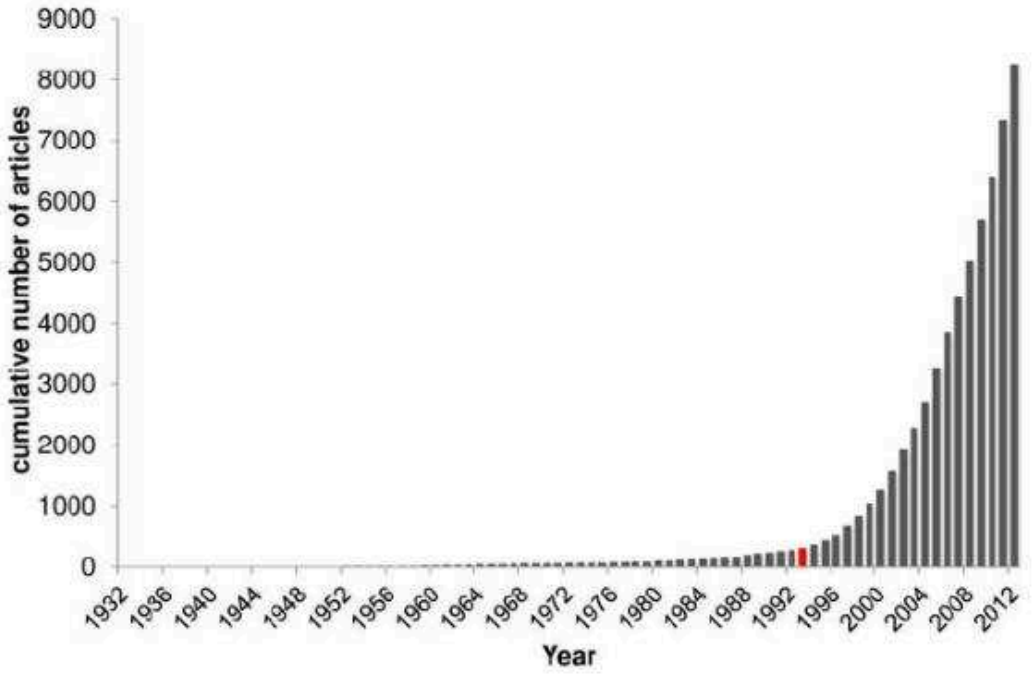

Figure 1 Cumulative number of MIP articles published in the period 1932-2012. Reproduced from [5].

In 2010 the first *in vivo* application of MIPs was reported by Hoshino et al., who employed MIPs imprinted against melittin (a peptide that is the principal component of bee venom) to remove that molecule from the bloodstream of living mice [4]. The mice were intravenously injected with melittin and MIPs were subsequently administered *via* the tail vein. The MIPs successfully

cleared melittin improving the survival rate of the mice over 24 h and reducing the toxic effects of the peptide (e.g., weight loss and peritoneal phlogosis). This study demonstrates the ability of MIPs for selective recognition of molecules *in vivo*.

Nevertheless, MIPs have not yet reached any real-life applications mainly due to the lack of comprehensive toxicological studies. A first biocompatibility assessment of MIPs (see also Chapter 3) shows that these nanoparticles are not cytotoxic for the concentrations typically used in biomedical applications. Shea et al showed the non-cytotoxicity of N-*tert*-butylacrylamide and acrylic acid MIPs cross-linked with either *N*,*N*′-Methylenebis(acrylamide) or *N*,*N*′-Ethylenebis(acrylamide) on human promyelocytic leukemia cells using the MTT cell viability assay up to particle concentrations of 100 µg/mL [6] or on fibrosarcoma cells using the Alamar Blue assay up to particle concentrations of 3000 µg/mL respectively [7]. In a more recent study, Canfarotta et al tested the cytotoxicity of methacrylic acid MIPs cross-linked with a mixture of EGDMA/Trimethylolpropane trimethacrylate (TRIM) on human keratinocytes, fibrosarcoma cells and mouse embryonic fibroblasts using the MTT test and found 100% viability for concentrations up to 50 µg/mL [8]. Similar results are obtained in our group for the cytotoxicity of AB/EGDMA-based polymers on human keratinocytes, where no cytotoxicity is observed for concentrations up to 100 µg/mL using MTT, though higher concentrations appear to be cytotoxic (unpublished results).

Because the toxicity of the polymerization precursors (monomers, solvents, template, initiator) and the final MIPs and the by-products of their synthesis (residual monomers, degradation products) could be a matter of concern for the future application of MIPs in the aforementioned fields, we propose to synthesize 'safer' MIPs by suppressing the use of initiators. Indeed, Dorn [9] has reported the danger of certain initiators to human health and the environment as they generate toxic decomposition products that may remain in the polymer or become incorporated in the polymer chain. Consequently, this study will have a dual function: simplifying the MIP precursor mixture, hence resolving the problem of finding a suitable solvent to solubilize both the initiator and the monomers, and the obtention of "greener" MIPs that would be more suitable for the fields of food industry and biomedicine.

Actually, most MIPs are synthesized by free radical polymerization, generated by the thermal or photo homolysis of a chemical bond on an initiator. The most widely used initiators for MIPs synthesis are benzoyl peroxide (BPO) [10,11], 2,2-dimethoxy-2- phenylacetophenone (DMPA) [12,13] and the azo compounds 2,2' -azobis(2-methylpropionitrile) (AIBN) [14–16] and 2,2' -azobis(2,4-dimethyl)valeronitrile) (ABDV) [17,18]. According to literature data [9,19] and the U.S Department of Health and Human Services, BPO decomposes into benzene, benzoic acid, phenyl benzoate, terphenyls, biphenyls, carbon monoxide and carbon dioxide; AIBN into tetramethylsuccinonitrile, hydrogen cyanide, carbon monoxide and carbon dioxide; additionally, DMPA, which bears a benzene ring, is suspected to have endocrine disrupting properties [19]. *In vivo* studies with a few micromoles of organic peroxides, an amount comparable to that used in routine MIPs' synthesis, and azo initiators have shown their carcinogenicity and toxicological effects on biological tissues [20,21].

Interestingly, a few acrylic monomers [22,23] like acrylic acid (AA), methacrylic acid (MAA), 2-hydroxyethyl acrylate, 2- hydroxyethyl methacrylate (HEMA), glycidyl acrylate, poly(- ethylene glycol) methacrylate and a styrenic monomer (styrene) [24] were reported to perform self-initiated photopolymerization and photografting under UV irradiation in the complete absence of photoinitiator or any other additives. Photodissociation of for instance AA can be due to cleavages of C-C and C-O bonds to form free radicals. These free radicals are then capable to initiate a chain process. Another explanation would be that the monomers are excited by the UV light to a triplet state (T_3) with enough energy to abstract hydrogen and induce radical formation. For styrene (St), a triplet state can also be reached after photon absorption. This triplet state is in equilibrium with a biradical species (˙St˙) which initiates a free radical in solution or can also abstract a hydrogen radical [24]. Additionally, styrene can also self-initiate by thermal polymerization. The mechanism first involves the formation of a Diels-Alder dimer of styrene, followed by hydrogen transfer from the dimer to styrene to generate two monoradical species that initiates polymerization [25]. Concerning the acrylic monomers, it has been reported that self-initiation occurs solely by UV irradiation as no polymers were formed when they were left in an oven at 80 °C [22].

However, it is not obvious and far from trivial that MIPs can be synthesized by exploiting the self-initiating abilities of these monomers, if we take into account the complexity of these materials and the specific conditions that have to be met for imprinting to occur (use of at least two different monomers, necessity of cross-linking, presence of the imprinting template and a solvent, necessity to adapt polymerization conditions to create both porosity and molecularly imprinted cavities etc.). In this work, we investigated whether the monomers typically used for MIPs could be photo or thermally polymerized by self-initiation, i.e. without adding any initiator, under conventional MIP preparation conditions. Since the functional monomers are generally present in a large excess in order to shift the equilibrium towards the formation of the template-monomer complex [26], this implies that even if the monomers act as initiators, the formation of the template-monomer complex will be little affected. In this chapter we describe several examples of MIPs synthesized with these monomers without adding any initiator, using previously developed and well-established protocols for initiator-based MIPs. The binding behaviour, which proves that the imprinting process has taken place, as well as the morphology and size of the MIPs, were examined and compared to initiator-synthesized MIPs. Our results show that initiator-free synthesis expands the potential use of MIPs to real-life applications, where toxicity can be of concern.

4.2 Results and Discussion

Monomers reported in the literature of self-initiation abilities are MAA and HEMA [22,23]. The templates were chosen accordingly: one protein template (trypsin) and three small-sized templates (S-propranolol, 2,4-dichlorophenoxyacetic acid (2,4-D) and testosterone) were imprinted, without adding any initiator. The polymerization conditions for each polymer are described in Table 1. These examples were chosen to illustrate the various MIPs synthesis protocols (different polymerization solvents, temperature, cross-linkers, etc), commonly practised for batch synthesis. The parameters (ratio of template: monomer: cross-linker, solvent, cross-linking degree) are those commonly employed by our group and others for the preparation of initiator-based MIPs.

Table 1 Preparation of self-initiated polymers.

Template (mmol)	Functional monomer (mmol)	Cross-linker (mmol)	Solvent (mL)	C_m;CL (%)	Polymerization conditions[b]	Yield (%) MIP(NIP)
Trypsin (0.006)	AB_{HCl}/HEMA (0.006)/(0.47)	EbAM (0.71)	Buffer[a] (9.7)	2; 60	6 °C[d], 18 h	93 (85)
Propranolol (0.2)	MAA (1.6)	EGDMA (8)	CH_3CN (15) (40)	10; 83 4; 83	20 °C[e], 20 h	96 (48) 60 (22)
2,4-D (0.2)	4VP (0.8)	EGDMA (4)	CH_3OH:H_2O (15)	5.5; 83	6 °C[d], 20 h	19 (9)
2,4-D (0.2)	4VP (0.8)	EGDMA (1.7)	CH_3CN (12)	4; 68	20 °C[d], 18 h	50 (16)
Testosterone (0.2)	MAA (1.6)	EGDMA (5)	CH_3CN (1.5)	43; 76	6 °C[d], 20 h	45 (38)
Testosterone (0.2)	MAA (1.6)	DVB (5)	CH_3CN (1.5)	34; 76	Thermal 90 °C[c], 24 h	23 (11)

a) 25 mM sodium phosphate pH 7.0.
b) UV irradiation except where indicated.
c) Oil-bath.
d) Temperature on the lamp: 18 °C.
e) Temperature on the lamp: 40 °C.
C_m: total mass of functional and cross-linking monomers upon total mass of solvent and monomers; CL: moles of cross-linking monomers upon total moles of functional and cross-linking monomers

4.2.1 Trypsin MIPs

The polymers were synthesized as previously described [3], except that no initiator was added. The polymerization mixture contains HEMA and *N,N'*-ethylenebis(acrylamide) (EbAM), as functional and cross-linking monomers respectively plus an anchoring monomer, 4-acrylamidophenyl)(amino)methaniminium chloride (AB_{HCl}). *p*-Aminobenzamidine is an inhibitor of serine proteases and therefore AB_{HCl}, added in a 1:1 stoichiometry, acted as a polymerizable affinity ligand for trypsin. The cross-linking degree (CL) was 60%, the monomer concentration (C_m) was 2% and the polymerization was done in 25 mM sodium phosphate buffer pH 7.0 during 18 h (Table 1). CL is defined as the number of moles of cross-linking monomers upon the total number of moles of functional and cross-linking monomers and C_m is the total mass of functional and cross-linking monomers upon total mass of solvent and monomers.

Generally, trypsin MIP microgels are synthesized in our group by UV polymerization using the water soluble azo-initiator Vazo 56 (1.5% mol per mol of polymerizable double bonds) [3] or by thermal polymerization using tetramethylethylenediamine/potassium persulfate (3% mol/mol with respect to polymerizable double bonds) [27]. In this work, no initiators were added. Interestingly, the yield of polymerization was ~90%, even under the high dilution conditions used (2% w/w of total monomer concentration). HEMA has already been reported to photopolymerize by self-initiation [22], but there is no information available about whether EbAM can auto-initiate. For this reason, a similar polymerization mixture containing EbAM alone was left to polymerize under the same conditions as the MIP mixture. Polymerization occurred indicating that acrylamide-based monomers can self-initiate as well. Both HEMA and EbAM probably contributed to the self-initiation polymerization, producing cross-linked MIPs. The affinity of the polymers for trypsin was determined by equilibrium binding assays. At equilibrium, the polymers were removed by centrifugation and the residual activity of trypsin in the supernatant was determined, using N_{α}-*p*-tosyl-*L*-arginine methyl ester hydrochloride (TAME), as substrate. Figure 2A shows that specific imprinted sites were created in the self-initiated MIP, as there was more trypsin bound to the MIP than to the NIP. The imprinting factor (IF) which corresponds to the ratio trypsin bound to the MIP versus trypsin bound to the NIP was ~3, similar to that of initiator-triggered MIPs [3]. The selectivity of the MIP for trypsin was investigated by performing competitive binding experiments with thrombin and kallikrein, two other serine proteases inhibited by *p*-aminobenzamidine. MIP was incubated with 100 nM FITC-trypsin (see section 4.3 for its synthesis) together with 1 μM of non-labeled trypsin, kallikrein or thrombin. After incubation, the particles were separated by centrifugation and the free FITC-trypsin was quantified by fluorescence measurement. Figure 2B shows that the binding of FITC-trypsin to MIP is almost totally suppressed in the presence of trypsin, whereas kallikrein and thrombin displace much less of the fluorescent probe. These results prove that the MIP contains imprinted cavities that are highly selective for the target trypsin. The particle size and morphology of the self-initiated MIP-trypsin microgels were then characterized by scanning electron microscopy (SEM) and dynamic light scattering (DLS) analysis. As seen in Figure 2C, the particles appear agglomerated with a hydrodynamic size of ~1.5 μm (Figure 2D).

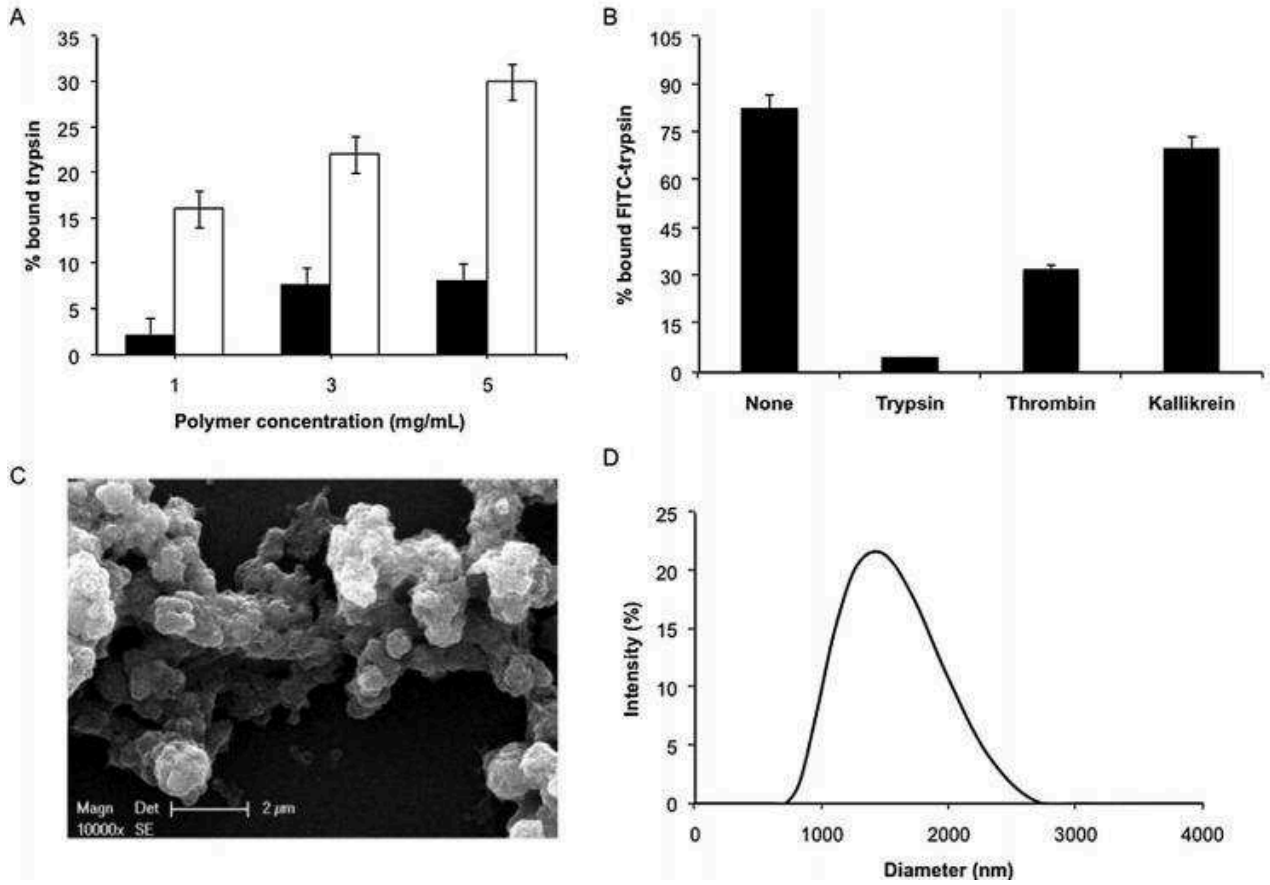

Figure 2(A) Equilibrium binding isotherms for trypsin (600 nM) on MIP (white) and NIP (black) microgels. Free trypsin was quantified by spectrophotometric measurements of its activity using TAME as substrate. (B) Displacement of bound FITC-trypsin (100 nM) from 3 mg/mL MIP by 1 µM trypsin, thrombin and kallikrein. Incubation medium: 5 mM Tris-HCl buffer, 10mM $CaCl_2$, pH 8.0. Dataaremeans from three independent experiments from two different batches of polymers.The error bars represent standard deviations. (C) SEM image and (D) DLS analysis of MIP-trypsin, prepared in water.

4.2.2 S-propranolol MIPs

MIPs for S-propranolol were synthesized by precipitation polymerization in acetonitrile as previously described [28], but no initiator was added. The polymerization mixture contains MAA as functional monomer and EGDMA as cross-linker with a ratio S-propranolol: MAA: EGDMA of 1:8:40 [29]. Monomer concentrations (C_m) of 10% and 4% were tested. In both cases, polymerization occurred (Figure 5B, inset), with a yield of 96% and 60%, respectively (Table 1). Similar yields, >95% have been reported for initiator-based polymers prepared by precipitation polymerization in acetonitrile, using trimethylolpropane trimethacrylate (TRIM) instead of EGDMA as crosslinker, a C_m of 2% and CL of 71% [30]. The binding properties of the polymers were evaluated by equilibrium binding assays in both ACN (the solvent of polymerization) and

in mixed-aqueous conditions (25 mM sodium citrate buffer pH 6.0:acetonitrile (50:50)) [30]. Figure 3A shows the binding behaviours of the polymers with C_m=10%; the MIPs adsorb the radioligand and show saturation-type behaviour, whereas the non-imprinted control polymers show nearly no binding, as reported for polymers prepared with initiators [28,30]. The high binding specificity was additionally confirmed by exploiting the intrinsic fluorescence of propranolol [31]. Thus, the binding was determined by measuring the fluorescence intensity of 1 nmol of S-propranolol ($\lambda_{ex=}$300 nm; λ_{em}=338 nm), incubated with various concentrations of polymers (Figure 4A). This amount is 1000-fold higher than the amount of radioactive analyte and allows to probe other binding sites with different affinities on the MIP; indeed, MIPs generated by the self-assembly approach generally contain a non-homogeneous distribution of binding sites [5,26,32,33].

The selectivity of the MIP for S-propranolol was studied by comparing the binding with the R-enantiomer. Competition studies at equilibrium were performed in ACN with the C_m=10% polymers. Fixed amounts of 0.1 mg of MIP and 0.7 pmol of radioactive S-propranolol and variable amounts of competing S-propranolol and R-propranolol from 1 nM to 100 µM were tested. The results are shown in Figure 3B. The values of IC_{50} (the concentrations of competing ligands required to displace 50% of the specifically bound radioligand) for S-propranolol and R-propranolol, determined from a non-linear regression fit were 3.4 and 47.3 µM respectively, which means that the cross-reactivity of R-propranolol with S-propranolol is 7.2%, comparable to the cross-reactivities (~5%) of initiator-based MIPs, assayed under similar equilibrium binding with a radioactive analyte [30]. This indicates that our MIP is selective for S-propranolol. Overall, these findings indicate that the recognition properties of the MIP are not affected when prepared in absence of initiator. It has been previously reported that the amount of initiator influences the performance of MIPs, in particular, large amounts of initiator increase the polymerization rate and the heat produced during the reaction, leading to an increase in the temperature inside the polymerization reaction thus causing the formation of poor quality imprinting sites [13]. In our case, a relatively mild temperature of maximum 37 °C was reached inside the polymerization mixture; this can explain the very good binding performance in terms of specificity and selectivity of the MIP (Figure 4B).

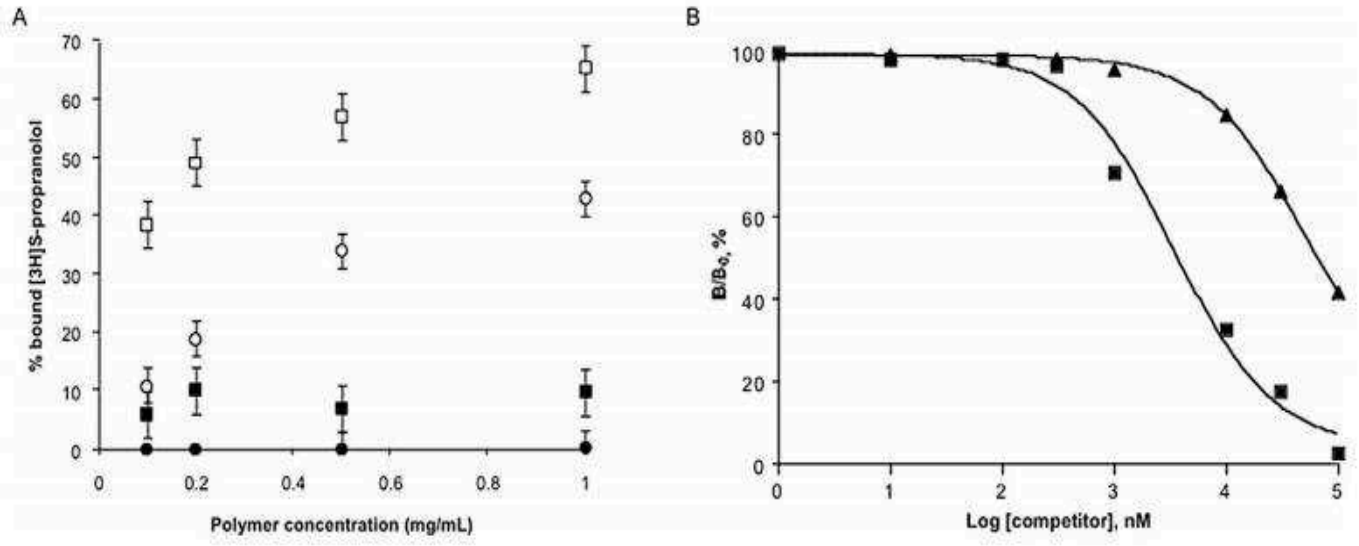

Figure 3 (A) Equilibrium binding isotherms for radiolabeled S-propranolol (0.7 pmol, 15 nCi) on MIP (open squares) and NIP (black squares) in acetonitrile and on MIP (open circles) and NIP (black circles) in 25 mM sodium citrate buffer pH 6.0:acetonitrile (50:50). Polymers were prepared with C_m: 10%. Data are means from three independent experiments from two different batches of MIP. The error bars represent standard deviations. (B) Inhibition of radioactive S-propranolol binding (0.7 pmol, 15 nCi) to 0.1 mg MIP-propranolol by S-propranolol (square) and R-propranolol (triangles) in ACN. B/B_0 is the ratio of the amounts of radioactive S-propranolol bound in the presence and absence of displacing ligand.

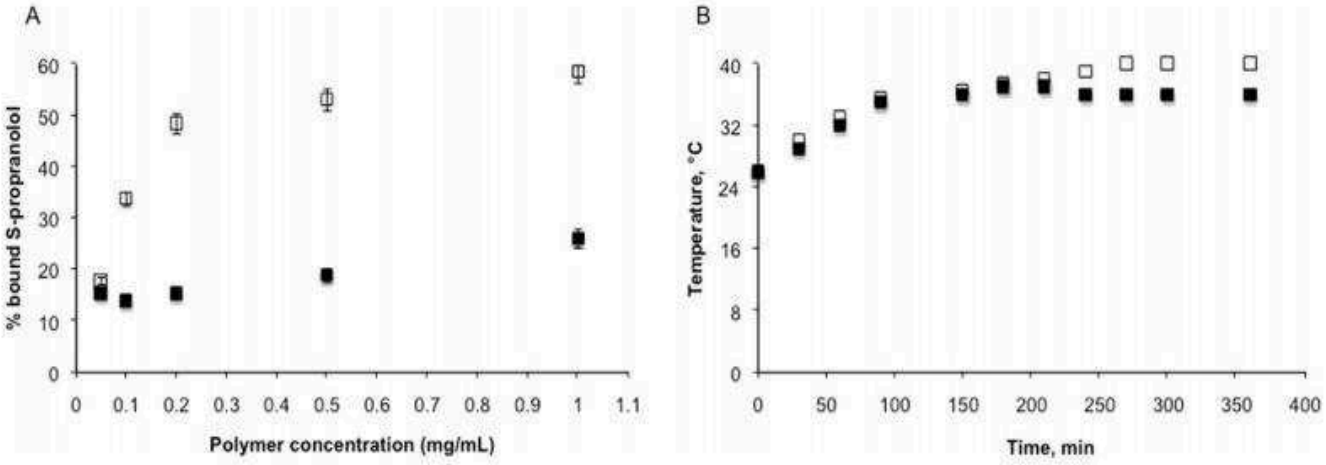

Figure 4 (A) Equilibrium binding isotherms for S-propranolol (1 nmol) on MIP (open squares) and NIP (black squares) in acetonitrile, as measured by fluorescence. Polymers were prepared with C_m: 10%. Data are means from three independent experiments. The error bars represent standard deviations. (B) Temperature inside the polymerization mixture, monitored with a thermocouple (black squares) and with a glass thermometer on the UV lamp (open squares). Polymerization vials were separated from the lamp by a glass Petri dish of 2-cm thickness.

The particle size of the MIP and the NIP, as measured by DLS is 441 nm and 340 nm respectively. The corresponding nanoparticulate clusters are seen on the SEM images (Figure 5); their morphologies are similar to ABDV-thermally initiated MAA-EGDMA polymers in ACN [28]. For the polymers with C_m 4%, the equilibrium binding isotherms in ACN indicate an equally high binding of the MIP but with a lower imprinting factor. The higher dilution of the polymerization mixture might account for both the lower number of good quality binding sites in the MIP and the lower polymerization yield. As expected for a more diluted medium, the MIP and NIP sizes are smaller than the polymers of C_m 10%, 350 nm and 273 nm respectively as measured by DLS (Figure 6).

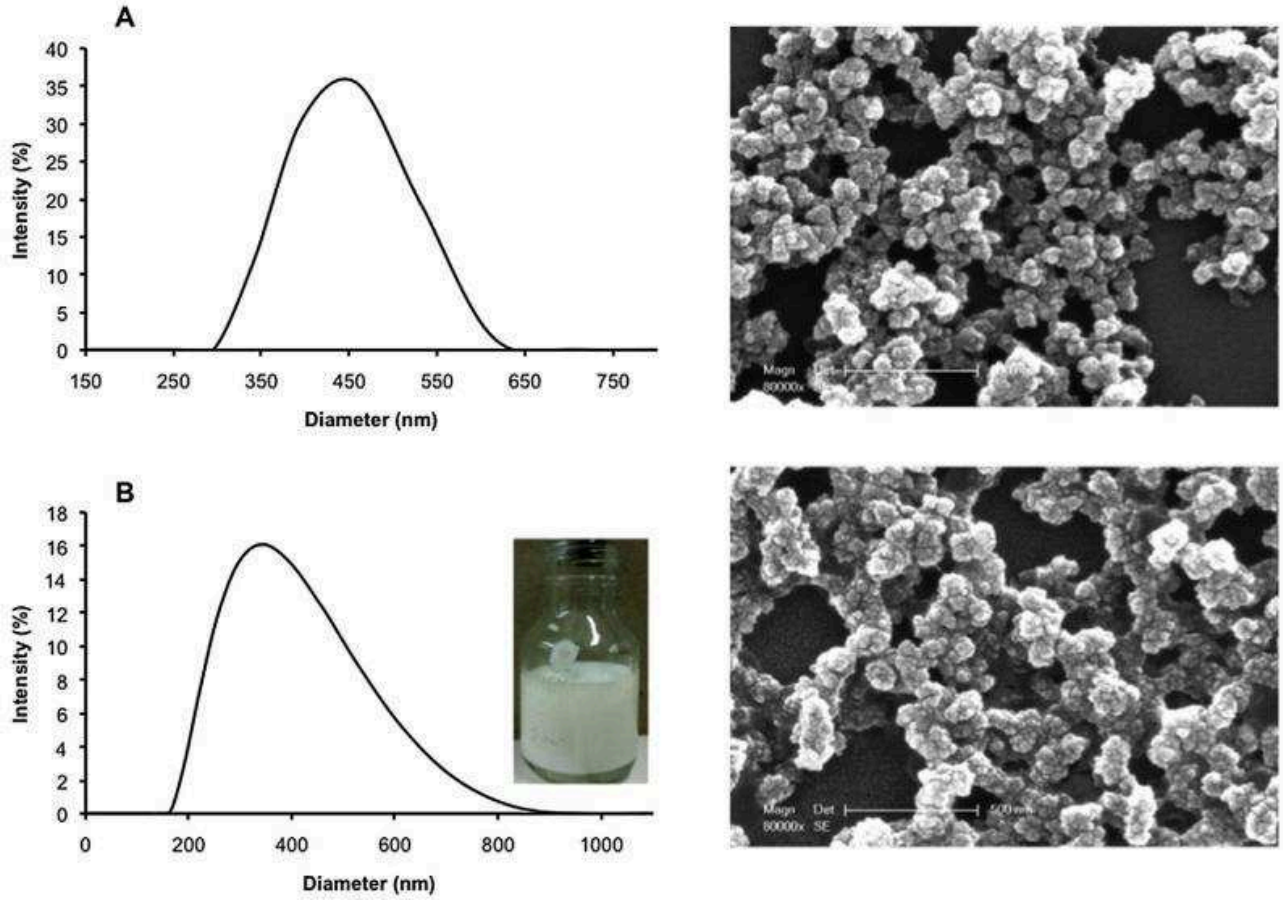

Figure 5 DLS measurements and SEM images (scale-bar represents 500 nm) of (A) MIP-propranolol and (B) NIP-propranolol. Inset: Photo of self-initiated MAA/EGDMA (C_m 10 %) polymer in ACN.

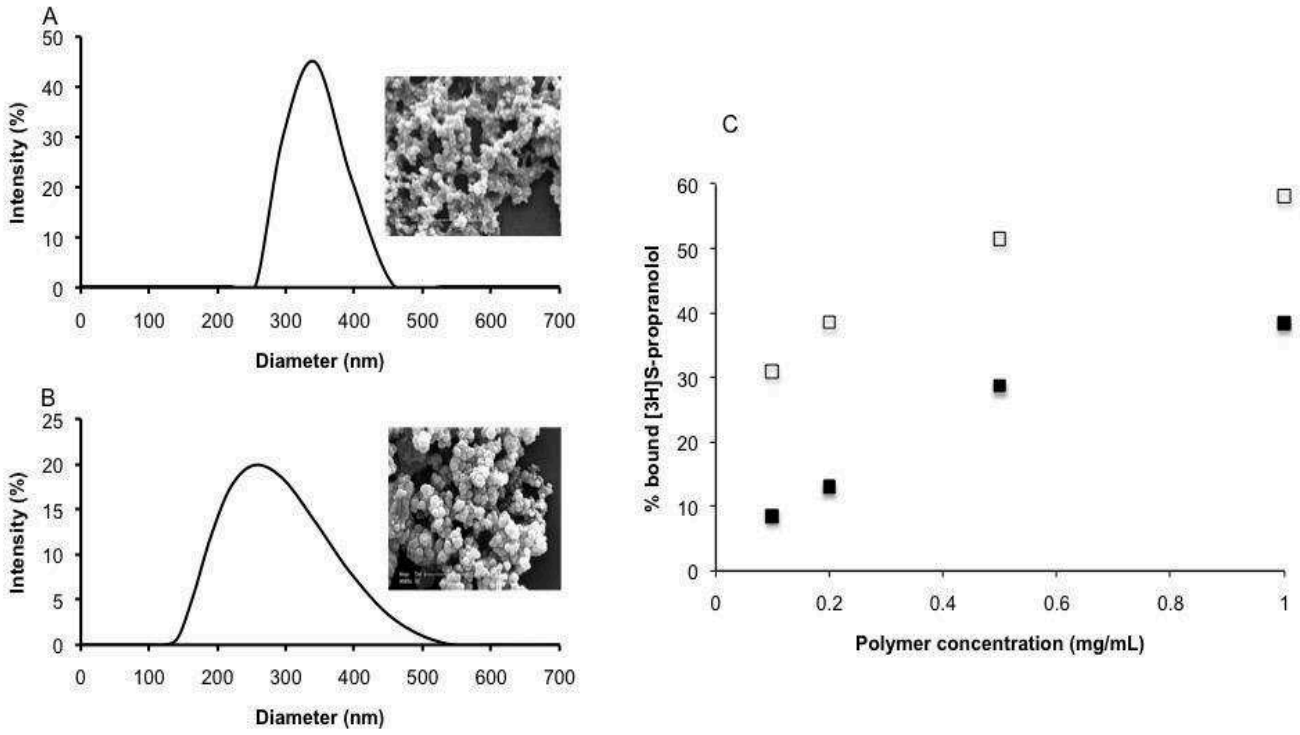

Figure 6 DLS measurements and SEM images of (A) MIP-S-propranolol and (B) NIP-S-propranolol, prepared in ACN. The scale-bar represents 1 µm. (C) Equilibrium binding isotherms for radiolabeled S-propranolol (0.7 pmol, 15 nCi) on MIP (open squares) and NIP (black squares) in acetonitrile. The polymers were prepared with a C_m of 4%.

4.2.3 MIPs 2,4-D

The first MIPs for 2,4-D were synthesized as bulk polymers by Haupt et al. [17]. The polymerization mixture contained 4-vinylpyridine, EGDMA and ABDV as functional, cross-linking monomers and initiator respectively, with a ratio 2,4-D: 4VP: EGDMA: ABDV of 1: 4: 20: 0.31. Thermal polymerization was done in methanol:water (4:1) at 60 °C. The specificity of the resulting MIP was very high when assayed in 20 mM sodium phosphate buffer pH 7.0 + 0.1% Triton X-100 (binding buffer), as only 0.2 mg of polymer was needed to adsorb 50% of the added radioligand whereas the NIP did not bind at all. In this study, we followed this recipe, except that precipitation polymerization using 15 times higher volume of solvent (C_m: 5.5%) (Table 1) was employed and no initiator was added. Polymerization occurred when irradiated under UV, though with a low yield (19%). A yield of 54% was reported for the synthesis of an iniferter-based MIP with C_m: 3.5% using photopolymerization and a temperature of 37 °C [34]. The low yield could probably be remedied by using a higher polymerization temperature [34] or leaving the polymerization for a longer time. Since we found no report about whether 4-

vinylpyridine can self-initiate, a similar polymerization mixture containing 4-vinylpyridine alone was left to polymerize under the same conditions as the MIP mixture. No polymerization was observed, which suggests that the initiation probably starts from the cross-linker EGDMA. This means that if at least one of the monomers is self-initiating, the MIP will still polymerize. Equilibrium binding experiments showed that the MIP was quite specific when assayed in binding buffer (Figure 7A). Though not described in the precedent work [17], the binding behaviour of the self-initiated polymers was further tested in methanol:water (4:1), the solvent of polymerization, which should be the most favourable medium as the imprinted sites were initially created there. MIP binding was higher but with a lower specificity, with an IF of ~2 (Figure 7B), similar to MIPs prepared by AIBN [35], reversible addition-fragmentation chain transfer (RAFT) [35] or iniferter-induced precipitation polymerization [34], assayed in similar solvents. These results indicate that the 2,4-D MIPs are perfectly water compatible as the imprinting factor is higher in aqueous conditions. In an attempt to increase the yield of polymerization, other protocols were tried.

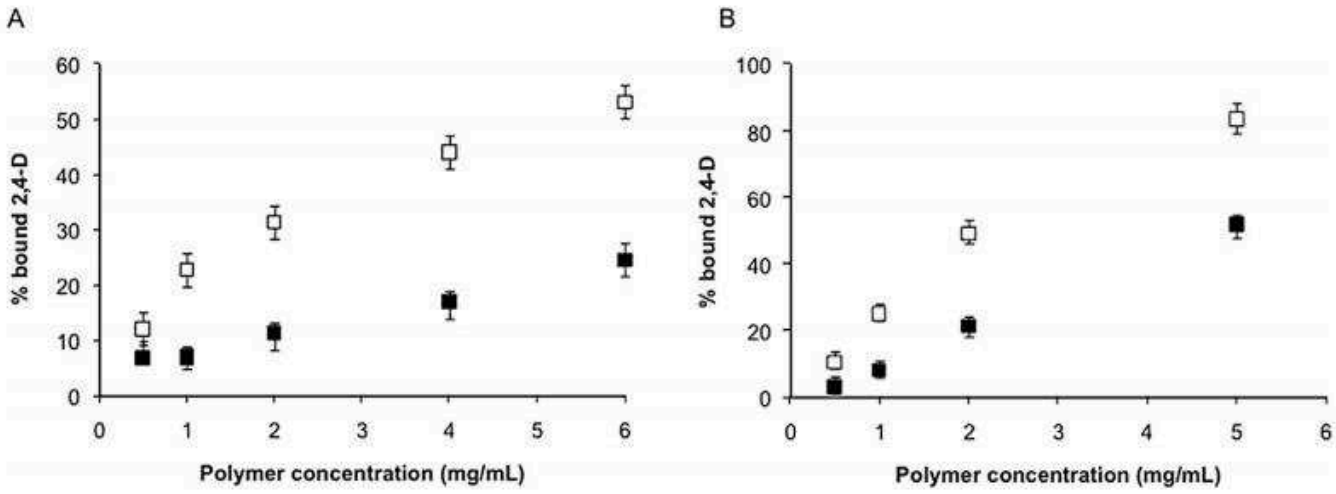

Figure 7 Equilibrium binding isotherms for radiolabeled 2,4-D (0.2 nmol, 10 nCi) on MIP (open squares) and NIP (black squares) in (A) 25 mM sodium phosphate buffer pH 7.0 + 0.1% triton X-100 (B) methanol:water (4:1). Data are means from three independent experiments with two different batches of polymers. The error bars represent standard deviations.

2,4-D MIPs using thermal polymerization in acetonitrile [36,37] instead of methanol:water have also been described. The polymerization mixture was based on a ratio 2,4-D: 4VP: EGDMA of

1: 4: 8.5, with a C_m: 4%. Using this protocol and without adding any initiator, MIPs were obtained with yields of 50% for the MIP (Table 1). The yields are higher despite a lower amount of EGDMA; this could be due to the higher polymerization temperature or the different medium used (ACN instead of methanol:water). High binding was observed but there was no imprinting neither in acetonitrile nor in the binding buffer (Figure 8). Low IF ~1.5-2 has been reported for initiator-induced MIPs prepared in ACN [36,37].

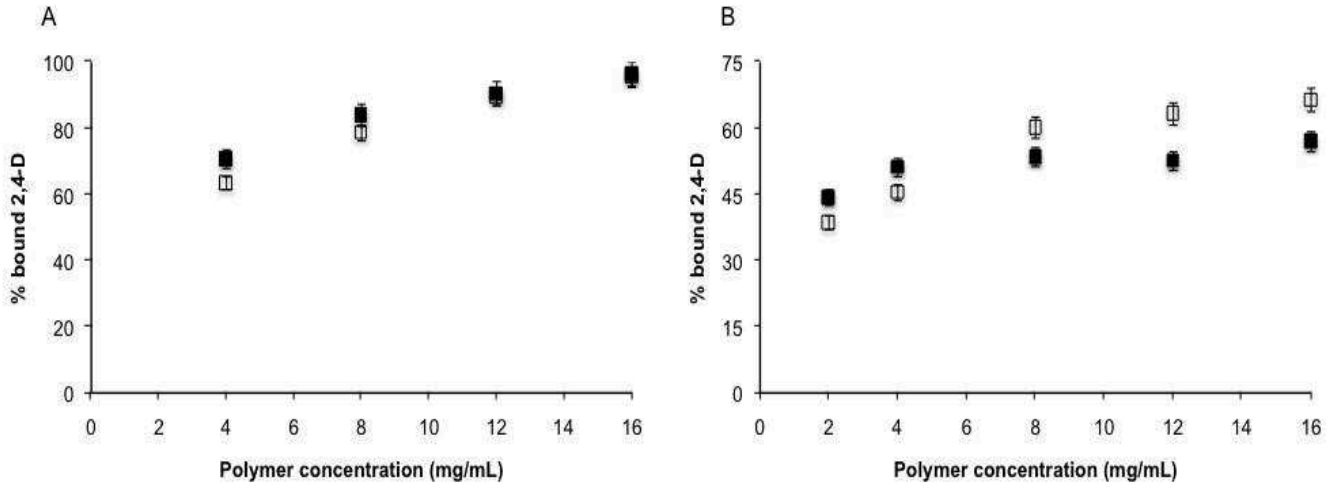

Figure 8 Equilibrium binding isotherms for radiolabeled 2,4-D (0.2 nmol, 10 nCi) on MIP (open squares) and NIP (black squares) synthesized in acetonitrile in (A) 25 mM sodium phosphate buffer pH 7.0 + 0.1 % triton X-100 (B) acetonitrile. Data are means from three independent experiments. The error bars represent standard deviations.

Thus, we can conclude that the most favourable polymerization solvent to obtain specific self-initiated 2,4-D MIPs, is methanol:water. The diameters of the MIP and NIP particles prepared in methanol:water, as deduced from SEM images are polydisperse and ~100 nm (Figure 9), smaller than those reported for an iniferter-based MIP (720 nm). As discussed by the authors, the presence of high initiator concentration in a precipitation polymerization system can result in large particle size [34]. However, quite similar morphologies were observed, as well with ABDV-initiated polymers [38].

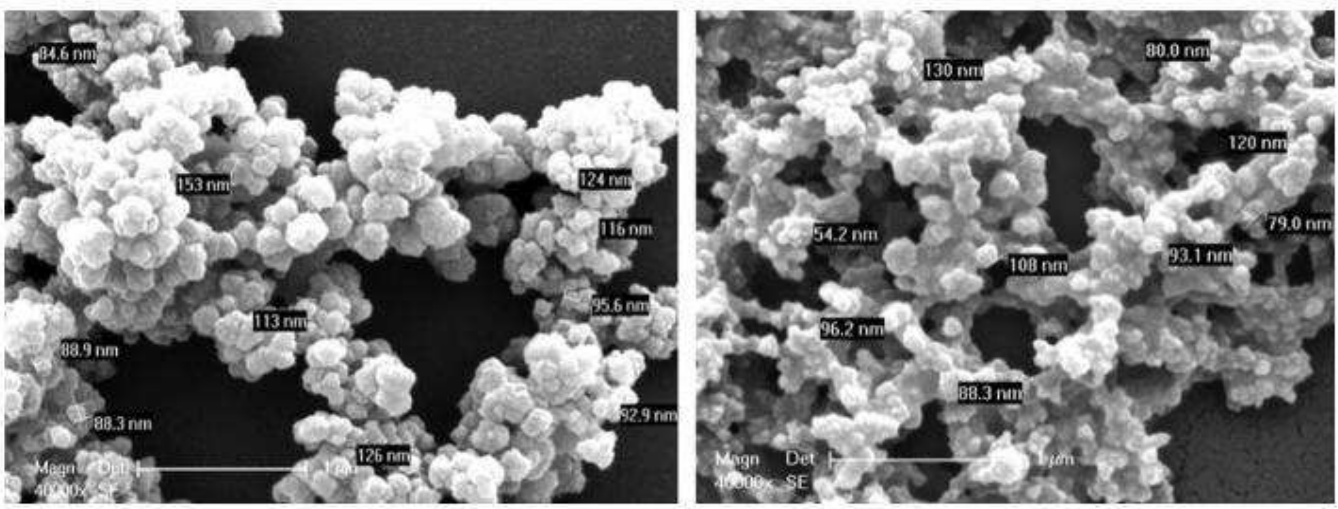

Figure 9 SEM images of 2,4-D MIP (left) and NIP (right) synthesized in methanol:water (4:1). Scale-bar: 1 µm.

4.2.4 Testosterone MIPs

As MAA and EGDMA are the most widely used monomers for imprinting, they were further tested for their auto-initiating abilities with another well-studied template, testosterone (Table 1). Self-initiated bulk MIPs were prepared in acetonitrile with a ratio testosterone: MAA: EGDMA of 1: 8: 25, as described in our previous report [18]. Figure 10A shows that the testosterone MIPs were very specific as no binding was observed with the NIPs. This behaviour is similar to that of initiator-based polymers. However, the extent of binding was 50% lower as compared to ABDV-thermally initiated polymers [18] although the plateau of the isotherm has not yet been reached. Nevertheless, this example shows once again that a MIP specific for a target analyte can be obtained without adding any initiator just by using the self-initiating capacities of its monomers. Testosterone MIPs have also been prepared by initiator-induced polymerization using the combination MAA/DVB, albeit with a lower imprinting factor [18]. Since styrene is known to self-initiate, either under UV light or by heat [24,25], it was interesting to investigate whether self-polymerized testosterone MIPs could be obtained if EGDMA is replaced with DVB (Table 1). Surprisingly, only a negligible amount of polymer was formed when irradiated by UV light but substantial amount of self-initiated MIPs were obtained when incubated at 90 °C (Table 1). The initiation starts from the DVB as a parallel experiment with MAA alone does not produce any polymer at 90 °C. The binding behaviour of the MAA/ DVB polymers (Figure 10B), shows that the MIP binds more than the NIP. This is a clear indication that imprinted sites have been created

in thermally self-initiated MAA/DVB MIPs. Though this example shows that MIPs can be obtained from thermally activated self-initiated monomers, the high temperature used is not economically viable for large scale synthesis.

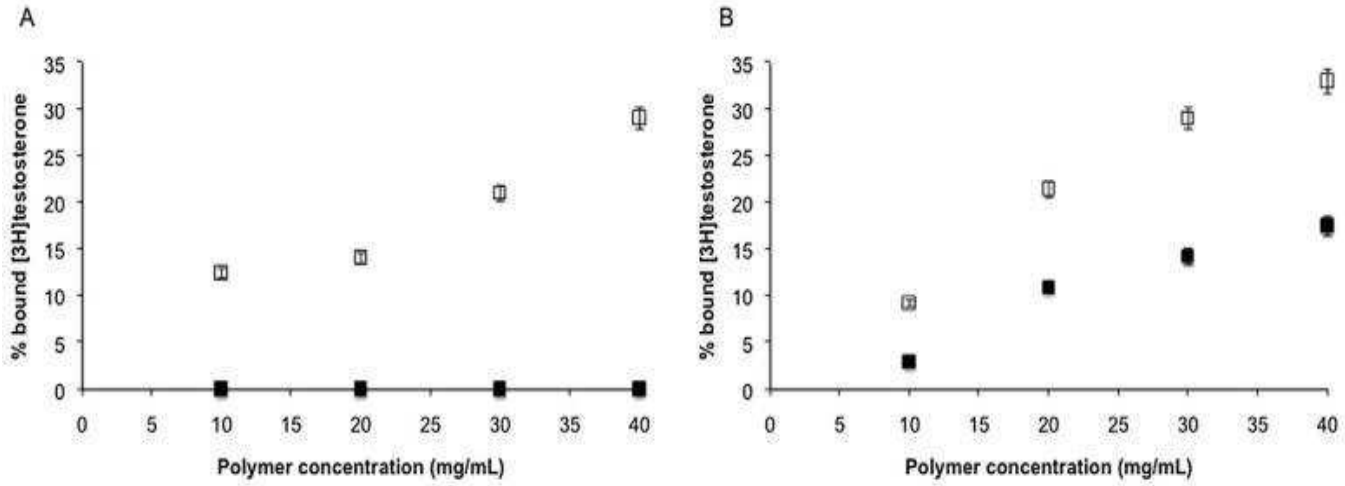

Figure 10 Equilibrium binding isotherms for radiolabeled testosterone (0.4 nM, 30 nCi) on (A) UV-MAA/EGDMA-MIP (open squares) and UV-MAA/EGDMA-NIP (black squares) and on (B) thermal-MAA/DVB-MIP (open squares) and thermal-MAA/DVB-NIP (black squares) in acetonitrile. Data are means from three independent experiments from two different batches of MIP. The error bars represent standard deviations.

4.3 Materials and Methods

Reagents and Materials

All chemicals and solvents were of analytical grade and purchased from VWR International (Strasbourg, France) or Sigma-Aldrich (St-Quentin Fallavier, France), unless otherwise stated. For sake of comparison, all monomers were treated in the same way as used previously for the preparation of initiator-triggered polymers. MAA (99%), HEMA (99%) and ethylene glycol dimethacrylate (EGDMA) (98%) contain 250 ppm, ≤ 50 ppm and 90-110 ppm of the inhibitor, monomethyl ether hydroquinone respectively and were used without purification. The inhibitor, hydroquinone (100 ppm) in 4-vinylpyridine (4VP, 95%) was removed by vacuum-distillation and p-tert-butylcatechol (1000 ppm) in divinylbenzene (DVB, 80%) was removed by passing through an alumina column. Water was purified using a Milli-Q system (Millipore, Molsheim,

France). 4-acrylamidophenyl)(amino)methaniminium chloride (AB_{HCl}) was synthesized as previously described (see Chapter 2). (S)-Propranolol hydrochloride and (R)-propranolol hydrochloride were converted into the free base by extraction from a sodium carbonate solution at pH 9.0 into chloroform. L-(-)-[4-^{3}H]- Propranolol (specific activity: 23.2 Ci/mmol, 1 mCi/mL in ethanol) was obtained from Perkin Elmer (Courtaboeuf, France); [1,2,6,7-3 H]testosterone (specific activity: 73 Ci/mmol, 1 mCi/mL) was from Amersham (Buckinghamshire, UK) and 2,4- dichlorophenoxy acetic acid [carboxyl-^{14}C] (specific activity 50 mCi/mmol, 100 mCi) was from Biotrend Chemicals (Koln, Germany). The latter solid was dissolved in 200 µL of methanol so as to constitute a stock solution. Trypsin activity measurements were done spectrophotometrically on a CARY60 UV-Vis spectrophotometer (Agilent Technologies). For UV polymerization, a Spectroline UV_{312nm} lamp transilluminator, TC-312A with 0.23 W/cm^2 intensity (Spectronics Corporation, Westbury, New York, USA) was employed. The polymerization vials stood on a 2-cm Petri dish, placed on the lamp and the whole system was covered with a box lined with aluminium foil.

4.3.2 Self-initiated synthesis of MIPs

Trypsin MIP

The protocol is the same as previously described [3]. Briefly, 15 mg trypsin (porcine pancreas, type IX-S) and a stoichiometric amount of 4-acrylamidophenyl)(amino)methaniminium chloride (AB_{HCl}) (0.14 mg), in 1 mL of 25 mM sodium phosphate buffer pH 7.0, were incubated at 6 °C for 45 min. Then, 57 µL (0.47 mmol) of HEMA, 118 mg (0.71 mmol) *N,N'*-ethylenebis(acrylamide) (EbAM) and 8.7 mL phosphate buffer were added so as to obtain a cross-linking degree (%CL) of 60% and a monomer concentration (Cm) of 2%. The mixture, kept on ice, was purged with nitrogen for 5 min and left to polymerize under UV irradiation at 6 °C for 18 h. After polymerization, water was added, followed by ultrasonication so as to obtain a homogeneous suspension. The polymers were centrifuged at 30,000 *g* for 30 min and then washed with a solution of 5% sodium dodecyl sulphate in water:acetic acid (9:1), followed by ethanol and water, four times each washing. A non-imprinted polymer (NIP) was prepared using the same protocol but in the absence of trypsin.

MIPs for small molecules

The template (S-propranolol, 2,4-D, testosterone), the functional monomer (MAA or 4VP) and the cross-linker (EGDMA or DVB) were dissolved in solvents (ACN or methanol:water) in a glass vial fitted with an airtight septum. The mixture, kept on ice, was then purged with a gentle flow of nitrogen. Self-initiation of the polymerization reaction was done either under UV irradiation (room temperature or at 6 °C) or heat at 90 °C (Table 1). Testosterone bulk polymers were ground with a mortar and pestle and then milled with 2.8 mm ceramic beads in the presence of methanol in a Precellys 24 homogeniser (Bertin Technologies, Montigny-les-Bretonneux, France), before starting the washing steps described below. Propranolol and 2,4-D polymers obtained by precipitation polymerization were directly transferred to 50 mL centrifuge tubes and washed with 2 rounds of methanol:acetic acid (4:1), 2 rounds of acetonitrile:acetic acid (4:1) and 2 rounds of ethanol:acetic acid (4:1), to remove the template and then rinsed with acetonitrile, methanol and ethanol. The polymers were finally dried overnight under vacuum. Non-imprinted polymers were synthesized under identical conditions but without the addition of the imprinting template.

4.3.3 Equilibrium binding assays

Trypsin MIP

Imprinted and non-imprinted particles were suspended in 5 mM Tris-HCl buffer containing 10 mM $CaCl_2$, pH 8.0 (buffer A), in a sonicating bath. From this stock suspension, polymer concentrations ranging from 1 to 5 mg/mL were pipetted in separate 1.5-mL polypropylene microcentrifuge tubes and trypsin solution (600 nM final concentration) in buffer A was added. The volume was adjusted to 1 mL. The samples were incubated at 6 °C overnight on a tube rotator. Control incubations containing only trypsin, without polymer were performed in parallel. The particles were then separated from the solution by centrifugation at 30,000 *g* for 30 min. The unbound trypsin in the supernatant was quantified by activity measurements with N_a-p-tosyl-*L*-arginine methyl ester hydrochloride (TAME) (final concentration 0.5 mM) as substrate in 50 mM Tris-HCl pH 8.0 at 25 °C [27]. The hydrolysis of TAME was monitored by the change in absorbance at 247 nm for 1.5 min. Binding was quantified using the equation $(A_b-A_s)/A_b$ x 100

with A_b: trypsin activity in the control (incubated without polymer); A_s: trypsin activity in the sample.

MIPs for small molecules

The polymer particles were suspended in the appropriate solvent in a sonicating bath. From the stock suspension, increasing amounts of polymer particles were pipetted in separate 1.5-mL polypropylene microcentrifuge tubes. After addition of the radioligand, either 0.4 pmol (30 nCi) of testosterone or 0.2 nmol (10 nCi) of 2,4-D or 0.7 pmol (15 nCi) of S-propranolol, the final volume was adjusted to 1 mL with solvent and the mixture was incubated overnight on a tube rotator. The samples were centrifuged at 30,000 *g* for 15 min and a 500 µL aliquot of the supernatant was pipetted into a scintillation vial that contained 4 mL of scintillation liquid (Ultra Gold, PerkinElmer). The amount of the free radioligand was measured with a liquid scintillation counter (Beckman LS-6000 IC) and the amount of the radiolabeled analyte bound to the polymer particles was calculated by subtracting the amount of the unbound analyte from the total amount of the analyte added to the mixture.

4.3.4 Competitive binding assays

Preparation of fluorescein isothiocyanate-labeled trypsin (FITC-trypsin)

FITC-trypsin was prepared according to Lakowicz et al. [39]. Since the reaction was performed in 100 mM sodium bicarbonate buffer pH 9.2 at room temperature for 2 h, the stability of trypsin in those conditions was checked beforehand. The residual activity of trypsin was 99 ± 3% (n=4), thus confirming the possibility to apply this protocol. Trypsin (2 mg/mL) was dissolved in 100 mM sodium bicarbonate buffer pH 9.2 and mixed with 78.5 µL of FITC solution (10 mg/mL in DMSO). The reaction mixture was incubated for 2 h at room temperature and the labeled protein was separated by gel filtration on a PD-10 column (GE Healthcare) equilibrated with 0.1 M Tris-HCl buffer + 0.15 M NaCl pH 7.2. To avoid trypsin autoproteolysis, the pH of the fraction containing FITC-trypsin was brought to 3.0 by adding a solution of 2 M HCl. The fraction was divided into aliquots which were then stored at -20 °C. To determine the fluorescein-trypsin ratio, trypsin concentration was measured with the Bradford method, whereas the bound fluorescein was determined via its absorption at 495 nm using a molar extinction coefficient of

FITC $\varepsilon_{495\ nm}$= 68000 M^{-1} cm^{-1}. The concentration of FITC-trypsin was found to be 21 mM with a ratio fluorescein/trypsin of 1.9.

Trypsin MIP

FITC-trypsin was prepared as described above. The selectivity of trypsin MIP was determined by competitive binding assays with unlabelled trypsin and other serine proteases, thrombin (bovine plasma) and kallikrein (porcine pancreas), using FITC-trypsin. Stock solutions (120 µM) of kallikrein, thrombin and unlabelled trypsin were separately prepared in H_2O or 1 mM HCl + 10 mM $CaCl_2$ (for unlabelled trypsin). In 1.5 mL polypropylene microcentrifuge tubes, 500 µL of a MIP stock suspension (6 mg/mL) was added to 5 µL of FITC-trypsin (100 nM final concentration) and the final volume was adjusted to 1 mL with buffer A. The samples were incubated for 30 min at 6 °C on a tube rotator. 8.5 µL of the competitor (final concentration: 1 µM) or buffer A (no competitor) was then added to the polymer samples previously incubated with FITC-trypsin. After 2.5 h incubation at 6 °C, the samples were centrifuged at 30,000 g for 30 min. The amount of unbound FITC-trypsin was measured on a FluoroLog-3 spectrofluorimeter (Horiba Jobin Yvon, Chilly Mazarin, France). The λ excitation/emission were set at 492/517 nm respectively. The binding efficiency was calculated using the equation $(I_b-I_s)/I_b$ x 100, where I_b: fluorescence intensity of 5 µL of FITC-trypsin in buffer A; I_s: fluorescence intensity of bound FITC-trypsin in the sample.

S-propranolol MIP

In order to compare the selectivity of S-propranolol MIP towards S-propranolol and R-propranolol, they were added to the binding assays to compete with radioactive S-propranolol. The competition assays were performed similarly to the binding studies described above. In 2-mL polypropylene microcentrifuge tubes were added, 0.1 mg of MIP, non-radiolabeled ligand ranging from 1 nM to 100 µM and 0.7 pmol (15 nCi) radioactive S-propranolol. The final volume was adjusted to 1 mL with ACN. Competitive binding was allowed to proceed overnight at ambient temperature. The amount of bound ligand was calculated by measuring the radioactivity from 500 µL of supernatant following centrifugation at 30,000 *g* for 15 min.

4.3.5 Particle size determination

The hydrodynamic size of the polymers was measured by dynamic light scattering (DLS) using a Zeta-sizer NanoZS (Malvern Instruments Ltd., Worcestershire, UK) at 25 °C. Scanning electron microscopy (SEM) imaging was carried out on a Philips XL30 Field Emission Gun Scanning Electron Microscope (Amsterdam, Netherlands). Polymer particles were sputter coated with gold prior to measurement.

4.4 Conclusion

In this chapter, we demonstrated that initiator-free molecularly imprinted polymers can be obtained by using acrylic monomers like HEMA, MAA, EbAM and EGDMA and styrenic monomers like DVB, which can self-initiate under UV irradiation or heat respectively. For our demonstrations, we employed the most commonly used functional monomers, cross-linkers and cross-linking degrees applied in MIP synthetic protocols and the polymerizations occurred under mild conditions and with good yields. The specificity and selectivity were as good as the MIPs prepared with initiators. For those with lower yields and binding performance, conditions of polymerization probably need to be re-optimized, as the parameters (ratio of template: monomer, cross-linker, solvent, cross-linking degree) employed, were taken from initiator-based MIPs protocols. These “greener” MIPs are very promising for applications in fields where toxicity of the polymerization precursors specially needs to be contained, like in biomedicine and in the food industry and would pave the way of MIPs to real-life applications. Nevertheless, in order to render this approach more universally applicable, further investigations on for instance the effect of lamp intensity and time/temperature of polymerization are still required. As perspectives, it would be interesting to perform and compare the biocompatibility of initiator-free MIPs to the initiator-based ones and especially to synthesize and characterize initiator-free MIPs targeting GlcA and NANA, which would broaden their applications in the aforementioned fields.

4.5 References

[1] X. Song, S. Xu, L. Chen, Y. Wei, H. Xiong, *J. Appl. Polym. Sci.* **2014**, *131*, 40766.

[2] F. Puoci, G. Cirillo, M. Curcio, O. I. Parisi, F. Iemma, N. Picci, *Expert Opin. Drug Deliv.* **2011**, *8*, 1379–93.

[3] A. Cutivet, C. Schembri, J. Kovensky, K. Haupt, *J. Am. Chem. Soc.* **2009**, *131*, 14699–14702.

[4] Y. Hoshino, H. Koide, T. Urakami, H. Kanazawa, T. Kodama, N. Oku, K. J. Shea, *J. Am. Chem. Soc.* **2010**, *132*, 6644–6645.

[5] J. L. Bowen, P. Manesiotis, C. J. Allender, *Mol. Imprinting* **2013**, *1*, 35–40.

[6] A. Weisman, Y. A. Chen, Y. Hoshino, H. Zhang, K. Shea, *Biomacromolecules* **2014**, *15*, 3290–3295.

[7] Y. Hoshino, H. Koide, K. Furuya, W. W. Haberaecker, S.-H. Lee, T. Kodama, H. Kanazawa, N. Oku, K. J. Shea, *Proc. Natl. Acad. Sci. U. S. A.* **2012**, *109*, 33–8.

[8] F. Canfarotta, A. Waters, R. Sadler, P. McGill, A. Guerreiro, D. Papkovsky, K. Haupt, S. Piletsky, *Nano Res.* **2016**, 1–15.

[9] M. Dorn, *Polymers - Opportunities and Risks II: Sustainability, Product Design and Processing*, Springer, Berlin, Heidelberg, **2010**.

[10] A. T. Larsen, T. Lai, V. Polic, K. Auclair, Z. Aleksey, B. Rita, V. Urlacher, R. D. Schmid, R. N. Patel, V. B. Urlacher, et al., *Green Chem.* **2012**, *14*, 2206.

[11] R. Ginzburg-Turgeman, D. Mandler, E. L. Holthoff, F. V. Bright, M. Ulbricht, A. L. Hillberg, K. R. Brain, C. J. Allender, A. Bossi, F. Bonini, et al., *Phys. Chem. Chem. Phys.* **2010**, *12*, 11041.

[12] M. E. Byrne, E. Oral, J. Zachary Hilt, N. A. Peppas, *Polym. Adv. Technol.* **2002**, *13*, 798–816.

[13] I. Mijangos, F. Navarro-Villoslada, A. Guerreiro, E. Piletska, I. Chianella, K. Karim, A. Turner, S. Piletsky, *Biosens. Bioelectron.* **2006**, *22*, 381–387.

[14] L. Ye, K. Yoshimatsu, D. Kolodziej, J. Da Cruz Francisco, E. S. Dey, *J. Appl. Polym. Sci.* **2006**, *102*, 2863–2867.

[15] M. S. da Silva, E. R. Vão, M. Temtem, L. Mafra, J. Caldeira, A. Aguiar-Ricardo, T. Casimiro, *Biosens. Bioelectron.* **2010**, *25*, 1742–7.

[16] H. Zhang, *Polymer (Guildf).* **2014**, *55*, 699–714.

[17] K. Haupt, A. Dzgoev, K. Mosbach, *Anal. Chem.* **1998**, *70*, 628–631.

[18] B. Tse Sum Bui, K. Haupt, *J. Mol. Recognit.* **2011**, *24*, 1123–1129.

[19] J. Muncke, *J. Steroid Biochem. Mol. Biol.* **2011**, *127*, 118–127.

[20] A. A. Shvedova, E. R. Kisin, A. Murray, C. Kommineni, V. Vallyathan, V. Castranova, *Biochem.* **2004**, *69*, 23–31.

[21] K. Terao, E. Niki, *J. Free Radic. Biol. Med.* **1986**, *2*, 193–201.

[22] H. Wang, H. R. Brown, *Macromol. Rapid Commun.* **2004**, *25*, 1095–1099.

[23] J. Deng, L. Wang, L. Liu, W. Yang, *Prog. Polym. Sci.* **2009**, *34*, 156–193.

[24] J. P. Deng, W. T. Yang, B. Rånby, *Macromol. Rapid Commun.* **2001**, *22*, 535–538.

[25] K. S. Khuong, W. H. Jones, W. A. Pryor, K. N. Houk, *J. Am. Chem. Soc.* **2005**, *127*, 1265–1277.

[26] B. Tse Sum Bui, K. Haupt, *Anal. Bioanal. Chem.* **2010**, *398*, 2481–2492.

[27] S. Ambrosini, S. Beyazit, K. Haupt, B. Tse Sum Bui, A. Bossi, F. Bonini, A. P. F. Turner, S. A. Piletsky, Y. Hoshino, H. Koide, et al., *Chem. Commun.* **2013**, *49*, 6746.

[28] M. Bompart, L. A. Gheber, Y. De Wilde, K. Haupt, *Biosens. Bioelectron.* **2009**, *25*, 568–571.

[29] L. I. Andersson, *Anal. Chem.* **1996**, *68*, 111–117.

[30] K. Yoshimatsu, T. Yamazaki, I. S. Chronakis, L. Ye, *J. Appl. Polym. Sci.* **2012**, *124*, 1249–1255.

[31] C. E. Hunt, R. J. Ansell, C. Alexander, H. S. Andersson, L. Andersson, R. J. Ansell, N. Kirsch, I. A. Nicholls, J. O'Mahony, M. R. Whitcombe, et al., *Analyst* **2006**, *131*, 678.

[32] C. Alexander, H. S. Andersson, L. I. Andersson, R. J. Ansell, N. Kirsch, I. A. Nicholls, J. O'Mahony, M. J. Whitcombe, *J. Mol. Recognit.* **2006**, *19*, 106–180.

[33] K. Haupt, *Anal. Chem.* **2003**, *75*, 376A–383A.

[34] J. Li, B. Zu, Y. Zhang, X. Guo, H. Zhang, *J. Polym. Sci. Part A Polym. Chem.* **2010**, *48*, 3217–3228.

[35] G. Pan, B. Zu, X. Guo, Y. Zhang, C. Li, H. Zhang, *Polym. (United Kingdom)* **2009**, *50*, 2819–2825.

[36] C. E. Hunt, P. Pasetto, R. J. Ansell, K. Haupt, G. Vlatakis, L. Andersson, R. Müller, K. Mosbach, R. J. Ansell, R. J. Ansell, et al., *Chem. Commun.* **2006**, *361*, 1754.

[37] C. Xu, L. Ye, A. Poma, A. P. F. Turner, S. A. Piletsky, S. Tokonami, H. Shiigi, T. Nagaoka, K. Yoshimatsu, L. Ye, et al., *Chem. Commun.* **2011**, *47*, 6096.

[38] X.-A. Ton, , **2013**, Ph.D thesis Compiègne University of Technology.

[39] J. R. Lakowicz, J. Malicka, S. D'Auria, I. Gryczynski, *Anal. Biochem.* **2003**, *320*, 13–20.

General Conclusions and Perspectives

In this thesis, we reviewed the state of the art in targeted fluorescent bioimaging with commonly used nanomaterials (aptamers, peptides, antibodies, organic and silica polymers doped with fluorophores such as organic dyes, quantum dots (QDs), upconverting nanoparticles, carbon dots, noble metals, and so forth) and demonstrated the high potential of fluorescently-labeled molecularly imprinted polymers (MIPs), also termed "plastic antibodies", as novel biorecognition agents for labeling and imaging of cells and tissues.

More precisely, we synthesized water-compatible MIPs, either labeled with a fluorescent dye or with QDs, for selectively targeting and imaging hyaluronan and sialylated glycosylation sites in fixed and living human keratinocytes and skin tissues. The MIPs were prepared with D-glucuronic acid (GlcA), a substructure of hyaluronan and N-acetylneuraminic acid (NANA), the most common member of sialic acids, as templates. An amidinium-based polymerizable monomer which makes strong stoichiometric electrostatic interaction with the carboxylate moieties of the templates, was used as functional monomer. Both MIPs were found to be highly selective towards their target monosaccharides in water, as no cross-reactivity was observed with other sugars like N-acetyl-D-glucosamine, N-acetyl-D-galactosamine, D-glucose and D-galactose, present on the cell surface.

To render the MIPs fluorescent, we incorporated a polymerizable rhodamine dye during MIP synthesis or prepared MIP as a thin shell around InP/ZnS QDs. For the latter, a novel versatile solubilization and functionalization strategy was proposed, which consists of creating MIP shells directly on QDs by photopolymerization using the particles as individual internal light sources. Simultaneous dual-color imaging of keratinocytes with two MIP-coated QDs of different emission colors (red QDs with MIP-NANA and green QDs with MIP-GlcA) were also demonstrated. For MIP staining, a standard immunostaining protocol was successfully adapted, indicating that simultaneous staining with antibodies and MIPs should be possible. However, molecular recognition and visualization with MIP is more advantageous as it is a one-step process and does not require primary and secondary antibodies as in standard immunostaining protocols.

In addition, an exemplary imaging of cancer cells was demonstrated, proving the versatility of our method. Importantly, the MIPs were not cytotoxic and could be applied to live cell labeling and imaging, which opens the way to the possibility of real-time imaging of glycosylation level and distribution in the cells. This kind of synthetic receptors has potential not only as a bioimaging tool but could also serve a specific blocking agent on/in cells and tissues.

Furthermore, we demonstrated that "greener", initiator-free molecularly imprinted polymers can be synthesized by using monomers like methacrylic acid, hydroxyethyl methacrylate, ethylene glycol dimethacrylate, ethylenebis(acrylamide) and divinylbenzene, which can self-initiate under UV irradiation and heat respectively. In the provided examples, we employed the most commonly used functional monomers, crosslinkers and solvents applied in MIP synthetic protocols and the polymerizations took place under mild conditions and with yields, specificity and selectivity comparable to the ones of MIPs prepared with initiators. These "safer" MIPs are very promising for applications in fields where toxicity of the polymerization precursors specially needs to be contained, like in biomedicine, cosmetology and food industry and can lead to real-life applications.

Future work may focus on the functionalization of near-infrared emitters, such as upconverting nanoparticles, in order to achieve higher light depth in biomedical samples during imaging. Since MIPs can be synthesized for target molecules of different sizes, from small molecules such as single amino acids or sugars, to peptides and even entire proteins, this makes them very versatile as antibody mimics. We therefore believe that MIPs as "plastic antibodies" have a great potential for bioimaging. The major limitation will reside on the choice of functional monomers enabling strong and selective interactions in aqueous media. The possibility to additionally attach drugs and to associate other functionalities such as superparamagnetic nanoparticles to the same material appears rather straightforward due to the synthetic polymeric nature of MIPs, which paves the way to new potential applications in theranostics.

ANNEX: Achievements

Publications

- Panagiotopoulou M., Beyazit S., Nestora S., Haupt K., Tse Sum Bui B., "Initiator-free synthesis of molecularly imprinted polymers by polymerization of self-initiated monomers" Polymer **(2015)**, *66*, 43-51.
- Kunath S., Panagiotopoulou M., Maximilien J., Marchyk N., Sänger J., Haupt K., "Cell and tissue imaging with molecularly imprinted polymers as plastic antibody mimics" Advanced Healthcare Materials **(2015)**, *4*, 1322-1326.
- Panagiotopoulou M., Salinas Y., Beyazit S., Kunath S., Duma L., Prost E., Mayes A. G., Resmini M., Tse Sum Bui B., Haupt K., "Molecularly imprinted polymer coated quantum dots for multiplexed cell targeting and imaging" Angewandte Chemie International Edition **(2016)**, *55*, 8244-8248.
- Panagiotopoulou M., Kunath S., Medina-Rangel P. X., Haupt K., Tse Sum Bui B., "Fluorescent molecularly imprinted polymers as plastic antibodies for selective labeling and imaging of hyaluronan and sialic acid on fixed and living cells" Biosensors and Bioelectronics **(2016)**, DOI 10.1016/j.bios.2016.07.080.
- Panagiotopoulou M., Kunath S., Haupt K., Tse Sum Bui B., "Cell and tissue imaging with molecularly imprinted polymers" Methods in Molecular Biology **(2016-Submitted manuscript)**.

Oral Communications

- 3rd NANODRUG International Scientific Meeting, July 2014, Coimbra, Portugal.
- 1st SAMOSS International Scientific Meeting, July 2014, Madrid, Spain.
- 2nd SAMOSS International Scientific Meeting, May 2015, Groningen, Netherlands.
- 3rd SAMOSS International Scientific Meeting, October 2015, Dead Sea, Israel.
- Biosensors 2016 Conference, May 2016, Gothenburg, Sweden.
- 4th SAMOSS International Scientific Meeting, June 2016, Reichenau, Austria.

Poster Presentations

- 8th International Conference on Molecular Imprinting (MIP 2014), September 2014, Zhenjiang, China.

Other

- Secondment in Biosensor srI from 5/07/2016 to 27/07/2016.
- Supervision of a Master 2 student.

Polymer 66 (2015) 43–51

Contents lists available at ScienceDirect

Polymer

journal homepage: www.elsevier.com/locate/polymer

Initiator-free synthesis of molecularly imprinted polymers by polymerization of self-initiated monomers

Maria Panagiotopoulou, Selim Beyazit, Sofia Nestora, Karsten Haupt*, Bernadette Tse Sum Bui*

Sorbonne Universités, Université de Technologie de Compiègne, CNRS Laboratory for Enzyme and Cell Engineering, CS60319, 60203 Compiègne Cedex, France

ARTICLE INFO

Article history:
Received 27 November 2014
Received in revised form
1 April 2015
Accepted 3 April 2015
Available online 13 April 2015

Keywords:
Molecularly imprinted polymer
Self-initiated monomer
Initiator-free polymerization

ABSTRACT

Molecularly imprinted polymers (MIPs) are tailor-made synthetic materials with binding affinities and specificities comparable to those of antibodies and enzymes. These 'plastic' antibodies are composed of two or more types of monomers, and are generally synthesized by free radical polymerization. Polymerization is initiated by reactive radicals generated by the thermal or photo homolysis of a chemical bond on an initiator. Here, we show through several examples, that MIPs can be synthesized, without adding any initiator by using at least one monomer in the precursor mixture that can be photo or thermally polymerized by self-initiation. The binding characteristics as well as the size and morphology of the MIPs were examined. Remarkably, even at high monomer dilutions prevailing during precipitation polymerization, the yield of polymerization was high but above all, the MIPs were very specific and selective for their target molecule, indicating the creation of high-fidelity imprinted sites.

1. Introduction

Molecularly imprinted polymers (MIPs) are tailor-made synthetic materials possessing specific cavities designed for a target molecule [1,2]. They are synthesized by co-polymerization of functional and cross-linking monomers in the presence of a molecular template, in a porogenic solvent. The template can be the target molecule or a derivative thereof. The most common approach to prepare MIPs is by the self-assembly method, due to the large variety of commercially available acrylic, vinylic and styrenic functional and cross-linking monomers. The functional monomers initially form a complex with the template, followed by the polymerization step. Thus, after polymerization, the monomer-template assembly is held in position by the highly cross-linked three-dimensional structure. Subsequent removal of the template leaves cavities with a size, shape and chemical functionality complementary to those of the template. The resulting binding sites can bind the target molecule with a very high specificity and affinity, comparable to that of biological receptors such as antibodies and enzymes (Scheme 1) [3,4].

These 'plastic' antibodies [2] have considerable advantages over their biological counterparts, as they possess greater chemical, thermal and mechanical stabilities. Hence, MIPs have become serious alternatives to biomolecules in affinity separation techniques [5,6], as recognition elements in sensors [7,8], as substitutes of antibodies in immunoassays [3,9], in catalysis [1,10] and more recently as controlled release vehicles in drug delivery [11–13] and as therapeutic drugs [14–16]. As judged by the exponential increase in the number of papers and patents related to the field each year, MIPs have a very promising future with great potential development in the food industry [17,18], theranostics and pharmaceutics [11–16], fields that have been little explored up till now. In 2010 was reported the first *in vivo* application of MIP, injected in the bloodstream of mice; the MIP targeted and neutralized the toxin melittin, a component of bee venom [15]. So far, MIPs have not reached any clinical applications, but toxicological concerns are important issues to consider; the precursors (monomers, solvents, template, initiator), the final MIPs and the by-products of their synthesis (residual monomers, degradation products) must be limited and if possible, be non-toxic. We propose here to suppress the use of initiators, one of the toxic ingredients. Indeed, Dorn [19] has reported the danger of certain initiators to human health and the environment as they generate toxic decomposition products that may remain in the polymer or become incorporated in the

* Corresponding authors. Tel.: +33 3 44234402; fax: +33 3 44203910.
E-mail address: jeanne.tse-sum-bui@utc.fr (B. Tse Sum Bui).

http://dx.doi.org/10.1016/j.polymer.2015.04.012
0032-3861/

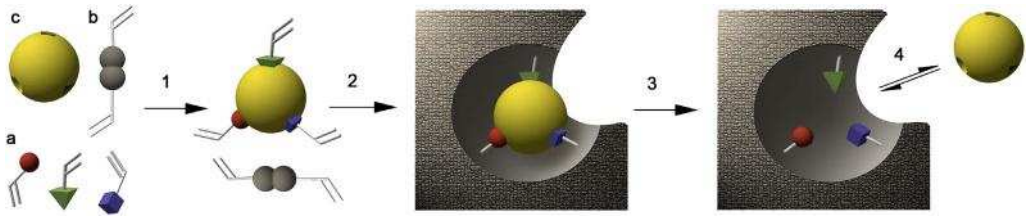

Scheme 1. Schematic representation of the molecular imprinting principle. a: Functional monomers, b: cross-linker, c: template molecule; 1: assembly of the prepolymerization complex, 2: polymerization, 3: extraction, 4: rebinding. Reproduced from Ref. [4] with permission. Copyright (2003) American Chemical Society.

polymer chain. Consequently, this study will have a dual function: simplifying the MIP precursor mixture, hence resolving the problem of finding a suitable solvent to solubilize both the initiator and the monomers, and the obtention of 'greener' MIPs.

Actually most MIPs are synthesized by free radical polymerization, generated by the thermal or photo homolysis of a chemical bond on an initiator. The most widely used initiators for MIPs synthesis are benzoyl peroxide (BPO) [20,21], 2,2-dimethoxy-2-phenylacetophenone (DMPA) [22,23] and the azo compounds 2,2′-azobis(2-methylpropionitrile) (AIBN) [24–26] and 2,2′-azobis(2,4-dimethyl)valeronitrile) (ABDV) [27,28]. According to literature data [19,29] and the U.S Department of Health and Human Services, BPO decomposes into benzene, benzoic acid, phenyl benzoate, terphenyls, biphenyls, carbon monoxide and carbon dioxide; AIBN into tetramethylsuccinonitrile, hydrogen cyanide, carbon monoxide and carbon dioxide; additionally, DMPA, which bears a benzene ring, is suspected to have endocrine disrupting properties [29]. *In vivo* studies with a few micromoles of organic peroxides, an amount comparable to that used in routine MIPs' synthesis, and azo initiators have shown their carcinogenicity and toxicological effects on biological tissues [30,31].

Interestingly, a few acrylic monomers [32,33] like acrylic acid (AA), methacrylic acid (MAA), 2-hydroxyethyl acrylate, 2-hydroxyethyl methacrylate (HEMA), glycidyl acrylate, poly(-ethylene glycol) methacrylate and a styrenic monomer (styrene) [34] were reported to perform self-initiated photopolymerization and photografting under UV irradiation in the complete absence of photoinitiator or any other additives. Photodissociation of for instance AA can be due to cleavages of C–C and C–O bonds to form free radicals. These free radicals are then capable to initiate a chain process. Another explanation would be that the monomers are excited by the UV light to a triplet state (T_3) with enough energy to abstract hydrogen and induce radical formation. For styrene (St), a triplet state can also be reached after photon absorption. This triplet state is in equilibrium with a biradical species (˙St˙) which initiates a free radical in solution or can also abstract a hydrogen radical [34]. Additionally, styrene can also self-initiate by thermal polymerization. The mechanism first involves the formation of a Diels–Alder dimer of styrene, followed by hydrogen transfer from the dimer to styrene to generate two monoradical species that initiates monoradical polymerization [35]. Concerning the acrylic monomers, it has been reported that self-initiation occurs solely by UV irradiation as no polymers were formed when they were left in an oven at 80 °C [32].

However, it is not obvious and far from trivial that MIPs can be synthesized by exploiting the self-initiating abilities of these monomers, if we take into account the complexity of these materials and the specific conditions that have to be met for imprinting to occur (use of at least two different monomers, necessity of cross-linking, presence of the imprinting template and a solvent, necessity to adapt polymerization conditions to create both porosity and molecularly imprinted cavities…). In this work, we investigated whether the monomers typically used for MIPs could be photo or thermally polymerized by self-initiation, i.e. without adding any initiator, under conventional MIP preparation conditions (Table 1). Since the functional monomers are generally present in a large excess in order to shift the equilibrium towards the formation of the template–monomer complex [3,36], this implies that even if the monomers act as initiators, the formation of the template–monomer complex will be little affected. We present here

Table 1
Preparation of self-initiated polymers.

Template (mmol)	Functional monomer (mmol)	Cross-linker (mmol)	Solvent (mL)	C_m; CL (%)	Polymerization conditions[b]	Yield (%) MIP (NIP)
Trypsin (0.006)	AB + HEMA (0.006) + (0.47)	EbAM (0.71)	Buffer[a] (9.7)	2; 60	6 °C[d], 18 h	93 (85)
Propranolol (0.2)	MAA (1.6)	EGDMA (8)	Acetonitrile (15)	10; 83	20 °C[e], 20 h	96 (48)
			(40)	4; 83		60 (22)
2,4-D (0.2)	4VP (0.8)	EGDMA (4)	CH_3OH/H_2O (15)	5.5; 83	6 °C[d], 20 h	19 (9)
2,4-D (0.2)	4VP (0.8)	EGDMA (1.7)	Acetonitrile (12)	4; 68	20 °C[d], 18 h	50 (16)
Testosterone (0.2)	MAA (1.6)	EGDMA (5)	Acetonitrile (1.5)	43; 76	6 °C[d], 20 h	45 (38)
Testosterone (0.2)	MAA (1.6)	DVB (5)	Acetonitrile (1.5)	34; 76	Thermal[c] 90 °C, 24 h	23 (11)

[a] 25 mM sodium phosphate pH 7.0.
[b] UV irradiation except where indicated.
[c] Oil-bath.
[d] Temperature on the lamp: 18 °C.
[e] Temperature on the lamp: 40 °C; C_m: total mass of functional and cross-linking monomers upon total mass of solvent and monomers; CL: moles of cross-linking monomers upon total moles of functional and cross-linking monomers.

several examples of MIPs synthesized with these monomers without adding any initiator, using previously developed and well-established protocols for initiator-based MIPs. The binding behaviour, which proves that the imprinting process has taken place, as well as the morphology and size of the MIPs, were examined and compared to initiator-synthesized MIPs.

2. Experimental

2.1. Materials and methods

All chemicals and solvents were of analytical grade and purchased from VWR International (Strasbourg, France) or Sigma–Aldrich (St-Quentin Fallavier, France), unless otherwise stated. For sake of comparison, all monomers were treated in the same way as used previously for the preparation of initiator-triggered polymers. MAA (99%), HEMA (≥99%) and ethylene glycol dimethacrylate (EGDMA) (98%) contain 250 ppm, ≤50 ppm and 90–110 ppm of the inhibitor, monomethyl ether hydroquinone respectively and were used without purification. The inhibitor, hydroquinone (100 ppm) in 4-vinylpyridine (4VP, 95%) was removed by vacuum-distillation and *p-tert*-butylcatechol (1000 ppm) in divinylbenzene (DVB, 80%) was removed by passing through an alumina column. Water was purified using a Milli-Q system (Millipore, Molsheim, France). *N*-acryloyl-*p*-aminobenzamidine was synthesized as previously described (see ESI) [37]. (S)-Propranolol hydrochloride and (R)-propranolol hydrochloride were converted into the free base by extraction from a sodium carbonate solution at pH 9.0 into chloroform. L-(-)-[4-^{3}H]-Propranolol (specific activity: 23.2 Ci/mmol, 1 mCi/mL in ethanol) was obtained from Perkin Elmer (Courtaboeuf, France); [1,2,6,7-^{3}H]testosterone (specific activity: 73 Ci/mmol, 1 mCi/mL) was from Amersham (Buckinghamshire, UK) and 2,4-dichlorophenoxy acetic acid [carboxyl-^{14}C] (specific activity 50 mCi/mmol, 100 mCi) was from Biotrend Chemicals (Koln, Germany). The latter solid was dissolved in 200 μL of methanol so as to constitute a stock solution. Trypsin activity measurements were done spectrophotometrically on a CARY60 UV-Vis spectrophotometer (Agilent Technologies). For UV polymerization, a Spectroline UV_{312nm} lamp transilluminator, TC-312A with 0.23 W/cm^2 intensity (Spectronics Corporation, Westbury, New York, USA) was employed. The polymerization vials stood on a 2-cm Petri dish, placed on the lamp and the whole system was covered with a box lined with aluminium foil.

2.2. Self-initiated synthesis of MIPs

2.2.1. Trypsin MIP

The protocol is the same as previously described [14]. Briefly, 15 mg trypsin (porcine pancreas, type IX-S) and a stoichiometric amount of *N*-acryloyl-*p*-aminobenzamidine (AB) (0.14 mg), in 1 mL of 25 mM sodium phosphate buffer pH 7.0, were incubated at 6 °C for 45 min. Then, 57 μL (0.47 mmol) of HEMA, 118 mg (0.71 mmol) N,N′-ethylenebis(acrylamide) (EbAM) and 8.7 mL phosphate buffer were added so as to obtain a cross-linking degree (%CL) of 60% and a monomer concentration (C_m) of 2%. The mixture, kept on ice, was purged with nitrogen for 5 min and left to polymerize under UV irradiation at 6 °C for 18 h. After polymerization, water was added, followed by ultrasonication so as to obtain a homogeneous suspension. The polymers were centrifuged at 30,000 *g* for 30 min and then washed with a solution of 5% sodium dodecyl sulphate in water/acetic acid (9/1), followed by ethanol and water, four times each washing. A non-imprinted polymer (NIP) was prepared using the same protocol but in the absence of trypsin.

2.2.2. MIPs for small molecules

The template (S-propranolol, 2,4-D, testosterone), the functional monomer (MAA or 4VP) and the cross-linker (EGDMA or DVB) were dissolved in solvents (ACN or methanol/water) in a glass vial fitted with an airtight septum. The mixture, kept on ice, was then purged with a gentle flow of nitrogen. Self-initiation of the polymerization reaction was done either under UV irradiation (room temperature or at 6 °C) or heat at 90 °C (Table 1). Testosterone bulk polymers were ground with a mortar and pestle and then milled with 2.8 mm ceramic beads in the presence of methanol in a Precellys 24 homogeniser (Bertin Technologies, Montigny-les-Bretonneux, France), before starting the washing steps described below. Propranolol and 2,4-D polymers obtained by precipitation polymerization were directly transferred to 50 mL centrifuge tubes and washed with 2 rounds of methanol/acetic acid (4/1), 2 rounds of acetonitrile/acetic acid (4/1) and 2 rounds of ethanol/acetic acid (4/1), to remove the template and then rinsed with acetonitrile, methanol and ethanol. The polymers were finally dried overnight under vacuum. Non-imprinted polymers were synthesized under identical conditions but without the addition of the imprinting template.

2.3. Equilibrium binding assays

2.3.1. Trypsin MIP

Imprinted and non-imprinted particles were suspended in 5 mM Tris–HCl buffer containing 10 mM $CaCl_2$, pH 8.0 (buffer A), in a sonicating bath. From this stock suspension, polymer concentrations ranging from 1 to 5 mg/mL were pipetted in separate 1.5-mL polypropylene microcentrifuge tubes and trypsin solution (600 nM final concentration) in buffer A was added. The volume was adjusted to 1 mL. The samples were incubated at 6 °C overnight on a tube rotator. Control incubations containing only trypsin, without polymer were performed in parallel. The particles were then separated from the solution by centrifugation at 30,000 *g* for 30 min. The unbound trypsin in the supernatant was quantified by activity measurements with N_{α}-*p*-tosyl-L-arginine methyl ester hydrochloride (TAME) (final concentration 0.5 mM) as substrate in 50 mM Tris–HCl pH 8.0 at 25 °C [38]. The hydrolysis of TAME was monitored by the change in absorbance at 247 nm for 1.5 min. Binding was quantified using the equation $(A_b - A_s)/A_b \times 100$ with A_b: trypsin activity in the control (incubated without polymer); A_s: trypsin activity in the sample.

2.3.2. MIPs for small molecules

The polymer particles were suspended in the appropriate solvent in a sonicating bath. From the stock suspension, increasing amounts of polymer particles were pipetted in separate 1.5-mL polypropylene microcentrifuge tubes. After addition of the radioligand, either 0.4 pmol (30 nCi) of testosterone or 0.2 nmol (10 nCi) of 2,4-D or 0.7 pmol (15 nCi) of S-propranolol, the final volume was adjusted to 1 mL with solvent and the mixture was incubated overnight on a tube rotator. The samples were centrifuged at 30,000 *g* for 15 min and a 500 μL aliquot of the supernatant was pipetted into a scintillation vial that contained 4 mL of scintillation liquid (Ultra Gold, PerkinElmer). The amount of the free radioligand was measured with a liquid scintillation counter (Beckman LS-6000 IC) and the amount of the radiolabeled analyte bound to the polymer particles was calculated by subtracting the amount of the unbound analyte from the total amount of the analyte added to the mixture.

2.4. Competitive binding assays

2.4.1. Trypsin MIP

FITC-trypsin was prepared as previously described [38] (see ESI). The selectivity of trypsin MIP was determined by competitive

binding assays with unlabelled trypsin and other serine proteases, thrombin (bovine plasma) and kallikrein (porcine pancreas), using FITC-trypsin. Stock solutions (120 μM) of kallikrein, thrombin and unlabelled trypsin were separately prepared in H_2O or 1 mM HCl + 10 mM $CaCl_2$ (for unlabelled trypsin). In 1.5 mL polypropylene microcentrifuge tubes, 500 μL of a MIP stock suspension (6 mg/mL) was added to 5 μL of FITC-trypsin (100 nM final concentration) and the final volume was adjusted to 1 mL with buffer A. The samples were incubated for 30 min at 6 °C on a tube rotator. 8.5 μL of the competitor (final concentration: 1 μM) or buffer A (no competitor) was then added to the polymer samples previously incubated with FITC-trypsin. After 2.5 h incubation at 6 °C, the samples were centrifuged at 30,000 *g* for 30 min. The amount of unbound FITC-trypsin was measured on a FluoroLog-3 spectrofluorimeter (Horiba Jobin Yvon, Chilly Mazarin, France). The λ excitation/emission were set at 492/517 nm respectively. The binding efficiency was calculated using the equation $(I_b - I_s)/I_b \times 100$, where I_b: fluorescence intensity of 5 μL of FITC-trypsin in buffer A; I_s: fluorescence intensity of bound FITC-trypsin in the sample.

2.4.2. S-propranolol MIP

In order to compare the selectivity of S-propranolol MIP towards S-propranolol and R-propranolol, they were added to the binding assays to compete with radioactive S-propranolol. The competition assays were performed similarly to the binding studies described above. In 2-mL polypropylene microcentrifuge tubes were added, 0.1 mg of MIP, non-radiolabeled ligand ranging from 1 nM to 100 μM and 0.7 pmol (15 nCi) radioactive S-propranolol. The final volume was adjusted to 1 mL with ACN. Competitive binding was allowed to proceed overnight at ambient temperature. The amount of bound ligand was calculated by measuring the radioactivity from 500 μL of supernatant following centrifugation at 30,000 *g* for 15 min.

2.5. Particle size determination

The hydrodynamic size of the polymers was measured by dynamic light scattering (DLS) using a Zeta-sizer NanoZS (Malvern Instruments Ltd., Worcestershire, UK) at 25 °C. Scanning electron microscopy (SEM) imaging was carried out on a Philips XL30 Field Emission Gun Scanning Electron Microscope (Amsterdam, Netherlands). Polymer particles were sputter coated with gold prior to measurement.

3. Results and discussion

Monomers reported in the literature of self-initiation abilities are MAA and HEMA [32,33]. The templates were chosen accordingly: one protein template (trypsin) and three small-sized templates (S-propranolol, 2,4-dichlorophenoxyacetic acid (2,4-D) and testosterone) were imprinted, without adding any initiator. The polymerization conditions for each polymer are described in Table 1. These examples were chosen to illustrate the various MIPs synthesis protocols (different polymerization solvents, temperature, cross-linkers, etc), commonly practised for batch synthesis. The parameters (ratio of template: monomer: cross-linker, solvent, cross-linking degree) are those commonly employed by our group and others for the preparation of initiator-based MIPs.

3.1. Trypsin MIPs

The polymers were synthesized as previously described [14], except that no initiator was added. The polymerization mixture contains HEMA and N,N′-ethylenebis(acrylamide) (EbAM), as functional and cross-linking monomers respectively plus an anchoring monomer, N-acryloyl-*p*-aminobenzamidine (AB). *p*-Aminobenzamidine is an inhibitor of serine proteases and therefore AB, added in a 1:1 stoichiometry, acted as a polymerizable affinity ligand for trypsin. The cross-linking degree (CL) was 60%, the monomer concentration (C_m) was 2% and the polymerization was done in 25 mM sodium phosphate buffer pH 7.0 during 18 h (Table 1). CL is defined as the number of moles of cross-linking monomers upon the total number of moles of functional and cross-linking monomers and C_m is the total mass of functional and cross-linking monomers upon total mass of solvent and monomers.

Generally, trypsin MIP microgels are synthesized in our group by UV polymerization using the water soluble azo-initiator Vazo 56 (1.5% mol per mol of polymerizable double bonds) [14] or by thermal polymerization using tetramethylethylenediamine/potassium persulfate (3% mol/mol with respect to polymerizable double bonds) [38]. In this work, no initiators were added. Interestingly, the yield of polymerization was ~90%, even under the high dilution conditions used (2% w/w of total monomer concentration). HEMA has already been reported to photopolymerize by self-initiation [32], but there is no information available about whether EbAM can auto-initiate. For this reason, a similar polymerization mixture containing EbAM alone was left to polymerize under the same conditions as the MIP mixture. Polymerization occurred indicating that acrylamide-based monomers can self-initiate as well. Both HEMA and EbAM probably contributed to the self-initiation polymerization, producing cross-linked MIPs.

The affinity of the polymers for trypsin was determined by equilibrium binding assays. At equilibrium, the polymers were removed by centrifugation and the residual activity of trypsin in the supernatant was determined, using N_α-*p*-tosyl-L-arginine methyl ester hydrochloride (TAME), as substrate. Fig. 1A shows that specific imprinted sites were created in the self-initiated MIP, as there was more trypsin bound to the MIP than to the NIP. The imprinting factor (IF) which corresponds to the ratio trypsin bound to the MIP versus trypsin bound to the NIP was ~3, similar to that of initiator-triggered MIPs [14]. The selectivity of the MIP for trypsin was investigated by performing competitive binding experiments with thrombin and kallikrein, two other serine proteases inhibited by *p*-aminobenzamidine. MIP was incubated with 100 nM FITC-trypsin (see ESI for its synthesis) together with 1 μM of non-labelled trypsin, kallikrein or thrombin. After incubation, the particles were separated by centrifugation and the free FITC-trypsin was quantified by fluorescence measurement. Fig. 1B shows that the binding of FITC-trypsin to MIP is almost totally suppressed in the presence of trypsin, whereas kallikrein and thrombin displace much less of the fluorescent probe. These results prove that the MIP contains imprinted cavities that are highly selective for the target trypsin.

The particle size and morphology of the self-initiated MIP-trypsin microgels were then characterized by scanning electron microscopy (SEM) and dynamic light scattering (DLS) analysis. As seen in Fig. 1C, the particles appear agglomerated with a hydrodynamic size of ~1.5 μm (Fig. 1D).

3.2. S-propranolol MIPs

MIPs for propranolol were synthesized by precipitation polymerization in acetonitrile as previously described [39], but no initiator was added. The polymerization mixture contains MAA as functional monomer and EGDMA as cross-linker with a ratio S-propranolol: MAA: EGDMA of 1:8:40 [40]. Monomer concentrations (C_m) of 10% and 4% were tested. In both cases, polymerization occurred (Fig. 2B, inset), with a yield of 96% and 60%, respectively (Table 1). Similar yields, >95% have been reported for initiator-based polymers prepared by precipitation polymerization in acetonitrile, using trimethylolpropane trimethacrylate (TRIM)

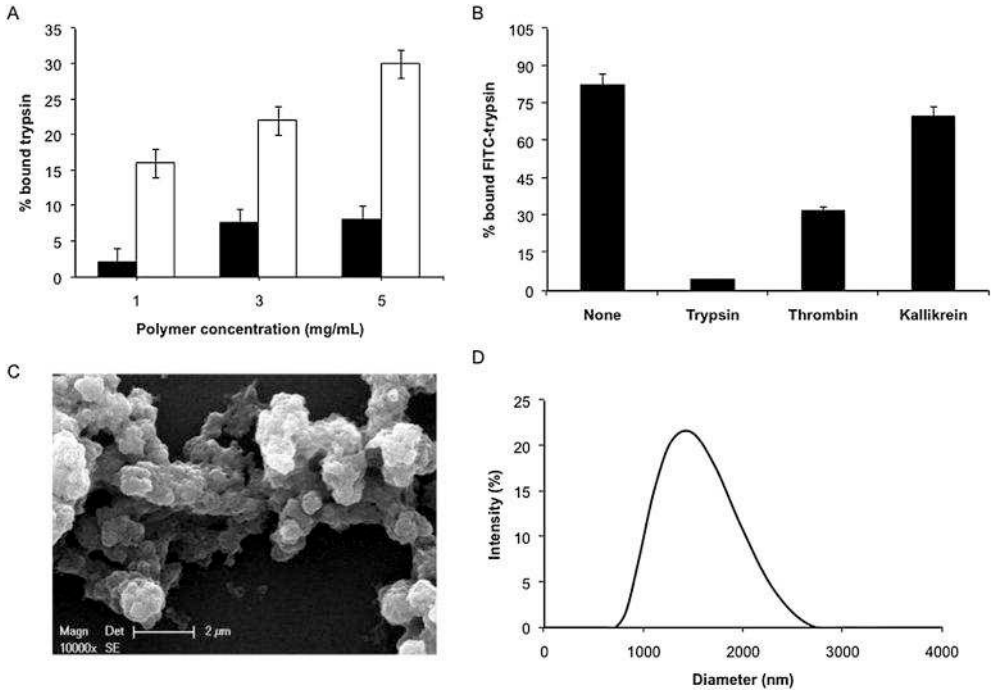

Fig. 1. (A) Equilibrium binding isotherms for trypsin (600 nM) on MIP (white) and NIP (black) microgels. Free trypsin was quantified by spectrophotometric measurements of its activity using TAME as substrate. (B) Displacement of bound FITC-trypsin (100 nM) from 3 mg/mL MIP by 1 μM trypsin, thrombin and kallikrein. Incubation medium: 5 mM Tris–HCl buffer, 10 mM $CaCl_2$, pH 8.0. Data are means from three independent experiments from two different batches of polymers. The error bars represent standard deviations. (C) SEM image and (D) DLS analysis, of MIP-trypsin, prepared in water.

instead of EGDMA as crosslinker, a C_m of 2% and CL of 71% [41]. The binding properties of the polymers were evaluated by equilibrium binding assays in both ACN (the solvent of polymerization) and in mixed-aqueous conditions (25 mM sodium citrate buffer pH 6.0/ acetonitrile (50/50)) [41]. Fig. 3A shows the binding behaviours of the polymers with $C_m = 10\%$; the MIPs adsorb the radioligand and show saturation-type behaviour, whereas the non-imprinted control polymers show nearly no binding, as reported for polymers

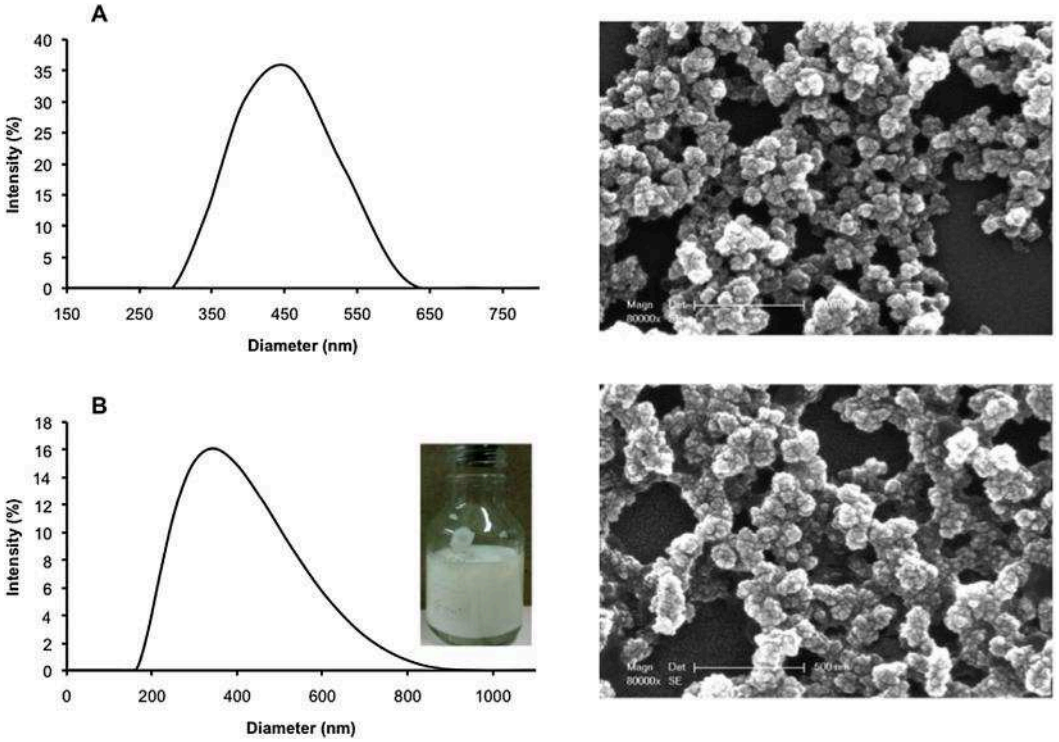

Fig. 2. DLS measurements and SEM images (scale-bar represents 500 nm) of (A) MIP-propranolol and (B) NIP-propranolol. Inset: Photo of self-initiated MAA/EGDMA (C_m 10%) polymer in ACN.

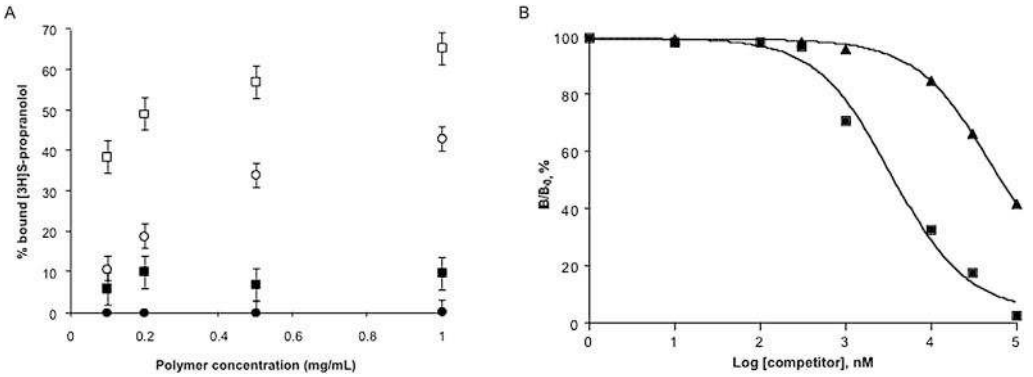

Fig. 3. (A): Equilibrium binding isotherms for radiolabeled S-propranolol (0.7 pmol, 15 nCi) on MIP (open squares) and NIP (black squares) in acetonitrile and on MIP (open circles) and NIP (black circles) in 25 mM sodium citrate buffer pH 6.0/acetonitrile (50/50). Polymers were prepared with Cm: 10%. Data are means from three independent experiments from two different batches of MIP. The error bars represent standard deviations. (B): Inhibition of radioactive S-propranolol binding (0.7 pmol, 15 nCi) to 0.1 mg MIP-propranolol by S-propranolol (square) and R-propranolol (triangles) in ACN. B/B_0 is the ratio of the amounts of radioactive S-propranolol bound in the presence and absence of displacing ligand.

prepared with initiators [39,41]. The high binding specificity was additionally confirmed by exploiting the intrinsic fluorescence of propranolol [42]. Thus, the binding was determined by measuring the fluorescence intensity of 1 nmol of S-propranolol (λ_{ex} = 300 nm; λ_{em} = 338 nm), incubated with various concentrations of polymers (Fig. 4A). This amount is 1000-fold higher than the amount of radioactive analyte and allows to probe other binding sites with different affinities on the MIP; indeed, MIPs generated by the self-assembly approach generally contain a non-homogeneous distribution of binding sites [3,4,9,36].

The selectivity of the MIP for S-propranolol was studied by comparing the binding with the R-enantiomer. Competition studies at equilibrium were performed in ACN with the C_m = 10% polymers. Fixed amounts of 0.1 mg of MIP and 0.7 pmol of radioactive S-propranolol and variable amounts of competing S-propranolol and R-propranolol from 1 nM to 100 μM were tested. The results are shown in Fig. 3B. The values of IC_{50} (the concentrations of competing ligands required to displace 50% of the specifically bound radioligand) for S-propranolol and R-propranolol, determined from a non-linear regression fit were 3.4 and 47.3 μM respectively, which means that the cross-reactivity of R-propranolol with S-propranolol is 7.2%, comparable to the cross-reactivities (~5%) of initiator-based MIPs, assayed under similar equilibrium binding with a radioactive analyte [41]. This indicates that our MIP is selective for S-propranolol.

Overall, these findings indicate that the recognition properties of the MIP are not affected when prepared in absence of initiator. It has been previously reported that the amount of initiator influences the performance of MIPs, in particular, large amounts of initiator increase the polymerization rate and the heat produced during the reaction, leading to an increase in the temperature inside the polymerization reaction thus causing the formation of poor quality imprinting sites [23]. In our case, a relatively mild temperature of maximum 37 °C was reached inside the polymerization mixture; this can explain the very good binding performance in terms of specificity and selectivity of the MIP (Fig. 4B).

The particle size of the MIP and the NIP, as measured by DLS is 441 nm and 340 nm respectively. The corresponding nanoparticulate clusters are seen on the SEM images (Fig. 2); their morphologies are similar to ABDV-thermally initiated MAA-EGDMA polymers in ACN [39].

For the polymers with C_m 4%, the equilibrium binding isotherms in ACN indicate an equally high binding of the MIP but with a lower imprinting factor. The higher dilution of the polymerization mixture might account for both the lower number of good quality binding sites in the MIP and the lower polymerization yield. As expected for a more diluted medium, the MIP and NIP sizes are smaller than the polymers of C_m 10%, 350 nm and 273 nm respectively as measured by DLS (Fig. S1).

3.3. MIPs 2,4-D

The first MIPs for 2,4-D were synthesized as bulk polymers by Haupt et al. [27]. The polymerization mixture contained 4-vinylpyridine, EGDMA and ABDV as functional, cross-linking monomers and initiator respectively, with a ratio 2,4-D: 4VP:

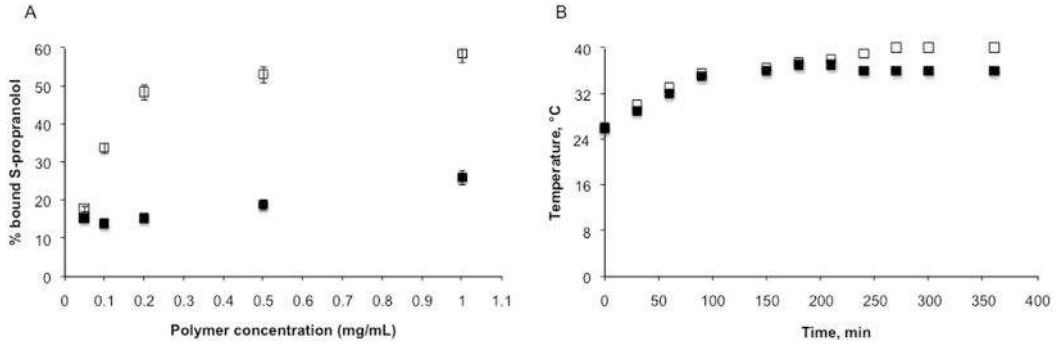

Fig. 4. (A) Equilibrium binding isotherms for S-propranolol (1 nmol) on MIP (open squares) and NIP (black squares) in acetonitrile, as measured by fluorescence. Polymers were prepared with C_m: 10%. Data are means from three independent experiments. The error bars represent standard deviations. (B) Temperature inside the polymerization mixture, monitored with a thermocouple (black squares) and with a glass thermometer on the UV lamp (open squares). Polymerization vials were separated from the lamp by a glass Petri dish of 2-cm thickness.

EGDMA: ABDV of 1: 4: 20: 0.31. Thermal polymerization was done in methanol/water (4/1) at 60 °C. The specificity of the resulting MIP was very high when assayed in 20 mM sodium phosphate buffer pH 7.0 + 0.1% Triton X-100 (binding buffer), as only 0.2 mg of polymer was needed to adsorb 50% of the added radioligand whereas the NIP did not bind at all. In this study, we followed this recipe, except that precipitation polymerization using 15 times higher volume of solvent (C_m: 5.5%) (Table 1) was employed and no initiator was added. Polymerization occurred when irradiated under UV, though with a low yield (19%). A yield of 54% was reported for the synthesis of an iniferter-based MIP with C_m: 3.5% using photopolymerization and a temperature of 37 °C [44]. The low yield could probably be remedied by using a higher polymerization temperature [44] or leaving the polymerization for a longer time.

Since we found no report about whether 4-vinylpyridine can self-initiate, a similar polymerization mixture containing 4-vinylpyridine alone was left to polymerize under the same conditions as the MIP mixture. No polymerization was observed, which suggests that the initiation probably starts from the cross-linker EGDMA. This means that if at least one of the monomers is self-initiating, the MIP will still polymerize.

Equilibrium binding experiments showed that the MIP was quite specific when assayed in binding buffer (Fig. 5A). Though not described in the precedent work [27], the binding behaviour of the self-initiated polymers was further tested in methanol/water (4/1), the solvent of polymerization, which should be the most favourable medium as the imprinted sites were initially created there. MIP binding was higher but with a lower specificity, with an IF of ~2 (Fig. 5B), similar to MIPs prepared by AIBN [43], reversible addition-fragmentation chain transfer (RAFT) [43] or iniferter [44]-induced precipitation polymerization, assayed in similar solvents. These results indicate that the 2,4-D MIPs are perfectly water compatible as the imprinting factor is higher in aqueous conditions.

In an attempt to increase the yield of polymerization, other protocols were tried. 2,4-D MIPs using thermal polymerization in acetonitrile [45,46] instead of methanol/water have also been described. The polymerization mixture was based on a ratio 2,4-D: 4VP: EGDMA of 1: 4: 8.5, with a C_m: 4%. Using this protocol and without adding any initiator, MIPs were obtained with yields of 50% for the MIP (Table 1). The yields are higher despite a lower amount of EGDMA; this could be due to the higher polymerization temperature or the different medium used (ACN instead of methanol/water). High binding was observed but there was no imprinting neither in acetonitrile or binding buffer (Fig. S2). Low IF ~1.5–2 has been reported for initiator-induced MIPs prepared in ACN [45,46]. Thus, we can conclude that the most favourable polymerization solvent to obtain specific self-initiated 2,4-D MIPs, is methanol/water.

The diameters of the MIP and NIP particles prepared in methanol/water, as deduced from SEM images are polydisperse and ~100 nm (Fig. 6), smaller than those reported for an iniferter-based MIP (720 nm). As discussed by the authors, the presence of high initiator concentration in a precipitation polymerization system can result in large particle size [44]. However, quite similar morphologies were observed, as well with ABDV-initiated polymers [47].

3.4. Testosterone MIPs

As MAA and EGDMA are the most widely used monomers for imprinting, they were further tested for their auto-initiating abilities with another well-studied template, testosterone (Table 1). Self-initiated bulk MIPs were prepared in acetonitrile with a ratio

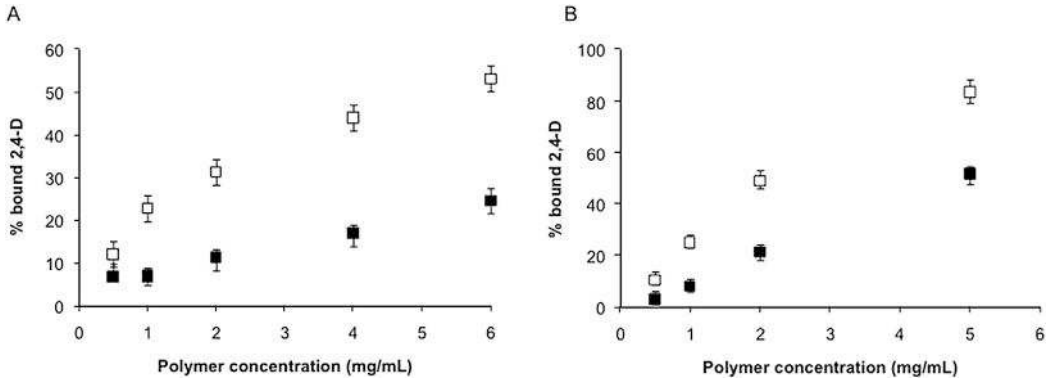

Fig. 5. Equilibrium binding isotherms for radiolabeled 2,4-D (0.2 nmol, 10 nCi) on MIP (open squares) and NIP (black squares) in (A) 25 mM sodium phosphate buffer pH 7.0 + 0.1% triton X-100 (B) methanol/water (4/1). Data are means from three independent experiments with two different batches of polymers. The error bars represent standard deviations.

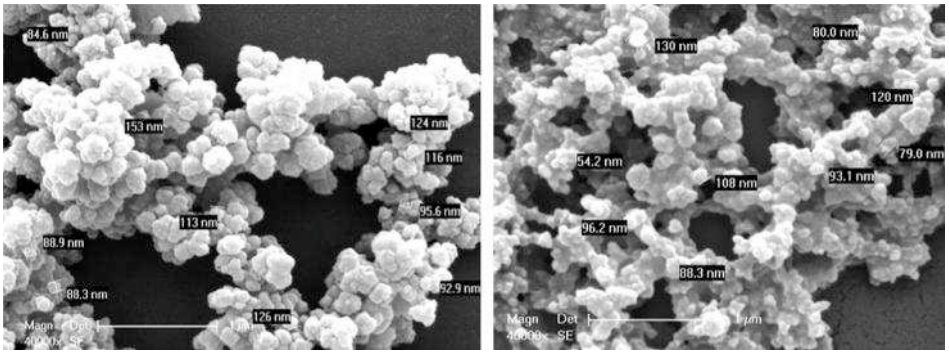

Fig. 6. SEM images of 2,4-D MIP (left) and NIP (right) synthesized in methanol/water (4/1). Scale-bar: 1 μm.

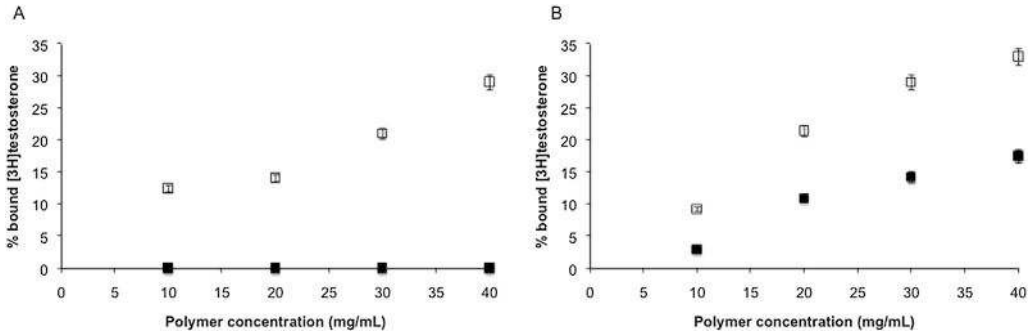

Fig. 7. Equilibrium binding isotherms for radiolabeled testosterone (0.4 nM, 30 nCi) on (A) UV-MAA/EGDMA-MIP (open squares) and UV-MAA/EGDMA-NIP (black squares) and on (B) thermal-MAA/DVB-MIP (open squares) and thermal-MAA/DVB-NIP (black squares) in acetonitrile. Data are means from three independent experiments from two different batches of MIP. The error bars represent standard deviations.

testosterone: MAA: EGDMA of 1: 8: 25, as described in our previous report [28]. Fig. 7A shows that the testosterone MIPs were very specific as no binding was observed with the NIPs. This behaviour is similar to that of initiator-based polymers. However, the extent of binding was 50% lower as compared to ABDV- thermally initiated polymers [28] although the plateau of the isotherm has not yet been reached. Nevertheless, this example shows once again that a MIP specific for a target analyte can be obtained without adding any initiator just by using the self-initiating capacities of its monomers.

Testosterone MIPs have also been prepared by initiator-induced polymerization using the combination MAA/DVB, albeit with a lower imprinting factor [28]. Since styrene is known to self-initiate, either under UV light or by heat [34,35], it was interesting to investigate whether self-polymerized testosterone MIPs could be obtained if EGDMA is replaced with DVB (Table 1). Surprisingly, only a negligible amount of polymer was formed when irradiated by UV light but substantial amount of self-initiated MIPs were obtained when incubated at 90 °C (Table 1). The initiation starts from the DVB as a parallel experiment with MAA alone does not produce any polymer at 90 °C. The binding behaviour of the MAA/DVB polymers (Fig. 7B), shows that the MIP binds more than the NIP. This is a clear indication that imprinted sites have been created in thermally self-initiated MAA/DVB MIPs. Though this example shows that MIPs can be obtained from thermally activated self-initiated monomers, the high temperature used is not economically viable for large scale synthesis.

4. Conclusions

We have demonstrated that initiator-free molecularly imprinted polymers can be obtained by using acrylic and styrenic monomers, which can self-initiate under UV irradiation or heat. In the majority of our demonstration, polymerization occurred under mild conditions and with good yields. The specificity and selectivity were as good as the MIPs prepared with initiators. For those with lower yields and binding performance, conditions of polymerization probably need to be re-optimized, as the parameters (ratio of template: monomer: cross-linker, solvent, cross-linking degree) employed, were taken from initiator-based MIPs protocols. Our method eliminates the problem of finding a suitable solvent to dissolve both the initiator and the monomers. These 'green' MIPs are very promising and should have potential applications in fields where toxicity specially needs to be contained, like in biomedicine and in the food industry. However, to render this approach more universally applicable, further investigations on for instance the effect of lamp intensity and time/temperature of polymerization are required.

Acknowledgements

M.P. and S.N thank the ERASMUS Program for financial support. This work was supported by the European Regional Development Fund ERDF, and co-funding of equipment under CPER 2007–2013, European Commission (FP7 Marie Curie Actions, projects NANO-DRUG, MCITN-2011-289554 and SAMOSS, PITN-2013-607590). We thank Frederic Nadaud for SEM measurements.

Appendix A. Supplementary data

Supplementary data related to this article can be found at http://dx.doi.org/10.1016/j.polymer.2015.04.012.

References

[1] Wulff G. Chem Rev 2002;102:1–27.
[2] Haupt K, Mosbach K. Trends Biotechnol 1998;16:468–75.
[3] Alexander C, Andersson HS, Andersson LI, Ansel RJ, Kirsch N, Nicholls IA, et al. J Mol Recognit 2006;19:106–80.
[4] Haupt K. Anal Chem 2003;75:376A–83A.
[5] Pichon V, Haupt K. J Liquid Chromatogr Relat Technol 2006;29:989–1023.
[6] Martin-Esteban A. J Chromatogr Sci 2013;47:254–6.
[7] Uchida A, Kitayama Y, Takano E, Ooya T, Takeuchi T. RSC Adv 2013;3:25306–11.
[8] Kotova K, Hussain M, Mustafa G, Lieberzeit PA. Sens Actuators B Chem 2013;189:199–202.
[9] Bowen JL, Manesiotis P, Allender CJ. Mol Impr 2013;1:35–40.
[10] Bonomi P, Servant A, Resmini M. J Mol Recognit 2012;25:352–60.
[11] Lago MA, Grinberg VY, Burova TV, Concheiro A, Alvarez-Lorenzo C. J Funct Biomater 2011;2:373–90.
[12] Salian VD, Byrne ME. Macromol Mater Eng 2013;298:379–90.
[13] Puoci F, Cirillo G, Curcio M, Parisi OI, Iemma F, Picci N. Expert Opin Drug Deliv 2011;8:1379–93.
[14] Cutivet A, Schembri C, Kovensky J, Haupt K. J Am Chem Soc 2009;131:14699–702.
[15] Hoshino Y, Koide H, Urakami T, Kanazawa H, Kodama T, Oku N, et al. J Am Chem Soc 2010;132:6644–5.
[16] Sellergren B. Nat Chem 2010;2:7–8.
[17] Song X, Xu S, Chen L, Wei Y, Xiong H. J Appl Polym Sci 2014;131:40766–84.
[18] Lok CM, Son R. Int Food Res J 2009;16:127–40.
[19] Dorn M. In: Eyerer P, Weller M, Hübner C, editors. Polymers-opportunities and risks II, Hdb. Env. Chem. Berlin Heidelberg: Springer; 2010. p. 147–62.
[20] Ginzburg-Turgeman R, Mandler D. Phys Chem Chem Phys 2010;12:11041–50.
[21] Larsen AT, Lai T, Polic V, Auclair K. Green Chem 2012;14:2206–11.
[22] Byrne ME, Oral E, Hilt JZ, Peppas NA. Polym Adv Technol 2002;13:798–816.
[23] Mijangos I, Navarro-Villoslada F, Guerreiro A, Piletska E, Chianella I, Karim K, et al. Biosens Bioelectron 2006;22:381–7.
[24] Ye L, Yoshimatsu K, Kolodziej D, Da Cruz Francisco J, Dey ES. J Appl Polym Sci 2006;102:2863–7.
[25] da Silva MS, Vão ER, Temtem M, Mafra L, Caldeira J, Aguiar-Ricardo A, et al. Biosens Bioelectron 2010;25:1742–7.
[26] Zhang H. Polymer 2014;55:699–714.
[27] Haupt K, Dzgoev A, Mosbach K. Anal Chem 1998;70:628–32.
[28] Tse Sum Bui B, Haupt K. J Mol Recognit 2011;24:1123–9.
[29] Muncke J. J Steroid Biochem Mol Biol 2011;127:118–27.

[30] Shvedova AA, Kisin ER, Murray A, Kommineni C, Vallyathan V, Castranova V. Biochem Mosc 2004;69:23–31.
[31] Terao K, Niki E. J Free Radic Biol Med 1986;2:193–201.
[32] Wang H, Brown HR. Macromol Rapid Commun 2004;25:1095–9.
[33] Deng J, Wang L, Liu L, Yang W. Prog Polym Sci 2009;34:156–93.
[34] Deng J-P, Yang W-T, Ranby B. Macromol Rapid Commun 2001;22:535–8.
[35] Khuong KS, Jones WH, Pryor WA, Houk KN. J Am Chem Soc 2005;127:1265–77.
[36] Tse Sum Bui B, Haupt K. Anal Bioanal Chem 2010;398:2481–92.
[37] Luong HT, Male KB, Nguyen AL. Biotechnol Bioeng 1988;31:439–46.
[38] Ambrosini S, Beyazit S, Haupt K, Tse Sum Bui B. Chem Commun 2013;49:6746–8.
[39] Bompart M, Gheber LA, DeWilde Y, Haupt K. Biosens Bioelectron 2009;25:568–71.
[40] Andersson LI. Anal Chem 1996;68:111–7.
[41] Yoshimatsu K, Yamazaki T, Chronakis IS, Ye L. J Appl Polym Sci 2012;124:1249–55.
[42] Hunt CE, Ansell RJ. Analyst 2006;131:678–83.
[43] Pan G, Zu B, Guo X, Zhang Y, Li C, Zhang H. Polymer 2009;50:2819–25.
[44] Li J, Zu B, Zhang Y, Guo X, Zhang H. J Polym Sci Polym Chem 2010;48:3217–28.
[45] Hunt CE, Pasetto P, Ansell RJ, Haupt K. Chem Commun 2006;16:1754–6.
[46] Xu C, Ye L. Chem Commun 2011;47:6096–8.
[47] Ton X-A. Ph.D. thesis, Compiègne University of Technology, 2013.

COMMUNICATION

Cell and Tissue Imaging with Molecularly Imprinted Polymers as Plastic Antibody Mimics

*Stephanie Kunath, Maria Panagiotopoulou, Jacqueline Maximilien, Nataliya Marchyk, Jörg Sänger, and Karsten Haupt**

In this Communication, we demonstrate the application of fluorescently labeled molecularly imprinted polymer (MIP) nanoparticles as "plastic antibodies" for cell and tissue imaging. As a model, we target hyaluronan on cell surfaces, and we show that it is possible to specifically localize and quantify a substructure (epitope) of these molecules on fixated and living cells and tissues.

In fundamental biology and medical diagnostics there is a constant need to localize and quantify specific molecular targets. Bioimaging comprises the localization and qualitative or quantitative determination of target molecules in and on cells. In this context, interactions of proteins, their dynamics and localization are of particular interest, to derive information about their function or to detect abnormalities. The routinely used analysis tools here are fluorescent proteins or detection by labeled antibodies. However, no really versatile approach for the recognition and imaging of glycosylation sites on proteins exists.

Glycosylation sites on cell surfaces are important biomarkers, and glycoproteins represent the majority of the biomarkers approved by the U.S. Food and Drug Administration.[1] They carry a very variable repertoire of oligosaccharides and play important roles that are often of biomedical relevance. Abnormal changes in glycosylation sites can cause variations in protein folding and thus, a change in protein activity and function. During tumor development tremendous changes in cell surface glycosylation patterns can occur.[2–4] Furthermore, viruses often use the glycosylation apparatus from the host to synthesize their own shell glycoproteins in order to not to be recognized by the immune system.[5] To detect abnormal glycosylation of proteins or lipids, chromatographic and electrophoretic methods, as well as Western Blot using lectins or antibodies are applied.[6] Thereby, the terminal part of a glycan is of particular interest as these structures are often associated with malignancy.[7] Unfortunately, the availability of recognition elements that can specifically bind relevant glycosylated biomarkers is very limited and no versatile imaging tool for these markers exists. In this context, tailor-made MIPs are promising synthetic receptors.

Molecular imprinting of synthetic polymers is a templating process at the molecular level. Monomers carrying functional groups self-assemble around a template molecule (the target or a derivative), followed by copolymerization with cross-linking monomers, which results in the formation of a polymeric mold around the template. Removal of the template then reveals 3D binding sites in the polymer that are complementary to the template in size, shape, and position of the functional groups. MIPs exhibit excellent binding properties with affinities and selectivities often comparable to those of antibodies.[8,9] Therefore, they are also referred to as "plastic antibodies."[10–14] In contrast to biological antibodies, their production is reproducible, relatively fast and economic, and no animals are necessary. MIPs are potentially superior receptor materials for cell imaging applications for a number of reasons: They are physically and chemically very stable and are not degraded by proteases or denatured by solvents, and they can be engineered and tailored for a given application. In principle, MIPs can be obtained for any target molecule, even when no natural receptor or antibody exists. They can be easily functionalized with fluorescence dyes or quantum dots,[15,16] and their size can be tuned according to the localization of the target. Indeed, during recent years, methods have become available allowing for the synthesis of MIPs in the form of nanoparticles and even quasi-soluble nanogels that appear to be the most suitable formats for imaging applications.[10,12–14,17]

In this Communication, we apply molecularly imprinted polymers antibody mimics for the first time for molecular imaging of cells and tissue in order to localize and quantify target molecules on the cell surface. Since molecular imprinting of entire biomacromolecules such as proteins or oligosaccharides is challenging, we opted for what is commonly called the "epitope approach",[18,19] which was inspired by nature. A monosaccharide, glucuronic acid is imprinted, and the MIP is then able to bind this molecule if present as the terminal unit on larger oligosaccharides (**Figure 1**). Glucuronic acid is abundant on the surface of cells such as keratinocytes in the form of hyaluronan as part of the glycocalix. The measurement of hyaluronan levels in blood is clinically relevant for the assessment of the degree of liver fibrosis and cirrhosis in chronic liver disease.[20] Here, we have used hyaluronan as a model to prove that MIPs can be applied as a specific staining material for glycosylations. Sugars[21–23] and glycoproteins[24] have been the targets for molecular imprinting in earlier work. We have recently developed a MIP imprinted with glucuronic acid for binding in aqueous solvents.[25] This

Dr. S. Kunath, M. Panagiotopoulou,
Dr. J. Maximilien, Dr. N. Marchyk, Prof. K. Haupt
Sorbonne Universités
Université de Technologie de
Compiègne, CNRS Institute for
Enzyme and Cell Engineering
CS30319, 60203, Compiègne, France
E-mail: karsten.haupt@utc.fr
Dr. J. Sänger
Institute of Pathology Bad Berka
Robert-Koch-Allee 9, 99438 Bad Berka, Germany

DOI: 10.1002/adhm.201500145

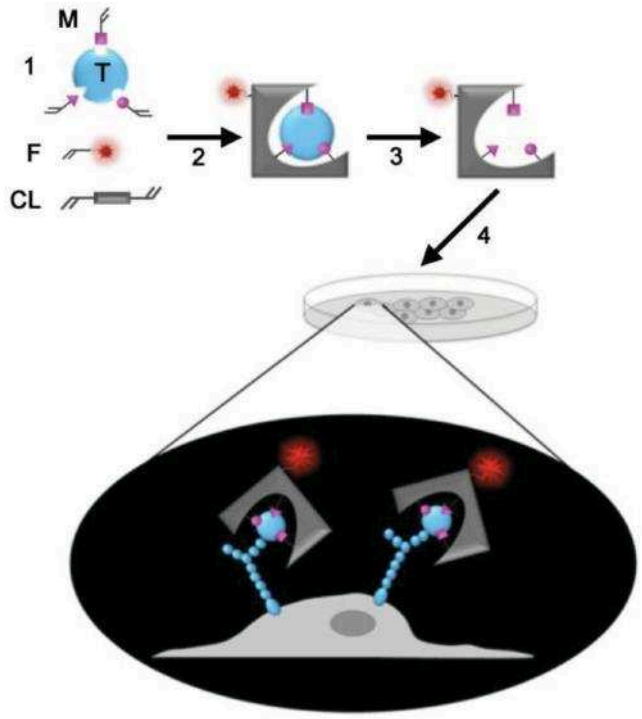

Figure 1. Schematic illustration of the cell imaging principle based on MIPs. Glucuronic acid-imprinted polymers with fluorescence label are prepared based on functional monomers M self-assembling with the imprinting template T (step 1), which copolymerize with fluorescent monomers F and cross-linking monomers CL (step 2). After template extraction (step 3) a MIP is obtained. The polymer particles are then applied to keratinocytes that carry hyaluronan as glycosylation on their surface (step 4). The imprinted fluorescently labeled polymer particles bind to the terminal glucuronic acid of hyaluronan, for cell imaging.

MIP was now synthesized in the form of dye-labeled nanoparticles, and used to image the hyaluronan on human keratinocytes and on adult skin specimens, by epifluorescence and confocal fluorescence microscopy. Polymers imprinted with glucuronic acid (GA) were synthesized according to an earlier developed protocol.[25] As functional monomers, (*N*-acrylamido)-benzamidine (AAB) and methacrylamide (MAM) were used (see Scheme S1, Supporting Information). To be able to use the polymer for cell imaging, a polymerizable rhodamine derivative was added to the prepolymerization mixture to incorporate fluorescent dye moieties into the polymer matrix. Its molar ratio with respect to the other monomers was optimized to maximize the fluorescence intensity of the particles (optimal ratio: 1:0.05 AAB:rhodamine). Higher dye content resulted in lower brightness due to reabsorption or energy transfer. Molecularly imprinted and nonimprinted control polymer (NIP) particles with diameters of ≈400 nm (less than 10% deviation between MIP and NIP) with a good monodispersity were obtained using a precipitation polymerization protocol.[17] This particle size was chosen to avoid possible internalization of the particles. The fluorescence intensities of the MIP and NIP particles were determined spectroscopically and were found to be similar with less than 10% deviation. This deviation was taken into account for quantification in microscopic images. The binding properties of the polymers were studied with equilibrium radioligand binding assays using radiolabeled glucuronic acid. The MIP has a high binding capacity and affinity in pure water and in a 9:1 methanol/water mixture. Its binding of glucuronic acid is specific, as the NIP binds much less of the target molecule, yielding an imprinting factor (binding to the MIP/binding to the NIP) of 3.2 in water (Figure S1, Supporting Information). The selectivity of the MIP was verified with competitive radioligand binding assays comparing the binding of GA with that of seven related or nonrelated molecules (Table S1 and Figure S1 of the Supporting Information). Phenyl-glucuronic acid has the same basic structure as GA, with an additional benzene ring. It does not bind as well as GA (58%), since it is larger and fits less well into the site. Acetic acid is equivalent to the carboxyl group of GA; it binds much less (31%), thus the rest of the GA molecule is important for binding. *N*-acetylneuraminic acid is an unrelated molecule; although it has a carboxyl group, it binds much less than GA (>1%). Other possible interfering molecules during the imaging application of the MIPs, namely, glucose, galactose, *N*-acetylglucosamine, *N*-acetylgalactosamine, do not bind to the MIP, which was expected as they also lack the charged carboxyl group. These results conform to the specificity of the MIP.

A standard immunostaining protocol was adapted to the application of MIPs for cell imaging, to localize and quantify hyaluronic acid on keratinocytes. The protocol with the different steps is shown in Figure S2, Supporting Information. Each step was optimized on HaCaT cells. The fixation of cells is based on paraformaldehyde, which has low background fluorescence. A blocking step is then performed with glycine, to stop the fixation and reduce nonspecific binding. The MIP and NIP particles were stable in suspension probably due to their positive surface charge (see zeta-potential in the Supporting Information). Glycine is not inducing aggregation of the MIP particles, unlike bovine serum albumin that was also tested. An (optional) additional step, to confirm the specificity of the MIP staining, is treatment with hyaluronidase. This enzyme hydrolyzes the endo-N-acetylhexosaminic bonds of hyaluronic acid, thus eliminating terminal glucuronic acid groups and generating terminal N-acetylglucosamine on the cell surface.[26] Hyaluronidase is also active on proteoglycans like chondroitin sulphate that can be found beside hyaluronan on the keratinocyte surface and that also contains glucuronic acid. The final step is the incubation with MIP particles, or with NIP particles as a control. The fluorescent particles were quantified on cells by an algorithm that considers only intensities that are higher than a background threshold. By applying this optimized protocol, the imprinted polymer showed 44% more binding to the cells than the NIP (**Figure 2**A). After hyaluronidase treatment, there was no significant difference anymore between MIP and NIP. The relatively high binding of the non-imprinted polymer is due to the presence in these particles of randomly distributed aminidinium groups originating from the functional monomer AAB. We should stress, though, that the NIP binding does not reflect the extent of non-specific binding of the MIP, since in the MIP the amidine groups are located in specific binding sites. The NIP was only used to confirm the molecular imprinting effect. Thus, these results illustrate the specificity of the binding of glucuronic acid-imprinted polymer particles to hyaluronan on human keratinocytes. One advantage of using molecularly imprinted polymers is their

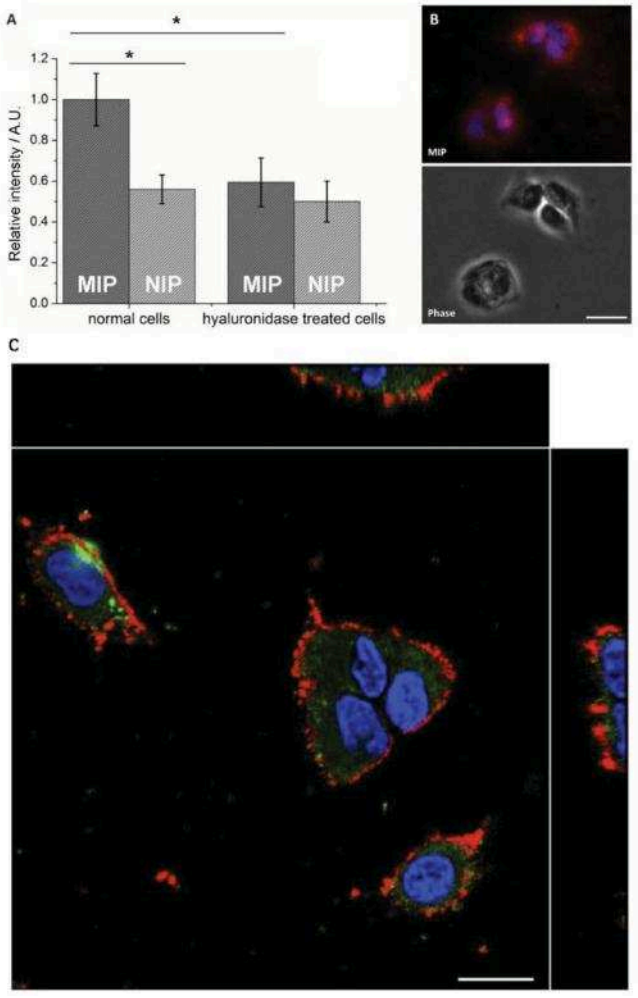

Figure 2. Fixated human keratinocytes (HaCaT) exposed to molecularly imprinted polymers. A) Relative fluorescence intensity of fluorescence microscopy images of keratinocytes that were used for cell imaging with molecularly imprinted (MIP) and nonimprinted control polymers (NIP) with and without hyaluronidase treatment. $N = 4$ replications, duplicates in each experiment. A *t*-test was used to determine the significance of the results. The mean values of MIP and NIP for normal cells, and of MIP for normal cells and MIP of hyaluronidase-treated cells, are different with more than 99% statistical certainty (1% significance level, *). B) Staining of glucuronic acid imprinted polymers on keratinocytes. Top: fluorescence of 4′,6-diamidin-2-phenylindol (DAPI) (blue) and rhodamine (red), bottom: phase contrast. Scale bar: 40 µm. C) Confocal microscopy image of MIP-stained human keratinocytes (HaCaT). Merge image of three color channels: DAPI blue signal (cell nucleus), 3,3′-dioctadecyloxacarbocyanine perchlorate (DiO) green signal (cell membrane), rhodamine red signal (MIPs on cells). Twenty three slices were captured within 14 µm of a z-stack, and one slice through the *z*-axis of this z-stack is illustrated. Scale bar: 20 µm.

physicochemical stability. Therefore, their binding can be performed in the presence of organic solvents, if this is required by the protocol or in order to tune their binding properties. Furthermore, the coupling of MIP and antibody staining at the same time is generally possible as the conditions for both staining procedures are very similar.

Beside the quantification of the targets, their localization is of high interest for cell imaging. The spatial distribution of MIPs targeted to hyaluronan on human keratinocytes (HaCaT cells) was determined with epifluorescence microscopy (Figure 2B). The particles can be found nearly exclusively in regions were cells are present. The pattern of hyaluronan distribution on confluent human keratinocytes imaged with MIPs is heterogeneous, which is in agreement with the literature[27,28] (Figure S3, Supporting Information).

Confocal microscopy was then used to study the distribution of MIPs along the *z*-axis, with additional labeling of the membrane and the nucleus (Figure 2C, and Figure S4, Supporting Information). The red fluorescent MIP particles are localized only on the cell surface due to specific binding to hyaluronan. This also shows that MIP staining can be easily coupled with other staining methods without interference or loss of specificity. As a reference method for hyaluronic acid localization and quantification on HaCaT cells, a biotinylated hyaluronic acid binding protein (HABP) was used. The protein was revealed with fluorescein isothiocyanat-labeled streptavidin. This reference method was applied using the same protocol as with MIPs, except for the buffer that was changed to PBS for better stability of the protein. Again, the nucleus was stained with DAPI to study the localization of the protein under the same conditions as with the MIP (Figure S5, Supporting Information). It can be seen that in the absence of enzymatic treatment there are areas with heterogeneous distribution of hyaluronan, some cells carrying less hyaluronan than others, which is consistent with the observations with the MIPs (Figure S4, Supporting Information) and with the literature.[27,28] As described above with MIPs, enzymatic treatment with hyaluronidase was performed prior to HABP staining as a control. The quantitative analysis of the images revealed a significant (52%) reduction in the fluorescence signal of hyaluronidase treated versus untreated cells. This is in agreement with the results obtained with the MIP (Figure 2A).

Molecularly imprinted polymers were also applied for imaging of living cells. First, cell viability was determined with an MTT assay for the polymer concentrations previously used for imaging (Figure S6A, Supporting Information). $CdCl_2$ was used as a positive control to induce cell death. The results show that the MIPs do not reduce the viability of keratinocytes incubated for 24 h up to a concentration of 0.03 mg mL^{-1}. We also observed that the polymer particles are stable and do not aggregate in the cell culture media. Vital keratinocytes were then incubated for 90 min with MIPs in cell culture media supplied with 10% FBS for imaging (Figure S6B, Supporting Information). It can be seen that the binding of the polymer particles is limited to the cell surface indicating specific binding to hyaluronic acid. No internalization of particles was observed, with these particles of 400 nm diameter. Furthermore, the cell morphology was not influenced by the presence of the polymer particles. Thus, imaging of living cells with these MIPs is possible.

Molecularly imprinted polymers were applied to human skin specimen to establish their usefulness for tissue imaging. Human skin specimen were sliced, immobilized on microscope slides, fixed with acetone and stained with MIPs imprinted with glucuronic acid (**Figure 3**A). MIPs bound to the skin tissue are mainly localized in the basal layer of the epidermis and the

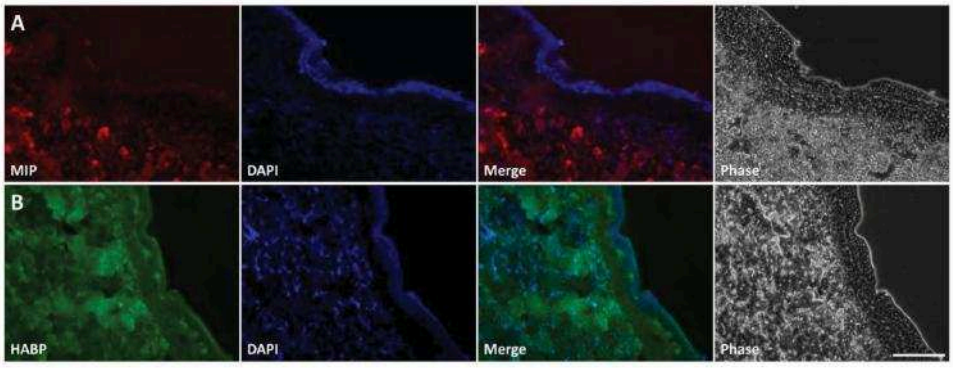

Figure 3. Human skin specimens stained with A) glucuronic acid imprinted polymers (MIP) and B) FITC-labeled hyaluronic acid binding protein (HABP). Scale bar: 100 µm.

papillary dermis. Lower amounts of imprinted polymer particles can be found in the cornified and granular cell layer and even lower amounts in the spinous cell layer. This is in good agreement with the reports in the literature[29–32] on hyaluronan localization, and also with the results obtained with FITC-labeled HABP applied to tissue samples from the same batch and prepared in the same way (Figure 3B). Only the localization of HABP in the spinous cell layer is slightly higher than that of MIPs. However, the shape and structure of the hyaluronan exposing regions of cells are very similar with both imaging methods. Again it should be noted that MIP staining could be easily coupled with two other dyes, DAPI and DiO, without interferences (Figure 3 and Figure S7, Supporting Information).

In conclusion, this study demonstrates for the first time the potential of molecularly imprinted polymers as synthetic antibody mimics for bioimaging, to localize and quantify a molecular target on fixed and living cells as well as on tissue samples. Fluorescently labeled polymers imprinted with glucuronic acid were used for the recognition of hyaluronic acid on keratinocytes as an illustrative example for the detection of glycosylations on cell surfaces. Especially for targets for which no natural receptors are available, such as some glycanes, MIPs are a promising synthetic alternative. Adapting a standard immunostaining protocol to the use with MIPs was rather straightforward, with very minor changes required. This also indicates that simultaneous staining with antibodies and MIPs should be possible. Moreover, molecular recognition and visualization is a one-step process with MIPs, in contrast to the application of primary and secondary antibodies in standard immunostaining protocols. Therefore, multiple labels are more easily implemented for staining several targets, as the existence of antibodies of different animal origins is not necessary. MIPs can be synthesized against target molecules of different sizes, from small molecules such as single amino acids or sugars, to peptides and even entire proteins, which makes them very versatile as antibody mimics. We therefore believe that MIPs as "plastic antibodies" have a great potential for bioimaging. The possibility to additionally attach drugs and to associate other functionalities such as superparamagnetic nanoparticles or fluorescent nanocrystals to the same material appears rather straightforward due to the synthetic polymeric nature of MIPs, which paves the way to new potential applications in theranostics.

Experimental Section

Experimental details (reagents and materials, synthesis and characterization of MIPs, cell and tissue staining and imaging) can be found in the Supporting Information.

Supporting Information

Supporting Information is available from the Wiley Online Library or from the author.

Acknowledgements

S.K. and M.P. contributed equally to this work. The authors thank Monique Meyer for excellent technical assistance. The authors thank EFRE (TNA VI-1/2009), the European Regional Development Fund and the Regional Council of Picardie (Glycosense project, and co-funding of equipment under CPER 2007–2013), the European Union (FP7 Marie Curie Actions, ITN NANODRUG, PITN-2011–289454, and ITN SAMOSS, PITN-2013–607590), and the French embassy in Germany (postdoctoral scholarship of S.K.), for financial support.

Received: March 2, 2015
Revised: March 31, 2015
Published online: April 16, 2015

[1] D. Meany, D. Chan, *Clin. Proteom.* **2011**, *8*, 7.
[2] T. Buskas, S. Ingale, G.-J. Boons, *Glycobiology* **2006**, *16*, 113R.
[3] C. R. Bertozzi, L. L. Kiessling, *Science* **2001**, *291*, 2357.
[4] A. Kobata, J. Amano, *Immunol. Cell Biol.* **2005**, *83*, 429.
[5] P. M. Rudd, T. Elliott, P. Cresswell, I. A. Wilson, R. A. Dwek, *Science* **2001**, *291*, 2370.
[6] G. Durand, N. Seta, *Clin. Chem.* **2000**, *46*, 795.
[7] D. H. Dube, C. R. Bertozzi, *Nat. Rev. Drug Discov.* **2005**, *4*, 477.
[8] K. Haupt, K. Mosbach, *Chem. Rev.* **2000**, *100*, 2495.
[9] S. A. Piletsky, N. W. Turner, P. Laitenberger, *Med. Eng. Phys.* **2006**, *28*, 971.
[10] P. Çakir, A. Cutivet, M. Resmini, B. Tse Sum Bui, K. Haupt, *Adv. Mater.* **2013**, *25*, 1048.
[11] K. Haupt, A. V. Linares, M. Bompart, B. Tse Sum Bui, *Top. Curr. Chem.* **2012**, *325*, 1.
[12] A. Cutivet, C. Schembri, J. Kovensky, K. Haupt, *J. Am. Chem. Soc.* **2009**, *131*, 14699.

[13] Y. Hoshino, H. Koide, T. Urakami, H. Kanazawa, T. Kodama, N. Oku, K. J. Shea, *J. Am. Chem. Soc.* **2010**, *132*, 6644.
[14] I. Chianella, A. Guerreiro, E. Moczko, J. S. Caygill, E. V. Piletska, I. M. Perez De Vargas Sansalvador, M. J. Whitcombe, S. A. Piletsky, *Anal. Chem.* **2013**, *85*, 8462.
[15] R. Y. Liu, G. J. Guan, S. H. Wang, Z. P. Zhang, *Analyst* **2011**, *136*, 184.
[16] C. I. Lin, A. K. Joseph, C. K. Chang, Y. D. Lee, *J. Chromatogr. A* **2004**, *1027*, 259.
[17] L. Ye, P. A. G. Cormack, K. Mosbach, *Anal. Commun.* **1999**, *36*, 35.
[18] A. Rachkov, N. Minoura, *Biochim. Biophys. Acta* **2001**, *1544*, 255.
[19] H. Nishino, C. S. Huang, K. J. Shea, *Angew. Chem. Int. Ed.* **2006**, *45*, 2392.
[20] V. S. Wong, V. Hughes, A. Trull, D. G. Wight, J. Petrik, G. J. Alexander, *J. Viral Hepatitis* **1998**, *5*, 187.
[21] A. G. Mayes, L. I. Andersson, K. Mosbach, *Anal. Biochem.* **1994**, *222*, 483.
[22] S. Striegler, *Macromolecules* **2003**, *36*, 1310.
[23] D. Singabraya, L. Bultel, F. Siñeriz, M. Mothéré, D. Lesur, J. Kovensky, D. Papy-Garcia, *Talanta* **2012**, *99*, 833.
[24] L. Li, Y. Lu, Z. J. Bie, H. Y. Chen, Z. Liu, *Angew. Chem. Int. Ed.* **2013**, *52*, 7451.
[25] S. Kunath, N. Marchyk, K. Haupt, K.-H. Feller, *Talanta* **2013**, *105*, 211.
[26] E. J. Menzel, C. Farr, *Cancer Lett.* **1998**, *131*, 3.
[27] J. P. Pienimaki, K. Rilla, C. Fulop, R. K. Sironen, S. Karvinen, S. Pasonen, M. J. Lammi, R. Tammi, V. C. Hascall, M. I. Tammi, *J. Biol. Chem.* **2001**, *276*, 20428.
[28] R. Tammi, D. MacCallum, V. C. Hascall, J. P. Pienimäki, M. Hyttinen, M. Tammi, *J. Biol. Chem.* **1998**, *273*, 28878.
[29] R. Tammi, J. A. Ripellino, R. U. Margolis, M. Tammi, *J. Investig. Dermatol.* **1988**, *90*, 412.
[30] C. Wang, M. Tammi, R. Tammi, *Histochemistry* **1992**, *98*, 105.
[31] Hyaluronsäure und Haut, *Trends in Clinical and Experimental Dermatology* Vol. *3* (Eds: W. Wohlrab, R. H. H. Neubert, J. Wohlrab), Shaker Verlag, Aachen, Germany **2004**.
[32] A. M. Alho, C. B. Underhill, *J. Cell Biol.* **1989**, *108*, 1557.

Bioimaging

International Edition: DOI: 10.1002/anie.201601122
German Edition: DOI: 10.1002/ange.201601122

Molecularly Imprinted Polymer Coated Quantum Dots for Multiplexed Cell Targeting and Imaging

Maria Panagiotopoulou, Yolanda Salinas, Selim Beyazit, Stephanie Kunath, Luminita Duma, Elise Prost, Andrew G. Mayes, Marina Resmini, Bernadette Tse Sum Bui, and Karsten Haupt**

Abstract: *Advanced tools for cell imaging are of great interest for the detection, localization, and quantification of molecular biomarkers of cancer or infection. We describe a novel photopolymerization method to coat quantum dots (QDs) with polymer shells, in particular, molecularly imprinted polymers (MIPs), by using the visible light emitted from QDs excited by UV light. Fluorescent core–shell particles specifically recognizing glucuronic acid (GlcA) or N-acetylneuraminic acid (NANA) were prepared. Simultaneous multiplexed labeling of human keratinocytes with green QDs conjugated with MIP-GlcA and red QDs conjugated with MIP-NANA was demonstrated by fluorescence imaging. The specificity of binding was verified with a non-imprinted control polymer and by enzymatic cleavage of the terminal GlcA and NANA moieties. The coating strategy is potentially a generic method for the functionalization of QDs to address a much wider range of biocompatibility and biorecognition issues.*

Fluorescent semiconductor nanocrystals, so-called quantum dots (QDs), have unique optical and electronic properties: size-tunable light emission, high signal brightness with reduced photobleaching, long-term photostability, and possible multiplexing due to narrow, symmetric, and well-resolved emission spectra. They have broad absorption spectra which enable simultaneous excitation of multiple QDs by a common excitation wavelength. QDs have been used as luminescent probes in bioassays, biosensors, and medical diagnostics,[1–4] such as cell imaging for cancer detection.[5–7] QD nanocrystals are generally synthesized in apolar solvents and are hydrophobic. Substantial progress in surface chemistry for rendering them soluble in aqueous media has been the key to their biocompatibility and functionalization for the coupling of specific affinity ligands (antibodies, nucleic acids, peptides). Different QD-solubilization strategies have been devised, including ligand exchange with small monodentate or polydentate thiol-containing molecules and encapsulation by a layer of amphiphilic polymers, polysaccharides, or proteins, silica shells, and phospholipid micelles.[1,2,4,8]

Herein, we present a novel versatile solubilization and functionalization strategy, which consists of creating a stable and robust hydrophilic cross-linked polymer coating directly on QDs by photopolymerization using the particles as individual internal light sources. Green- and red-emitting InP/ZnS QDs, hereafter referred to as green-QDs and red-QDs, which are less toxic than cadmium-based QDs,[7,9] were employed. Emitted fluorescent light from green (550 nm) or red QDs (660 nm), when excited with a UV lamp (365 nm), locally photopolymerizes a thin polymer shell on the surface of the QDs, thus yielding core–shell nanoparticles (Figure 1 A).

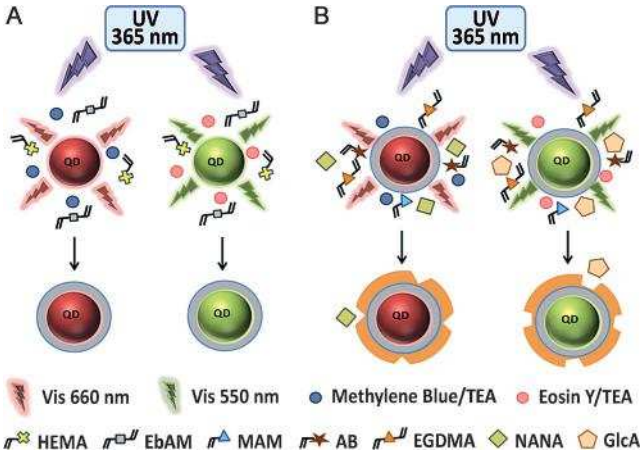

Figure 1. A) Red or green light emitted from InP/ZnS quantum dots excited by UV irradiation is used to synthesize a polymeric shell in situ around the particles by photopolymerization. Methylene blue/triethylamine (TEA) are used as the initiator system for red-QDs and eosin Y/TEA for green-QDs. B) A second shell of MIP is synthesized by reinitiation in the presence of functional and cross-linking monomers and a molecular template (GlcA or NANA).

Since emission from QDs is weak as compared to direct light, polymerization is confined to the QD surface; however, appropriate initiator systems must be used.[10] The emission

[*] M. Panagiotopoulou, Dr. S. Beyazit, Dr. S. Kunath, Dr. L. Duma, E. Prost, Dr. B. Tse Sum Bui, Prof. K. Haupt
Sorbonne Universités, Université de Technologie de Compiègne
CNRS Enzyme and Cell Engineering Laboratory
Rue Roger Couttolenc, CS 60319, 60203 Compiègne Cedex (France)
E-mail: jeanne.tse-sum-bui@utc.fr
karsten.haupt@utc.fr
Homepage: http://www.utc.fr/mip
Dr. Y. Salinas, Prof. M. Resmini
School of Biological and Chemical Sciences
Queen Mary University of London
London E1 4NS (UK)
Dr. A. G. Mayes
School of Chemistry, University of East Anglia
Norwich Research Park, Norwich NR4 7TJ (UK)

Supporting information for this article, including experimental details (reagents and materials, synthesis and characterization of MIP-QDs, equilibrium and competitive binding assays, TEM and DLS analysis, ^{1}H NMR studies of the AB–template complex, and cell and tissue staining and imaging), can be found under: http://dx.doi.org/10.1002/anie.201601122.

wavelength of the QD must overlap with the absorption wavelength of the initiator (see Figures S1 and S2 A in the Supporting Information), and the latter must not be activated by the UV light. Preliminary experiments confirmed that these requirements are met in the systems described (Figure 1; see the Supporting Information for details). At the same time, we verified that there was no self-initiated polymerization, a phenomenon frequently observed in the presence of numerous monomers and under lower-wavelength UV light.[11]

A MIP shell specific for glucuronic acid (GlcA; green-QDs) or *N*-acetylneuraminic acid (NANA; red-QDs) was grafted on top of the hydrophilic first shell (Figure 1 B) to target glycosylation sites on cells, since altered glycosylation levels or distributions are indicators of infection or malignancy. Recent advances in glycobiology and cancer research have defined the key processes underlying aberrant glycosylation with sialic acids or hyaluronan in cancer and its consequences.[12–15] Consequences include effects on tumor growth, escape from apoptosis, metastasis formation, and resistance to therapy. Polysaccharides involved in the glycosylation procedure have a highly conserved simple composition and are ubiquitously expressed in all animals that have a developed immune response. The natural production of antibodies that specifically recognize these "weak antigens" is difficult;[16] hence, traditional immunohistochemical methods for detecting glycosylations on cells are rare. An alternative would be "plastic antibodies" or MIPs.[17,18] MIPs are tailor-made synthetic antibody mimics that can recognize and bind target molecules specifically. They are synthesized by copolymerizing functional and cross-linking monomers in the presence of a molecular template, thus resulting in the formation of binding sites with affinities and specificities comparable to those of natural antibodies. Their molecular-recognition properties, combined with a high chemical and physical stability, make them interesting substitutes for antibodies in immunoassays,[19] biosensors,[20] bioseparation,[18,21] controlled drug release,[22] and bioimaging.[23–25]

In this study, MIP-coated QDs were applied for the first time for the simultaneous multiplexed pseudoimmunolabeling and imaging of human keratinocytes. Core–shell MIP nanoparticles for GlcA and NANA, (125 ± 17) nm in size, were obtained, thus enabling the specific targeting of both intracellular and pericellular terminal glycosylations. We previously reported 400 nm rhodamine-labeled MIP particles specific for GlcA that could only target the extracellular hyaluronan of the cell glycocalix.[23] We have now synthesized a dedicated stoichiometric functional monomer,[26] (4-acrylamidophenyl)(amino)methaniminium acetate, a polymerizable benzamidine referred to as AB in the text (see the Supporting Information for the synthesis of AB; see also Figure S3), which can form strong electrostatic interactions with the −COOH moiety of GlcA and NANA. Commonly, boronate-based monomers are employed[25,27] for targeting NANA and other monosaccharides, but the use of only noncovalent interactions is preferred for sugar imprinting in terms of binding and exchange kinetics.[28]

Green-QDs were prepared according to a previous report (see the Supporting Information).[29] A water-compatible shell was synthesized by using the hydrophilic monomers 2-hydroxyethyl methacrylate (HEMA) and *N*,*N*′-ethylene-bis(acrylamide) (EbAM), the initiator couple eosin Y/triethylamine (TEA), and green-QDs in toluene/dimethyl sulfoxide (DMSO; 1:1). This shell stabilizes the QDs for their further conjugation in polar solvents. Its presence (HEMA-QDs) was confirmed by transmission electron microscopy (TEM) and dynamic light scattering (DLS) (Figure 2 A,B). Further evidence was provided by another

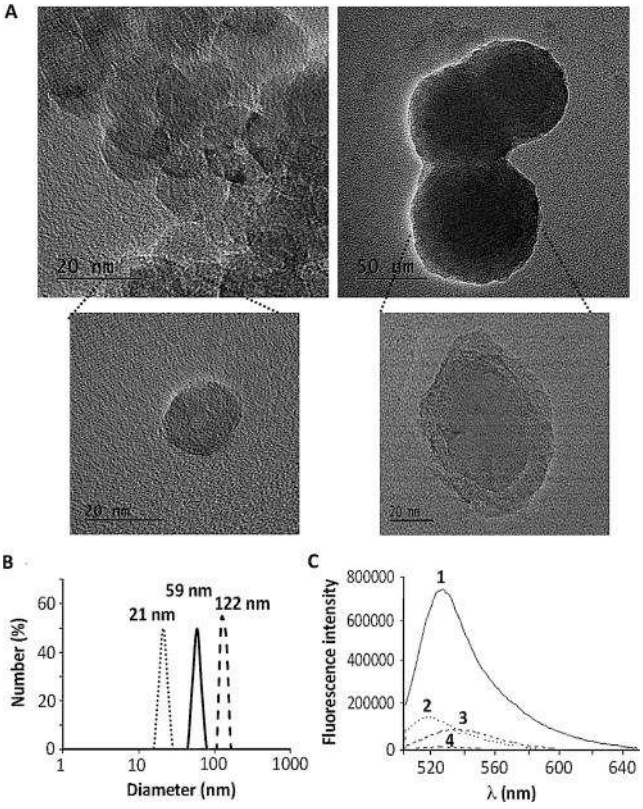

Figure 2. Evidence for the formation of a polymer shell around green-QDs. A) TEM images of bare QDs (left) and HEMA-QDs (right). B) Size distribution as measured by DLS of bare QDs (dotted line), HEMA-QDs (solid line), and MIPGlcA-QDs (dashed line). C) Emission spectra ($\lambda_{ex} = 495$ nm) of propargyl-functionalized QDs before (4) and after fluorescein labeling (1). The presence of fluorescein ($\lambda_{em} = 525$ nm) was clearly visible after labeling, whereas in control experiments with bare QDs, no fluorescein was seen before (2) or after labeling (3).

experiment, in which propargyl acrylamide was added to the polymerization mixture described above. The resulting propargyl-functionalized shell was then labeled with azidofluorescein (see the Supporting Information for synthetic details) by click chemistry. Fluorescein ($\lambda_{ex} = 495$ nm) was incorporated, as shown by the emission spectrum of the core–shell particles (Figure 2 C).

A MIP was photopolymerized on top of the first shell, again by using green light emitted by the QDs. The HEMA-QD particles were resuspended in DMSO, and the second shell (MIPGlcA-QDs) was obtained by irradiation with UV light using an MIP-precursor mixture containing GlcA, AB,

methacrylamide (MAM), ethylene glycol dimethacrylate (EGDMA), and eosin/TEA. MAM was added to provide hydrogen-bonding interactions with GlcA and to render the MIP more hydrophilic to prevent aggregation in the aqueous cell-imaging medium. A control non-imprinted polymer (NIP) was prepared in the same way but without the addition of GlcA. The stoichiometry and binding constant of the AB–GlcA complex were deduced from NMR titration studies in [D_6]-DMSO, which yielded a 1:1 ratio and a high association constant (K_a) of $7.1 \times 10^3\,\text{M}^{-1}$ (see Figure S4).

The recognition properties of MIPGlcA-QDs were evaluated by equilibrium radioligand-binding assays with [^{14}C]glucuronic acid in water. Figure 3A shows that MIPGlcA-QDs bound much more GlcA than NIPGlcA-QDs, thus indicating the creation of imprinted sites. MIP

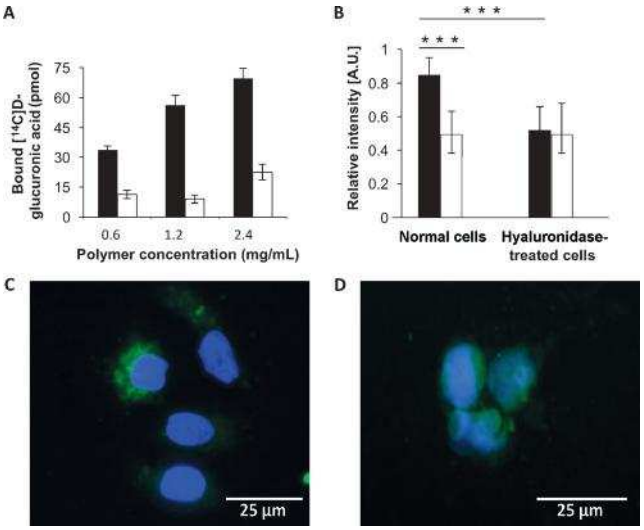

Figure 3. A) Equilibrium binding assay of MIPGlcA-QDs (black) and NIPGlcA-QDs (white) with [^{14}C]glucuronic acid in water. B) Relative fluorescence intensity of keratinocytes after imaging with MIP-QDs (black) and NIP-QDs (white), with and without hyaluronidase treatment ($n = 4$ independent replicates with quadruplicates for each experiment). Mean values of MIP and NIP for normal cells, and of MIP for normal cells and MIP for hyaluronidase-treated cells, are significantly different at 99.9% confidence ($p \leq 0.001$***). C, D) Staining of keratinocytes (C) and KU812 cells (D) with MIP-QDs (green); nuclear staining with 4′,6-diamidino-2-phenylindole (DAPI; blue).

selectivity was confirmed by competitive binding assays comparing the binding of GlcA with that of other monosaccharides, such as *N*-acetylgalactosamine, *N*-acetylglucosamine, galactose, glucose, and NANA, present in the terminal parts of glycolipids or glycoproteins that could potentially interfere during cell imaging. Since a large amount of particles are needed for competition studies, MIPGlcA and MIP-NANA polymers obtained by precipitation polymerization were employed instead of MIP-coated QDs. Less than 1% cross-reactivity was observed (see Figure S6 and Table S1).

For quantitative cell imaging, a standard immunostaining protocol was adopted for visualizing the MIP-QDs on human keratinocytes (HaCaT cells). To avoid possible interference from the fluorescence of entrapped residual eosin Y, the dye was photobleached prior to imaging experiments (see the Supporting Information for details). After cell fixation, MIPGlcA-QDs were added and left to incubate for 90 min before imaging (Figure 3C). Fluorescent particles on the cells were quantified after background subtraction by epifluorescence microscopy (see the Supporting Information for sample preparation, cell fixation, and fluorescent-image analysis). MIPGlcA-QDs showed 42% more binding to the cells than NIPGlcA-QDs (Figure 3B). MIPGlcA-QDs were also applied to another cell type, leukemia KU812, thus showing the versatility of the staining method (Figure 3D).

To confirm the selectivity of MIP-QD staining, we treated cells with hyaluronidase to remove terminal glucuronic acid moieties from the glycosylation sites (see Figure S8). Quantitative analysis of images revealed a 40% reduction in the fluorescence signal of hyaluronidase-treated versus untreated cells, whereas no change was observed for NIP-QD stained cells (Figure 3B). These results were validated by comparison with a previously reported method with a biotinylated hyaluronic acid binding protein (HABP).[30] The protein was revealed with fluorescein isothiocyanate labeled streptavidin. Quantitative analysis of the images revealed a 52% reduction in the fluorescence signal of hyaluronidase-treated versus untreated cells (see Figure S10), which is comparable to the reduction in recognition observed with MIPs.

To prove the versatility of our method for functionalizing QDs, commercially available red-QDs emitting at 660 nm were tested. Methylene blue/TEA was used for initiation to ensure spectral overlap between QD emission and initiator absorption. A HEMA/EbAM shell was grafted around the QDs, followed by a MIPNANA shell, by the same procedure as described for green-QDs. The polymers were then photobleached to eliminate any methylene blue fluorescence. The increase in size of the QDs after coating was verified by DLS measurements (see Figure S2B). The stoichiometry and binding constant of the AB–NANA complex were obtained by NMR titration studies in [D_6]-DMSO, which yielded a 1:1 ratio and a high K_a value of $41 \times 10^3\,\text{M}^{-1}$ (see Figure S5).

The specificity of MIPNANA-QDs was evaluated by equilibrium binding assays with [^{3}H]sialic acid in water. MIPNANA bound more sialic acid than NIPNANA (Figure 4A), thus indicating the creation of imprinted sites. Competitive equilibrium binding assays showed that there was $< 10\%$ cross-reactivity with GlcA and negligible cross-reactivity with other terminal sugars: *N*-acetylglucosamine, *N*-acetylgalactosamine, galactose, and glucose (see Figure S7 and Table S1). In quantitative cell imaging, MIPNANA-QDs showed 48% more binding than NIPNANA-QDs. MIP staining specificity was confirmed by enzymatic treatment of the cells with neuraminidase (see Figure S9), which yielded a fluorescence profile similar to that of NIP-QD stained cells (Figure 4B).

Our next step was to investigate whether multiplexed imaging of GlcA and NANA on fixed keratinocytes was possible. The spatial distribution of MIP-QDs targeting GlcA or NANA on keratinocytes was determined with epifluorescence microscopy (Figures 3C and 4C). As expected, the particles were found almost exclusively in regions where cells were present. Confocal microscopy was then used to study the

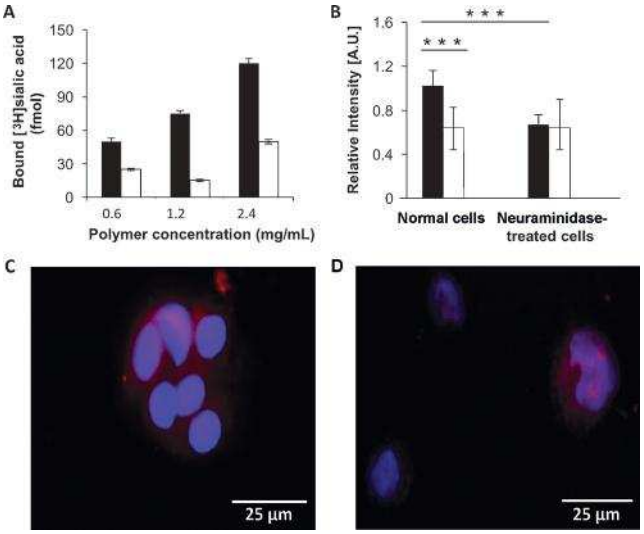

Figure 4. A) Equilibrium binding assay of MIPNANA-QDs (black) and NIPNANA-QDs (white) with [^{3}H]sialic acid in water. B) Relative fluorescence intensity of keratinocytes after imaging with MIP-QDs (black) and NIP-QDs (white), with and without neuraminidase treatment ($n = 4$ independent replicates with quadruplicates in each experiment). Mean values of MIP and NIP for normal cells, and of MIP for normal cells and MIP for hyaluronidase-treated cells, are significantly different at 99.9% confidence ($p \leq 0.001$***). C, D) Staining of keratinocytes (C) and KU812 (D) with MIP-QDs (red); nuclear staining with DAPI (blue).

distribution of MIP-QDs along the z axis. The MIPGlcA-QDs (green) were localized extracellularly, pericellularly, and intracellularly, even within the nucleus in some cases (see Figure S11 A). Nuclear staining, due to the distribution of hyaluronan in nuclear clefts, has been reported previously.[31] MIPNANA-QDs (red) were localized mainly extra- and pericellularly (see Figure S11 B), in accord with the localization of terminal sialic acids in human cells.[24,32] The use of organic dyes to stain the nucleus shows that MIP-QD staining can be readily coupled with other staining methods without interference or loss of specificity (Figure 5). This study demonstrates for the first time the potential of molecularly imprinted polymers when conjugated to quantum dots of different emission colors as a versatile multiplexed imaging tool.

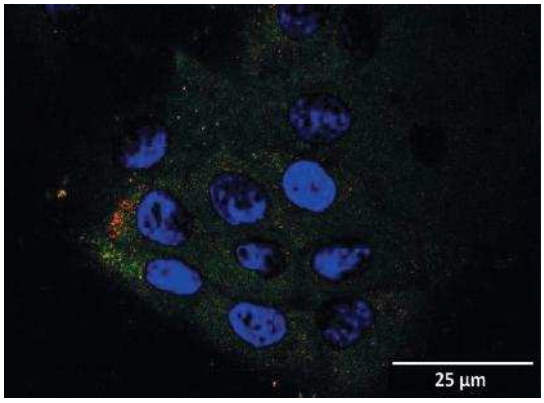

Figure 5. Confocal microscope image showing simultaneous multiplexed staining of GlcA and NANA on human keratinocytes by MIPGlcA-QDs (green) and MIPNANA-QDs (red). Nuclear staining with DAPI (blue).

In conclusion, we have developed a convenient and generic strategy to coat QDs with thin polymer shells to impart functionalization and biocompatibility by photopolymerization using the visible fluorescent light emitted from QDs upon excitation by UV light. MIP-coated QDs imprinted with glucuronic and *N*-acetylneuraminic acid were used for the recognition of hyaluronic acid and sialylated glycoproteins and glycolipids on keratinocytes as an illustrative example of the multiplexed detection of glycosylations in cells. The application of MIP-coated QDs as artificial receptors and imaging agents for glycosylation sites paves the way for new applications in diagnostics, theranostics, and therapeutics.

Acknowledgments

This research was supported by the European Regional Development Fund, the Region of Picardy (CPER 2007–2013), and the European Commission (FP7 Marie Curie Actions, projects NANODRUG, MCITN-2011-289554, and SAMOSS, PITN-2013–607590). We thank F. Nadaud and C. Boulnois for TEM measurements.

Keywords: bioimaging · molecularly imprinted polymers · nanocomposites · quantum dots · synthetic receptors

How to cite: *Angew. Chem. Int. Ed.* **2016**, *55*, 8244–8248
Angew. Chem. **2016**, *128*, 8384–8388

[1] X. Michalet, F. F. Pinaud, L. A. Bentolila, J. M. Tsay, S. Doose, J. J. Li, G. Sundaresan, A. M. Wu, S. S. Gambhir, S. Weiss, *Science* **2005**, *307*, 538–544.
[2] A. P. Alivisatos, W. W. Gu, C. Larabell, *Annu. Rev. Biomed. Eng.* **2005**, *7*, 55–76.
[3] F. Wei, G. Hu, Y. Wu, X. Wang, J. Yang, L. Liu, P. Zhou, Q. Hu, *Sens. Actuators B* **2016**, *229*, 38–46.
[4] E. Petryayeva, W. R. Algar, I. L. Medintz, *Appl. Spectrosc.* **2013**, *67*, 215–252.
[5] X. Gao, Y. Cui, R. M. Levenson, L. W. K. Chung, S. Nie, *Nat. Biotechnol.* **2004**, *22*, 969–976.
[6] T. Pons, E. Pic, N. Lequeux, E. Cassette, L. Bezdetnaya, F. Guillemin, F. Marchal, B. Dubertret, *ACS Nano* **2010**, *4*, 2531–2538.
[7] K. T. Yong, H. Ding, I. Roy, W. C. Law, E. J. Bergey, A. Maitra, P. N. Prasad, *ACS Nano* **2009**, *3*, 502–510.
[8] P. D. McNaughter, J. C. Bear, D. C. Steytler, A. G. Mayes, T. Nann, *Angew. Chem. Int. Ed.* **2011**, *50*, 10384–10387; *Angew. Chem.* **2011**, *123*, 10568–10571.
[9] H. Chibli, L. Carlini, S. Park, N. M. Dimitrijevic, J. L. Nadeau, *Nanoscale* **2011**, *3*, 2552–2559.
[10] S. Beyazit, S. Ambrosini, N. Marchyk, E. Palo, V. Kale, T. Soukka, B. Tse Sum Bui, K. Haupt, *Angew. Chem. Int. Ed.* **2014**, *53*, 8919–8923; *Angew. Chem.* **2014**, *126*, 9065–9069.
[11] M. Panagiotopoulou, S. Beyazit, S. Nestora, K. Haupt, B. Tse Sum Bui, *Polymer* **2015**, *66*, 43–51.
[12] V. C. Hascall, A. K. Majors, C. A. de la Motte, S. P. Evanko, A. Wang, J. A. Drazba, S. A. Strong, T. N. Wight, *Biochim. Biophys. Acta Gen. Subj.* **2004**, *1673*, 3–12.

[13] N. M. Varki, A. Varki, *Lab. Invest.* **2007**, *87*, 851 – 857.
[14] S. Seton-Rogers, *Nat. Rev. Cancer* **2012**, *12*, 228.
[15] C. Büll, M. A. Stoel, M. H. den Brok, G. J. Adema, *Cancer Res.* **2014**, *74*, 3199 – 3204.
[16] a) A. Kawamura, I. Kijima-Suda, M. Sugimoto, M. Itoh, K. Takada, K. Tomita, T. Ogawa, Y. Nagai, *Biochim. Biophys. Acta* **1990**, *1033*, 201 – 206; b) X. Xu, A. K. Jha, D. A. Harrington, M. C. Farach-Carson, X. Jia, *Soft Matter* **2012**, *8*, 3280 – 3294.
[17] a) M. J. Whitcombe, N. Kirsch, I. A. Nicholls, *J. Mol. Recognit.* **2014**, *27*, 297 – 401; b) L. Ye, *Adv. Biochem. Eng./Biotechnol.* **2015**, *150*, 1 – 24.
[18] L. Chen, X. Wang, W. Lu, X. Wu, J. Li, *Chem. Soc. Rev.* **2016**, *45*, 2137 – 2211.
[19] a) B. Tse Sum Bui, K. Haupt, *J. Mol. Recognit.* **2011**, *24*, 1123 – 1129; b) C. Baggiani, L. Anfossi, C. Giovannoli, *Mol. Imprinting* **2013**, *1*, 41 – 54.
[20] a) X. A. Ton, B. Tse Sum Bui, M. Resmini, P. Bonomi, I. Dika, O. Soppera, K. Haupt, *Angew. Chem. Int. Ed.* **2013**, *52*, 8317 – 8321; *Angew. Chem.* **2013**, *125*, 8475 – 8479; b) G. Ertürk, H. Özen, M. A. Tümer, B. Mattiasson, A. Denizli, *Sens. Actuators B* **2016**, *224*, 823 – 832; c) P. S. Sharma, Z. Iskierko, A. Pietrzyk-Le, F. D'Souza, W. Kutner, *Electrochem. Commun.* **2015**, *50*, 81 – 87.
[21] V. Pichon, F. Chapuis-Hugon, *Anal. Chim. Acta* **2008**, *622*, 48 – 61.
[22] a) B. Li, J. Xu, A. J. Hall, K. Haupt, B. Tse Sum Bui, *J. Mol. Recognit.* **2014**, *27*, 559 – 565; b) E. V. Piletska, B. H. Abd, A. S. Krakowiak, A. Parmar, D. L. Pink, K. S. Wall, L. Wharton, E. Moczko, M. J. Whitcombe, K. Karim, S. A. Piletsky, *Analyst* **2015**, *140*, 3113 – 3120.
[23] S. Kunath, M. Panagiotopoulou, J. Maximilien, N. Marchyk, J. Sänger, K. Haupt, *Adv. Healthcare Mater.* **2015**, *4*, 1322 – 1326.
[24] S. Shinde, Z. El-Schich, A. Malakpour, W. Wan, N. Dizeyi, R. Mohammadi, K. Rurack, A. G. Wingren, B. Sellergren, *J. Am. Chem. Soc.* **2015**, *137*, 13908 – 13912.
[25] a) D. Yin, S. Wang, Y. He, J. Liu, M. Zhou, J. Ouyang, B. Liu, H. Y. Chen, Z. Liu, *Chem. Commun.* **2015**, *51*, 17696 – 17699; b) S. Wang, D. Yin, W. Wang, X. Shen, J. J. Zhu, H. Y. Chen, Z. Liu, *Sci. Rep.* **2016**, *6*, 22757 – 22767.
[26] S. Nestora, F. Merlier, S. Beyazit, E. Prost, L. Duma, B. Baril, A. Greaves, K. Haupt, B. Tse Sum Bui, *Angew. Chem. Int. Ed.* **2016**, *55*, 6252 – 6256; *Angew. Chem.* **2016**, *128*, 6360 – 6364.
[27] A. Kugimiya, T. Takeuchi, *Biosens. Bioelectron.* **2001**, *16*, 1059 – 1062.
[28] A. G. Mayes, L. I. Andersson, K. Mosbach, *Anal. Biochem.* **1994**, *222*, 483 – 488.
[29] S. Xu, J. Ziegler, T. Nann, *J. Mater. Chem.* **2008**, *18*, 2653 – 2656.
[30] C. A. de la Motte, J. A. Drazba, *J. Histochem. Cytochem.* **2011**, *59*, 252 – 257.
[31] S. P. Evanko, W. T. Parks, T. N. Wight, *J. Histochem. Cytochem.* **2004**, *52*, 1525 – 1535.
[32] L. M. Steirer, G. R. Moe, *PLoS One* **2011**, *6*, e27249.

Received: January 31, 2016
Revised: March 17, 2016
Published online: May 30, 2016

Biosensors and Bioelectronics 88 (2017) 85–93

Contents lists available at ScienceDirect

Biosensors and Bioelectronics

journal homepage: www.elsevier.com/locate/bios

Fluorescent molecularly imprinted polymers as plastic antibodies for selective labeling and imaging of hyaluronan and sialic acid on fixed and living cells

Maria Panagiotopoulou, Stephanie Kunath, Paulina Ximena Medina-Rangel, Karsten Haupt*, Bernadette Tse Sum Bui*

Sorbonne Universités, Université de Technologie de Compiègne, CNRS Enzyme and Cell Engineering Laboratory, Rue Roger Couttolenc, CS 60319, Compiègne Cedex, 60203 France

ARTICLE INFO

Article history:
Received 18 June 2016
Received in revised form
11 July 2016
Accepted 23 July 2016
Available online 25 July 2016

Keywords:
Molecularly imprinted polymers
Hyaluronan
Glycosylation
Sialic acid
Cell imaging
Quantum dots

ABSTRACT

Altered glycosylation levels or distribution of sialic acids (SA) or hyaluronan in animal cells are indicators of pathological conditions like infection or malignancy. We applied fluorescently-labeled molecularly imprinted polymer (MIP) particles for bioimaging of fixed and living human keratinocytes, to localize hyaluronan and sialylation sites. MIPs were prepared with the templates D-glucuronic acid (GlcA), a substructure of hyaluronan, and N-acetylneuraminic acid (NANA), the most common member of SA. Both MIPs were found to be highly selective towards their target monosaccharides, as no cross-reactivity was observed with other sugars like N-acetyl-D-glucosamine, N-acetyl-D-galactosamine, D-glucose and D-galactose, present on the cell surface. The dye rhodamine and two InP/ZnS quantum dots (QDs) emitting in the green and in the red regions were used as fluorescent probes. Rhodamine-MIPGlcA and rhodamine-MIPNANA were synthesized as monodispersed 400 nm sized particles and were found to bind selectively their targets located in the extracellular region, as imaged by epifluorescence and confocal microscopy. In contrast, when MIP-GlcA and MIP-NANA particles with a smaller size (125 nm) were used, the MIPs being synthesized as thin shells around green and red emitting QDs respectively, it was possible to stain the intracellular and pericellular regions as well. In addition, simultaneous dual-color imaging with the two different colored QDs-MIPs was demonstrated. Importantly, the MIPs were not cytotoxic and did not affect cell viability; neither was the cells morphology affected as demonstrated by live cell imaging. These synthetic receptors could offer a new and promising imaging tool to monitor disease progression.

1. Introduction

Altered glycosylation levels or distributions on the surface of cells are indicators of pathological conditions like infection or malignancy. Recent advances in glycobiology and cancer research have defined the key processes underlying aberrant glycosylations with sialic acids or hyaluronan in cancer and its consequences (Hascall et al., 2004; Fuster and Esko, 2005; Varki and Varki, 2007; Varki et al., 2009; Büll et al., 2014). Hyaluronan is a linear glycosaminoglycan composed of alternating units of D-glucuronic acid (GlcA) and N-acetyl-D-glucosamine (GlcNAc) (Fig. S-1, SI). Sialic acid (SA) is a generic term used to describe *N* and *O*-derivatives of neuraminic acid, of which the most common member is N-acetylneuraminic acid (NANA). Because the polysaccharides involved in the glycosylation procedure have a highly conserved simple composition and are ubiquitously expressed in all animals that have a developed immune response, they are so-called weak antigens. Therefore, production of antibodies that specifically recognize them is naturally difficult, and traditional immunohistochemical methods for detecting glycosylations on cells are rare (Kawamura et al., 1990; De la Motte and Drazba, 2011).

In this context, tailor-made molecularly imprinted polymers (MIPs) are promising synthetic receptor materials (Haupt et al., 2012; Piletsky and Whitcombe, 2013). Molecular imprinting is based on a templating process at the molecular level. Monomers carrying functional groups self-assemble around a template molecule (the target or a derivative), followed by copolymerization with cross-linking monomers, which results in the formation of a polymeric mold around the template. Subsequent removal of the template reveals three-dimensional binding sites in the polymer that are complementary to the template in size, shape and

* Corresponding authors.
E-mail addresses: maria.panagiotopoulou@utc.fr (M. Panagiotopoulou), stephanie.kunath@web.de (S. Kunath), paulina.rangel@utc.fr (P.X. Medina-Rangel), karsten.haupt@utc.fr (K. Haupt), jeanne.tse-sum-bui@utc.fr (B. Tse Sum Bui).

http://dx.doi.org/10.1016/j.bios.2016.07.080
0956-5663/

position of the functional groups. MIPs exhibit binding affinities and specificities comparable to those of antibodies. Their use as antibody mimics was first proposed by Mosbach's group (Vlatakis et al., 1993), and they are now sometimes referred to as 'plastic antibodies' (Haupt and Mosbach, 1998). In contrast to antibodies, their production is reproducible, relatively fast and economic, and no animals are necessary. Moreover, they are physically and chemically stable and are not degraded by proteases or denatured by solvents. Thus, MIPs have a great potential in providing a robust and specific imaging tool that reveals the location/distribution, time of appearance and structure of glycosylation sites on/in cells, which would lead to a better insight of the tremendously diverse biological processes in which these molecules are involved.

Very recently, we have published short communications on bioimaging of cells and tissues with MIPs labeled with organic dyes and quantum dots (QDs) (Kunath et al., 2015; Panagiotopoulou et al., 2016). To the same end, Sellergren's group has coated silica cores with a MIP shell containing nitrobenzoxadiazole as a fluorescent reporter group, to target SA on cell surface glycans (Shinde et al., 2015). Liu's group has reported SA-imprinted silica nanoparticles for surface enhanced Raman scattering imaging of cancer cells and tissues (Yin et al., 2015) as well as FITC-labeled silica particles with a shell imprinted with either SA, fucose or mannose to image these monosaccharides, overexpressed on cancer cells (Wang et al., 2016). Herein, we describe a more thorough study with MIPs labeled with organic dyes or quantum dots for multiplexed cell targeting and imaging, where we also show that single and dual-color imaging on live cells is feasible. To this goal, we synthesized fluorescently labeled molecularly imprinted polymers for imaging of human keratinocytes in order to localize and quantify hyaluronan and sialylation moieties on and in the cells. Since molecular imprinting of entire biomacromolecules like proteins or oligosaccharides is challenging, we opted for what is called the "epitope approach", which was inspired by nature (Bossi et al., 2007; Kryscio and Peppas, 2012; Bie et al., 2015). The monosaccharides, GlcA and NANA were used as templates to prepare the MIPs. Thus if GlcA and NANA are present and not sterically hindered, as for instance at the terminal end of hyaluronan or proteoglycans or glycoconjugates, they would be recognized and labeled. NANA is reported to be located extracellularly, at the end of sugar chains of sialylated proteins and sphingolipids on the glycocalix, whereas GlcA, apart from being extensively found in hyaluronan, is also present in some proteoglycans such as chondroitin sulfate, heparan sulfate and dermatan sulfate, though in lower proportions (Fig. 1) (Varki et al., 2009). Rhodamine-labeled MIP nanoparticles of size ~400 nm were synthesized in order to probe extracellular targets, and MIPs as a thin shell on InP/ZnS quantum dot particles with size ~125 nm were prepared for probing intracellular and pericellular hyaluronan (Evanko and Wight, 1999, 2001; Tammi et al., 2001).

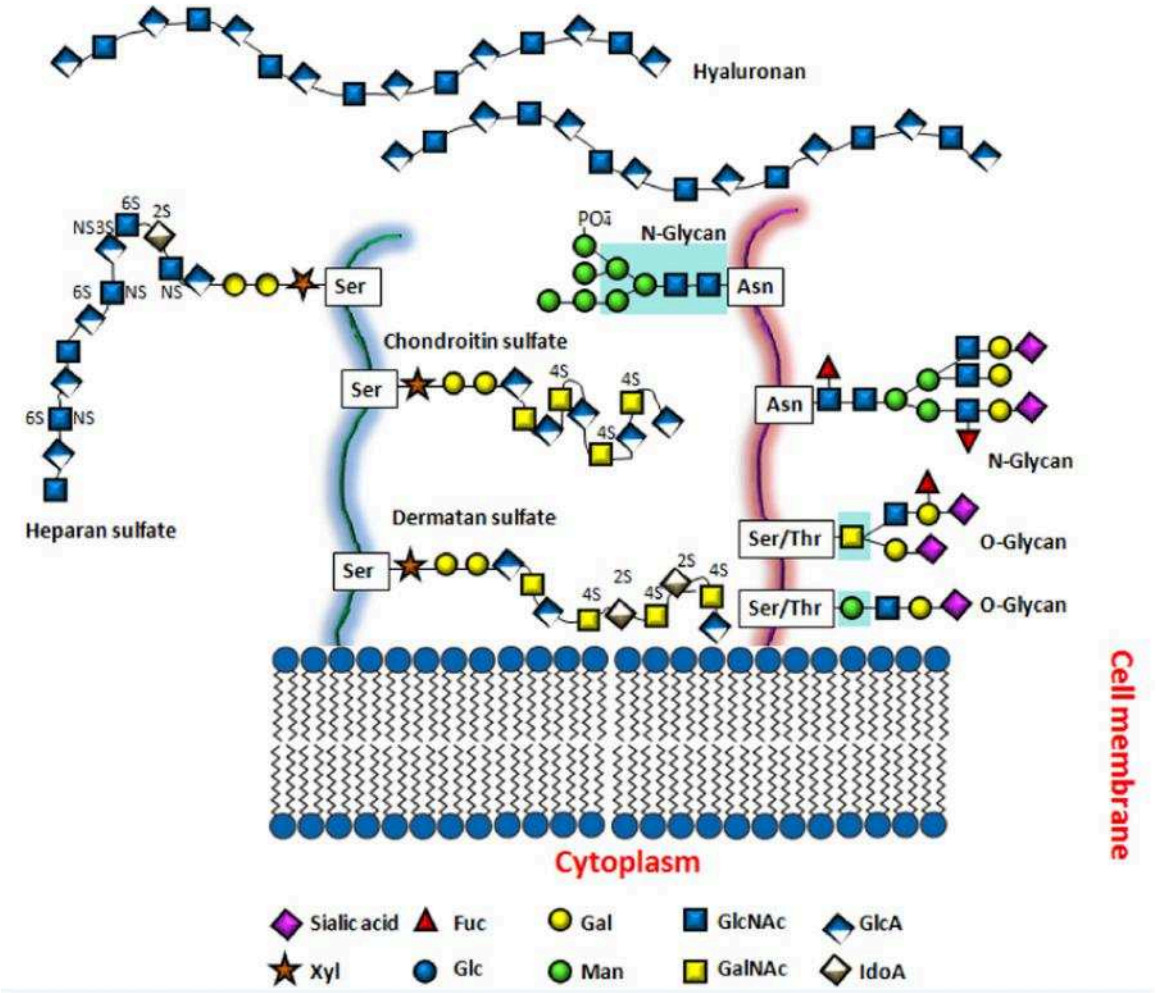

Fig. 1. The glycocalyx is a cell-coat structure of glycans and glycoconjugates that surrounds the cell membranes. Glucuronic acid (GlcA) is found extensively in hyaluronan and in smaller proportions, in dermatan sulfate, chondroitin sulfate and heparan sulfate while N-acetylneuraminic acid (sialic acid) is found at the terminal end of glycoproteins. Fuc: fucose; Gal: galactose; GlcNAc: N-acetylglucosamine; Xyl: xylose, Glc: glucose; Man: mannose; GalNAC: N-acetylgalactosamine; IdoA: iduronic acid. Adapted from Varki et al., 2009.

These particles were then used to image the presence of GlcA and NANA in both fixed and living human keratinocytes by epifluorescence and confocal fluorescence microscopy.

2. Materials and methods

2.1. Reagents and materials are described in SI

2.1.1. Preparation of MIP-GlcA and MIP-NANA

0.022 mmol of GlcA or NANA and 0.022 mmol of the functional monomer (4-acrylamidophenyl)(amino)methaniminium acetate (AB), were incubated for 1 h in 1 mL dimethylsulfoxide (DMSO). AB was synthesized as previously described (Nestora et al., 2016). This mixture was then transferred to a 4 mL glass vial containing 0.066 mmol methacrylamide (MAM), 0.423 mmol ethylene glycol dimethacrylate (EGDMA), 0.0055 mmol ABDV (stock solution of 3.4 mg ABDV in 1300 μL DMSO from which 524 μL was pipetted into the vial) and 270 μL DMSO. The vials were sealed with an airtight septum and the mixture was purged with nitrogen for 5 min under ice. The polymerization was thermally initiated at 48 °C for 18 h. As a control, non-imprinted polymers were synthesized in the same way but in the absence of the template molecule. The polymer particles were transferred to 50 mL polypropylene centrifuge tubes and washed on a tube rotator (SB2, Stuart Scientific), 3 times with methanol: acetic acid (9:1) followed by 3 times with a 7:3 mixture of 100 mM NH_3 (in water): methanol, twice with water and 3 times with methanol. The particles were dried overnight under vacuum.

Rhodamine-labeled MIPs were prepared as described above by additionally incorporating polymerizable rhodamine B (PolyFluor 570) at a ratio 0.05:1 (rhodamine B: AB) to the polymerization mixture.

2.2. Preparation of MIPGlcA-QDs and MIPNANA-QDs

Green (λ_{em}=550 nm) and red (λ_{em}=660 nm) InP/ZnS QDs were used to label MIPGlcA and MIPNANA respectively. Green QDs (size ~20 nm) were synthesized as previously described (Panagiotopoulou et al., 2016) and red QDs (size ~5 nm) were purchased from SIGMA. The polymers are synthesized as described below. First a shell of poly(2-hydroxyethyl methacrylate (HEMA)-*N,N′*-ethylenebis(acrylamide) (EbAM)) was synthesized. In a 4 mL glass vial containing 16.4 mg (0.097 mmol) of EbAM, 26.5 μL (0.22 mmol) of HEMA and 100 μg green-QDs (100 μL from a 1 mg/mL solution diluted from a stock (5 mg/mL) in toluene), were added 300 μL DMSO: toluene (1:1), 20 μL of eosin Y (10 mM in DMSO: toluene (1:1)) and 10 μL of triethylamine (TEA) (72 mM in DMSO: toluene (1:1)). The vial was sealed with an airtight septum and the mixture was purged with nitrogen for 2 min. Polymerization was initiated by irradiation at 365 nm with a UV lamp placed at ~2 cm from the vials. After 2 h of reaction at room temperature, the content was transferred to 2 mL polypropylene microcentrifuge tubes. Subsequently, 500 μL of DMSO: toluene (1:1) was added and the particles were ultrasonicated, then sedimented by centrifugation for 15 min at 17,500*g*. The particles were washed 4 times with 800 μL DMSO: toluene (1:1), followed by DMSO, and twice with water. Finally, the nanoparticles, called HEMA-QDs, were dried overnight under vacuum.

A MIP shell was then synthesized on the HEMA-QDs. 5.46 mg (0.022 mmol) of AB and 4.27 mg (0.022 mmol) GlcA were incubated for 1 h in 1 mL DMSO. Following the pre-incubation step, the contents of the vial were transferred to a 4 mL glass vial containing HEMA-QDs. Subsequently, 80 μL (0.423 mmol) of EGDMA, 5.62 mg (0.066 mmol) MAM, 20 μL of eosin Y and 10 μL of TEA were added. The same procedure was followed in the absence of the template, for the synthesis of the NIP. The vials were sealed with an airtight septum and the mixture was purged with nitrogen for 2 min. The polymerization was initiated by irradiation at 365 nm. After 2 h of reaction at room temperature, the content was transferred to 2 mL polypropylene microcentrifuge tubes and the particles were washed 3 times with methanol: acetic acid (9:1) followed by 3 times with 100 mM NH_3 (in water):methanol (7:3), twice with water and 3 times with methanol. Eosin Y trapped inside the particles was photobleached overnight with a fluorescent tube. The particles were dried overnight under vacuum. MIPNANA-QDs were synthesized using the same protocol as described above using NANA as template, red-QDs instead of green-QDs and methylene blue instead of eosin Y.

2.3. Evaluation of the binding properties of MIP-GlcA and MIP-NANA

The binding properties of the polymers towards GlcA and NANA in water were evaluated by equilibrium binding experiments. Rhodamine-MIPs/NIPs or QDs-MIPs/NIPs (5 mg/mL) were suspended in water in a sonicating bath. From this stock suspension, increasing amounts of polymer particles were pipetted in separate 2-mL polypropylene microcentrifuge tubes. After addition of either radiolabeled glucuronic acid (225 pmol, 12 nCi) or sialic acid (500 fmol, 10 nCi), the final volume was adjusted to 1 mL with water and the mixture was incubated overnight on a tube rotator. The samples were centrifuged at 30,000*g* for 15 min and a 500 μL aliquot of the supernatant was pipetted into a scintillation vial that contained 4 mL of scintillation liquid. The amount of free radioligand was measured with a liquid scintillation counter and the amount of radiolabeled analyte bound to the polymer particles was calculated by subtracting the amount of the unbound analyte from the total amount of the analyte added to the mixture.

Competitive binding assays were performed on non-labeled MIP-GlcA and MIP-NANA in a similar way to the binding studies described above but in methanol: water (1:9), a solvent which is closer in composition to the one used for cell preparation and fixation before imaging. Stock solutions of GlcA, NANA, acetic acid, glucose, N-acetylglucosamine, galactose and N-acetylgalactosamine (2 mM) were prepared in water. The competitors were added at concentrations ranging from 0.1 nM to 100 μM, in order to compete with 0.5 nM [6-^{3}H]sialic acid or 0.225 μM D-[6-^{14}C]glucuronic acid in the binding assays, with a constant amount of 0.3 mg of MIP per vial.

2.4. Cell culture

Human adult low calcium high temperature (HaCaT) cells were cultured in Dulbecco's Modified Eagle Medium (DMEM)-high glucose with 10% fetal bovine serum (FBS) and 1% penicillin/streptomycin medium, hereafter referred as cell culture medium in the text, at 37 °C, 5% CO_2 and 100% humidity. Cells were passaged when confluent using 0.25% trypsin/ethylenediaminetetraacetic acid (EDTA) in PBS buffer. For biochemical assays and microscopic studies, the cells were cultured in 12-well plates (well diameter 22.1 mm) equipped with round glass cover slips (diameter 12 mm). 100 μL of 1×10^5 suspended HaCaT cells were pipetted onto each cover slip. After 3 h of incubation, 2 mL of medium was added to the cells. Afterwards, they were left to grow to confluency for 48–60 h.

2.5. Sample preparation and cell fixation for epifluorescence and confocal microscopy imaging

Each cover slip with confluent HaCaT cells in 12-well plates was washed 3 times with 2 mL PBS and fixed at room temperature for

10 min in 600 μL paraformaldehyde (3% w/v) in PBS. To stop fixation, each cell sample was incubated 3 times with 1 mL 20 mM glycine in PBS for 20 min at room temperature and finally they were washed 3 times with 2 mL PBS. After fixation, the cells were incubated for 90 min with 600 μL hyaluronidase (sheep testis) (75 U) or neuraminidase (*Arthrobacter ureafaciens*) (25 U) solution in PBS at 37 °C (positive control) or left in PBS without enzyme (untreated samples). The cells were then washed 3 times with 1 mL methanol: water (1:30) and then incubated with either 1 mL of a sonicated polymer suspension of 0.06 mg/mL MIPGlcA-QDs or MIPNANA-QDs or 0.027 mg/mL rhodamine MIPGlcA or rhodamine MIPNANA, in methanol: water (1:30) at 37 °C for 90 min. Afterwards, each fixed cell layer was washed 3 times with 1 mL methanol: water (1:30) and then mounted for fluorescence microscopy imaging on a microscope slide with 5 μL mounting medium. The mounting medium consisted of 0.5 mL water, 0.5 mL 1 M Tris-HCl buffer pH 8 and 9 mL glycerol.

For the staining of the cell nucleus, a stock solution of 1 mg/mL 4′,6-diamidin-2-phenylindol (DAPI) in water was diluted 10 times with mounting media. 5 μL from that solution was placed on a microscope slide to mount the cells on cover slips. After 3 min, the image capture took place (see SI).

2.6. Cytotoxicity testing

Cell viability in presence of MIPs was determined using the MTT assay (Mosmann, 1983). The MTT assay is a colorimetric assay for assessing the metabolic activity of living cells. NAD(P)H-dependent cellular oxidoreductase enzymes reflect in this case the number of viable cells present. These enzymes reduce the tetrazolium dye 3-(4,5-dimethylthiazol-2-yl)−2,5-diphenyltetrazolium bromide (MTT) to form insoluble formazan, which has a purple color. HaCaT cells were grown to confluency as described in Section 2.4. After trypsinisation, the cells were diluted with cell culture medium to 15,000 cells, which were seeded in each well of a 96-well plate. After 24 h, cells were incubated with MIP (1–27 μg/mL) or $CdCl_2$ (0–45 μM) for 24 h in cell culture medium. Dissolution of the blue crystals of MTT was achieved by DMSO and Sorensen's buffer. Cell viability was determined by dividing the absorbance obtained for treated cells by that of the untreated controls.

2.7. MIP incubation on live cell samples

2.7.1. Rhodamine-labeled

HaCaT cells were grown on cover slips to confluency in duplicate as described in Section 2.4. Afterwards, they were washed 3 times with PBS and 3 times with cell culture medium and incubated with 1 mL of a 0.027 mg/mL rhodamine-MIPs suspension in cell culture medium at 37 °C for 90 min. Then, the samples were washed 3 times with cell culture medium and mounted on microscopy slides for imaging.

2.7.2. Multiplexed imaging

For multiplexed imaging, the cells were prepared as described above and incubated with suspensions of 1 mL of 0.027 mg/mL rhodamine-MIPNANA and 1 mL of 0.06 mg/mL MIPGlcA-QDs in cell culture medium at 37 °C for 90 min. Then, the samples were washed 3 times with cell culture medium and mounted on microscopy slides for imaging.

3. Results and discussion

3.1. Synthesis and characterization of polymers

MIPs for GlcA and NANA without any fluorescent labeling, were first synthesized and their binding performances evaluated by equilibrium binding studies. Precipitation polymerization in DMSO was used (Kunath et al., 2013). AB and MAM were used as functional monomers and EGDMA as crosslinker, with a molar ratio template: AB:MAM: EGDMA of 1:1:3:20 (Fig. S-2, SI). MAM was added to provide hydrogen bonding interactions with the template and to render the MIP more hydrophilic to prevent aggregation in the aqueous cell imaging medium. AB contains an amidinium moiety and is called a 'stoichiometric monomer' (Wulff and Knorr, 2001) since it can form strong 1:1 electrostatic interactions with –COOH groups on the template (association constants: $K_{a(GlcA)} = 7.1 \times 10^3\ M^{-1}$ and $K_{a(NANA)}\ 41 \times 10^3\ M^{-1}$), as deduced from ^1H NMR titrations in DMSO-d_6 (Panagiotopoulou et al., 2016).

The recognition properties of the polymers were evaluated by radioligand equilibrium binding assays in water. Fig. 2A shows that both MIPs were specific towards their respective template as the binding with the control non-imprinted polymer was lower. To evaluate their selectivity, competitive binding assays at equilibrium were performed. A fixed amount of MIPGlcA was incubated with radiolabeled glucuronic acid (225 nM) or MIPNANA was incubated with radiolabeled sialic acid (0.5 nM), in the presence of varying amounts of other sugar molecules present on the glycocalix or structurally related compounds at concentrations between 0.1 nM and 100 μM (Fig. S-3, SI). The values of IC_{50} (the concentrations of non-labeled GlcA or NANA required to displace 50% of the radioligand) for MIPGlcA and MIPNANA respectively, determined from a nonlinear regression fit, were 495 nM and 4500 nM. Moreover, the two MIPs exhibited negligible affinity for all of the competitors, and very little cross-reactivity is observed between GlcA and NANA, thus confirming their selectivity for their target (Table S-1, SI). Therefore, these MIPs if labeled with fluorescent tags would constitute powerful selective recognition tools for cell labeling and imaging. For this purpose, MIPs were either labeled with the dye rhodamine or with QDs.

3.2. Synthesis and characterization of MIPGlcA and MIPNANA labeled with rhodamine B

Fluorescent dye moieties were incorporated into the polymer matrix by adding a polymerizable rhodamine derivative to the prepolymerization mixture. Its molar ratio with respect to the other monomers was optimized to maximize the fluorescence intensity of the particles (optimal ratio 1:0.05, AB: rhodamine). Higher dye content resulted in lower brightness due to reabsorption or energy transfer. Using a precipitation polymerization mixture with a C_m (total mass of functional and cross-linking monomers/total mass of solvent and monomers) of 5% and a CL (moles of cross-linking monomers/total moles of functional and cross-linking monomers) of 83%, MIP and NIP particles with diameters of ~400 nm, with a good monodispersity were obtained (Fig. 2C). This particle size was chosen to avoid possible internalization of the particles, so as to target the extracellular hyaluronan and sialylation sites. The fluorescence intensities of the MIP and NIP particles were determined with a spectrofluorimeter and were found to be similar with less than 10% deviation (Fig. 2D), which was taken into account for quantification in microscopic images. Their binding characteristics were similar to those of unlabeled polymers (Fig. 2A).

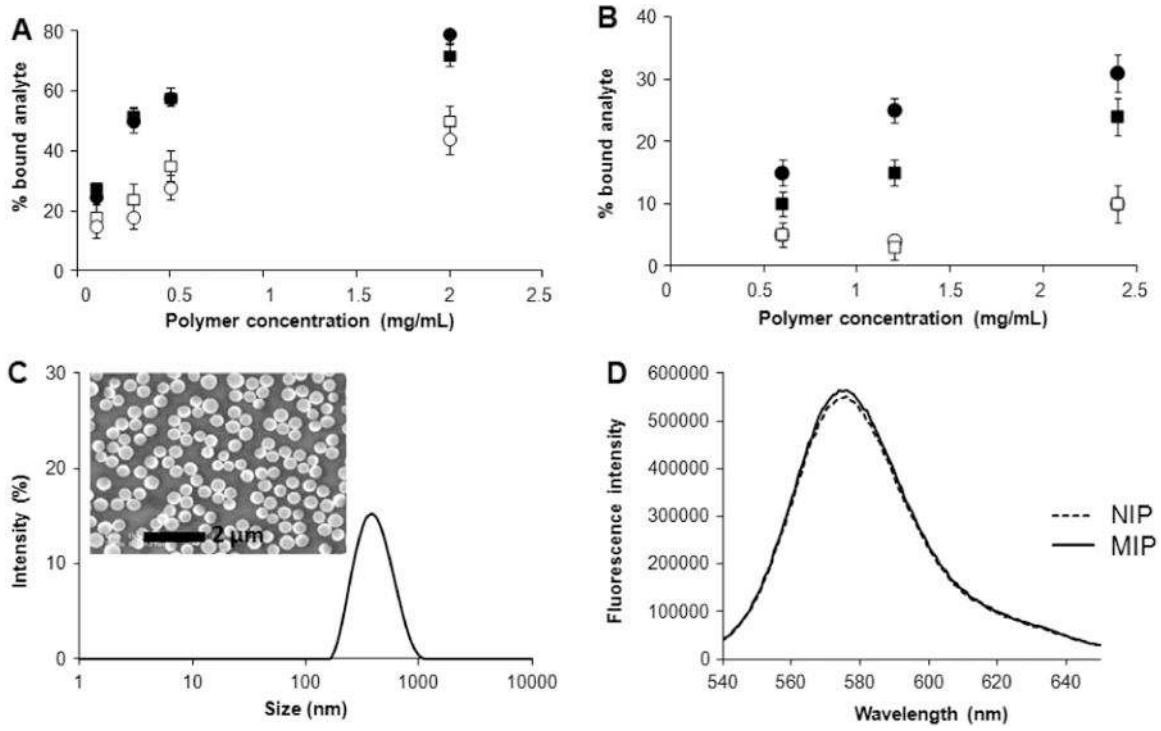

Fig. 2. (A) Equilibrium binding isotherms in water of [^{14}C]D-glucuronic acid (225 pmol,12 nCi) and [^{3}H]sialic acid (500 fmol, 10 nCi) respectively to: (A) MIPGlcA (full circles), NIPGlcA (empty circles), MIPNANA (full squares) and NIPNANA (empty squares); (B) MIPGlcA-QDs (full circles), NIPGlcA-QDs (empty circles), MIPNANA-QDs (full squares) and NIPNANA-QDs (empty squares). Values are means from three independent experiments and the error bars represent the standard deviation; (C) Size distribution of MIPGlcA as measured by dynamic light scattering in water, SEM image (inset); (D) Fluorescence emission spectra of rhodamine-MIPGlcA and rhodamine-NIPGlcA, λ_{ex}=540 nm).

3.3. MIPGlcA and MIPNANA labeled with rhodamine B for imaging fixed cells

A standard immunostaining protocol was adapted and optimized to the application of MIPs for cell imaging, to localize and quantify hyaluronic acid or sialic acid on keratinocytes (HaCaT cells). The protocol with the different steps is shown in Fig. 3A. The fixation of cells is based on paraformaldehyde, which has a low background fluorescence. A blocking step is then performed with glycine, to stop the fixation and reduce nonspecific binding. Glycine does not induce aggregation of the MIP particles, unlike bovine serum albumin which was also tested. An (optional) additional step, to confirm the specificity of the MIP staining, is treatment with hyaluronidase or neuraminidase. Hyaluronidase hydrolyzes the *endo*-N-acetylhexosaminic bonds of hyaluronan, thus eliminating terminal glucuronic acid groups and generating terminal N-acetylglucosamine on the cell surface, and neuraminidase eliminates terminal sialic acid residues. The final step is the incubation with MIP particles, or with NIP particles as a control. The spatial distribution and localization of rhodamine-labeled MIPs on the cells was determined by epifluorescence and confocal microscopy. The red fluorescent MIP particles, due to their large size, are localized on the cell surface (Fig. 3B-C).

By applying this optimized protocol, MIPGlcA and MIPNANA showed respectively 44% and 48% more binding to the cells than their corresponding NIPs (Fig. 3D). After hyaluronidase or neuraminidase treatment, there was no significant difference anymore between MIP and NIP, thus confirming the specific labeling of the MIPs for their targets. These results are comparable to those obtained with a reference method where staining was done with a biotinylated hyaluronic acid binding protein (De la Motte and Drazba, 2011), coupled with fluorescein isothiocyanate-labeled straptavidin in the place of rhodamine-MIPGlcA (Kunath et al., 2015).

The relatively high binding of the non-imprinted polymer is due to the presence in these particles of randomly distributed aminidinium groups from the functional monomer AB ($K_a > 10^3\ M^{-1}$, as deduced from ^{1}H NMR). We should stress, though, that the NIP binding does not reflect the extent of non-specific binding of the MIP, since in the MIP the amidine groups are located in specific binding sites. The NIP was only used to confirm the molecular imprinting effect. Thus, these results illustrate the specificity of the binding of GlcA-imprinted polymer particles to hyaluronan and NANA-imprinted particles to sialylation sites on human keratinocytes.

3.4. MIPGlcA and MIPNANA labeled with rhodamine B for imaging live cells

MIPGlcA and MIPNANA, labeled with rhodamine B were also applied for imaging living cells. First, an assessment of the cytotoxicity of the MIPs was done using an MTT assay with polymer concentrations previously used for fixed cell imaging. $CdCl_2$ was used as a positive control to induce cell death. Fig. 4A shows that the MIP, up to a concentration of 27 µg/mL, does not reduce the viability of keratinocytes incubated for 24 h. Furthermore, the polymer particles are stable and do not seem to aggregate in the culture medium. Subsequently, vital keratinocytes were incubated for 90 min with MIPs in cell culture medium. Fig. 4B-C shows that the binding of the polymer particles is limited to areas where cells were present, indicating specific binding to hyaluronic acid or sialic acid. Interestingly, one can observe that the cell morphology was not influenced by the presence of the polymer particles, and this even after 48 h incubation (results not shown). Thus, imaging

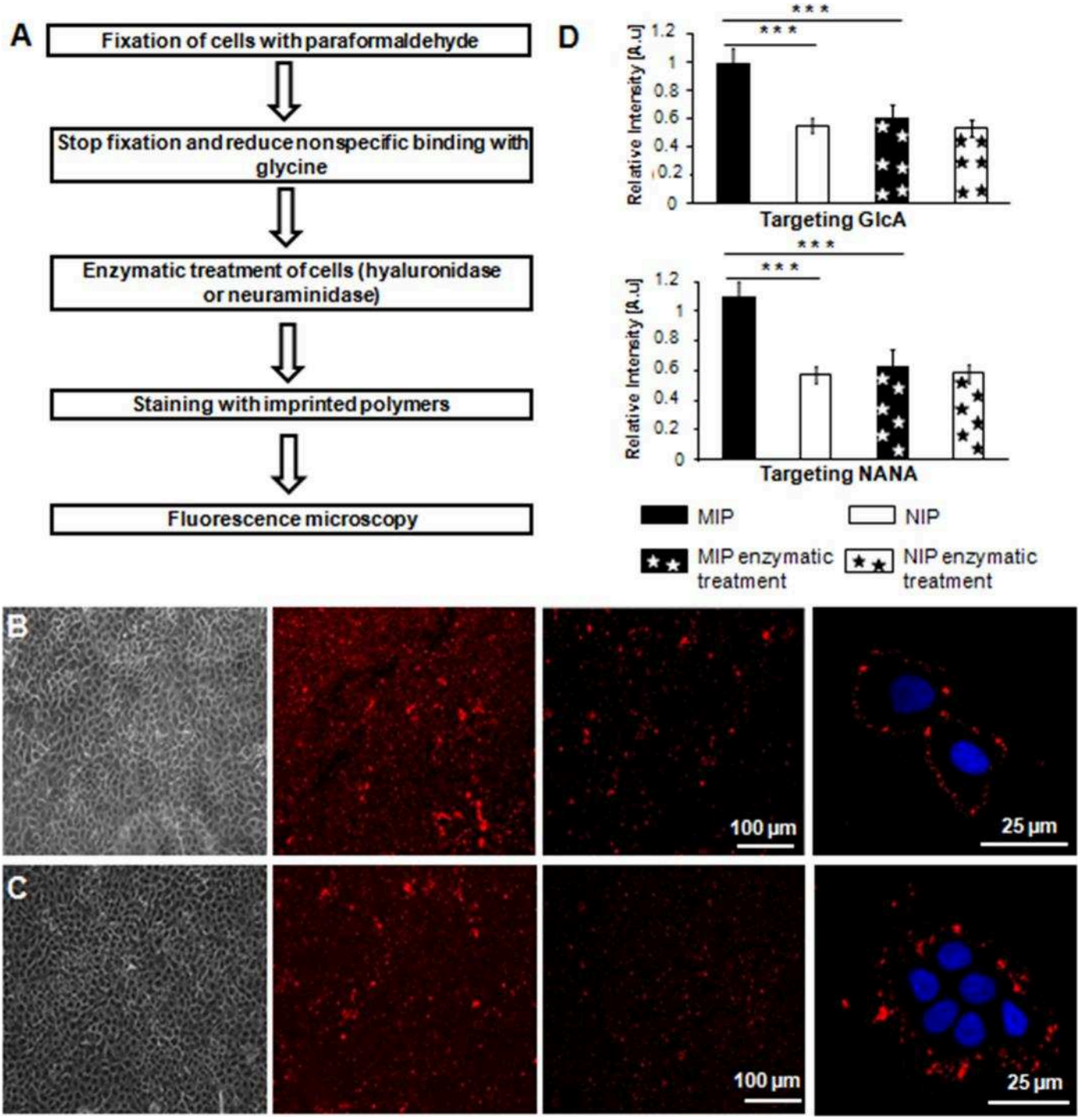

Fig. 3. (A) Protocol for cell staining with molecularly imprinted polymers; Representative microscope images of confluent HaCaT cells that were fixed and stained with (B) rhodamine-MIPGlcA and (C) rhodamine-MIPNANA. From left to right: phase contrast image, cells stained by MIP, cells enzymatically (hyaluronidase or neuraminidase) treated and stained by MIP (all epifluorescence images), corresponding confocal image showing extracellular labeling, cell nucleus stained with DAPI; (D) Relative fluorescence intensities of cells after imaging with MIP-QDs (black) and NIP-QDs (white), with and without enzymatic treatment, n=4 independent replicates with quadruplicates for each experiment. Error bars represent the standard deviation. Mean values of MIP and NIP for normal cells, and of MIP for normal cells and MIP of enzymatically-treated cells, are significantly different at 99.9% confidence ($p \leq 0.001^{***}$).

of live cells is possible; this paves the way to real-time imaging of changes in hyaluronan or sialic acid within the cells.

3.5. *Synthesis and characterization of MIPGlcA-QDs and MIPNANA-QDs*

Green QDs were used to prepare MIP-GlcA and red QDs to prepare MIP-NANA. A thin shell of MIP was synthesized around single QDs by making use of the visible light emitted from the QDs when excited by a UV light source (365 nm). The QDs were used with appropriate initiator systems, whereby the emission wavelength of the QDs must overlap with the absorption of the initiator (Beyazit et al., 2014) (Fig. S-4, SI). Since emission from QDs is weak as compared to direct light, polymerization is confined to the close proximity of the QD surface, yielding core-shell particles (Fig. S-5, SI). For instance, for preparing MIPGlcA, a water-compatible shell

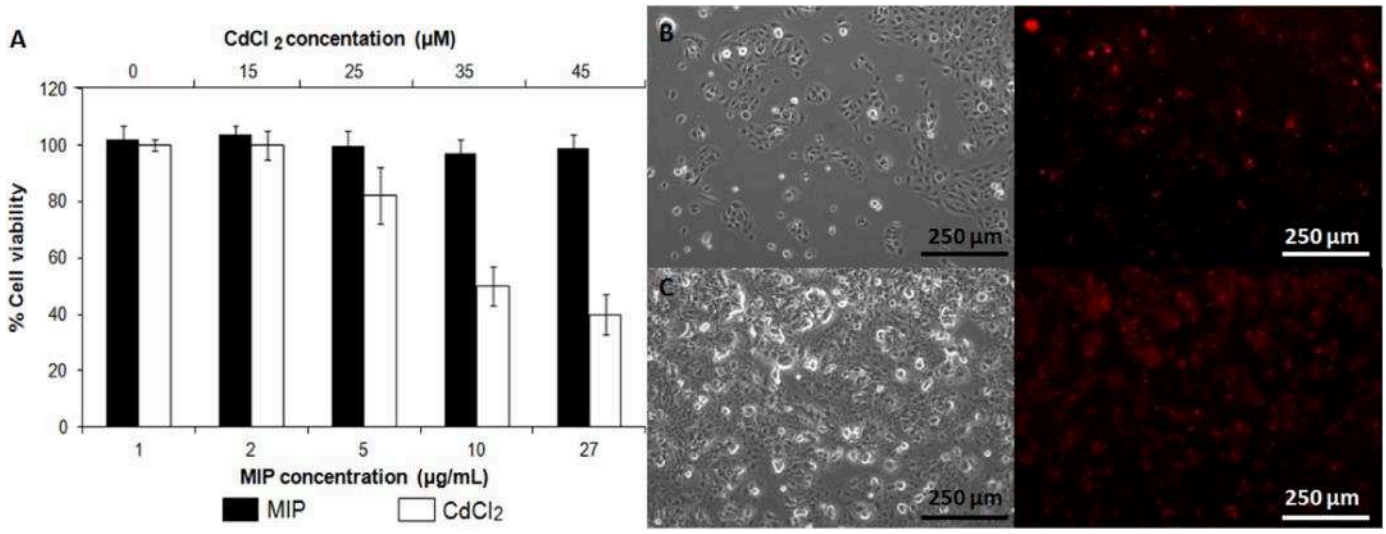

Fig. 4. Living human keratinocytes exposed to rhodamine-MIPs. (A) Cell viability (MTT) assay in cell culture medium with MIPGlcA and $CdCl_2$ serving as a positive control. Results were obtained from 2 independent experiments from different days with 8 replications each, error bars represent the standard deviation; Vital keratinocytes grown on cover slips and stained with (B) rhodamine-MIPGlcA and (C) rhodamine-MIPNANA (right) with their corresponding phase contrast (left).

obtained by polymerization of HEMA and EbAM in the presence of the initiator couple, eosin Y/TEA, was first polymerized around the green-QDs using the green light emitted by the QDs. This shell stabilizes the QDs for their further conjugation in polar solvents. The MIP shell imprinted with GlcA was then photopolymerized on top of the first shell. The MIP precursors mixture contained GlcA, AB, MAM, EGDMA and eosin/TEA. A control non-imprinted polymer (NIP) was prepared in the same way but without the addition of GlcA. A similar procedure was adopted for preparing MIPNANA-QDs, except that red QDs and the initiator couple, methylene blue/TEA, were employed. The formation of polymer shells around green and red QDs was monitored by dynamic light scattering measurements (Fig. S-6, SI).

To make sure that entrapped residual eosin and methylene blue do not interfere with fluorescence measurements, the resulting MIPs were photobleached before imaging experiments. Both MIPs were specific towards their respective template (Fig. 2B). However, the extent of binding was lower due to the lower capacity of the thinner MIP shell, as compared to the rhodamine-MIPs (Fig. 2A). It is important to note that the thickness of the MIP shell can be controlled by varying the photopolymerization time. This allows to fine-tune the particle size; in this case we chose a smaller particle size than the rhodamine MIPs to be able to target intracellular hyaluronan.

3.6. MIPGlcA-QDs and MIPNANA-QDs for imaging fixed cells

For quantitative cell-imaging with the MIP-QDs on human keratinocytes, the same optimized immunostaining protocol as described for the rhodamine-labeled MIPs was applied. The localization of the MIPGlcA-QDs (green) and MIPNANA-QDs (red) on the cells are shown in Fig. 5A-B. MIPGlcA-QDs and MIPNANA-QDs showed 42% and 48% more binding to the cells than their respective NIP-QDs (Fig. 5C). The specificity of the MIP staining was confirmed by hyaluronidase or neuraminidase treatment, which resulted in the same fluorescence profile as staining by the NIP. Thus, these results illustrate the specificity of the binding of GlcA-imprinted polymer particles to hyaluronan and NANA-imprinted particles to sialic acids on human keratinocytes.

3.7. Simultaneous dual-color imaging of fixed and living human keratinocytes with two different color MIPs

3.7.1. Fixed keratinocytes

Since selective labeling and imaging could be achieved by the individual fluorescent MIPs, it was interesting to prove the flexibility of our cell staining protocol (Fig. 3A) by applying it for multiplexing with two different colored MIPs. Confocal microscopy was used to study the distribution of MIPGlcA-QDs and MIPNANA-QDs. Fig. 6A and Fig. 5B show that the MIPNANA-QDs (red) were localized mainly extra- and pericellularly, in accord with the localization of terminal sialic acids in human cells (Fuster and Esko, 2005; Varki et al., 2009; Shinde et al., 2015; Wang et al., 2016). MIPGlcA-QDs (green) were localized extracellularly, pericellularly and intracellularly, even within the nucleus in some cases. Nuclear staining, due to the distribution of hyaluronan in nuclear clefts, has previously been reported (Evanko and Wight, 1999, 2001). The use of organic dyes to stain the nucleus shows that MIP-QDs staining can be easily coupled with other staining methods without interference or loss of specificity.

3.7.2. Living keratinocytes

Alterations in glycosylations have been found to regulate cell cycle progression and cytokinesis; more specifically, enhanced glycosylation has been associated to certain phases of the cell cycle like mitosis (Chou and Omary, 1993; Evanko and Wight, 1999; Stevens and Spang, 2013). Therefore, multiplexed imaging of the overexpressed polysaccharides could provide some information on the levels of the extracellular and intracellular glycosylations during the cell cycle. MIPGlcA-QDs (green) and rhodamine-MIPNANA (red) were used to demonstrate multiplexed staining in living cells. Fig. 6B shows that some cells seem to be more brightly stained by the MIPs. This could correspond to the G_2 and mitosis phases indicating the presence of more glycosylation sites. Hence, imaging in live cells with our MIPs could help to correlate glycosylation activity with cell growth.

4. Conclusions

We have synthesized molecularly imprinted polymers, either

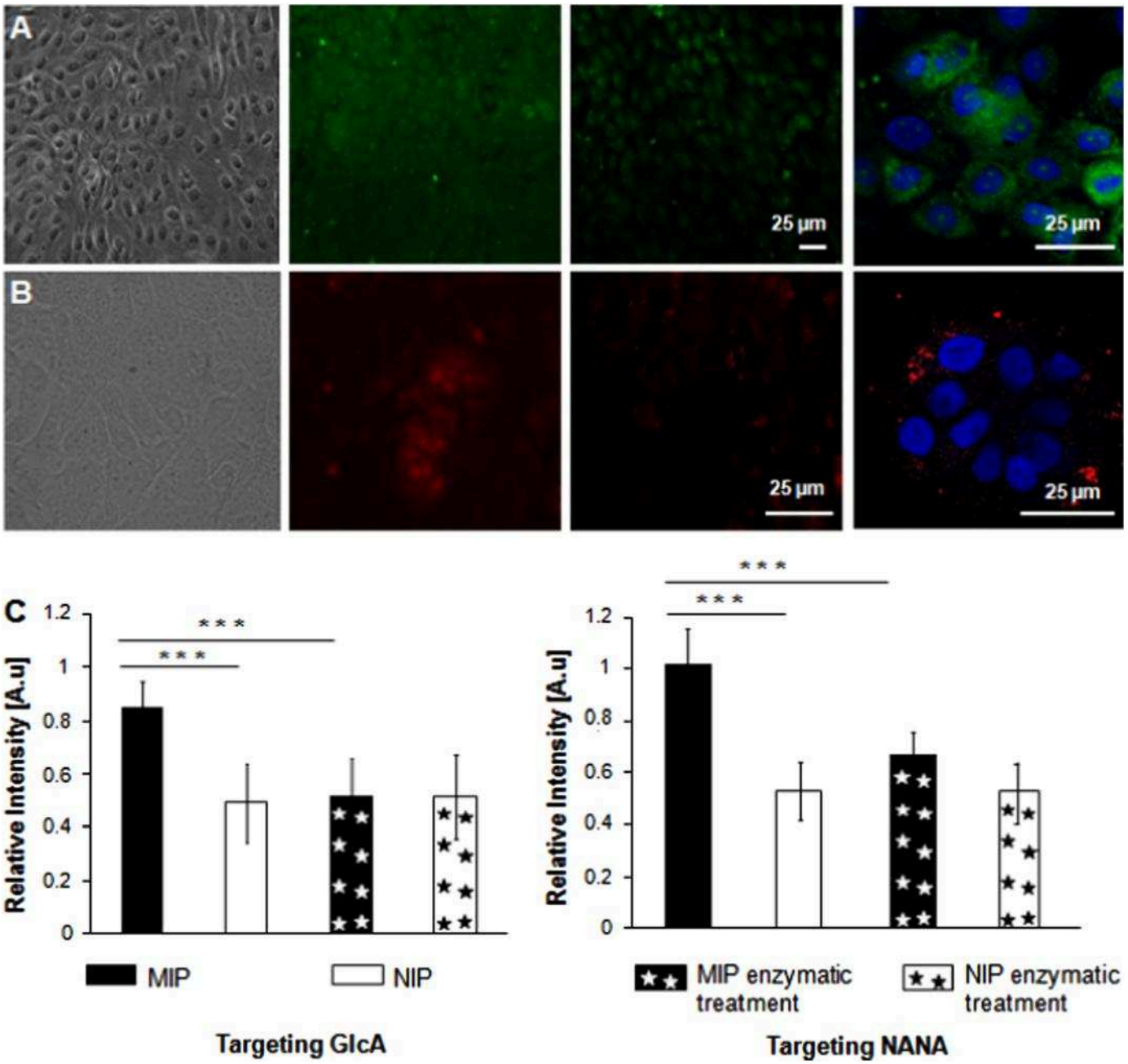

Fig. 5. Representative microscope images of confluent HaCaT cells that were fixed and stained with (A) MIPGlcA-QDs (green) and (B) MIPNANA-QDs (red). From left to right: phase contrast image, cells stained by MIP, cells enzymatically (hyaluronidase or neuraminidase) treated and stained by MIP (all epifluorescence images), corresponding confocal image showing the location of the particles, cell nucleus stained with DAPI; (C) Relative fluorescence intensities of cells after imaging with MIP-QDs (black) and NIP-QDs (white), with and without enzymatic treatment, n=4 independent replicates with quadruplicates for each experiment, error bars represent the standard deviation. Mean values of MIP and NIP for normal cells, and of MIP for normal cells and MIP of enzymatically-treated cells, are significantly different at 99.9% confidence ($p \leq 0.001^{***}$). (For interpretation of the references to color in this figure legend, the reader is referred to the web version of this article.)

labeled with a fluorescent organic dye or with QDs, for selectively targeting and imaging hyaluronan and sialylated glycosylation sites on/in human keratinocytes. A standard immunostaining protocol was successfully adapted for MIP staining on fixed cells. It is worth noting that the MIP protocol is more advantageous as it is straightforward and does not require primary and secondary antibodies. Simultaneous dual-color imaging of the cells with two MIP-coated QDs of different emission colors (red for targeting the sialic acid moiety and green for targeting the glucuronic acid of hyaluronan) was also demonstrated, proving the versatility of our method. Moreover, the MIPs were not cytotoxic and could be applied to live cell labeling and imaging, which opens the way to the possibility of real-time imaging of glycosylation level and distribution in the cells. For application to other molecular targets on and in cells and tissues, suitable functional monomers have to be found for the MIP that allow for strong yet specific interactions even in aqueous media, which may be a limitation in some cases. Also, care needs to be taken concerning the size and surface properties of the particles. Particles below 150 nm can sometimes be passively and non-specifically internalized by the cell. This kind of synthetic receptors has potential not only as a bioimaging tool but also can behave as a targeted drug delivery device or a specific blocking agent on cells and tissues.

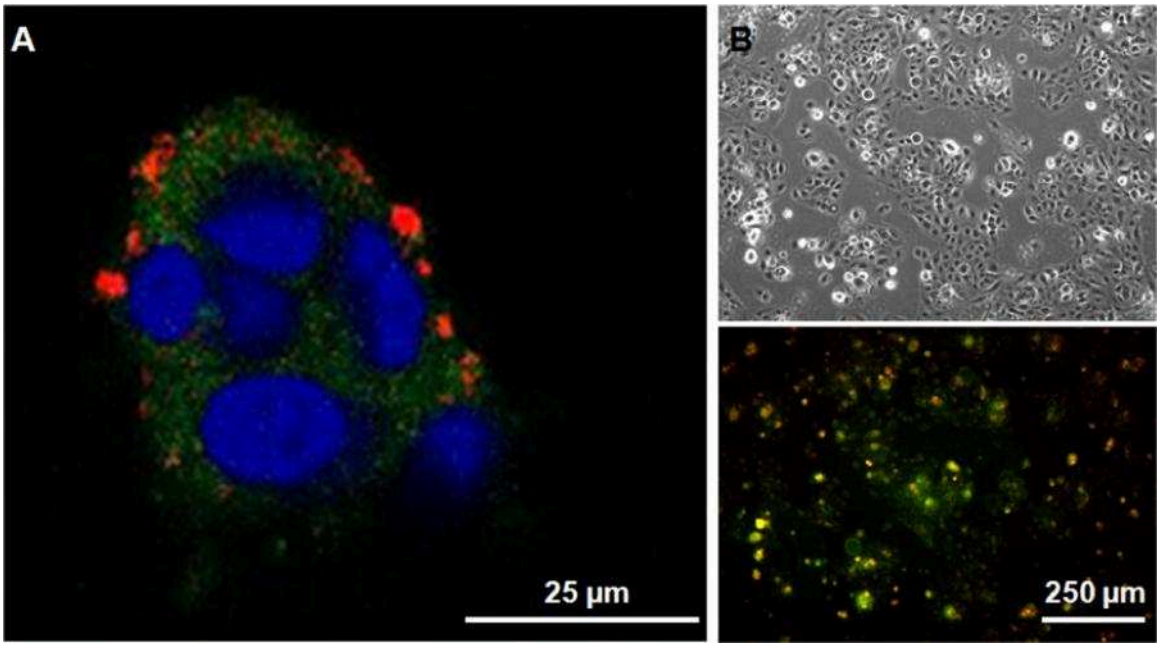

Fig. 6. (A) Confocal image showing simultaneous multiplexed labeling of GlcA and NANA on fixed human keratinocytes by MIPClcA-QDs (green) and MIPNANA-QDs (red) respectively. Nuclear staining with DAPI; (B) Epifluorescence image of vital keratinocytes grown on cover slips and stained with both MIPGlcA-QDs (green) and rhodamine-MIPNANA (red) (bottom) and phase contrast (top). (For interpretation of the references to color in this figure legend, the reader is referred to the web version of this article.)

Acknowledgments

This work was supported by the European Regional Development Fund, the Region of Picardy (CPER 2007–2013), the European Commission FP7 Marie Curie Actions (SAMOSS, PITN-2013-607590) and the French embassy in Germany (postdoctoral scholarship of S. Kunath). We thank F. Nadaud and C. Boulnois for SEM and TEM measurements.

Appendix A. Supplementary material

Supplementary data associated with this article can be found in the online version at http://dx.doi.org/10.1016/j.bios.2016.07.080.

References

Beyazit, S., Ambrosini, S., Marchyk, N., Palo, E., Kale, V., Soukka, T., Tse Sum Bui, B., Haupt, K., 2014. Angew. Chem. Int. 53, 8919–8923.
Bie, Z., Chen, Y., Ye, J., Wang, S., Liu, Z., 2015. Angew. Chem. Int. 54, 10211–10215.
Bossi, A., Bonini, F., Turner, A.P.F., Piletsky, S.A., 2007. Biosens. Bioelectron. 22, 1131–1137.
Büll, C., Stoel, M.A., Den Brok, M.H., Adema, G.J., 2014. Cancer Res. 74, 3199–3204.
Chou, C.-F., Omary, M.B., 1993. J. Biol. Chem. 268, 4465–4472.
De la Motte, C.A., Drazba, J.A., 2011. J. Histochem. Cytochem. 59, 252–257.
Evanko, S.P., Wight, T.N., 1999. J. Histochem. Cytochem. 47, 1331–1341.
Evanko, S.P., Wight, T.N., 2001. ⟨http://glycoforum.gr.jp/science/hyaluronan/HA20/HA20E.html⟩.
Fuster, M.M., Esko, J.D., 2005. Nat. Rev. Cancer 5, 526–542.
Hascall, V.C., Majors, A.K., De la Motte, C.A., Evanko, S.P., Wang, A., Drazba, J.A., Strong, S.A., Wight, T.N., 2004. Biochim. Biophys. Acta 1673, 3–12.
Haupt, K., Mosbach, K., 1998. Trends Biotechnol. 16, 468–475.
Haupt, K., Linares, A.V., Bompart, M., Tse Sum Bui, B., 2012. Top. Curr. Chem. 325, 1–28.
Kawamura, A., Kijima-Suda, I., Sugimoto, M., Itoh, M., Takada, K., Tomita, K., Ogawa, T., Nagai, Y., 1990. Biochim. Biophys. Acta 1033, 201–206.
Kryscio, D.R., Peppas, N.A., 2012. Acta Biomater. 8, 461–473.
Kunath, S., Marchyk, N., Haupt, K., Feller, K.-H., 2013. Talanta 105, 211–218.
Kunath, S., Panagiotopoulou, M., Maximilien, J., Marchyk, N., Sänger, J., Haupt, K., 2015. Adv. Healthc. Mater. 4, 1322–1326.
Mosmann, T., 1983. J. Immunol. Methods 65, 55–63.
Nestora, S., Merlier, F., Beyazit, S., Prost, E., Duma, L., Baril, B., Greaves, A., Haupt, K., Tse Sum Bui, B., 2016. Angew. Chem. Int. Ed. 55, 6252–6256.
Panagiotopoulou, M., Salinas, Y., Beyazit, S., Kunath, S., Mayes, A.G., Duma, L., Prost, E., Resmini, M., Tse Sum Bui, B., Haupt, K., 2016. Angew. Chem. Int. Ed. 55, 8244–8248 ⟨10.1002/anie.201601122R1⟩.
Piletsky, S.A., Whitcombe, M.J., 2013. Designing Receptors for the Next Generation of Biosensors, first ed. Springer-Verlag, Berlin, Heidelberg.
Shinde, S., El-Schich, Z., Malakpour, A., Wan, W., Dizeyi, N., Mohammadi, R., Rurack, K., Gjörloff Wingren, A., Sellergren, B., 2015. J. Am. Chem. Soc. 137, 13908–13912.
Stevens, J., Spang, A., 2013. PLoS One 8, e63687.
Tammi, R., Rilla, K., Pienimäki, J.-P., MacCallum, D.K., Hogg, M., Luukkonen, M., Hascall, V.C., Tammi, M., 2001. J. Biol. Chem. 276, 35111–35122.
Varki, N.M., Varki, A., 2007. Lab. Invest. 87, 851–857.
Varki, A., Cummings, R.D., Esko, J.D., Freeze, H.H., Stanley, P., Bertozzi, C.R., Hart, G. W., Etzler, M.E., 2009. Essentials of Glycobiology, second ed. Cold Spring Harbor, New York.
Vlatakis, G., Andersson, L.I., Müller, R., Mosbach, K., 1993. Nature 361, 645–647.
Wang, S., Yin, D., Wang, W., Shen, X., Zhu, J.J., Chen, H.Y., Liu, Z., 2016. Sci. Rep. 6, 22757–22767.
Wulff, G., Knorr, K., 2001. Bioseparation 10, 257–276.
Yin, D., Wang, S., He, Y., Liu, J., Zhou, M., Ouyang, J., Liu, B., Chen, H.Y., Liu, Z., 2015. Chem. Commun. 51, 17606–17699.